
The propagation and nucleation of magnetic domain walls in multi-turn counter sensor devices

Dissertation submitted

for the award of the title

"DOCTOR OF NATURAL SCIENCES"

Dissertation submitted

to the Faculty of Physics, Mathematics, and Computer Science

of Johannes Gutenberg University Mainz

in Mainz

BENJAMIN BORIE



JOHANNES GUTENBERG
UNIVERSITÄT MAINZ

Born in Cannes, France

Mainz, December 2017

Declaration of Authorship

I, Benjamin Borie, declare that this thesis titled, “The propagation and nucleation of magnetic domain walls in multi-turn counter sensor devices” and the work presented in it are my own. I confirm that:

- This work was done wholly or mainly while in candidature for a research degree at this University.
- Where any part of this thesis has previously been submitted for a degree or any other qualification at this University or any other institution, this has been clearly stated.
- Where I have consulted the published work of others, this is always clearly attributed.
- Where I have quoted from the work of others, the source is always given. With the exception of such quotations, this thesis is entirely my own work.
- I have acknowledged all main sources of help.
- Where the thesis is based on work done by myself jointly with others, I have made clear exactly what was done by others and what I have contributed myself.

Date:

Signature:

Zusammenfassung

Magnetische Domainwände sind Quasipartikel, welche Umlaufrichtung der Magnetisierung auf einer limitierten Längenskala angeben. In magnetischen Nanoleiterbahnen ist es möglich Domainwände mit einem angelegten magnetischen Feld zu manipulieren. Die hierbei auftretenden verschiedenen Prozesse und ihre Dynamik sind Gegenstand aktueller Forschung. Trotz dieser Tatsache werden Domainwände bereits als essenzieller Bestandteil nichtflüchtiger Sensoren genutzt. Erst der Einsatz von Domainwänden erlaubt diesen Sensoren eine „True Power On“ Funktionalität, welche von der Industrie für eine verbesserte Automatisierung benötigt wird. Derzeit ist das Arbeitsfenster dieser Sensoren stark beschränkt durch den Mangel an Erkenntnissen über die physikalischen Abhängigkeiten der ihn kontrollierenden Parameter. Diese Wissenslücke verhindert eine weitere Verbesserung derzeitiger Geräte und blockiert außerdem eine weitere Entwicklung und Skalierung der Technologie.

In dieser Arbeit präsentieren wir eine detaillierte Studie über die Propagation und Nukleation von Domainwänden in verschiedenen Schleifen Strukturen, welche relevant sind für die eigentliche Applikation. Außerdem werden innovative Konzepte der Sensor Geometrien vorgestellt und realisiert, welche ein Voranschreiten der Technologie zu ermöglichen. Um Einsicht in die Physik zu erhalten, welche die Propagations- und Nukleationswerte der Domainwände bestimmt, werden Parameter wie die Dicke, Breite und Profil der magnetischen Leiterbahnen untersucht. Weiterhin werden der Einfluss der Materialzusammensetzung, dessen Herstellungsbedingungen und die Lithographie

Prozesse eingehend getestet. Die zum Test verwendeten Magnetfeld Sequenzen ermöglichen eine komfortable Messung der beiden für den späteren Sensor wichtigen Feld Werte mittels verschiedener Messtechniken, wie dem magneto-optischen Kerr-Effekt oder dem Riesenmagnetowiderstand. Die auf diese Weise ermittelten Propagationsfelder der Domainwände scheinen robust gegenüber geometrischen Veränderungen des Leiters zu sein, jedoch stark abhängig von dem benutzten Material. Die Propagation der Domainwand zeigt eine deutlich höhere Sensitivität auf Pinning Stellen, welche durch Defekte im Herstellungsprozess verursacht werden. Durch ihr willkürliches Auftreten stellt der Nachweis dieser Art von Defekten eine besondere Herausforderung dar. Im Gegensatz hierzu finden wir für das Nukleationsfeld eine hyperbolische Abhängigkeit von der Streifenbreite und eine lineare Abhängigkeit von der Schichtdicke des magnetischen Materials. Letzteres erlaubt ein einfaches Anpassen und Verbessern des Arbeitsfensters des Sensors. Die experimentellen Ergebnisse zeigen eine gute Übereinstimmung mit mikromagnetischen Simulationen, was es ermöglicht, die physikalischen Ursachen für die Saturation des Nukleationsfeldes mit zunehmender Dicke zu identifizieren. Untersuchungen bezüglich der Abhängigkeit des Arbeitsfensters des Sensors von den Modifikationen der Depositionsbedingungen ergeben eine Robustheit gegenüber der Variation der Parameter. Einen höheren Einfluss hat hingegen die Benutzung von Elektronenstrahlolithographie, welche zu einer deutlichen Verringerung des Arbeitsfensters führt. Die Kombination der Ergebnisse dieser umfassenden Studie hebt die Bedeutung der untersuchten Parameter hervor und ermöglicht es systematisch eben diese den Anforderungen anzupassen, um das Arbeitsfenster für die angepeilte Applikation zu verbessern.

Im Anschluss wird ein innovatives Konzept vorgestellt, welches auf dem parallelen Zählen von teilerfremden, geschlossenen Schleifen Strukturen basiert. Diese geschlossenen Schleifen Strukturen beinhalten essenziell wichtige Kreuzungen von Magnetstreifen. Diese Kreuzungen zeigen eine hohe Störanfälligkeit bei der Rotation eines angelegten externen magnetischen Feldes, solange kein

zusätzlicher Siphon an jedem Arm der Kreuzung verwendet wird. Mittels mikromagnetischer Simulationen werden die Winkelabhängigkeit dieser Kreuzungen und der Siphon Struktur ermittelt. Die so erhaltenen physikalischen Prozesse erlauben eine Vorhersage für die Arbeitsfenster der Einzelemente. Die Überschneidung dieser Bereiche ermöglicht es die Arbeitsbereiche des kombinierten Elementes aus Siphons und Kreuzung abzuleiten und ergibt dessen Abhängigkeit von Parameter wie dem Winkel des Siphons oder der Größe der Kreuzung. Diese geometrischen Strukturen werden im Anschluss experimentell realisiert und über Variationen der Kreuzungsgeometrie als auch der des Siphons getestet. Die hierbei ermittelten Ergebnisse zeigen eine gute Übereinstimmung mit den Simulationen.

Als letztes werden Arbeiten an einem kompletten Sensor vorgestellt. Aus diesen geht hervor, dass die Nukleation von Domainwänden in der Mitte der Kreuzung ein limitierender Faktor für die Verbesserung des Konzepts ist, was in früheren Simulationen nicht beobachtet wurde. Diese experimentelle Realisierung demonstriert die Machbarkeit eines magnetischen Domainwand Sensors zur Erfassung von einer Million Umdrehungen.

Abstract

Magnetic domain walls are quasi-particles indicating the rotation of the magnetization direction on a constrained length scale. In magnetic nanoconduits, domain walls can be manipulated by an applied magnetic field, and the dynamics of the various processes occurring is still under active investigation. Despite being a state of the art research topic, domain walls are already utilized in nonvolatile sensors. In this sensor type, domain walls allow a true power on functionality as demanded by the industry for improved automatization. Currently, the field operating window of these sensors remains limited due to the lack of physical understanding of the parameters controlling it. This gap in our knowledge hinders an improvement of current devices and therefore blocks a route to a higher scaling of the technology.

In this thesis, we present a detailed study of the propagation and the nucleation of domain walls in various looping structures relevant for applications and realize innovative concepts for the advancement of the field. To grasp insight on the physics controlling the propagation and nucleation field values, parameters such as the cross-sectional shape, the thickness, and the width of wires, as well as material stack, deposition conditions, and patterning processes, are modified. Applied field sequences are created that allow the comfortable measurement of both field values with a various range of measurement techniques such as the magneto-optical Kerr effect or the giant magneto-resistance effect. The propagation field of domain walls appears mostly insensitive to geometrical changes but affected by changes of the material used as the conduit. The propagation of domain walls shows a much higher sensitivity to pinning sites created by defects of the patterning processes thus constituting a challenge due to their arbitrary occurrence. In contrast, the nucleation field exhibits a large hyperbolic and linear scaling, respectively, with the width and the thickness of the wire thus yielding a more comfortable handle for the improvement of the field operating window. The results appear in good agreement with micromagnetic simulations that allow the identification of the physical processes at the origin of the saturation of the scaling of the nucleation field. Also, the field operating window shows a robustness towards modifications of the deposition conditions but a significant decrease after the use of electron beam patterning. The combination of the results from this comprehensive study highlights the impact of the investigated parameters and enables the systematic tuning of the ones needed for improvement of the field operating window.

An innovative concept using the parallel coprime counting of closed-loop structures is then introduced. The closed-loop contains an essential cross-shape element, which appears unreliable under the rotation of an applied field without the placement of a syphon element on each arm of the cross. With the use of micromagnetic simulations, the individual angular dependence of the cross and the syphon are generated. The obtained physical processes provide with the field operation windows of the device concept for each element. The overlapping of their contribution yields a numerically working concept and its dependence on parameters such as syphon angle or cross-center dimension. The idea is then experimentally realized with variations in the cross and syphon geometry, and the results are in good agreement with the simulations. Finally, a complete built device helps to identify the nucleation in the center of the cross as a limiting factor for the improvement of the operating window of this concept, which was not observed in the previous simulations. This experimental realization demonstrates the feasibility of a magnetic domain wall based million-turn counting sensor device.

Contents

Declaration of Authorship	ii
Abstract	iii
1 Introduction	1
2 Theory notions	5
2.1 The magnetic terms	6
Spin of an electron	6
Micromagnetism	7
2.1.1 Zeeman energy	7
2.1.2 Exchange energies	8
Direct exchange	8
Magnetism in 3d-Metals	11
2.2 Anisotropy Energies	16
Magneto-crystalline anisotropy	16
Dipolar interaction	18
Other anisotropies	21
2.3 Dynamics of Magnetization	22
2.3.1 Landau-Lifshitz-Gilbert equation	22
2.3.2 The Stoner-Wohlfarth model	24
2.4 Domain Walls	26
2.4.1 Topology	26
Mathematical description of Topological defects	27
Non-trivial topological defect	27
Topology arguments for real samples	29
2.4.2 Magnetic domain walls	30
Transition from Superparamagnetism to multi-domain	30
1-Dimensional Domain wall model	31
In-plane Domain walls	35
2.4.3 Domain Wall Dynamics and Walker breakdown	37
2.4.4 Vortex motion under field	41
3 Experimental techniques	43
3.1 Investigated Materials	43
3.1.1 Spin-valve	45
3.2 Material processing techniques	46
3.2.1 Sputtering	47
3.2.2 Ion beam etching	48
3.3 Patterning methods	50

3.3.1	Resists processing	50
	Photolithography	51
	Electron beam lithography	53
3.4	Measurement techniques	53
3.4.1	Four-point-probe electrical measurement	53
3.4.2	BH-looper	54
3.4.3	Magneto-optical Kerr effect microscopy	55
	Semi-classical description of the Magneto-optical Kerr effect	55
	MOKE setup	60
3.4.4	Giant magneto-resistance effect	61
	Generale description of the GMR	61
	Mott's two current model	63
	Valet-Fert model	65
3.4.5	Atomic Force Microscopy	66
3.4.6	Scanning Electron Microscopy	68
3.4.7	X-ray diffraction	70
3.5	Sample fabrication	71
3.5.1	Lift-off method approach	72
3.5.2	Etching method	72
3.5.3	Standard manufacturing for the multiturn devices at Sensitec	74
3.5.4	Processing at Johannes Gutenberg University	75
	Etching	75
	Lift-off	76
3.6	Micromagnetic simulations	76
3.6.1	Mumax3	77
3.6.2	Simulated system	77
4	The open-16-loop structure	79
4.1	The open-loop sensor device	79
4.1.1	Advantages of the technology	80
4.1.2	Disadvantages of the technology	81
4.2	The investigated system	81
4.3	The structure and its shape characterization	83
4.3.1	Characterization of the cross-sectional shape	84
4.4	Sensor operation conditions	85
4.4.1	MOKE investigation	85
	Depinning field limit	86
	Nucleation field	89
4.4.2	GMR investigation	94
	Measurement algorithm	94
	Measurement results	96
4.5	Conclusion	98
5	Prospect for the improvement of the FOW of open-loop structures	99
5.0.1	Influence of the spatial spread over a wafer	100
	Nucleation field in a uniaxial applied field	100
	Depinning field in a uniaxial applied field	103
5.1	The creation of innovative designs for an improvement of the FOW	104
5.1.1	Modifications to the original open-16-loop device	105
5.1.2	Influence of the length of the wire	107

	Various length of open-2-loop devices	109
5.1.3	Influence of the reduction of the number of vertices in the corners	110
	Simulation of the nucleation for various vertices	111
	Structure characterization	112
5.1.4	Influence of an oscillatory width and pad geometry	113
5.1.5	Conclusion	115
5.2	Depinning field under large count of turns versus large number of elements	115
5.2.1	Measurement for a large number of sensor elements	115
5.2.2	Measurement for a large number of turns	116
5.2.3	Comparison between large number of element and large count of turns	120
5.2.4	Conclusion	120
5.3	Improvement of the nucleation field of the open-loop structures	120
5.3.1	Influence of the thickness of the magnetic layer	121
	Single layer thicknesses	121
	GMR stacks with changing free layer thickness	129
	Conclusion	130
5.3.2	Cross-sectional Shape modifications	131
	Desentanglement of the contributions to the scaling factor	131
	Experimental realization of cross-sectional shape modifications	133
	Conclusion	136
5.3.3	Modification of Ni ₈₁ Fe ₁₉ deposition conditions	136
	Processing at Sensitec	137
	Processing at Singulus	139
	Comparison between the Sensitec and Singulus processed wafers	141
	Conclusion	144
5.3.4	Influence of the patterning process	144
	Issues encountered	144
	Patterning using ebeam lithography with various negative tone resists	145
	Conclusion	149
5.4	Conclusion	150
6	The closed-loop structures for the uniturn sensor concept	152
6.1	Introduction	152
6.2	Concept for a DW based multi-turn counter with crosses and syphons elements	155
6.3	Micromagnetic simulations	162
6.3.1	Crossing of two magnetic stripes	162
	Variations of the initial chirality of the DW	166
	Change of the geometry of the cross	169
6.3.2	Syphon element	171
6.4	Full device geometry	173
6.5	Conclusion	175
7	Experimental realization of the closed-loop sensor device	177
7.1	Introduction	177
7.2	Fabrication and characterization	178
7.3	Cross-shaped intersection	179
7.3.1	Geometrical modifications to the center of the cross	182

7.4	Syphon structure	183
7.5	Combined and complete device	185
7.6	Conclusion	189
8	Conclusion	190
8.1	Outlooks	193
A	Valet-Fert model	196
B	Ebeam patterning parameters	200
C	Ion etching parameters	204
C.0.1	Etching sequences	204
D	AR-N 7520.073 patterning	206
E	HSQ resist	208
F	AR-N 7520.17 patterning	210
G	Mumax3 script	212
G.0.1	Python script for the automatization of simulations	212
G.0.2	Initial magnetic configuration	213
G.0.3	Dynamic simulation	214
H	Working Scheme of the device	215
I	Python scripts	219
I.0.1	Python script for the slicing of the AFM profiles	219
I.0.2	Code slicing the AFM micrograph	222
J	Innovative Designs	227
K	Data from the thickness simulations	240
	Bibliography	242

Abbreviations

- Domain wall: **DW**
- Stoner-Wohlfarth: **SW**
- Field operating window: **FOW**
- Giant magneto-resistance: **GMR**
- Magneto-optical Kerr effect: **MOKE**
- Superconducting quantum interference device: **SQUID**
- X-ray diffraction: **XRD**
- Standard deviation: **SD**

Chapter 1

Introduction

Magnetic domain walls (DWs) trace back to the origin of magnetism with some investigations already reported by Bloch in (1932), Landau and Lifshitz in (1935) and Néel in (1944). They constitute the interface between two magnetically ordered domains. In a domain wall, the magnetization usually rotates by 90° , 180° , or 360° . Despite its long history, the field of magnetic domain wall based applications is limited if not inexistent. Indeed, to use magnetic domain walls as quasi-particles, they need to reach nanometer size. Nevertheless, some ideas have been put forward such as the racetrack memory (1), which provides a memory storage in 3 dimensions and makes use of magnetic domain orientations in a wire to store information. The potential 3 dimensions can drastically improve the storage capabilities and boost the market of magnetic technological applications. However, so far, no domain wall based application for storage is used due to the extreme difficulty to control these objects. The magnetic domain wall based sensor devices field then position itself as the first industrial application of domain walls. The first essential historical milestones that enabled the creation of such sensors is the Giant Magneto-Resistance effect (GMR effect) (2, 3) discovered by Albert Fert and Peter Grünberg in 1988, respectively 1989, for which they were granted a Noble price. This discovery was possible due to improvements in the deposition techniques allowing for the growth of high-quality films with nanometer-sized layer thicknesses. The latter provided the industry with a mean of fast measurement of the magnetization directions which ultimately led to the flourishing of the DW based sensing industry. Also, the development of nano-patterning methods such as the photolithography allowed the mass-production of nanometer-sized structures, such as loops with 200 nm wire widths. Finally, the introduction of investigation methods with an atomic resolution allowed the necessary improvement of nanostructures unlocking their reliability and commercialization. In the past decade, the propagation of DWs in magnetic conduits was vastly researched (4–7) and their structure, as well as their dynamics, was starting to be known enough to generate larger structures than single wires. The nucleation field of DWs in nanowires was also addressed (8) and the development of a method for the introduction of DWs from a pad to a narrower wire (9) ultimately generated the first domain wall based devices. The propagation and nucleation field of domain walls in nanowires are essential features as they are the limiting bounds of the field operating window of domain wall based sensor devices. The first concepts of this novel type of sensors were introduced by the Institute of Photonic Technology in Jena (10–13), and in partnership with the company Novotechnik. It is now manufactured and developed by Sensitec GmbH and Novotechnik. This sensor had, and still has, for primary aim to count the number of full rotations performed by an applied magnetic field placed parallel to the plane of the sensor. Nowadays, in a world that is increasingly concerned by green technologies and reduction of energy consumption, magnetic domain wall based sensors offer a workable solution. In fact, magnetic

sensors in contrast to electrically based sensors do not require any power for the storage of their current state. Possibly even more relevant, no external power is needed for the change of the state of the sensor since a moving permanent magnet is enough to nucleate and propagate a domain wall in nanometer-sized magnetic wires. Finally, the electrical current density used for the operation of the sensor is limited thus there is virtually no damages done to the sensors guaranteeing a robustness to the concepts. Despite, being already ground-breaking, these sensor devices can still benefit from research. One of the big challenges is still the lack of knowledge on the effects governing the field operating window of the device. The improvement could be performed by modifications to the width or the thickness of the wires constituting the devices, or a change of the material ($\text{Ni}_{81}\text{Fe}_{19}$). Furthermore, the scaling of the current technology is limited to small counted numbers due to the dramatic decrease of the field operating window as the structure of the device is increased.

In this thesis, we address these issues by first choosing relevant investigation tools and creating magnetic applied field sequences allowing the comfortable research of the two limits constituting the field operating window. Some critical parameters in the structure and the patterning process are modified in order to obtain more physical insight on the parameters governing the FOW. Ultimately, these research are allowing the identification of the handles enabling a drastic improvement of the FOW. Finally, the limited scaling of the current structure is answered by presenting an innovative concept of DW based sensor device. The structure is then investigated numerically and then experimentally assessing its viability.

The thesis is divided into 8 parts:

Chapter II gives the theoretical background that allows for the understanding of the notion presented further. The origin of magnetism in 3d metals is explained as well as the energy terms that are acting in a magnetic material patterned at a micro- or nanometer scale. The equations of motion of magnetic spins under applied fields are described and the behavior of domain wall under an applied field as well. Concerning the propagation of domain walls, a brief introduction to Walker breakdown and depinning processes is given. Finally, the Stoner-Wohlfarth model is introduced.

Chapter III provides an introduction of the various tools used for the investigation of the FOW of the sensor devices. The material stacks are provided along with the patterning techniques and parameters used for the fabrication of the open-loop structure. The two principal physical effect used for the acquisition of the data, i.e., the magneto-optical Kerr and the giant magneto-resistance effect, are described along with the way we use them.

Chapter IV presents the different setups and applied field sequences used for measurement of the propagation and of nucleation fields of domain walls in an open-16-loop structure. The propagation field is first investigated with the MOKE microscope, and results are plotted as a function of the wire width. In a second part, the nucleation field is tested as a function of the width and simulations are performed for a better understanding of the results. These experiments yield the necessary steps to start the investigation of the FOW, i.e., field sequences and tools for study. Finally, the exact nucleation field of thousands of devices is measured using the GMR effect. This experiment allows deducing a relationship between the electrical resistance of the device and the nucleation field

value. The results of this chapter have been published in (14).

Chapter V describes the influence of a homogeneous process yielding inhomogeneous devices on the performances of the latter and consequently its production yield. Novel architectures are designed and presented with the aim to reduce the testing time of the FOW for various variations to the key parameters of the device. The results on the geometrical changes are compared to the results obtained in the previous chapter. The propagation field is then investigated for a large number of elements as compared to a large count of turns to understand the impact of patterning processes. Finally, the nucleation field appearing as a more sensitive handle for the increase of the FOW is thoroughly tested. Parameters such as the thickness of the magnetic layer, the cross-sectional shape of the wires, the material deposition conditions and the patterning method are changed, and results are extracted yielding guidelines for the realization of a magnetic structure with a large nucleation field.

Chapter VI exposes an innovative concept and structure (closed-loop structure) for a reliable multi-turn counter able to achieve the count of millions of turns of an applied magnetic field. The various possible outcomes of the DW passing through a cross-shaped element are detailed, and it is concluded that the cross requires another element (syphon structure) to avoid a failure of the operation of the concept. We then present the results of micromagnetic simulations on the propagation of DWs through the syphon and the cross elements. We numerically obtain the characteristic processes occurring in the center of the cross (pinning, reversal of the right or the wrong arm for a successful operation) by applying various angles and strengths of the applied field. The angular dependence of the syphon element is also simulated and is mathematically modeled. Finally, a combined device is built by overlapping the angular dependence of the two individual elements, and the results yield possible geometries (syphon angles, cross center dimensions) that enable the realization of the device concept. The results of this chapter have been published in (15).

Chapter VII presents the results of the experimental realization of the innovative closed-loop concept exposed in the previous chapter. Various cross-shaped geometries are processed and are tested in an applied field, similarly for the syphon structure. The results are combined and are compared to the measurement performed on a complete structure. From the latter, we understand that the nucleation in the center of the cross is a crucial process driving the FOW. Furthermore, the modifications to the geometry of the syphon exhibit much less impact on the FOW as long as the operation of the sensor is possible. Finally, the results allow providing some guidelines for the industrial realization of the concept.

Chapter VIII is a conclusion on the manuscript and an outlook to the possible experiments that could be performed to pursue the work.

The first author publications (14, 15) have been written by B. Borie with comments and suggestions from all co-authors. The publication (16) has been written by D. Heinze and B. Borie with comments and suggestions from all co-authors. The samples investigated in chapter 4 have been deposited by J. Wahrhusen and processed by the company Sensitec. B. Borie has performed the measurements with the MOKE microscope located at Johannes Gutenberg University and the GMR setup situated at Sensitec. The full films presented in chapter 5 have been deposited either by the company Sensitec (J. Wahrhusen) or by S. Jaiswal using a Rotaris from Singulus. The GMR measurements have been realized by B. Borie and A. Kehlberger. B. Borie performed the MOKE measurements. The measurements at the IPHT have been done by M. Diegel and B. Borie. The patterning of the samples presented in this chapter has been either made by Sensitec using the photolithography or by B. Borie utilizing the ebeam lithography. The simulations of chapter 6 have been performed and developed by B. Borie and M. Voto. Finally, the samples of chapter 7 have been deposited by Sensitec and patterned by B. Borie. The measurement of the MOKE data has been done by B. Borie, and F. Kammerbauer has acquired few images.

Chapter 2

Theory notions

This chapter provides some fundamental knowledge about magnetism in nanometric structures. The first subsection describes the origin of ferromagnetic ordering in 3d metals, followed by an overview of the different energy terms encountered in micromagnetism. We then present the dynamics of spins under the Landau-Lifshitz-Gilbert equation (LLG), followed by the simplest magnetization switching process described by the Stoner-Wohlfarth model. The domain wall shapes and topology are presented, and the dynamic of a 1D domain wall under an applied field is derived. Finally, an introduction to the Walker breakdown is provided as well as some simple depinning processes.

Constants:

a_0 : Bohr's radius = 52,92 pm

h : Plack's constant = $6,62.10^{-34}$ J.s

m_e : Electron mass = $9,10.10^{-31}$ kg

e : Elementary charge = $1,6.10^{-19}$ C

ϵ_0 : Vaccum permitivity = $8,85.10^{-12}$ C.V⁻¹.m⁻¹

μ_0 : Vaccum permeability = $4\pi.10^{-7}$ T.A.m⁻¹

μ_B : Bohr's magneton = $9,274.10^{-24}$ A.m⁻¹

μ_s : Spin magnetic moment

γ : Gyromagnetic ratio = $\frac{q}{2.m}$ | For an electron: $\gamma_e = \frac{-e}{2.m_e}$

Operators :

Gradient (∇)

Divergent ($\nabla \cdot$)

Curl ($\nabla \times$)

Note:

Inside the SI system, two definition are coexisting:

The physicist are using $\mathbf{B} = \mu_0(\mathbf{H} + \mathbf{M})$ with \mathbf{M} and \mathbf{H} in A.m⁻¹

The electronics and material manufacturers prefer $\mathbf{B} = \mu_0\mathbf{H} + \mathbf{J}$ with $\mathbf{J} = \mu_0\mathbf{M}$. We also define that vectors will be in bold $\vec{r} = \mathbf{r}$, and matrices will wear a hat \hat{H} .

2.1 The magnetic terms

The different energy terms presented in this section refer to the domain theory of magnetism. This theory appeared with a publication from L.D. Landau and E. Lifshitz (17) in 1935. The principal calculation goal of the method is the minimization of the system's energy or the system's torque. Nowadays, despite the fact that most of the energy terms are exactly known, they are often impossible to compute analytically, and the use of simulation tools are required. For the simulation of the time evolution of a system, the energies are numerically evaluated for a set of parameters and re-evaluated until the lowest energy state is found. The results are then compared with experimental data for assessment of a physical meaning. The utility of simulation tools is growing as imaging of phenomena on a nanosecond timescale, and of nanometer scale characteristic length remain a gargantuan challenge. Furthermore, with the increase of computational power, it is simpler and simpler, and sometimes even more efficient, to simulate the expected outcome of an experiment. We wish to begin with the basics of magnetism to arrive at the description of the magnetic energies that are computed for the description of magnetic ground states.

Spin of an electron

In the field of Spintronic, it is of obvious importance to first describe the spin of an electron. The spin is a quantum observable, an intrinsic property of particles. In contrast to the energy or the momentum, and despite being frequently vulgarized as the precession of the particle around one of its axes, it does not have an equivalent in classical mechanics. However, this common representation stems from its mathematical description, as it exhibits the characteristics of an angular momentum (commutation relations). This spin information has a significant influence in the world of physics and especially in magnetism which would not exist if not for it. The spin classifies particles of different attributes. The bosons, such as photons, possess an integer spin while the fermions, such as electrons, exhibit a half-integer spin. The result of such spin information is observable in systems constituted of many similar particles and especially when the particles interact with each other. The bosons obey the Bose-Einstein statistics while the fermions follow the Fermi-Dirac statistics and also importantly the Pauli exclusion principle (18). This last principle states that the total wavefunction of many-Fermion-system requires antisymmetry under permutation of two particles. So two fermions cannot have all the same quantum numbers, and consequently, implies a strong correlation between similar-species fermions. On the other hand, bosons do not obey such restrictions and can accumulate and form what is called a condensate (19). The spin creates a magnetic moment, and those two are related as such:

$$\mu_s = -g_s \mu_B \frac{\mathbf{S}}{\hbar} \quad (2.1)$$

where \mathbf{S} is the vector of the intrinsic spin, μ_B is the Bohr's magneton expressed like $\mu_B = \frac{h}{2\pi} \frac{e}{2m_e}$ with the quanta of momentum $\frac{h}{2\pi}$ and g_S is the g-factor of the electron approximately equal to 2.

Micromagnetism

A useful tool for the evaluation of many spin nanosystems is the micromagnetic model. It is derived from thermodynamics principles, as presented in Ref. (20) which gives us an instinctive feeling alike what classical mechanics can provide. This theory refers to a simplification of the reality by taking the following approximation: Well below the Curie temperature, the vector field of the magnetization direction $\mathbf{m}(r) = \mathbf{M}(r)/M_s$ is taken to obtain a total free energy that reaches an absolute minimum under the constraint $\mathbf{m} \cdot \mathbf{m} = 1$. A consequence of the principle of least energy is that the torque that is acting on the spins must go down as an equilibrium is reached. Those torque conditions lead to the equations of micromagnetism. It is then essential to refer to torques in magnetization-dependent energy terms in the framework of the domain theory. For more natural understanding, it is useful to compartmentalize between local and non-local energy terms acting on the spins. The local energy terms refer to energy densities that only take into account local spins and thus their relative direction compared with the nearest neighbors. The general equations consist solely of an integration of the energy density function $f(\mathbf{m})$ over the whole sample. The local magnetic energies are anisotropy energies, Zeeman energy, the magneto-elastic energy and the exchange energy. The non-local terms are called as such since each vector ($\mathbf{m}(r)$) is influenced by every other vector in the system. The stray field energy is a non-local energy. Usually, non-local energy terms are onerous to calculate analytically, since it requires a second integral over all the interactions between all the different spins in the sample. We should now see a more detailed description of those energy terms.

2.1.1 Zeeman energy

The Zeeman energy is an essential term for the work presented here. Most of the experiments take advantage of the energy provided to move a magnetic domain wall. In this case, we refer to the energy of an external applied magnetic field corresponding to, for example, the stray field of a permanent magnet or produced by a set of Helmholtz coils. The non-local stray field of the sample (2.2) is not included in this calculation.

The interaction of \mathbf{m} the magnetization of a sample with an external field $\mathbf{H}_{applied}$ is :

$$E_{Zeeman} = -\mu_0 M_S \int_V \mathbf{H}_{applied}(\mathbf{r}) \cdot \mathbf{m}(\mathbf{r}) d^3 \mathbf{r} \quad (2.2)$$

The value of the Zeeman energy increases with the field applied opposite to the direction of the magnetization. The system has the lowest energy when most of the magnetic moments are aligned with the field and still fulfill the condition of the other energies. The absolute energy value increases with increasing applied magnetic field. For nanomagnetic samples, the external field is most of the time uniform over the whole magnetic volume which simplifies the calculation ($\mathbf{H}_{\text{applied}}(\mathbf{r}) = \mathbf{H}_{\text{applied}}$). Furthermore, we only care about the average value of the magnetization over the whole sample and not the particular spin structures that usually arises in domain walls. If the domain wall has a simple spin structure such as a transverse domain wall (21) which in the frame of the 1D model (22) is a single spin. We can approximate the relation between the external field and the domain wall as the interaction between two spins which is hugely convenient for simple case explanations.

2.1.2 Exchange energies

The exchange energy comprises different exchange mechanisms in between electronic spins. In this subsection, we try to give an overview of the most useful ones for our understanding of the nanomagnetic systems.

Direct exchange

This energy is one of the energies giving birth to the long-range ordering. The spins are stabilized in a parallel configuration, the directionality of the interaction (aligned or anti-aligned) is determined by the sign of the interaction. To express the direct exchange, we first consider the interaction between two particles. The isotropic Heisenberg interaction between two spins which is solved from a two-particle problem as follows (23):

$$\hat{H} |\psi(\mathbf{r}_1, \mathbf{r}_2)\rangle = -\frac{\hbar^2}{2m} (\nabla_1^2 + \nabla_2^2) |\psi(\mathbf{r}_1, \mathbf{r}_2)\rangle + \hat{V}(\mathbf{r}_1, \mathbf{r}_2) |\psi(\mathbf{r}_1, \mathbf{r}_2)\rangle = E |\psi(\mathbf{r}_1, \mathbf{r}_2)\rangle \quad (2.3)$$

The first term is the kinetic energy and describes the electron moving freely. The second term refers to potential energy that we identify as the Coulomb interaction between the two electrons. Due to the commutation relation of the spin and position operator, the eigenstate can be a product of a position-dependent function with a spin-dependent function. The Pauli principle, introduced previously, excludes that two fermions like electrons have the same quantum state. The first wavefunction for the electron (1) at position \mathbf{r}_1 is $\phi_a(\mathbf{r}_1)$ and for the electron (2) at position \mathbf{r}_2 is $\phi_b(\mathbf{r}_2)$. To make sure that the two functions are eigenstates, we assume that they are orthogonal. Taking into account the space parameter of the wave function, we have a symmetrical and anti-symmetrical combination of the position (23):

$$\psi_S(\mathbf{r}_1, \mathbf{r}_2) = \frac{1}{\sqrt{2}}[\phi_a(\mathbf{r}_1)\phi_b(\mathbf{r}_2) + \phi_b(\mathbf{r}_1)\phi_a(\mathbf{r}_2)] \quad (2.4)$$

$$\psi_A(\mathbf{r}_1, \mathbf{r}_2) = \frac{1}{\sqrt{2}}[\phi_a(\mathbf{r}_1)\phi_b(\mathbf{r}_2) - \phi_b(\mathbf{r}_1)\phi_a(\mathbf{r}_2)] \quad (2.5)$$

In the spatially symmetric case, the Pauli principle bounds us to an anti-symmetric spin state which is from (23):

$$\frac{1}{\sqrt{2}}(|\uparrow\downarrow\rangle - |\downarrow\uparrow\rangle) \quad (2.6)$$

Inversely, the symmetric spin states are given as:

$$|\uparrow\uparrow\rangle, |\downarrow\downarrow\rangle, \frac{1}{\sqrt{2}}(|\uparrow\downarrow\rangle + |\downarrow\uparrow\rangle) \quad (2.7)$$

For the physical interpretations, the symmetric spin state implies a strong spatial correlation. Indeed, it affects the system by the creation of nodal planes when the electrons are getting close to each other. This effect is a consequence of the impossibility to be located at the same spatial position. This effect is known as the "exchange hole." The latter does not occur in the spin anti-symmetric case where a spatial correlation is non-existent. Due to the stable positions created by the Pauli principle and the zero probability of finding two electrons at the same position, the energy is then reduced in the symmetric spin case. Now if we only consider the spatial position part of the wavefunction the energy difference of the eigenvalue is:

$$E_S - E_A = \frac{\langle \psi_S | \hat{\mathcal{H}} | \psi_S \rangle}{\langle \psi_S | \psi_S \rangle} - \frac{\langle \psi_A | \hat{\mathcal{H}} | \psi_A \rangle}{\langle \psi_A | \psi_A \rangle} \quad (2.8)$$

This difference of energies is the difference between the Singlet state (S=0), and the Triplet state (S=1) described respectively in the equations 2.4 and 2.5. The energy of the Triplet state is lower than the Singlet state in the two-electron model. This effect demonstrates in a simple case that the relative direction of the spins induces an increase or decrease of the energy of the system.

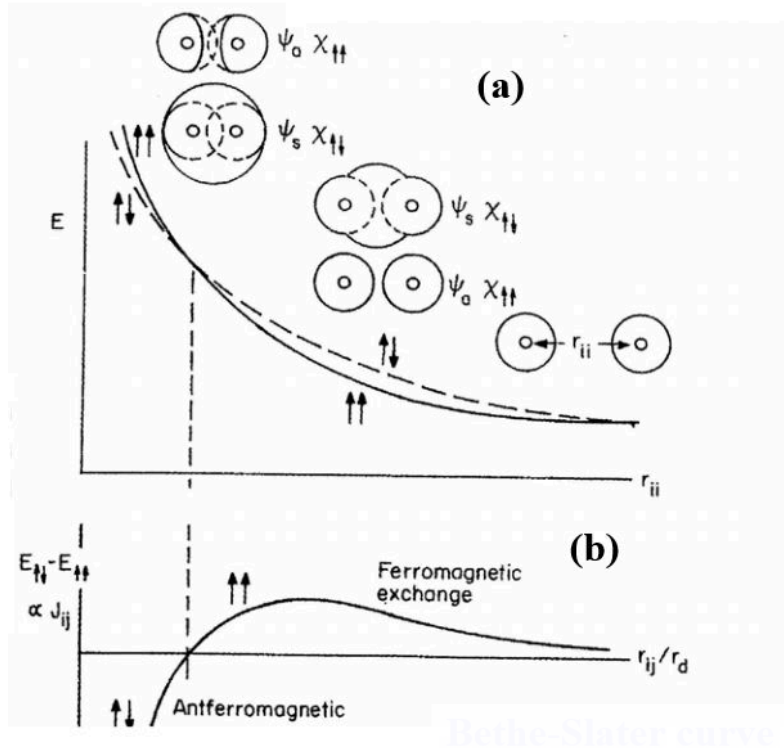


FIGURE 2.1: (a) Dependence of the energy for spatially symmetric and antisymmetric wavefunctions versus atomic separation r_{ij} . (b) The energy difference between the anti-symmetric and symmetric states versus the radius between the two atoms normalized to the d-electron radius (r_d). This curve is called the Bethe-Slater curve and describes the behavior of the ordering as a function of the distance. Positive values yield a ferromagnetic ordering while anti-ferromagnetic is obtained for negative values of the energy difference (see (24))

The direct exchange is extracted from the previous conclusion. In the case of a many-electron system, the expression is given by the expectation value of the Heisenberg Hamiltonian:

$$\hat{\mathcal{H}}_{Exchange} = -2 \sum_{i < j} J_{ij} \hat{S}_i \cdot \hat{S}_j \quad (2.9)$$

with J_{ij} being the coefficient giving the intensity of the effect regarding the overlap of the wavefunctions of the two neighboring electrons. The sign of J_{ij} describes the ferromagnetic ordering (i.e., positive sign) or anti-ferromagnetic ordering (i.e., negative sign). The overlap of the wavefunctions is related to the distance between the two electrons giving their contribution in the equation. An increase of the overlap is bound to a decrease in the distance and an intensification of the effect. At the opposite, an increase of the distance, logically, leads to a reduction of the overlap and eventually the exchange energy is too weak compared to the thermal energy to maintain a self-ordering of the spins. This decrease of the overlap causes the appearance of paramagnetism in the system.

The exchange energy can also be considered as a local term since we evaluate the integral over a function of the derivatives of the direction of neighboring spins.

In the micromagnetic approximation, the exchange energy is described as a “stiffness” equation. The exchange energy is then expressed in the form:

$$E_{exchange} = A \int_V (\nabla \mathbf{m}(\mathbf{r}))^2 d^3 \mathbf{r} \quad (2.10)$$

Where $A = \frac{JS^2n}{a}$ with S is the spin quantum number, a is the lattice constant, and n is the number of atoms per unit cell. The nabla of the magnetic vector provides a representation of the increase in energy if the magnetic vectors are not collinear. The latter equation represents the approximation of the Heisenberg model.

Magnetism in 3d-Metals

Most of the elements of the periodic table in atomic form are usually magnetic. The requirements of Hund’s rules (23) state that an atom possessing non-full electronic shells is magnetic. In the case of many-body systems such as in a solid-state material, it is, in fact, rare to find ferromagnetic ordering. Although the alignment of spins is favored, the solid-state system faces a loss in kinetic energy and a delocalization of the valence electrons which in turn counteract the ordering. In magnetism, the ‘Itinerant’ behavior can be treated with the Band Theory calculation to prove that specific materials retain a ferromagnetic order. In the following section, we will develop the Stoner model by the use of the Density Functional Theory (DFT) (25, 26) to describe metals such as Co, Fe, and Ni, which retain magnetism in their bulk form. This method exhibits some limitations due to the electron-electron correlation effects not being treated precisely. However, it allows one to grasp some understanding of the ferromagnetic ground state in 3d-metals.

The Density Functional Theory is a widely used tool, in fact, it is rather successful when it comes to calculating many-electron problems. The fundamental principle is to reduce the complex systems to a single-electron problem. Indeed, instead of approximating the ground-state of a many-electron system by taking the ground-state of many single-electrons, we calculate the ground-state energy of a density of electrons at different positions.

Mathematically, the ground state density yields a single ground state wavefunction given correctly by a Slater determinant, used to include the required antisymmetry of the wavefunction for fermions.

$$\psi_{KS}[n(\mathbf{r})] = \frac{1}{\sqrt{N!}} \det[\psi_1(r_1)\psi_2(r_2)\dots\psi_n(r_n)] \quad (2.11)$$

Within the K-S theory (26), the Hamiltonian is expressed as:

$$\langle \psi[n(\mathbf{r})] | \hat{H} | \psi[n(\mathbf{r})] \rangle = T_S[n(\mathbf{r})] + E_H[n(\mathbf{r})] + E_{XC}[n(\mathbf{r})] + E_{ext}[n(\mathbf{r})] \quad (2.12)$$

with $T_S[n(\mathbf{r})]$ being the kinetic energy of a non-interacting electron gas of density $n(\mathbf{r})$, $E_{ext}[n(\mathbf{r})]$ is describing the potential between electrons and ions, which is materials dependent, and $E_H[n(\mathbf{r})]$ being a classical electrostatic interaction between electrons:

$$E_H[n(\mathbf{r})] = \frac{e^2}{2} \iint \frac{n(\mathbf{r})n(\mathbf{r}')}{|\mathbf{r} - \mathbf{r}'|} d^3\mathbf{r}d^3\mathbf{r}' \quad (2.13)$$

with e the electronic charge, and finally, the small energy term $E_{XC}[n(\mathbf{r})]$ is the exchange-correlation energy, which accounts for the difference between the interacting and non-interacting kinetic energies and also for any non-classical contributions to the Coulomb (Hartree) energy term. To evaluate magnetic systems, we break the symmetry between the two allowed spin-states by the application of an external magnetic field. A Zeeman energy term with the field direction pointing along the z-axis is added to the previous Hamiltonian. This term is of the form $-(\pm\mu_B\mathbf{H})$ with a minus sign at the front to depict the lower energy state for the majority electrons n^\uparrow , as opposed to the minority electrons n^\downarrow , which are anti-aligned with the applied field direction. The majority electrons are represented by the \uparrow sign and the minority ones by the \downarrow sign, no deviations from the z-direction are taken into account to facilitate the equations. Furthermore, for the analysis, it is necessary to define the local density of spin up and down and the total electron density issued from it.

$$n(\mathbf{r}) = n^\uparrow(\mathbf{r}) + n^\downarrow(\mathbf{r}) \quad (2.14)$$

where the spin density of majority up spins is n^\uparrow and $n(\mathbf{r})$ is the electron density defined previously. The magnetization density is also defined as:

$$m_z(\mathbf{r}) = n^\uparrow(\mathbf{r}) - n^\downarrow(\mathbf{r}) \quad (2.15)$$

The energies with an explicit spin dependence are:

$$\begin{aligned} E_{tot}[n^\uparrow(\mathbf{r}), n^\downarrow(\mathbf{r})] &= T_S[n^\uparrow(\mathbf{r}), n^\downarrow(\mathbf{r})] + \frac{e^2}{2} \iint \frac{n(\mathbf{r})n(\mathbf{r}')}{|\mathbf{r} - \mathbf{r}'|} d^3\mathbf{r}d^3\mathbf{r}' \\ &+ \int n^\uparrow(\mathbf{r})V_{ext}^\uparrow(\mathbf{r})d^3\mathbf{r} + \int n^\downarrow(\mathbf{r})V_{ext}^\downarrow(\mathbf{r})d^3\mathbf{r} + E_{XC}[n^\uparrow(\mathbf{r}), n^\downarrow(\mathbf{r})] \end{aligned} \quad (2.16)$$

here, a distinction is made in the external potential for up and down electron spin. The exchange-correlation also exhibits a spin direction dependence. We focus on solving this functional for the majority (up) spin state, the resolution for the minority spin state is trivial, only requiring to invert the spin direction in the equations. The latter functional can be minimized and a ground state can be

obtained by selecting the ansatz: $n^\uparrow(\mathbf{r}) = \sum_i |\psi_i^\uparrow(\mathbf{r})|^2$ with $\psi_i^\uparrow(\mathbf{r})$ being a sum of one-electron orbitals. We then obtain the Kohn-Sham equations (26):

$$\left(-\frac{\hbar^2}{2m}\nabla_{\mathbf{r}}^2 + V_{eff}^\uparrow(\mathbf{r})\right)\psi_i^\uparrow(\mathbf{r}) = \epsilon_i^\uparrow\psi_i^\uparrow(\mathbf{r}) \quad (2.17)$$

with

$$V_{eff}^\uparrow(\mathbf{r}) = e^2 \int \frac{n(\mathbf{r}')}{|\mathbf{r} - \mathbf{r}'|} d^3\mathbf{r}' + V_{ext}^\uparrow(\mathbf{r}) + \frac{\delta E_{XC}[n^\uparrow(\mathbf{r})]}{\delta n^\uparrow(\mathbf{r})} \quad (2.18)$$

The local-spin-density approximation is used to define the E_{XC} term. In that approximation, the true exchange-correlation energy is replaced by the exchange-correlation energy of a homogeneous electron gas of the same density. It is only in this approximation that the energy term is precisely known. However, this is a crude estimate, and it shunts any local variations of the exchange-correlation. The exchange-correlation energy is then written:

$$E_{XC}^{LDA}[n^\uparrow(\mathbf{r})] \approx \int_V n(\mathbf{r}) \epsilon_{XC}^{homo}(n^\uparrow(\mathbf{r})) d^3\mathbf{r} \quad (2.19)$$

for every point in space, a constant spin density is used resulting in a constant magnetization density. An approximation of ϵ_{XC}^{homo} can be found in Ref. (23). The potential derived from the energy with respect to n^\uparrow is then:

$$V_{XC}[n^\uparrow(\mathbf{r})] = -\alpha e^2 \left(\frac{6}{\pi}\right)^{\frac{1}{3}} (n^\uparrow(\mathbf{r}))^{\frac{1}{3}} \quad (2.20)$$

where α is a free parameter introduced in the $X\alpha$ method. The setting α is simulating the effect of the electronic correlation when the local potential of a homogeneous electron gas is of the form $V_z = \alpha\rho^{1/3}$. Usually, this expression gives an over-estimation for magnetism in materials, due to the inaccurate assumption over rigid orbitals for atoms with delocalized electrons. The orbital relaxation is not taken into account, which added to the fact that electrons are uncorrelated leads to a wrong assumption over a homogeneous spin density. All the previous calculations can be made with the spin down instead of spin up to obtain the potential for the other spin direction. Thankfully, nowadays better estimations can be obtained by using quantum Monte-Carlo simulations (27) or the generalized gradient approximation (GGA) (28).

Stoner Model: It is now of keen interest to develop the Stoner model based on the previous calculations to obtain more quantitative arguments. We know from the equation 2.14 and 2.15 that the magnetization $m_z(\mathbf{r})$ exhibits a small value compared with $n(\mathbf{r})$ for most materials. It then appears natural to apply a Taylor expansion to the previous exchange correlated potential. We restrict ourselves to the first order term and neglect the higher orders terms:

$$V_{XC}(\mathbf{r}) = V_{XC0}(\mathbf{r}) \mp m_z(\mathbf{r})V(n(\mathbf{r})) \quad (2.21)$$

where $V_{XC0}(\mathbf{r})$ is the non-magnetic exchange correlation potential and the average value of $V(n(\mathbf{r}))$ is positive. It appears that a positive potential acts on the majority electrons taking them to lower energy while a negative one acts on the minority electrons. In the Stoner model, we approximate the difference of the potentials by a constant value I:

$$V_{XC}(\mathbf{r}) = V_{XC0}(\mathbf{r}) \mp \frac{1}{2}IM \quad M = \int_{V_{atom}} m_z(\mathbf{r})d^3\mathbf{r} \quad (2.22)$$

where M appears as the integral of the local magnetization over a unit cell of the lattice, and I is called the Stoner parameter which is an exchange integral. The shift in the potential will then change the eigenvalues of our Hamiltonian, and it will also affect the density of states for the up and down electrons.

$$\epsilon^\uparrow(\mathbf{k}) = \epsilon_0(\mathbf{k}) - \frac{1}{2}IM \quad \epsilon^\downarrow(\mathbf{k}) = \epsilon_0(\mathbf{k}) + \frac{1}{2}IM \quad (2.23)$$

The density of states is then:

$$n^\uparrow(E) = n_0(E - \frac{1}{2}IM) \quad n^\downarrow(E) = n_0(E + \frac{1}{2}IM) \quad (2.24)$$

where n_0 is the density of state of the same metal but in a non-magnetic state. It is then possible to redefine the number of electrons N and the magnetization M in a unit cell. That can be done in integrating up to the Fermi energy, the sum or the difference of the density of states obtained previously.

$$N = \int^{E_F} [n_0(E - \frac{1}{2}IM) + n_0(E + \frac{1}{2}IM)]dE \quad (2.25)$$

$$M = \int^{E_F} [n_0(E + \frac{1}{2}IM) - n_0(E - \frac{1}{2}IM)]dE \quad (2.26)$$

From this, we obtain that the Fermi energy is a function of the M parameter and that $M = F(M)$ with:

$$F(M) = \int^{E_F(M)} [n_0(E + \frac{1}{2}IM) - n_0(E - \frac{1}{2}IM)]dE \quad (2.27)$$

This function $F(M)$ satisfies the 4 following criteria: $F(M) = -F(-M)$, $F(0) = 0$, $F(\pm\infty) = \pm M_\infty$, and $F'(M) > 0$ where the last condition comes from the fact that $n_0(E) > 0$. By taking the derivative of $F(M)$, $F'(M)$, we calculate that for $M = 0$ it gives:

$$F'(0) = In_0(E_F) \quad (2.28)$$

from which we can deduce that a sufficient condition for magnetism is $F'(0) > 1$. The Stoner criterion is then defined as:

$$In_0(E_F) > 1 \quad (2.29)$$

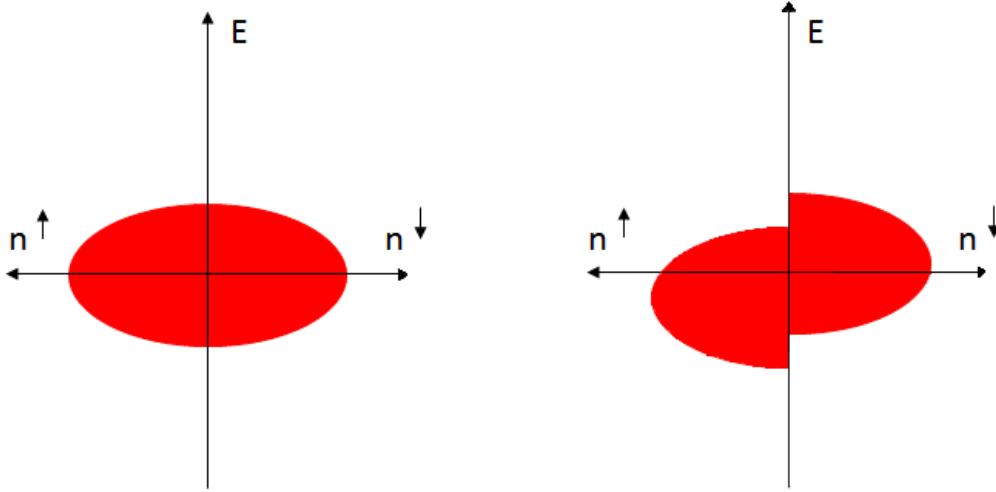


FIGURE 2.2: (a) Schematic representation of the 3d-band in a non-magnetic metal. (b) Schematic representation of the 3d-band splitting of the 3d band at the Fermi level for metals due to the exchange-correlation on the right side.

The ferromagnetic ordering is then favored for a high density of state at the Fermi energy in a non-magnetic configuration and if the exchange integral is large. The Stoner criterion relates to the density of states at the Fermi energy and thus the degeneracy of the last band. We know that the density of states is connected to the width of the energy band. In a simple approximation, we write that the width of a band is:

$$\int_W n_l(E) dE = 2l + 1 \quad (2.30)$$

providing the relation between the width of a band and the angular momentum quantum number. The consequence is that for delocalized electrons such as s-band like orbitals, the width is large, and for localized ones such as d-band like, the width of the band is narrow. The metals naturally providing a significant difference in density of states at the Fermi energy at room temperature are Fe, Co, and Ni. Thus they fulfill the Stoner criterion and are ferromagnetic materials. The calculated magnetic moment per atom of Co, Ni, and Fe is $1.7 \mu_B$, $0.6 \mu_B$, and $2.2 \mu_B$, respectively. Those values were calculated with the Spin-Density-Functional Theory calculations found in Ref. (23). The experimentally measured values are $\text{Co} = 1.56 \mu_B$, $\text{Ni} = 0.55 \mu_B$ and $\text{Fe} = 2.12 \mu_B$ (23), which are in good agreement. It is important to note that the majority spin band for Ni and Co is full, while the

one of Fe is not entirely filled with electrons. Co and Ni are then called strong ferromagnets while Fe is known as a weak ferromagnet.

2.2 Anisotropy Energies

A normalized order parameter, the magnetization $\mathbf{m}(\mathbf{r}) = \frac{\mathbf{M}(\mathbf{r})}{M_s}$ is now obtainable, we will be able to study its interaction with other potential energy terms. Without the presence of an externally applied field or a spin current to induce a preferred direction for the exchange interaction, the magnetization $\mathbf{m}(\mathbf{r})$ aligns in the directions defined by the anisotropy energy terms. Such anisotropies, in simple words, describes the quantity of work that has to be provided to rotate the magnetization from the preferred axes defined by the latter anisotropy. There are several contributions to the magnetic anisotropies, and it is often hard to describe them effectively.

Magneto-crystalline anisotropy

The magneto-crystalline anisotropy has a significant contribution to fully crystalline material and sits at the origin of the hysteretic effect in thin films of large areas. Indeed, a consequence of the magneto-crystalline preferred directions is the creation of easy and hard axes for the magnetization. The magnitude of this anisotropy energy is usually less than the exchange energy since magneto-crystalline anisotropy is spin-orbit coupling related effect. So far only all the considered interactions did not include spin-orbit coupling. For the present anisotropy, spin-orbit coupling is required and is at its origin. In the non-relativistic approximation $v_e \ll c$ where v_e is the velocity of the electron, there is a coupling of the spin angular momentum \mathbf{S} and the orbital angular momentum \mathbf{L} . In the rest frame of the electron the nucleus orbits around it, the latter results in the induction of a magnetic field to the electron. This electron is travelling through an electric field, there is the creation of $\mathbf{B} = -\frac{\mathbf{v} \times \mathbf{E}}{c^2}$. The electric field is radial and has spherical symmetry associated to it, so $\mathbf{E} = \frac{E}{r} \mathbf{r} = -\nabla V$. Finally, with the classical angular momentum being $\mathbf{L} = \mathbf{r} \times \mathbf{p}$, the expression of the magnetic field generated is then:

$$\mathbf{B} = \frac{1}{m_e c^2} \frac{1}{r} \frac{\partial U(\mathbf{r})}{\partial r} \mathbf{L} \quad (2.31)$$

The term $\frac{\partial U(\mathbf{r})}{\partial r}$ is the expression of the spherical potential which decreases with increasing distance r . The orbital angular momentum represented in the formula by \mathbf{L} is usually associated with the quantum number l . Since the coupling comes from the interaction between the spin angular momentum (i.e., the intrinsic spin) and the orbital angular momentum. This effect is expressed by a

Hamiltonian that closely resembles the Zeeman energy term for two spins (for details see Ref. (23)):

$$\hat{\mathcal{H}}_{SO} = -\hat{\mu} \cdot \hat{B} \quad (2.32)$$

$$\hat{\mathcal{H}}_{SO} = \frac{\mu_B}{\hbar m_e c^2} \frac{1}{r} \frac{\partial U(\mathbf{r})}{\partial r} (\hat{L} \cdot \hat{S}) = C_{nl}(\mathbf{r})(\hat{L} \cdot \hat{S}) \quad (2.33)$$

where $C_{nl}(r)$ is in the range 10-100 meV. Multiplied by the norm of the two spins the spin-orbit interaction has a lower energy than the exchange interaction. In a solid-state environment, the overlapping of the wavefunctions of the neighboring atoms is establishing some preferred directions of the crystal, which in turns builds the crystalline structure that we know such as bcc or fcc for the most common ones. Magneto-crystalline anisotropy takes full advantage of the spin-orbit coupling, and of the crystal preferred directions, to reduce its energy by also aligning the spins in the crystallographic orientations. An important message is that the magneto-crystalline anisotropy possesses a symmetry similar to the symmetry of the crystal that is considered. Anisotropies are usually invariant by rotation around the preferred axes. Thus their derivation is easier with functions that retain similar characteristics such as spherical harmonics. It is relevant to note that thermal agitation of the spins tends to make the higher-order harmonics extremely small. Therefore only the two first orders are necessary to represent the free energy density $F_{anisotropy}$ of the anisotropy. This free energy density is made of a series of harmonics from the different spatial components m_i of the unit vectors $\mathbf{m}(\mathbf{r})$:

$$F_{anisotropy} = \sum_{i,j,k} K_{i,j,k} m_1^i m_2^j m_3^k \quad (2.34)$$

The anisotropy, in this case, is distinguished from the shape anisotropy (details see 2.2), which is not described by this term. For the case of a cubic crystalline structure, the expression of the Free energy is:

$$F_{cubic} = K_1(m_1^2 m_2^2 + m_1^2 m_3^2 + m_2^2 m_3^2) + K_2 m_1^2 m_2^2 m_3^2 + \text{higher-order terms} \quad (2.35)$$

here the higher orders are supposed to be negligible. The coefficients K are setting the magnitude and the direction of the effect. In a cubic case, the sign of K_1 indicates whether (100) or (111) is the easy direction for the magnetization (20). In the present study, magneto-crystalline anisotropy is relevant especially for the $\text{Co}_{90}\text{Fe}_{10}$ samples shown in the experimental section. The $\text{Ni}_{81}\text{Fe}_{19}$ possesses a near zero magneto-crystalline anisotropy (29), which is convenient to achieve extremely soft magnetic layers.

Dipolar interaction

This anisotropy is originating from the dipolar interaction. The magnetic dipole-dipole interaction is a non-local term and is a direct consequence of the finite size of the system. In soft magnetic nanostructures, it plays a substantial role together with the exchange energy for the design of the spin structure of the sample. This potential energy E_{dipole} is expressed as follows:

$$E_{dipole} = -\frac{\mu_0 M_S^2}{4\pi |\mathbf{r}|^3} (3(\mathbf{m}_1 \cdot \mathbf{r})(\mathbf{m}_2 \cdot \mathbf{r}) - \mathbf{m}_1 \cdot \mathbf{m}_2) \quad (2.36)$$

with \mathbf{m}_1 and \mathbf{m}_2 being two magnetic moments, separated by a distance $|\mathbf{r}|$ in the direction of the unit vector \mathbf{r} . This equation couples any two magnetic moments hence the non-locality of the dipolar energy. We notice that a reduction of the energy is obtained for increasing distances and magnetic moments parallel to the vector \mathbf{r} . The shape anisotropy energy or stray field energy is related to the dipolar interaction. The stray field of a structure can be defined as the magnetic field lines coming out of the sample and entering back into it. The analytical definition of the stray field from Maxwell's equation, in the absence of currents \mathbf{j} , is:

$$\nabla \times \mathbf{H} = 0 \quad (2.37)$$

$$\nabla \cdot \mathbf{B} = 0 \quad (2.38)$$

The equation 2.37 states that the field \mathbf{H} is conservative thus $\mathbf{H} = -\nabla \Phi_{demag}$. Furthermore, magnetic flux density \mathbf{B} is connected to the connected to the magnetic field \mathbf{H} and \mathbf{m} through the equation:

$$\nabla \cdot \mathbf{B}(\mathbf{r}) = \mu_0 \nabla \cdot (\mathbf{H}(\mathbf{r}) + \mathbf{M}(\mathbf{r})) \quad (2.39)$$

If we now assume that the external field is zero, we then obtain the following Poisson's equation:

$$-\nabla \cdot \mathbf{H}_{demag}(\mathbf{r}) = \nabla \cdot \mathbf{M}(\mathbf{r}) = \Delta \Phi_{demag} \quad (2.40)$$

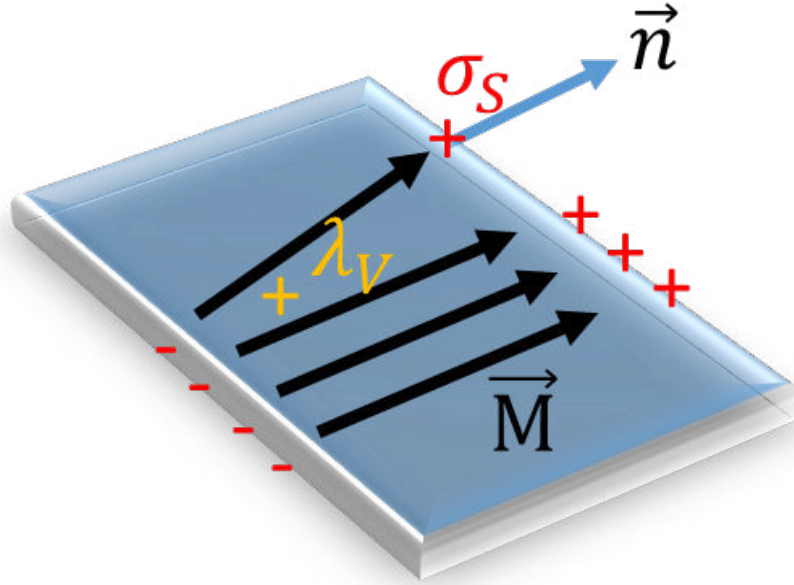


FIGURE 2.3: Schematic representation of the magnetic charges generated at the boundaries of a sample and inside a sample. The magnetization has a component normal to the surface leading to the creation of the charges σ . The magnetization is also non-divergent free creating the volume charges λ .

where $\mathbf{H}_d(\mathbf{r})$ refers to the demagnetizing field. This field is usually calculated in two ways, by a current circulating method or by considering 'magnetic charges.' We describe the second method which appears more straightforward and is easier to grasp due to its similarities with electrical charges. Magnetic charges, unlike electrical charges, are not stand alone, they are always counter-balanced by opposite charges thus forming a dipole. The magnetic field lines are the representation of the gradient from a positive charge to a negative charge. The magnetic charges are created when the direction of the magnetization is not uniform and in case of abrupt discontinuities such as edges. Two types of charges are distinguished, the surface charges and the volume charges. The density of those charges is noted σ_s and λ_v , respectively. Volume charges appear inside the sample if the magnetization is diverging. Thus domain walls are the generators of the magnetic volume charges. In contrast, the surface charges are created at the surfaces of the system. In fact, at the boundaries, the spatial inversion symmetry is broken, which results in the creation of positive charges on a side compensated by negative charges on the opposite side. The magnetic charges are defined as follows:

$$\sigma_s = \mathbf{m}(\mathbf{r}') \cdot \mathbf{n} , \quad \lambda_v = -\nabla' \cdot \mathbf{m}(\mathbf{r}') \quad (2.41)$$

The Poisson's equation described earlier can be solved by the potential Φ_{demag} of the following form (details see Ref. (20)) :

$$\Phi_{demag}(\mathbf{r}) = \frac{M_S}{4\pi} \left[- \int_V \frac{\lambda_v(\mathbf{r}')}{|\mathbf{r} - \mathbf{r}'|} d^3\mathbf{r}' + \int_{\partial V} \frac{\sigma_s(\mathbf{r}')}{|\mathbf{r} - \mathbf{r}'|} d^2\mathbf{a}' \right] \quad (2.42)$$

where the integration is performed over the whole volume and surfaces of the magnetic material. By applying the divergence theorem, we obtain the simplified potential:

$$\Phi_{demag}(\mathbf{r}) = \frac{M_S}{4\pi} \int_V \nabla' \cdot \mathbf{m}(\mathbf{r}') \frac{1}{|\mathbf{r} - \mathbf{r}'|} d^3\mathbf{r}' \quad (2.43)$$

The demagnetizing field can then be constructed by taking the gradient of the previous equation.

$$\mathbf{H}_{demag}(\mathbf{r}) = -\nabla \Phi_{demag}(\mathbf{r}) = -\frac{M_S}{4\pi} \int_V \hat{N}(\mathbf{r} - \mathbf{r}') \mathbf{m}(\mathbf{r}') d^3\mathbf{r}' \quad (2.44)$$

with $\hat{N}(\mathbf{r} - \mathbf{r}')$ a 3×3 matrix, called the demagnetizing tensor, and accounting for the strength of the dipolar interaction. It is a real diagonal matrix with a trace equal to 1, for a sphere all components are equal to $1/3$. The form of the components is the following:

$$n_{i,j} = -\partial_i \partial'_j \frac{1}{|\mathbf{r} - \mathbf{r}'|} \quad (2.45)$$

Finally, we derive the energy by taking the integral over \mathbf{m} and the volume V

$$E_{demag} = -\frac{\mu_0 M_S}{2} \int_V \mathbf{H}_{demag}(\mathbf{r}) \cdot \mathbf{m}(\mathbf{r}) d^3\mathbf{r} \quad (2.46)$$

with the $1/2$ factor correcting the double counting of the interaction. This formula displays the general difficulty to produce analytical results for the shape anisotropy, and even the enormous computational power necessary to obtain exact numerical results. Thankfully, some elementary systems (ellipses) allow us to grasp the idea of the magnetic charges and the stray field produced. From the demagnetizing field expression, it appears straightforward that an increase in the number of magnetic charges denotes an increase of the demagnetizing field. In the case of nanopatterned samples, the shape anisotropy is of prime relevance. For a single domain magnetization state, the number of charges is qualitatively proportional to the area of the surface normal to the direction of the magnetization vector. In the sample represented in Fig.2.5, the magnetization is in the ground state. The strongest demagnetization field points in the z-axis and x-axis directions, thus forcing the magnetization to lay in the -y-direction.

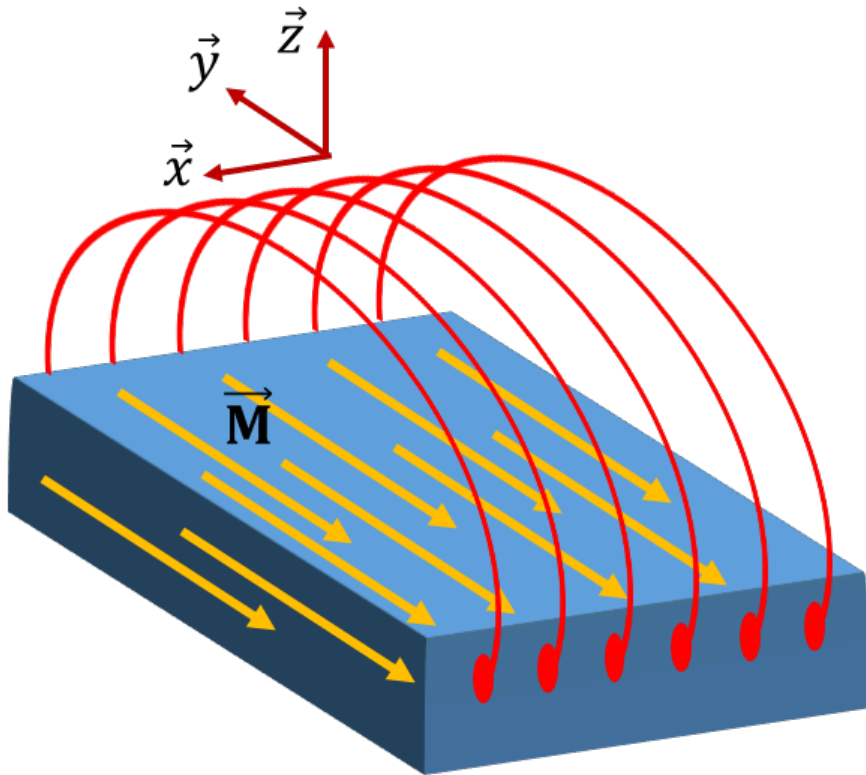


FIGURE 2.4: Schematic representation of the magnetization in a wire only governed by the exchange energy and shape anisotropy.

This result is of real importance for the determination of dynamic processes in nanomagnetism. Indeed, when an external field is applied opposite to the direction of the magnetization, the Zeeman energy might destabilize the system enough for the magnetization to switch direction. To perform the latter, the system has two options either a coherent rotation (see Stoner-Wohlfarth section 2.3.2) of all the magnetic moments or the creation of a domain wall that propagates and switches the stripe. As we will see in the following sections, in the case of nanostructures, the coherent rotation is extremely energetically costly. This results, at a point in time, in configuration with the magnetic moments all facing either the surface XY or YZ, generating a consequent amount of magnetic charges. In general, the magnetic energies are favoring the creation of domain walls and their propagation to realize the switching event.

Other anisotropies

Other anisotropies are experienced in magnetic materials such as surface anisotropy for ultra-thin films or magneto-elastic anisotropies. However, they are not relevant to the work presented here and are then left out. The reader might want to consult (20) for a general overview other all the possible anisotropies. To conclude, the anisotropies are a consequence of the magnetic order parameter being present in an organized and discrete (atoms) crystal of finite dimensions and a

consequence of the spin-orbit interaction. The impact of the latter is the conformation of the magnetization to the organization of the matter that supports it.

2.3 Dynamics of Magnetization

2.3.1 Landau-Lifshitz-Gilbert equation

In the following section, we develop the dynamic of the magnetization, or of single spins depending on the approximation considered (micromagnetism or atomistic model). From the exchange energy, the spin-spin misalignment results in the creation of torque. The dynamic of this process is described via the Landau-Lifshitz-Gilbert equation (20). The equation provides an explanation of the magnetization dynamics and the loss of energy through damping. A quantum mechanical approach inspired by (30) is used to derive the LLG equation. The idea is to start with the Heisenberg equation of motion of a single spin \mathbf{S} . It can be formulated starting with the Heisenberg equation of motion:

$$\frac{d\hat{S}_j}{dt} = \frac{i}{\hbar} [\hat{H}, \hat{S}_j] = \frac{i}{\hbar} \left(\sum_k \frac{\partial \hat{H}}{\partial \hat{S}_k} [\hat{S}_k, \hat{S}_j] + O(\hbar^2) \right) \quad (2.47)$$

where \hat{H} is the Hamiltonian of our studied system. $O(\hbar^2)$ is a function that is quadratic in \hbar . The spin is an angular momentum; the components are then tied to each other with the general commutation relation:

$$[\hat{S}_k, \hat{S}_j] = -i\hbar \sum_l \epsilon_{jkl} \hat{S}_l \quad (2.48)$$

with ϵ_{jkl} being the Levi-Civita symbol which constitutes a matrix of Kronecker symbols. Entering this into the equation (2.47) gives

$$\frac{d\hat{S}_j}{dt} = \sum_{k,l} \frac{\partial \hat{H}}{\partial \hat{S}_k} \epsilon_{jkl} \hat{S}_l + O(\hbar) \quad (2.49)$$

In a vector notation, it translates into:

$$\frac{d^3\mathbf{S}}{dt} = -\mathbf{S} \times \frac{\partial \hat{H}}{\partial \mathbf{S}} + O(\hbar) \quad (2.50)$$

with the operator $\partial/\partial \mathbf{S} = (\partial/\partial S_x, \partial/\partial S_y, \partial/\partial S_z)$.

As for the previous sections, in the semi-classical formalism, an approximation can be made concerning the spins. The sum is transformed in an integral if the elements are small and close enough, the field of spins is transformed into a continuous vector field of the magnetization \mathbf{M} while using the fact that \hbar goes to

0. This approximation is usable if the change in orientation of the spins from one site to the following is limited to small values. Namely, the characteristic length scale of the change in the direction of the magnetization needs to exceed the intra spin distance widely. If the latter conditions are fulfilled, we can use the micro-magnetic approximation to describe the process. The magnetization is defined as a single classical spin $\mathbf{M}(\mathbf{r}) = M_s \mathbf{m}(\mathbf{r})$ that precesses around a time-dependent effective magnetic field. The equation of motion is expressed as:

$$\frac{\partial \mathbf{m}(\mathbf{r}, t)}{\partial t} = -\mu_0 \gamma \mathbf{m}(\mathbf{r}, t) \times \mathbf{H}_{eff}(\mathbf{r}, t) \quad (2.51)$$

where the gyromagnetic ratio $\gamma = g\mu_B/\hbar$ and the effective field is derived from the free energy as

$$H_{eff} = \frac{\partial F}{\partial M} \quad (2.52)$$

Here the free energy contains all the relevant terms such as anisotropies, Zeeman energy, exchange terms, and dipolar interaction. This equation depicts the precessional motion of the single magnetic moment around the effective magnetic field. The equation 2.51 is conservative, and no energy loss is present. Indeed, if a magnetic field is applied in a non-collinear direction with the magnetization vector, the magnetization precesses for the time the field is applied. However, it has been shown that the magnetization aligns with the applied field. The precession must then be altered by another term that accounts for relaxations and energy losses. A dissipative term such as friction or resistance in classical mechanics, is introduced. This term is phenomenological and was derived by Landau and Lifshitz (1935) and reformulated by Gilbert in (1955) to achieve finally:

$$\frac{\partial \mathbf{m}(\mathbf{r}, t)}{\partial t} = -\mu_0 \gamma (\mathbf{m}(\mathbf{r}, t) \times \mathbf{H}_{eff}(\mathbf{r}, t)) - \alpha_G (\mathbf{m}(\mathbf{r}, t) \times \frac{\partial \mathbf{m}(\mathbf{r}, t)}{\partial t}) \quad \text{LLG equation} \quad (2.53)$$

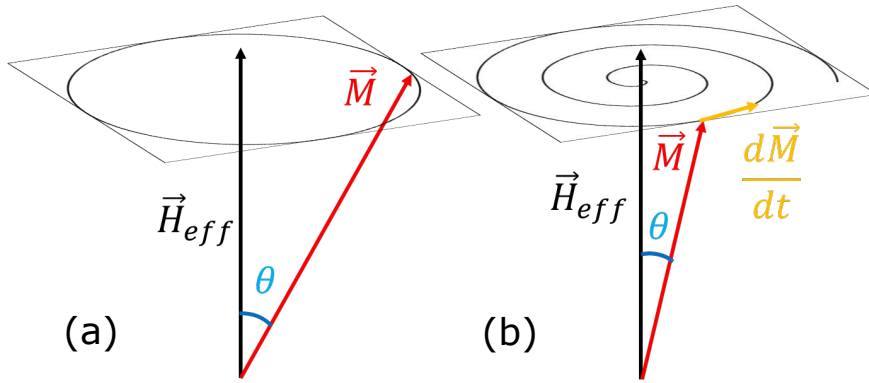


FIGURE 2.5: (a) The effective field H_{eff} (black arrow) acts on the magnetization and generates a torque resulting in a precessional motion of the magnetization (red arrow) on the path. (b) The motion is damped due to an additional term, the damping is represented by $\frac{d\vec{M}}{dt}$. The magnetization leaves the original orbit and spirals toward the direction of the effective field.

with the second term representing the relaxation process, this process is depicted in Fig. 2.5. The factor α_G is called the Gilbert damping factor; it is a material dependent property describes any loss process. Without the latter term, the magnetization vector could not relax in the effective field direction, and no control of the magnetization could be performed. Some more sophisticated versions of the equation exists, which includes a dependence on the spin current flowing through a wire (31). For the work presented here, the first one is sufficient since we focused on driving the magnetization with applied fields. An insignificant current is applied during the experiment to detect the GMR effect, which would not affect the local magnetization. We have now derived the dynamics that govern the micromagnetic vectors; we have to apply those equations to domain walls and other magnetic spin textures to qualify their behavior.

2.3.2 The Stoner-Wohlfarth model

The dynamics of single micromagnetic vectors follows a rather simple equation of motion. Due to the competition of the various energies governing magnetism, a magnetic sample of finite size is rarely composed of a single direction of the magnetic vector. The shape anisotropy competes with exchange energy for the formation of flux-closure (32). This competition leads to the creation of magnetic domain walls, which are detailed later in the manuscript 2.4. For very particular cases of shapes and sizes of the magnetic media, a single-domain state of the magnetization is achieved where all the micromagnetic spins are aligned in the same direction. The latter occurs for sample dimensions smaller than the exchange length (33) $\lambda = 2\pi\sqrt{\frac{A}{\mu_0 M_S^2}}$ with A the exchange constant and M_S the saturation magnetization, and for ellipsoidal shapes. For lengths smaller than the exchange length $L < \lambda$, the exchange energy dominates over the dipolar interaction thus forbidding a multi-domain state then resulting in an alignment of all spins. At

this dimensions, the formation of domain walls requires significant energies, and the magnetization is reversing following a uniform rotation or a more disordered curling mode for slightly larger sizes.

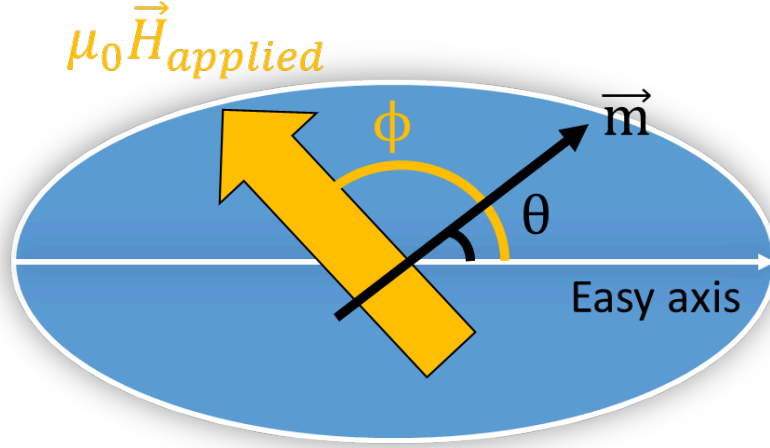


FIGURE 2.6: Schematic representation of the configuration for the Stoner-Wohlfarth model problem. The blue area represents the sample's shape. The angle θ is defined between the easy axis and the magnetization vector. The angle ϕ is defined between the easy axis and the applied field direction.

In this subsection, we describe the dynamics and mechanisms of single-domain particles under a driving applied field in the presence of a uniaxial anisotropy. Stoner and Wohlfarth (34) followed by Neel (35) developed the simplest version of the classical rotation of the magnetization. Their approximations were that the exchange energy tightly holds together the spins of the sample, and no intra spin dynamic is permitted. This assumption yields to a constant exchange energy over time, and thus no torque is generated by this term. The magnetization dynamics can then be entirely described by the competition between the applied field and the uniaxial anisotropy, which was the subject of the original study from Stoner and Wohlfarth. More recently, Thiaville generalized the model to include any arbitrary anisotropy. In the SW description, the energy of the particle is:

$$E_{tot} = KV \sin^2(\phi) - \mu_0 M_S V H_{applied} \cos(\phi - \theta) \quad (2.54)$$

with $KV = \frac{\mu_0 M_S^2 V}{4}$ being the uniaxial anisotropy energy defined by the shape of the sample, and $H_{applied}$ is the applied magnetic field. ϕ and θ are the angles of the magnetization and the applied field with the easy axis of the sample defined by the longest length. We are interested in the destabilization of the magnetization and more precisely in the values for $H_{applied}$ and θ for which the magnetization switches. In the present configuration, the total energy exhibits 2 minima in both orientations of the easy axis, which are separated by an energy barrier defined by the hard axis formed by the shape anisotropy. We want to equate the minimal field to switch from one side to the other; the latter can be performed by

solving $\partial E/\partial\psi = \partial^2 E/\partial\psi^2 = 0$. After a few equations described in (36), we can obtain the switching field H_0 , and in dimensionless units:

$$h_0 = \frac{H_0}{H_{anis}} = \frac{1}{(\sin^{2/3}(\theta) + \cos^{2/3}(\theta))^{3/2}} \quad (2.55)$$

where $H_{anis} = 2K/(\mu_0 M_S)$ is the anisotropy field. We can readily see that a minimum is found for the angle value $\theta = 135^\circ$. The latter result is of importance for the work presented here. For larger particles that are single domain like in a ground state, a non-uniform reversal mode is often the one considered. This mode is cumbersome to derive analytically, and micromagnetic simulations are necessary to obtain the correct magnetic field switching and magnetic spin structure.

2.4 Domain Walls

2.4.1 Topology

Mathematical tools are necessary for a clear description of the domain wall characteristics and dynamics. Domain walls can be considered as composite objects comprising magnetic topological charges, which are a consequence of magneto-static considerations of the discontinuities of the magnetization vector field (37). Those discontinuities are called topological defects (38, 39) and are essential for the understanding of the latest topics Domain Walls, Skyrmions, etc... The topology, in a mathematical sense, is the geometrical study of an object, which constrained under continuous transformations retains its topological properties (continuous map). A topology is describing a topological space, and the notion of topological spaces deals with the set theory and mostly the open sets. This branch of mathematics is widely used for the possible simplification of intricate problems through geometrical consideration allowing the reader to "picture" the mathematical relations of abstract groups. It is a powerful, and intuitive mathematical formalism that allows the description of defects in order media in an elegant manner. We will give here only a mere description of the topic; I invite the interested readers to refer to (39, 40) for a more advanced description of the mathematics involved. The topology is then the natural language that can describe ordered media with the inclusion of point, line and sphere defects. In this section, we evidently focus on the ferromagnetism for the examples to the mathematical notions. Before any topological description, we wish to convey that caution needs to be taken when directly transferring topological arguments to the physical world. The reasons for the latter are the followings:

Physically, energy barriers are, for obvious reasons, never infinite. Also, in reality, the medium carrying the ferromagnetic phase is not constant and not continuous, which alters the described topological properties. Despite all the recent arguments against the use of topology, the mathematical theory succeeds in proving and explaining in simplified terms some observed physical phenomena such

as the nucleation of domain walls through creation soliton-antisoliton pair (40) or the stabilization of skyrmions.

Mathematical description of Topological defects

In topological notions, the media described is called the order parameter. From the allowed orientations or values of the order parameter, there exists an order parameter space (X). An example of an order parameter is a vector $\mathbf{m}(\mathbf{r})$ of a 2-dimensional spin plane (easy-plane), which can be obtained for example in a thin film with an easy-plane anisotropy. For this case, the order parameter space is represented by a circle (1-sphere) describing all the directions that the vector can take. In simple terms, the possibility of topological defects is defined by the connectedness of a global set (G) representing the allowed transformation of the order parameter (e.g., rotation of vector), and more precisely the transformations that leave the order parameter unchanged (H). Often, several transformation's paths ($a, b \in G$) yield the same transformed object ($f', f \in X$ then $f' = af = bf$). Now if there exist a continuous family of h_x with $x \in [0,1]$, such that $h_0 = a$ and $h_1 = b$ then the transformations are homotopic. In other words, the paths can be gradually changed into one another by continuous modification. The usual example is that the surface of doughnut can be continuously deformed to the surface of a mug, they are then homotopic surfaces. The principle of homotopy allows the description of the connectedness of the previously mentioned sets ($G, H..$). If a set is not *simply* connected then non-trivial topological defects might exist (the sphere is a simply connected object, every loop drawn on its surface can be reduced to a point). The connectedness of a set is the core of the characterization of topological defects. Looking at the allowed-transformation set (G), it is possible to define the existence of a topological defects by determining the breaking of the continuity of the subset H of the invariant transformations in G . In a physical meaning, if two different transformations (identity and some other random transformation) leave a reference order parameter (one spin) unchanged, and the transformations are not homotopic, then H is not simply connected, and a topological defect can exist. Formally, the cosets of the set containing the identity H_0 in H (H/H_0) need not be the single element 0.

Non-trivial topological defect

We wish to give a more straightforward representation of the latter explanation on topological defects, which can be very abstract. In simpler terms, the possible topological defects are identified as contours on the order parameter that do not reduce to a point when transferred to the order parameter space (see Fig. 2.7-(a)).

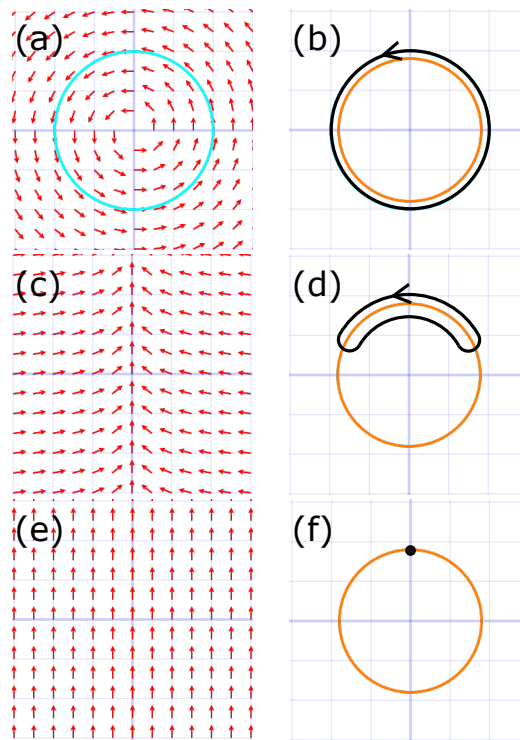


FIGURE 2.7: The order parameter space is a for the planar spin system. (a) The vector field for the field $\mathbf{F}(\mathbf{x}(\mathbf{t}), \mathbf{y}(\mathbf{t})) = (-\mathbf{y}(\mathbf{t}), \mathbf{x}(\mathbf{t}))$ showing a 2-d vortex in a planar spin system, the turquoise circle represent a contour on the order parameter. (b) Mapping of the order parameter contour in order parameter space. (c) Vector field of different form in a planar spin system. (d) The mapping of the contour on (c) transferred to the order parameter space. (e) Ferromagnetic order in a planar spin system. (f) Mapping of (e) onto the order parameter space.

The figure 2.7-(b) provides with a standard geometrical representation of a topological defect in the planar spin configuration. We suppose that the vector field in Fig. 2.7-(a) is continuous $\mathbf{m}(x, y)$ and that a possible point of discontinuity D lies in the center of it. It is possible to conclude that the point is a singularity if the field is known in a circle of radius R away from D and not define at D . Let us assume that we circulate in a counter-clockwise direction on the contour in Fig. 2.7-(a). We integrate the angle between the magnetization and the $+x$ -axis direction. We count counter-clockwise angle increments as positive and clockwise as negative. For the present case, we find the integral to be equal to 2π . We clearly see that the contour in Fig. 2.7-(b) cannot be reduced further, thus the singularity D . For the vector field in Fig. 2.7-(c), the same procedure is performed, and a similar contour is transferred to the order parameter space as seen in 2.7-(d). We notice that the contour can be reduced to a point as in 2.7-(f). The conclusion of the latter is that (c) and (e) exhibit the same topology, in other words, the pattern (c) can be continuously modified to the one in (e). Generalizing the previous observation, for a vector field in 2-dimension (planar spins), the group of all allowed transformations in 2-dimension is $SO(2)$, the translations are not included since the order parameter space is universal and thus translational invariant. We know that the group $SO(2)$ is isomorphic to the group $T(1)$ of translation over a

line (only an angle value is required to describe the rotations in the plane), which is simply connected. Now, the values leaving the order parameter invariant are the rotation of angle values n modulo 2π constituting the set $n = 0, \pm 1, \pm 2, \dots$ of signed integers. It is then straightforward to notice that since the group is discrete the only element of H_0 is the identity ($n = 0$) and that H/H_0 is directly the set H . Thus the possible topological defects are represented by \mathbb{Z} , with the notation $\pi_1(S^1) = \mathbb{Z}$. The latter results can be expanded for a vector field in n -dimension yielding $\pi_n(S^n) = \mathbb{Z}$. For the planar spins, the number associated with this defect is called the **winding number** (40) with formula:

$$n = \frac{1}{4\pi} \int \left(\frac{\partial \mathbf{m}}{\partial x} \times \frac{\partial \mathbf{m}}{\partial y} \right) \cdot \mathbf{m} \, dx dy \quad (2.56)$$

The spin circulations observable in Fig. 2.7-(a) are a direct consequence of the existence of a topological defect. An interesting feature of this singularity D of the vector field of winding number n is its observable signature (circles Fig. 2.7) at an arbitrary distance from the defect. From topology arguments, it is then possible to remove singularities of winding number $n = 0$ without altering the order parameter (39) (see Fig. 2.7-(e)). The previous characteristic does not hold for winding numbers $n \neq 0$ thus guaranteeing the topological stability of such defects shown in Fig. 2.7-(b).

Topology arguments for real samples

For the general case of a ferromagnetic material, the order parameter is a vector of 3-dimension and constant norm in the limit of fixed M_S . The order parameter space is then a 2-sphere of radius the norm of the vector. We provide an expression for the relation between the dimension of the considered spaces, which is derived in Ref. (40). We take d = dimensionality of the considered system, m = dimension of the order parameter space and d' = dimension of the defect. The relation is given by:

$$d = d' + m + 1 \quad (2.57)$$

For a system in 3-dimension in space $d = 3$, with an order parameter space with dimension $m = 2$ then the defect is of dimension 0. The defect is a point in the center of a 'hedgehog.' An example of the latter is the Skyrmion allowed in out-of-plane magnetized samples with the DMI anisotropy unlocking a 2-dimensional order parameter space. A non-trivial topological defect has the great advantage of being topologically stabilized meaning that it cannot be annihilated by a continuous deformation of the order parameter (i.e., no simple connection between the identity set and another element of H). The only way to annihilate the defect is to bring another singular point of opposite winding number close enough for the annihilation. However, the latter does not obviously mean that the energy to destroy the topological defect is infinite mainly due to the escape of the stray field in magnetic samples.

2.4.2 Magnetic domain walls

After this mathematical interlude, we can describe the domain walls in ferromagnetic materials. As described previously, a magnetic material in the uniform state exhibits a single direction of its spin angular momenta. The coherent orientation on its own is isotropic, and solely the anisotropy energies are turning the magnetization in a preferred direction. In a nanopatterned ferromagnetic sample, anisotropies are always present due to its finite size. Furthermore, for the sizes considered in this manuscript (hundreds of nanometers to micrometers), the switching defined in the Stoner-Wohlfarth model is unlikely, and the creation of ferromagnetic domain walls is favorable.

Transition from Superparamagnetism to multi-domain

As described in the Stoner-Wohlfarth section, a sample of small size and spherical shape exhibits a single domain state coherently rotating when driven by an applied field. We should define the length scale for the transition from this state to the multi-domain state for larger dimensions. In a simple picture, a DW is a π -twist of the magnetization over a distance L , the cost in exchange energy of the latter is $A(\partial_x m)^2 \approx A\frac{\pi^2}{L^2}$. Furthermore, in a cylindrical sample, the maximum contribution from magneto-statics energy is $\frac{\mu_0}{4}M_s^2$. By only taking a ratio of the two, the length that favors the creation of domain walls over the coherent rotation of the magnetization is:

$$L > 2\pi\sqrt{\frac{A}{\mu_0 M_s^2}} \quad (2.58)$$

This length defines the superparamagnetic limit (33) below which the system becomes extremely sensitive to thermal fluctuations. This result constitutes a drawback for magnetic applications with the implication of a substantial probability of losing the stored state if the size of the sample is reduced to this dimensions. The superparamagnetic limit can be changed by tuning the strength of the anisotropies governing the system (e.g., increasing the magneto-crystalline anisotropy in the direction of the easy axis defined by the shape). For magnetic structures at ambient temperature and under no applied field, the lowest energy state is obtained by the minimization of the stray field. This result gives rise to magnetic structures such as the Landau state, the S and C state (41), which are favorable due to the flux closure they generate. Indeed, on the edges, the magnetization is curling to avoid the creation of magnetic charges. The Landau state, in Fig. 2.9 is formed with four 90° domain walls and a 180° domain wall at the center.

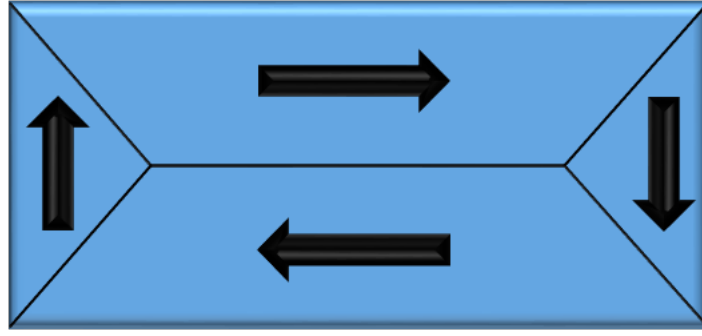


FIGURE 2.8: Landau state with the 5 domain walls allowing a considerable reduction of the stray field as compared to a uniform magnetic state.

1-Dimensional Domain wall model

In usual cases, domain walls are sophisticated spin structures. We can, however, restrict the study to a 1-dimensional spin chain of 2-sphere order parameter space for the magnetization, which greatly simplifies the analytic calculations of its dynamics. We should first start with this configuration. The energy terms acting on the magnetization have been defined in the previous sections. The system considered is a wire with infinite length as compared with the thickness and the width. The width (w) and the thickness (t) are smaller than the exchange length of the material considered of the wire:

$$w, t < \pi\delta_m = 2\pi\sqrt{\frac{A}{\mu_0 M_s^2}} \quad (2.59)$$

To ease the equations, we also select a material with no other anisotropy than the shape anisotropy. We define a 3-dimensional spin system in an easy axis shape anisotropy.

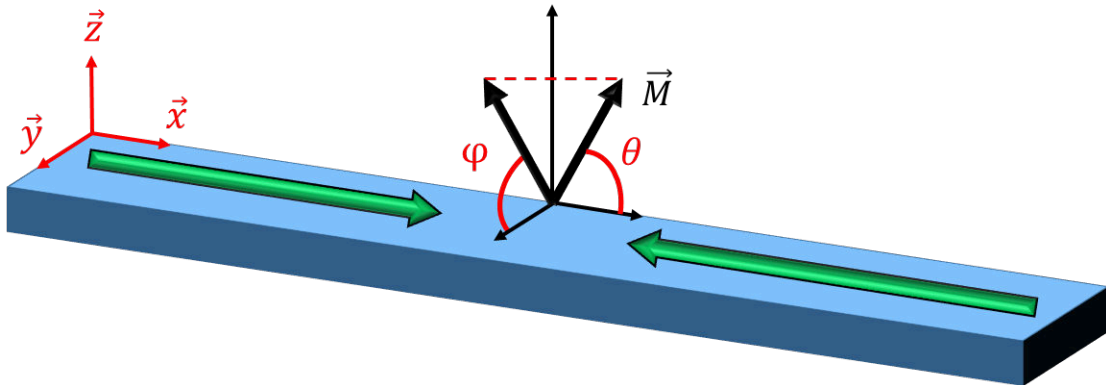


FIGURE 2.9: A wire containing a 1-spin head-to-head DW configuration. The system of coordinates depicted here the one used for the following sections.

We express the exchange energy as in the section 2.1.2:

$$E_{Exchange} = \int_V A(\nabla \mathbf{m}(\mathbf{r}))^2 d^3 \mathbf{r} \quad (2.60)$$

and express it in terms of the spherical coordinate system:

$$\mathbf{m}(x, y, z) = M_S(\cos(\theta), \sin(\theta)\cos(\phi), \sin(\theta)\sin(\phi))$$

$$E_{Exchange} = \int_V (A(\nabla \theta)^2 + A\sin^2(\theta)(\nabla \phi)^2) d^3 \mathbf{r} = \int_V A(\nabla \theta)^2 d^3 \mathbf{r} \quad (2.61)$$

In the previous expression, we used the fact that $\cos(\theta) \approx \theta$ when $\theta = \frac{\pi}{2} \pm \delta$, and ϕ is constant. We can directly derive the effective field of the latter by using the identity $2(\nabla \mathbf{m})^2 = \Delta(\mathbf{m}^2) - 2\mathbf{m} \cdot \Delta \mathbf{m}$:

$$H_{Exchange} = -\frac{1}{\mu_0 M_S} \frac{\delta E}{\delta \mathbf{m} \partial V} = \frac{2A}{\mu_0 M_S} \Delta \mathbf{m} \quad (2.62)$$

The second term to consider is the demagnetizing energy. We take the expression 2.46 obtained in the section 2.2:

$$E_{Demag} = \frac{\mu_0 M_S^2}{2} \iint_V (\mathbf{m}(\mathbf{r}) \cdot \hat{N}(\mathbf{r} - \mathbf{r}') \mathbf{m}(\mathbf{r}')) d^3 \mathbf{r}' d^3 \mathbf{r} \quad (2.63)$$

The matrix \hat{N} is containing the demagnetizing factors. In this case, where one dimension is infinite compared to the two others, the matrix is of the form (42):

$$\hat{N} = \begin{pmatrix} N_x & 0 & 0 \\ 0 & N_y & 0 \\ 0 & 0 & N_z \end{pmatrix} \approx \begin{pmatrix} 0 & 0 & 0 \\ 0 & 1/2 & 0 \\ 0 & 0 & 1/2 \end{pmatrix} \quad (2.64)$$

The 1/2 value is obtained only if the thickness has the same dimension as the width. We change basis again and obtain the demagnetizing energy in the spherical coordinate system:

$$E_{Demag} = \frac{\mu_0 M_S^2}{2} \int_V (N_x \cos^2(\theta) + N_y \sin^2(\theta) \cos^2(\phi) + N_z \sin^2(\theta) \sin^2(\phi)) d^3 \mathbf{r} \quad (2.65)$$

after simplification and stating that the DW remains in the plane $\phi = \pm \pi/2$, the demagnetization energy term is:

$$E_{Demag} = \frac{\mu_0 M_S^2}{4} \int_x \sin^2(\theta) dx \quad (2.66)$$

This is a crude approximation, and still, the energy remains hard to evaluate analytically. Finally, the Zeeman energy ($-\mu_0 M_S \int_V \mathbf{H}_{applied}(\mathbf{r}) \cdot \mathbf{m}(\mathbf{r}) d^3\mathbf{r}$) is included. We stay in the limit where $m_z = 0$. The total energy is then:

$$E_{Total} = E_{Exchange} + E_{Demag} + E_{Zeeman} = 2K \int_x \left(\frac{1}{2} \delta_m^2 (\partial_x \theta)^2 + U(\theta) \right) dx \quad (2.67)$$

with $K = \frac{\mu_0 M_S^2}{4}$, $U(\theta) = \frac{1}{2} \sin^2(\theta) - h \cos(\theta)$, and h is the reduced external field:

$$h = \frac{\mu_0 H_{ext} M_S}{2K} \quad (2.68)$$

We can observe the similarity with the equation of the Stoner-Wohlfarth model to which we add the contribution from the exchange energy. An equilibrium state can be obtained by integration of the Euler-Lagrange equation :

$$\frac{\partial}{\partial x} \frac{\delta E_{Total}}{2K \delta \theta} = -\delta_m^2 \partial_x^2 \theta + U'(\theta) = 0 \quad (2.69)$$

with δ being a functional derivative. The condition for the magnetization is also:

$$\frac{1}{2} \delta_m^2 (\partial_x \theta)^2 - U(\theta) = c \quad (2.70)$$

$$\delta_m^2 (\partial_x \theta)^2 = \sin^2(\theta) \quad (2.71)$$

with c is an integration constant larger than $-U$. The interest is to obtain a domain wall which is a solitary object to do so we fix $\partial_x \theta = 0$ at $x = \pm\infty$. A solution to the latter equation under no applied field is:

$$\theta\left(\frac{x}{\delta_m}\right) = 2 \arctan(\exp\{x/\delta_m\}) \quad (2.72)$$

The solution obtained for our particular case is a "transverse" domain wall in an "in-plane" system. By symmetry consideration, we notice that the solution is the same if the anisotropy considered is of a different physical origin, and is pointing out of the plane (e.g., surface anisotropy in a thin film). In this case, the magnetization is pointing out-of-plane and the solution obtained is the Bloch domain wall represented in Fig. 2.10. The change of the magnetization angle through the domain wall is:

$$dx = \delta_m \sin^{-1}(\theta) d\theta \quad (2.73)$$

We insert the latter in equation 2.67 and obtain the energy density per unit area:

$$E_{DW}/S = 2\sqrt{AK} \int_0^\pi \sin(\theta) d\theta = 4\sqrt{AK} \quad (2.74)$$

which is going to be determined by the competition between the exchange constant, the anisotropy. From the previous equation, two domain walls can be solutions, the Bloch wall with the magnetization curling around the x -axis (see Fig. 2.10-(a)) and the Néel wall with the rotation around the y -direction (see Fig. 2.10-(b)). In Bloch walls, the rotation is on the plane made by the domain wall, while for the Néel wall type it is perpendicular to it.

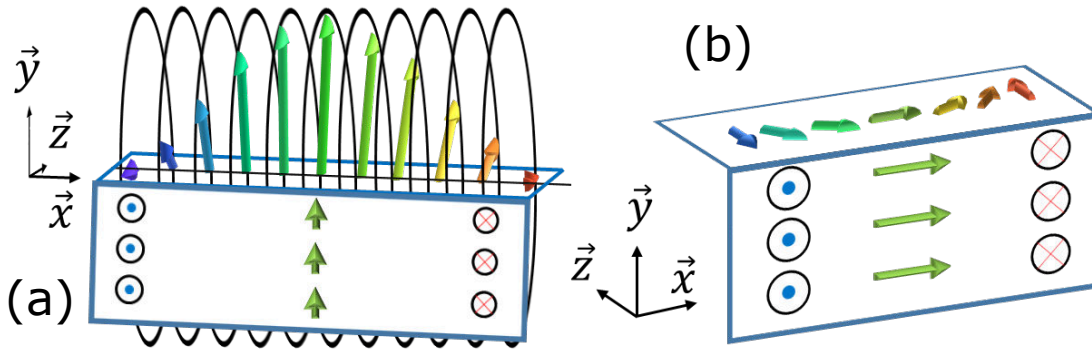


FIGURE 2.10: a) Schematic of a Bloch domain wall. b) Schematic of a Néel domain wall

The symmetries imply a fourfold degeneracy of the Bloch wall. The solution can then be rewritten.

$$\psi_{QC}\left(\frac{x}{\delta_m}\right) = 2QC * \arctan(\exp\{x/\delta_m\}) \quad (2.75)$$

with C being the DW (soliton) chirality ± 1 and is related to the winding number and Q is the charge of the domain wall. C is a consequence of the use of the 2-dimensional spins and the homotopy group of $\pi_1(S^1)$ while the Q is a result of the non-triviality of $\pi_0(S^0)$, which is extracted from the first order transition issued from the bounded Ising model. In the in-plane system, the charge can be expressed as follows:

$$Q = -\frac{1}{2} \int_x (\partial_x m) dx \quad (2.76)$$

and the chirality:

$$C = \frac{1}{\pi} \int_x (m \times \partial_x m) dx \quad (2.77)$$

We should now provide some relation between the topological defects described earlier, and the observable domain walls in micromagnetic simulations or experiments. The topological arguments provide a good guideline for defining

the stability of domain walls. However, realistic physical systems often combine more than one of the aspect discussed in this section. First, domain walls are often rotating the magnetization by π and not 2π as used for the definition of the winding number. In magnetic systems, the hard anisotropy axis is also not characterized by an infinite energy barrier and the magnetization can then 'escape' in the third dimension thus leading to a trivial topology of winding number $n = 0$. No domain wall is topologically nontrivial. However, those topologies of total winding number 0 can be metastable and constituted by topologically stable soliton-antisoliton configurations because the conservation of the total winding number is not violated.

In-plane Domain walls

For the present manuscript, only in-plane magnetized materials are investigated. We then present the most encountered domain walls structures in the range of size that are of our interest. For nanowires in an in-plane configuration, there exists either head-to-head domain walls (43, 44) meaning that the magnetization is pointing in the direction of the domain wall as described in the 1 Dimensional model paragraph, or tail-to-tail domain walls (Fig. 2.11). For in-plane materials, the two simplest domain walls identified are 'transverse' domain walls or 'vortex' domain walls. The vortex-wall is found for large wire widths and thickness while transverse walls are found for smaller cross-sections. Regarding dimensions, we have a 1-dimensional like the behavior of the magnetization at small thicknesses and widths yielding the transverse domain wall. For more significant dimensions, the easy axis character is lost to an easy plane allowing the stabilization of the vortex wall structure.

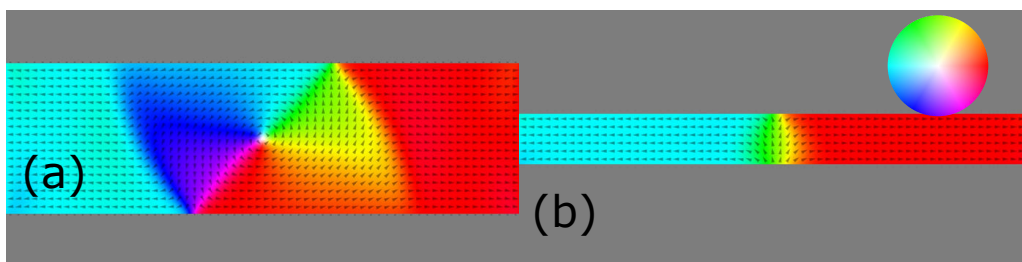


FIGURE 2.11: Two domain walls of 180° type. a) Vortex domain wall in Permalloy sample with a $w = 200$ nm and $t = 30$ nm. (b) Transverse domain wall in Permalloy sample with a $w = 100$ nm and $t = 5$ nm. Both simulations were performed for a 1 nm cell size.

As described earlier, the domain wall is a composite object, which possesses a total winding number of 0.5 in the definition we gave in section 2.4.1. Those objects are confined objects which are not topologically protected meaning that they can be annihilated for example by diminishing the width of the wire to a point. The advantage of the creation of those object is the avoidance of the generation of a large number of magnetic charges. Indeed, most of the dipolar energy is constrained to the topological defects of the DW. The simplest obtainable winding

numbers for a minimum of exchange and dipolar energy are $-1/2$, $+1/2$, $+1$ and -1 . We did not previously mention the existence of fractional topological winding numbers; we should indicate their origins. In a 3 dimensional system, a flux closure is required by the dipolar interaction. Due to the finite size of the samples, the translational symmetry is broken, and a discontinuity of the magnetism takes place. However, to close the flux two magnetic charges of opposite polarity are created on facing wire sides. Those 'edge' defects can be defined by the method of the images (details in Ref. (37)). The charges are confined to the edges since their peeling from the edges creates a line defect in between the charge and the edge. The latter effect, in turn, provides an attractive potential that prevents their depinning. From topological considerations, if the wire is rolled-up around the x-axis, and a cylinder is formed two vortexes are defined with opposite winding number leading to their annihilation. In an in-plane wire system, the meta-stability of the two shown DWS is provided by the existence of the side edge topological defects. Combination of those defects can obtain three various cases of DW spin structure. It is necessary to keep in mind that the creation and annihilation of the defects need to fulfill the conservation of topological charges.

a) The transverse domain wall is consisting of two edge defects which carry a fractional topological winding number $+1/2$ and $-1/2$. This DW appears to be the stable DW in the condition of thickness and width answering to $wt < C(A/\mu_0 M_s^2)$. In the case, of $\text{Ni}_{81}\text{Fe}_{19}$ this argument is valid for $wt < 2400 \text{ nm}^2$ (details can be found in Ref. (21)).

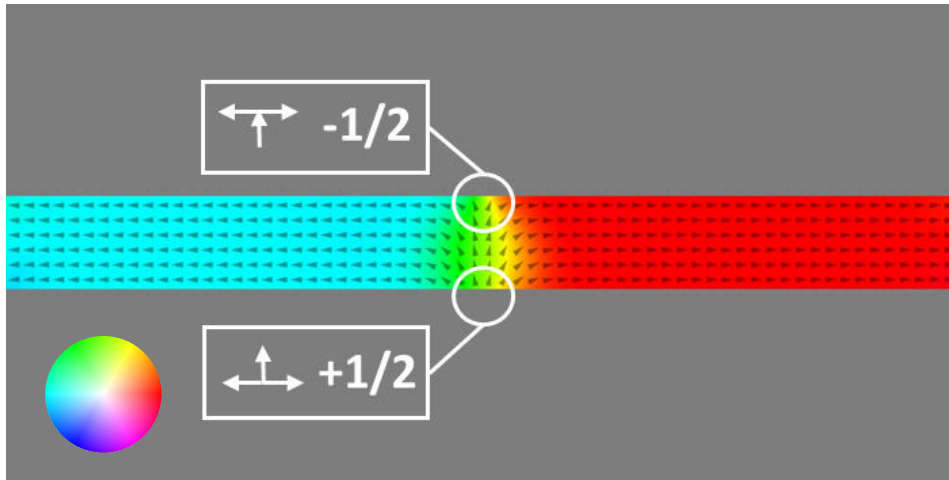


FIGURE 2.12: Topological defects of a transverse domain wall.

From the simulation snapshot in Fig. 2.12, we observe that the winding number $+1/2$ carries only similar charges since all magnetization vectors are pointing out of the defect. From symmetry consideration, the latter defect also exists for magnetization vectors pointing to it. The $-1/2$ defect exhibit less stray field since positive and negative charges are found in its vicinity.

b) The second configuration, is made of an anti-vortex with winding number -1 and two edge defects $+1/2$. This arrangement is energetically not favorable due to the finite amount of magnetic charges carried by the $+1/2$ edge defect

resulting in a substantially higher magnetostatic energy than the defects $-1/2$, $+1$ and -1 (45). The $+1/2$ has then a tendency to decay in a $+1$ and $-1/2$ defect.

c) The last common type is stable when $wt > C(A/\mu_0 M_s^2)$ (21), and is the vortex DW with a center defect of winding number $+1$ and two edge defects of number $-1/2$. As compared with a transverse DW, this configuration is more stable in thick and wide wires since the center core reduces the stray field generated by the edge defects. This configuration is called vortex domain wall (Fig. 2.13) and was imaged in magnetic wires in dimensions typically above 100 nm width and 10 nm thickness.

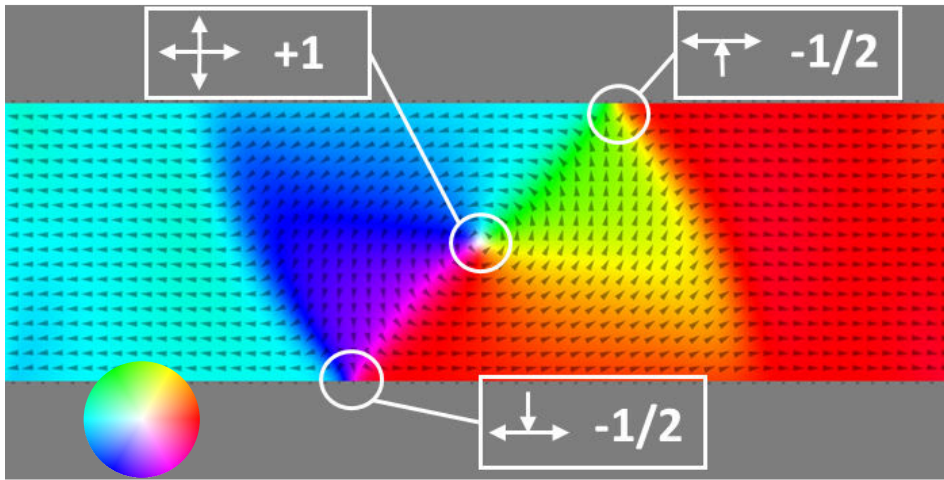


FIGURE 2.13: Topological defects of a vortex domain wall.

Finally, some more exotic domain walls (i.e., more than one core) also exist but usually require systems with higher energies, i.e., with higher saturation magnetization to remain stable (43) under no applied field. As a final note, it was observed that defects interact strongly with their environment (pinning of DW). In fact, the defects possessing a large density of magnetic charges manifest some strong attraction or repulsion with another generator of charges such as abrupt changes of the shape of the sample (edge roughness), magnetic defects (vacancies), etc.. Those observations are of prime importance for the analysis of propagation and nucleation of domain walls in nanowires.

2.4.3 Domain Wall Dynamics and Walker breakdown

In the following subsection, the behavior of the propagation of a domain wall in a confined environment is analyzed for a 180° domain wall. The energy terms considered for the present system are the demagnetizing, the exchange and the Zeeman energy. As it was pointed out previously, the exact integration of the energy terms remains complicated because of the non-linearity of the equations of motion. In 1974, L.R. Walker defined a 1-dimensional model to describe the motion of magnetic transverse domain walls under a DC applied field (46). We

will then derive the equations of motion of a 1-dimensional domain wall following (47): We have noticed previously that the 1-dimensional behavior can be described by three parameters. The domain wall width $\Delta = \sqrt{\frac{A}{K+K_1\sin^2(\phi)}}$ in the case where the azimuthal angle is considered, the domain wall center position x_0 and the azimuthal angle ϕ . We take the same magnetization profile as previously described in section 2.4.2:

$$\theta(x, t) = 2 \arctan\left(\exp\left\{\frac{x - x_0(t)}{\Delta(t)}\right\}\right) \quad (2.78)$$

$$\phi(x, t) = \phi(t) \quad (2.79)$$

The function θ exhibit $\partial_x\theta = \sin(\theta/\Delta)$. We start again with the same previous energy terms except that we derive the magnetization projection on the cross-section plane for the effective anisotropy density.

$$E_{an} = K\sin^2(\theta(x)) + K_1\sin^2(\theta(x))\sin^2(\phi) = (K + K_1\sin^2(\phi))\sin^2(\theta) \quad (2.80)$$

The anisotropy takes into account a rectangular shape. We express the LLG-equation regarding the new system of coordinates.

$$\dot{\theta} + \alpha\sin(\theta)\dot{\phi} = \gamma_0 H_\phi, \quad \alpha\dot{\theta} - \sin(\theta)\dot{\phi} = \gamma_0 H_\theta \quad (2.81)$$

where the two components of the effective field have the form:

$$H_\theta = -\frac{1}{\mu_0 M_s} \frac{\delta E}{\delta \theta}, \quad H_\phi = -\frac{1}{\mu_0 \sin(\theta) M_s} \frac{\delta E}{\delta \phi} \quad (2.82)$$

We introduce two functions, the first of which is the Lagrangian density (48):

$$L = E + \frac{\mu_0 M_s}{\gamma_0} \dot{\phi} \cos(\theta) \quad (2.83)$$

and a dissipative function of the form:

$$F = \frac{\alpha\mu_0 M_s}{2\gamma_0} (\dot{m})^2 = \frac{\alpha\mu_0 M_s}{2\gamma_0} (\dot{\theta}^2 + \sin^2(\theta)\dot{\phi}^2) \quad (2.84)$$

In the 1D approximation and with $\partial_x\theta = \sin(\theta/\Delta)$. We have:

The exchange energy:

$$\int_x A \left(\frac{\partial\theta}{\partial x}\right)^2 dx = \frac{2A}{\Delta} \quad (2.85)$$

The effective anisotropy energy:

$$\int_x \sin^2(\theta)(K + K_1 \sin^2(\phi)) dx = 2\Delta(K + K_1 \sin^2\phi) \quad (2.86)$$

The applied field:

$$-\mu_0 M_s \int_x H_{ext} \cos(\theta) dx = -2\mu_0 M_s H_{ext} x_0 \quad (2.87)$$

and the dynamic term:

$$-\frac{\mu_0 M_s}{\gamma_0} \int_x \dot{\phi} \cos(\theta) dx = \frac{2\mu_0 M_s}{\gamma_0} \dot{\phi} x_0 \quad (2.88)$$

We take for definition the ratio of the anisotropies $\kappa = K_1/K$. Finally, the integration of the dissipation function yield:

$$\int F dx = \frac{\alpha \mu_0 M_s}{\gamma_0} \left(\Delta \dot{\phi}^2 + \frac{\dot{x}_0^2}{\Delta} + a \frac{\Delta^2}{\Delta} \right) \quad (2.89)$$

where $a = \pi^2/12$.

The dynamic equations, also called Slonczewski equations (49) are:

$$\alpha \frac{\dot{x}_0}{\Delta} + \dot{\phi} = \gamma_0 H_{ext}, \quad \frac{\dot{x}_0}{\Delta} - \alpha \dot{\phi} = \gamma_0 H_K \frac{\sin(2\phi)}{2}, \quad (2.90)$$

$$\dot{\Delta} = \frac{\gamma_0}{\alpha \mu_0 M_s a} \left[\frac{A}{\Delta} - (K + K_1 \sin^2(\phi)) \Delta \right] \quad (2.91)$$

The two firsts correspond to the LLG equation, but the last one interestingly describes a relaxation of the domain wall width. This relaxation has a characteristic time, and for Ni₈₁Fe₁₉, it is of the order of $\tau = 0.5$ ps. It is now possible to define the angular momentum of the azimuthal angle by a combination of the two first previous equations:

$$\dot{\phi} = \frac{\gamma_0}{1 + \alpha^2} \left(H_{ext} - \frac{\alpha}{2} H_K \sin(2\phi) \right) \quad (2.92)$$

where H_K is the transverse anisotropy. The latter equations constitute the basics of the dynamic in the 1D model.

When no anisotropy field is present, we can see that:

$$\dot{\phi} = \frac{\gamma_0 H_{ext}}{1 + \alpha^2} \quad (2.93)$$

The precession is linear with time giving us a uniform angular momentum. The wall velocity, in this case, can then be expressed:

$$\dot{x}_0 = \gamma_0 \Delta H_{ext} \frac{\alpha}{1 + \alpha^2} \quad (2.94)$$

When some transverse anisotropy is present (in almost every case in physical systems), the angular momentum has a dependency to a field called the Walker field defined as:

$$H_W = \frac{\alpha H_K}{2} \quad (2.95)$$

If the applied field is lower than the Walker field and equilibrium value of the angle ϕ exist. The domain wall is just propagating in the x-direction with a fixed angle. At equilibrium, we find (46):

$$\dot{x}_0 = \frac{\gamma \Delta}{\alpha} H_{ext} \quad (2.96)$$

$$\sin 2\phi = \frac{H_{ext}}{H_W} \quad (2.97)$$

This 1D model is, however, limited to the strict conditions of a small field and low transversal anisotropy. In the case of large anisotropy and higher field, the domain wall width is largely varying and even changing conformation. Those effects make the velocity relation non-linear and thus hard to analyze. We picture the behavior predicted by the previous equations for a field applied in a nanowire with a transverse domain wall with a magnetization component in the y-direction. We summarize the different acting torques, such as the precession like torque in the first column of the table owing to the precessional term of the LLG-equation, and the damping like torque in the second column.







Term		Precession	Damping
External applied field (+x)		+z 	+x 
Demagnetizing field (-z)		+x 	-z 

FIGURE 2.14: Torques acting on the magnetization containing a Head-to-Head domain wall under an external applied field from (20).

The two out-of-plane components compensate each other, and the domain wall propagates only by increasing the angle ϕ to a constant value correlated to an applied field value. The demagnetizing field is not modified because defined by the material parameters and especially the shape. When the field applied is strong enough, the out-of-plane component from the precession overcomes the stray field component from the damping, and a vortex core is created at the edge. The limit angle value that can be reached is:

$$\phi_W = \frac{\pi}{4} \quad (2.98)$$

Above this angle value, the theory of Walker (46) predicts an oscillatory behavior of the domain wall velocity as well as a change in DW spin structure. The effect is named the Walker breakdown, and its consequences on the DW velocity are shown in Fig. 2.15. Above the Walker breakdown, the DW changes its spin structure and oscillate between vortex and transverse wall. The transverse wall can be accurately represented in the 1D model, but the latter highly fails when it comes to composite objects such as vortices. In general, the velocity of the DW is much lower in a vortex state due to the dynamic of the vortex core (see 2.4.4). The velocity suffers a substantial decrease right above the Walker field and starts increasing again as shown in the Fig. 2.15.

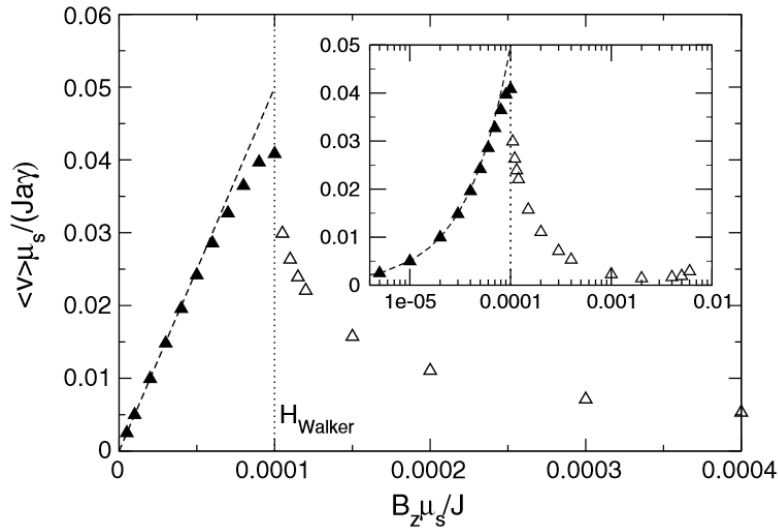


FIGURE 2.15: Velocity as a function of the applied field (Adapted from (43))

In the condition where $H \gg H_W$, after the reduction of velocity, the velocity is followed, anew, by a linear increase. With increasing applied field, the precession of the DW is enhanced, and the velocity of the DW can be seen as an average of the velocity in the different processes of the Walker breakdown.

2.4.4 Vortex motion under field

Qualitatively, a transverse domain wall made of two opposite half charges $+1/2$ and $-1/2$ (see section 2.4.2) can transform in a vortex state with the expulsion of a vortex core of ± 1 charge. When an external field is applied, the transverse DW is moving along the wire with the positive charge faster than the negative one (50). The vortex DW similarly possesses two edge charges of the same sign, and the motion of the two is then comparable with the one of the transverse domain wall. The difference stands in the core motion which is transversal. In this case, the 1D model fails to explain the reduced speed. The velocity reduction was blamed on the magnetization rotating around the core of the vortex. We try to explain

the core dynamics with the Thiele equation (51, 52), which reformulates the LLG-equation for an understanding of the motion. The equation considers a fixed spin structure in motion at constant velocity.

The stationary motion implies:

$$\frac{\partial \mathbf{m}}{\partial t} = -(\mathbf{v} \cdot \nabla) \mathbf{m} \quad (2.99)$$

$$\mathbf{F} + \mathbf{G} \times \mathbf{v} + D\alpha \mathbf{v} = 0 \quad (2.100)$$

where \mathbf{F} is the force on the spins, \mathbf{G} represents the gyrovector, and the last term is the dissipation of energy. They have the form:

$$\mathbf{G} = -\frac{M_S}{\gamma} \int_V \cos\theta (\nabla\theta \times \nabla\psi) d^3\mathbf{r} \quad (2.101)$$

$$D = -\frac{M_S}{\gamma} \int_V (\nabla\theta \otimes \nabla\theta + \cos^2\theta \nabla\psi \otimes \nabla\psi) d^3\mathbf{r} \quad (2.102)$$

The \mathbf{G} term comes from the precessional term of the LLG (see section 2.3.1) while D is more of a damping term. For a vortex core, the term \mathbf{G} yields:

$$\mathbf{G} = -\frac{2\pi}{\gamma} M_S C Q \cdot \mathbf{x} \quad (2.103)$$

where C represents the winding number exposed in the last subsection and Q is the polarity of the core. The gyromotion moves the core toward the edges of the wire. This core also interacts with a restoring force, which emanates from a parabolic potential with the lowest energy at the center, due to the demagnetizing field. The interplay between the two effects keeps the core in constant motion under an applied field. The movement, however, remains transverse and does not help the propagation in the forward direction. Only the two edge defects guide the domain wall in the direction of the applied field. The annihilation of the vortex at the edge, the expulsion of the vortex and the crossing of the core constitute the limiting factors in the DW velocity above Walker breakdown and then the propagation.

Chapter 3

Experimental techniques

In this chapter, we introduce the different tools and techniques that allowed the processing of the samples and their investigations.

3.1 Investigated Materials

Most of the experiments described in this manuscript were realized on single magnetic layers for the possibility to use rather fast and accurate simulations for the reproduction of the results. The dynamics of DWs are complicated enough without the disturbance of stray fields originating from other magnetic layers. Despite the latter, transport measurements such as giant magneto-resistance measurements require the use of a complete stack of several layers for the resistive detection of the direction of the magnetic layers. In this section, we describe the different materials that are used in the result section.

Substrate is a 5-inch wafer used for mass-production. It is a 625 μm thick disk of silicon with a notch on the left to facilitate the alignment during the different process steps. The surface is covered with a 500 nm isolating layer of Al_2O_3 or 1500 nm of SiO_x . The Al_2O_3 or SiO_x allows the electrical isolation of the magnetic metallic layers. These layers are grown at the company Sensitec GmbH.

$\text{Ni}_{81}\text{Fe}_{19}$ or Permalloy (53) is an alloy made out of Fe and Ni. It is a metal, ferromagnetic at ambient temperature with a Curie temperature of 873 K (54). The Ni and Fe elements are brought together in the quantities $\text{Ni}_{81}\text{Fe}_{19}$. In our case after sputtering on the SiO_x wafers, it exhibits a polycrystalline structure, but it can also be epitaxially grown on $\text{MgO}(100)$, $\text{MgO}(110)$, $\text{Cu}(001)$ or $\text{Si}(001)/\text{Cu}(001)$ (55). The $\text{Ni}_{81}\text{Fe}_{19}$ is soft which means that the coercive field and the remanence are small. The NiFe alloy in the right stoichiometry and grown by magnetron sputtering exhibits near zero magneto-crystalline anisotropy as well as zero magneto-striction (29). Thanks to these characteristics, it is very suitable and then used for industrial applications since the 1920s (56). It also has been highly investigated in the past four decades, and it is now coming to maturation as it is seen by the plateau in Fig. 3.1. Permalloy is then a popular material in the community, and consequently, obtained results can be easily reproduced.

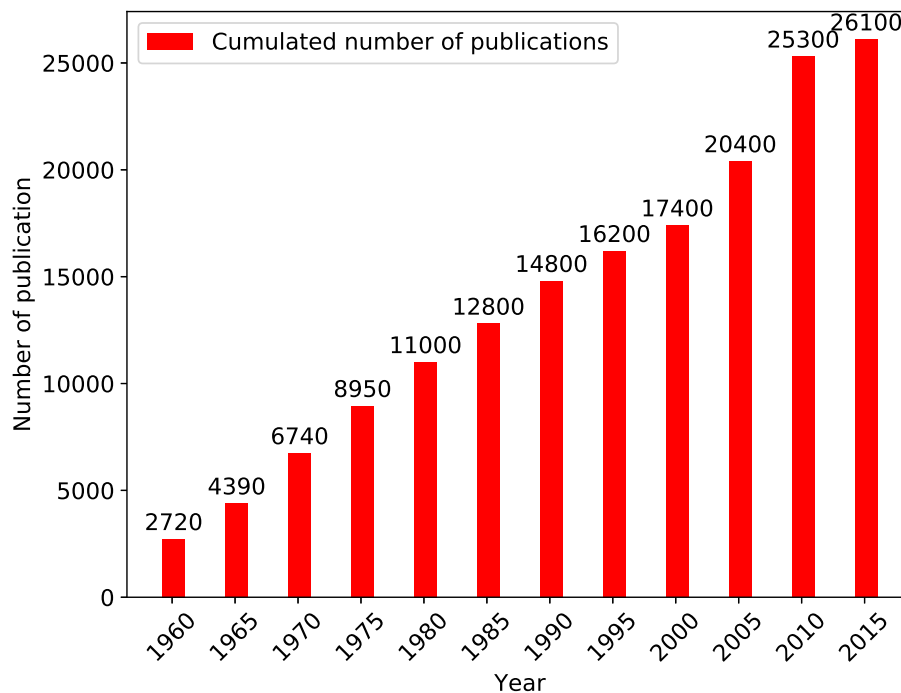


FIGURE 3.1: Bar plot indicating the cumulated number of publications with the word 'Permalloy' through the years. The plot is made by obtaining the number of publications by slices of 5 years on the website Google scholar (57).

$\text{Co}_{90}\text{Fe}_{10}$ is an alloy of Co and Fe. This metal is also ferromagnetic at room temperature (58), the Curie temperature of this compound does not appear in the literature we then provide the Curie temperature of Co which is 1388 K (59). As compared with $\text{Ni}_{81}\text{Fe}_{19}$, it exhibits an enhanced M_S provided by the Co atoms (Slater-Pauling rule (60–62)). However, a significant disadvantage of this metal is its strong magnetocrystalline anisotropy (58). In the polycrystalline phase, the difference in orientation of the preferred axes of neighboring crystallites can trigger highly inhomogeneous landscape of the magnetocrystalline energy term potentially leading to the pinning of DWs.

The capping layer is a non-magnetic layer used for protective purposes, which does not interact with the phenomena measured. Our capping layer is made of 4 nm of Ta. Tantalum is a robust metal that only oxides on 3 nanometers in contact with air (63), thus suitable for protection of the underneath magnetic layers. Concerning the interaction of non-magnetic and magnetic layers, it was, previously, observed that tantalum and other metals intermix with the underlying magnetic layer which results in a magnetic dead layer at the interface described in Ref. (64). In our case, the dead layer is not expected to perturb much the magnetic properties and the dynamics of domain walls because the magnetic layer is much thicker than the dead layer.

3.1.1 Spin-valve

A spin-valve is composed of a complicated stacking of different materials necessary to obtain a particular transport measurement. The transport mechanism used here is the giant magneto-resistance (GMR), which is described further in the manuscript 3.4.4. The intrinsic purpose of the spin-valve is to allow the measurement of different resistance values depending on the relative orientation of a 'fixed' magnetic layer as compared to a 'free' one (see 'Free' Ferromagnet in Fig. 3.2).

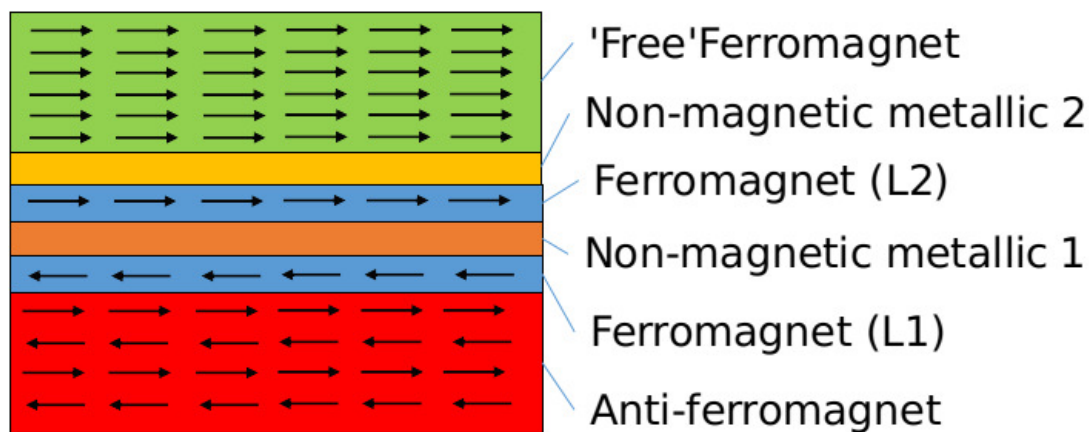


FIGURE 3.2: Schematic representation of the exchange-bias coupling between an antiferromagnet and a ferromagnet (L1) plus an RKKY coupling with the ferromagnetic layer (L2) and a decoupled 'free' magnetic layer.

In Fig. 3.2, we represent the general configuration of a synthetic antiferromagnet (65). It is composed of an anti-ferromagnet on which is deposited a ferromagnetic layer (L1) coupled to the layer (L2) through a non-magnetic spacing layer (Non-magnetic metallic 1 in Fig. 3.2). The first layers necessary for the exchange-bias coupling (66) are the actual antiferromagnet and the ferromagnetic layer (L1). The anti-ferromagnet used for the presented spin-valve is a 15 nm thick PtMn layer (67), which is a strong anti-ferromagnet with a low Néel temperature ensuring an ease of industrial processing and its compatibility with the polycrystalline ferromagnetic materials. The low Néel temperature is a must have to avoid jeopardizing the complete stack. In fact, at high temperatures, crystallization can change the magnetic properties drastically, e.g., increase of the dead layer at the interfaces(68). It is then a necessity to prevent any intermixing of the layers during the annealing procedures to keep flat interfaces. The exchange-bias locks the ferromagnetic layer L1 with the antiferromagnet. Furthermore, the strength of the locking of the whole stack is then improved by an antiferromagnetic coupling of the layers L1 and L2 through an RKKY coupling mechanism (69, 70). The latter is achieved by inserting a spacing layer composed of a non-magnetic metal. Ru is selected, and a thin layer (typically lower than 1 nm (71)) is deposited on top of L1, the control of the thickness is required to obtain antiferromagnetic coupling between the $\text{Co}_{90}\text{Fe}_{10}$ layers L1 and L2. The two ferromagnetic layers are usually

ultra-thin to maintain a stable coupling. In the present case, the ferromagnetic layers are 1.5 nm of $\text{Co}_{90}\text{Fe}_{10}$ that we name L1 and L2. Finally, the detection of the GMR effect with the spin-valve is possible if a non-magnetic layer is deposited between the artificial antiferromagnet and the magnetic free layer (non-magnetic metallic 2 in Fig. 3.2). A layer of Cu is used, which thanks to a considerable spin diffusion length and a good band matching with $\text{Co}_{90}\text{Fe}_{10}$, allows for measurements of a large GMR signal. In our present architecture, the free layer must be decoupled from the rest of the system. The thickness of the Cu layer is carefully controlled since it must yield a zero-RKKY-constant coupling to avoid any exchange-bias effect.

3.2 Material processing techniques

A large variety of deposition and growth techniques are available for industrial and academic purposes (72–75). The method used is often dependent on the required material, throughput, quality, and crystalline phase. A distinction is already made between the wet and dry growth. The wet growth employs chemical reactions usually catalyzed by electric fields (electrodeposition) or merely catalytic agents (76). A wet growth is often extremely fast (compared with dry growth), and potentially troublesome to precisely control. Wet techniques are then used to grow thick layers such as the one required for contacting layers.

For the present manuscript, we are more interested in dry growth techniques, which allow the deposition of a few atoms up to micrometers thick layers. One category of these methods is the chemical vapor deposition (CVD) (77), which employs volatile fluids to produce chemically-deposited coatings on the substrate. The second type of technique is called the physical vapor deposition (PVD) (78), which is mainly based on the sputtering and thermal evaporation of source compounds in a solid phase.

Thermal evaporation The thermal evaporation (75) involves a solid state material placed in a crucible, which is heated up to the sublimation point in an ultra-high vacuum environment. The sublimated source material is then spreading in the chamber from the crucible. The emitted atoms then agglomerate on the substrate facing the crucible.

Two primary heating methods are used:

- Resistive heating of a tungsten filament placed in the crucible at the back of the source material.
- Electron or laser beam directed to the source material.

Thin-film evaporation systems can offer the advantages of relatively high deposition rates, with real-time thickness control. Another used PVD technique is sputtering. We describe this method in details since most of our investigated layers were deposited with it.

3.2.1 Sputtering

The sputtering technique (73) is utilized for the deposition of various materials from metals to insulating oxides in thin layers. The high quality and variety of films available for deposition with this technique make it a good candidate for the investigation of nanostructures. In Fig. 3.3, we provide a schematic representation of the general mechanisms used during a sputtering process.

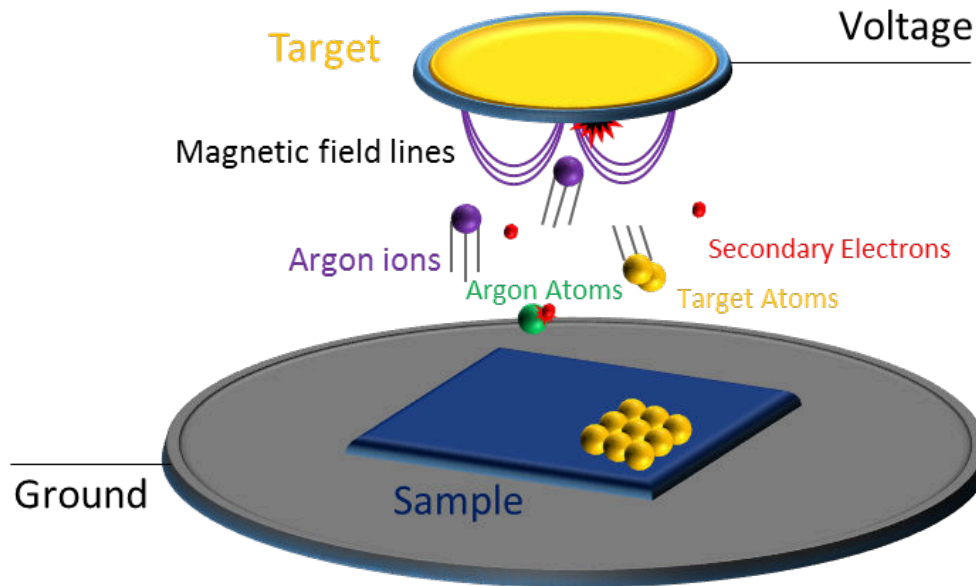


FIGURE 3.3: Schematic of the inside of a sputtering tool. A strong electric field is applied across the target and the sample that attracts the ionized Ar atoms to the target, thus sputtering the target atoms.

A sputtering machine is a complicated system involving several chambers, pumps, and targets. For the sputtering of a source material, a range of conditions needs to be met. The chamber is maintained at low pressure, typically in the 10^{-8} mBar range of base pressure or less, to ensure the least amount of contamination possible in the deposited layer. The sample is usually held in a fixed position on the holder in the deposition tool. If a high uniformity of growth is needed, the sample can be mounted on a spinning plate facing the target. The plate can also be tilted to allow sputtering under an angle with the surface (79). A target of the desired material is mounted in a chamber filled with an Ar gas. The system can be used in a DC mode where the target is at a negative bias voltage, or in an AC mode where the voltage is varying over time. For the deposition process, a plasma needs to be generated by the ionization of the Ar gas. The application of a large electric field across the gas is sufficient to obtain a stable plasma. In the DC configuration, the electrons are accelerated away from the target due to the negative voltage. On their path, they might collide with neutral species and drive the outer shell electrons out of the gas into the ground potential where they are lost

in the electric circuit. This dynamic process leaves the gas unbalanced and positively charged. The Ar^+ ions are now free to move in the direction of the target and strike into the source material. The kinetic energy released in the compound allows the breaking of the bounds of the material and the creation of flakes of size ranging from few atoms to nanometer clusters. The denser and more compact the target is the smaller are the ejected species. In our case, the $Ni_{81}Fe_{19}$ target only grants neutral atoms and a few ions. During the process, secondary electrons are also leaving the targets and participate in the self-maintenance of the plasma. If the mean free path is long enough, the target's atoms and flakes being ejected collide with the sample and agglomerate. The process is sustained until the formation of a polycrystalline or crystalline film depending on the substrate and the sputtering conditions. Metals are easily sputtered in a DC configuration since they source electrons for the generation and stabilization of the plasma, on the other hand, insulators need to be sputtered in the AC settings. With insulators, the Ar^+ ions colliding the surface of the target agglomerate and build a positive screening potential, thus reducing the sputtering rate. The potential at the target is inverted to release the ions from the surface.

Magnetron sputtering: For our samples, we used the magnetron sputtering configuration. A magnetic field is added, hence the name magnetron, at the back of the target to confine and densify the plasma at the target. This technology was not present in the first generations of sputtering machines but is of great interest. The technique takes advantage of the fact that the magnetic field lines parallel to the surface of the target allow the constraint of electrons in its vicinity. The electrons follow a helical trajectory and provide more ionizing collisions with the Ar gas close to the surface. This process results in a denser plasma close to the target which increases the sputtering rate. The Ar^+ ions are also affected by the magnetic field forcing them to deviate from their original trajectory, but the radius of the helical path is much larger than the distance between the species and the target thus leaving them on a mostly linear trajectory. The target species being uncharged, they are not affected by the magnetic field. The disadvantage of the technique is in part coming from the kinetic energy released by the target atoms onto the substrate, thus heating it up. The sample holder is kept cold by a flux of He gas or a water flux. The latter effect is detrimental to the sputtering of amorphous phases. The state-of-the-art-sputtering tools (e.g., Singulus machines (80)) have the advantage of being extremely precise enabling the deposition of subnanometer thickness layers even for amorphous materials.

3.2.2 Ion beam etching

Ion beam etching (81) is a controlled dry etching tool allowing the carving in materials with a vertical precision of the order of a nanometer. The ion etching method is performed with a similar setup as the one used for the sputtering of a source material. The fundamental difference with sputtering lies in the trajectory of the Ar^+ ions, which in the present case are directed toward the surface of the sample to be etched. The aim is then to sputter away material on the surface.

This physical etching has the advantages of being anisotropic and relatively well controlled. A mass-spectrometer can even be added to the chamber for a real-time control of the etched thickness. For the disadvantages, the first one is the damaging of the substrate and the non-etched material due to ion implantation and the second one is a low etching rate.

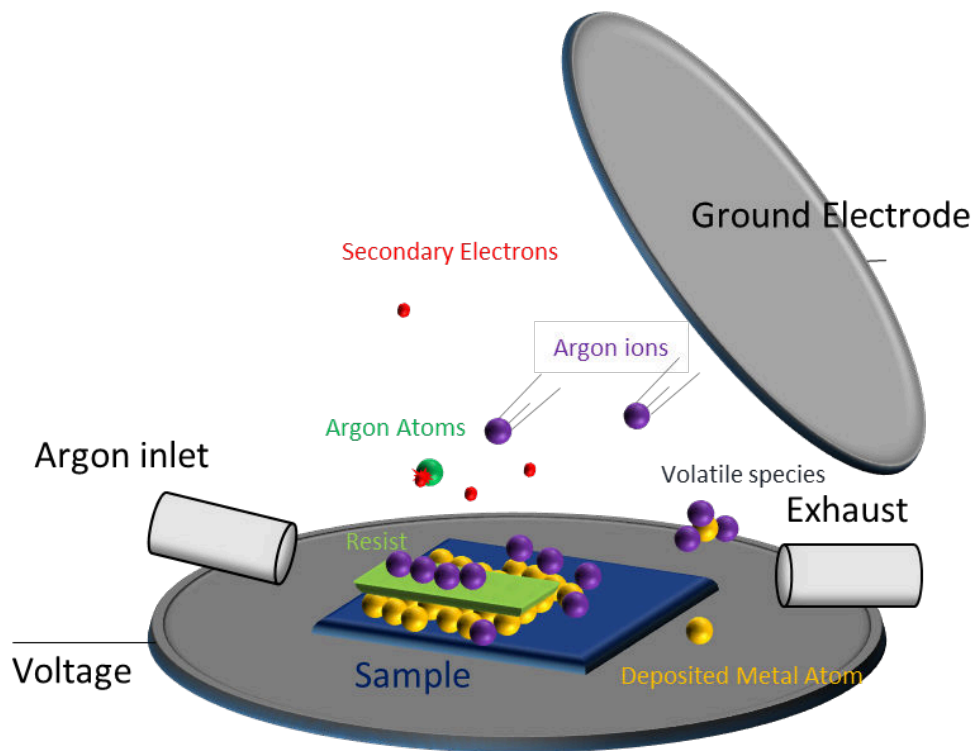


FIGURE 3.4: Schematic of the inside of an ion milling tool during the carving of a wafer. The resist allows the protection of the underlying material and the transfer of the desired structures to the material.

The process: The chamber is maintained under vacuum conditions (10^{-5} to 10^{-4} mbar). Inside the chamber, two metallic plates are placed as represented as in Fig. 3.4. They constitute the electrodes of the applied electric field. The lower electrode serves as a support for the wafer and is electrically isolated from the rest of the chamber. The other electrode and the chamber are connected to the ground. An angle can be set between the two electrodes to allow for directional etching of the film. Similarly to the sputtering method, the chamber is filled with an Ar gas. The plasma is generated by the application of an intense radio-frequency electric field in between the electrodes. The gas is ionized by removing some of the outer electrons yielding free electrons and Ar^+ ions. Due to the number of species present in the chamber, the mean free path of the free electrons is reduced, and they tend to collide. In the occurrence of scattering event with a cation, a recombination takes place which releases a photon of characteristic wavelength

depending on the chemical species. If electrons collide with a neutral molecule or atom, it is ionized. The chain reaction helps then the creation and the stabilization of the plasma. During the oscillatory behavior of the electric field, some free electrons enter into contact with the walls of the chamber. The electrons that go into the electrode connected to the ground are absorbed in the electric circuit and disappear. The ones that are hitting the other electrode are trapped at the surface and generate a negative potential. The ions, too heavy, are lowly affected by the oscillating electric field. However, the built negative potential attracts the positive ions; they are accelerated in the direction. The some of the important reactions are:

- The Ar^+ ions bombard the wafer with a substantial kinetic energy. The ions transfer their momentum to the species present at the surface of the sample. The species are then ejected out of the surface.
- The chemical etch comprise the capture of electrons by the cations in the vicinity of the sample's surface. They then turn into radicals which chemically reacts and carve into the material. The species produced during the chemical reaction are often more volatile and are quickly withdrawn from the surface and evacuated through the exhaust.

For the present study, the wafers were etched on a rotating plate at various angles to provide a uniform etching.

3.3 Patterning methods

Nanostructures are the pillar of the electronic industry allowing a downscaling to the atomic size. In this section, the reader can find a description of the two methods of lithography: the photolithography and electron beam lithography. These two nanofabrication methods make use of a patterned resist, we then first start with a description of it.

3.3.1 Resists processing

In a lithography process, a resist is utilized as a mask for further processes such as sputtering or ion etching. Resists are conventionally made of a polymer matrix diluted in a solvent providing a degree of viscosity. There exist two main categories of resists, the positive and the negative ones. The positive resists are composed of a polymer as compared to negative resists which contain shorter monomers. The importance of this feature is observable in the chemical reaction triggered by photons or electrons. On the one hand, a positive resist is destroyed by the photons, the long branches of the polymer are cut in monomers during exposure. On the other hand, the negative resists exhibit the opposite reaction, and the monomers are polymerized during exposure. For extremely detailed structures, selecting a proper resist is a must. The usual parameters to consider are the photo-sensitivity, the viscosity, the adhesion and the thermal stability.

Spin-coating The first step in resist processing is the deposition of the resist on the sample's surface, which is called the spin-coating. The spin-coating consists in spreading the resist on the surface of the substrate using the centrifugal force.

There are four important steps during the spin-coating:

1. The drop-coating of the resist on the sample.
2. The uniform distribution of the resist by spinning the sample around its surface axis.
3. The removal of the surplus by an increase of the speed of the rotation.
4. A constant speed spinning to establish the thickness and evaporate the solvent.

For the finalization of the evaporation of the solvent, the resist is baked on a hot plate. The baking time and the temperature should be precisely controlled to avoid cracks in the resist. When the resist is coated on the sample, different irradiations can be used to pattern it.

Photolithography

The oldest nano-patterning method is the photolithography (82). It was first invented in 1820 by a scientist named Nicephore Niepce (83). The photolithography is now a well-known and controlled process for nanofabrication. Indeed, it is the most used technique by the industry. Its success stems from its reliability and the ability of parallelization. A vast region is printed simultaneously with a decent homogeneity of the energy provided, and thus of the lateral dimensions of the created structures.

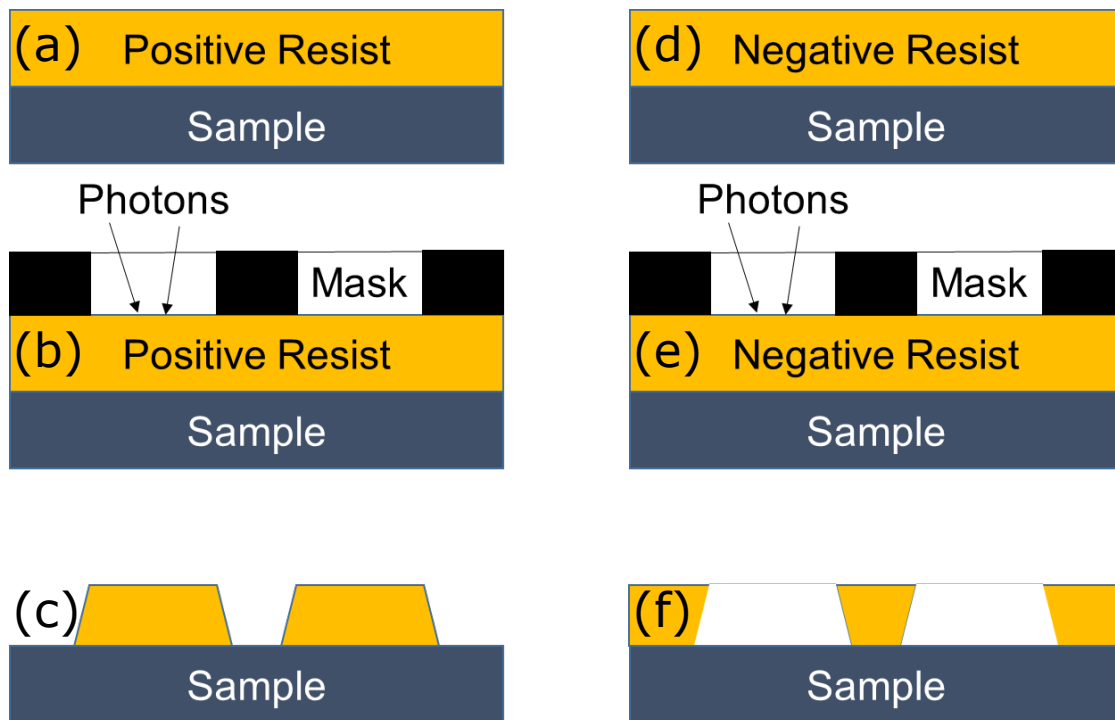


FIGURE 3.5: (a) Positive resist on a sample after spin-coating. (b) Mask positioned in a contact made on top of the resist. The dark rectangles indicate sections that are not transparent to Ultra-Violet light. (c) Exposed resist after development. (d, e, f) Same process with a negative type of resist.

The photons are the fundamental elements used for the exposure of the resist. The precision of the details of a structure is enforced by the wavelength of the incoming light (diffraction limit of a microscope (84)). For the detail of the process, similarly to a conventional optical microscope, the light is guided through a path until it reaches the sample's surface. A mask, containing a non-transparent material shaped in the matrix to be imprinted, is placed in this optical path. The non-transparent part is most often composed of tungsten or chromium for their absorption capability in the UV range. The transfer of the pattern from the mask is then made onto the resist. After the exposure of the resist, the pattern is transferred and needs to be separated from the unexposed/exposed parts of the resist. This process is called the development and is performed by dipping the sample in a basic solution that removes the monomers from the sample's surface. After this step, the resist can be baked to improve its stability. A few different operative configurations are implemented for photolithography. The easiest one is the contact mode, which relies on the direct contact of the resist with the mask Fig. 3.3. This approach provides an immediate impression of the motif and a better conformity between the developed resist and the mask used. One of the drawbacks is the limitation to the exact size of the pattern on the mask. Also, the mask eventually gets covered with resist if used extensively. A cleaning of the tools is never appreciated in a fast-paced production environment. Another configuration is called the stepper mode in a non-contact, due to the provided distance between the mask and the sample, more optics, and lenses can be positioned to

reduce the size of the projected image. Nowadays, the semiconductor's industry utilizes photons produced by plasma formed by laser excitation to manufacture elements of 15 nm pitch sizes. The tool used here is equipped with a Hg lamp that shines around 300 nm wavelength photons, which leads to a lateral resolution of 200 nm at best.

Electron beam lithography

The resists are not solely sensitive to photons. Electrons are also utilized for a different method of resist exposure straightforwardly named the electron beam lithography or for the shorter version, ebeam lithography¹ (85). Similarly to the previous technique, the electrons are used to make/destroy the bounds of the polymers. The wavelength of the electron (around 7 pm for an acceleration voltage of 30 kV) being much smaller than the one of the UV photons (300 nm), the lateral dimensions of the patterned element are enormously shrunk. Furthermore, the ebeam lithography method does not require an expensive mask. The process in that aspect is less costly, but it is mainly providing with more flexibility, due to the possibility of almost spontaneous creation/modification of the exposed designs. The process is the following:

A source of free electrons is extracted from a heated tungsten wire (thermionic emission) and collimated with the help of electromagnets. The electrons are drawn to the surface of the sample by the application of a high bias voltage (see section on scanning electron microscopy 3.4.6). The focused electron beam then exposes the resist under its spot, and after a dwell time, it is deflected and moved to draw the rest of the structure. One of the drawbacks of the ebeam lithography is the strong natural interaction of the sample with the electrons often leading to backscattering and exposure from the bottom of the resist. The necessary sequential exposure results in a much slower exposure than the optical lithography. Hence the ebeam lithography remains a technique reserved for academic purposes.

3.4 Measurement techniques

3.4.1 Four-point-probe electrical measurement

The four-point-probe is a standard measurement method for the resistivity of a metallic thin-film (86). The resistivity obtained can often be correlated to the defect density as well as the thickness of the layers (87, 88). The measurement procedure consists in contacting the sample with four parallel tungsten needles. The needles, placed at equidistance, are contacted on the surface of the sample. A small current is applied between the outer probes while a voltage is measured

¹We want to thank S. Kauschke and K. Litzius for introducing us to the technique.

between the inner probes. As opposed to a conventional 2-point resistance measurement, this technique subtracts the contact resistance between the tungsten needles and the surface in contact. The resistance value of the latter effect being usually more significant than the sheet resistance, it is necessary to measure thin-films in this configuration.

3.4.2 BH-looper

A BH-Looper (89) is built to perform fast measurement of the magnetic characteristic of a thin-film wafer. However, it does not allow the measurement of materials with a coercivity higher than a hundred of Oersted. The latter is a flaw of the Helmholtz coils not powerful enough to reverse the magnetization. Another significant drawback is the requirement of a rather large sample area to sense a large enough signal, thus not allowing the measurement of $1\text{ cm} \times 1\text{ cm}$ area, which is the typical academic sample size. Thankfully, for the present study, we use 5-inch wafers entirely covered with the desired magnetic material².

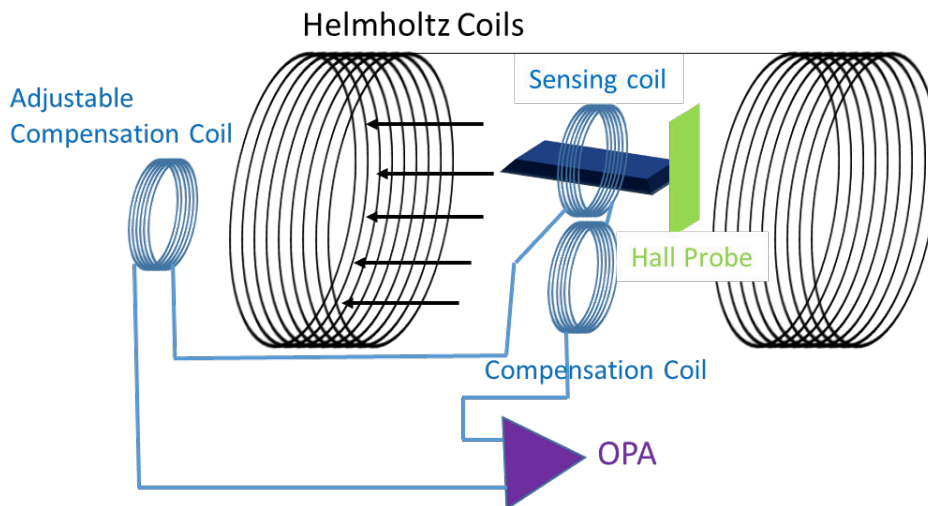


FIGURE 3.6: Schematic of a BH-looper, the sample is position in the center of the sensing coil. A field is swept by oscillating the current provided to the Helmholtz resulting in the switching of the magnetization in the sample. The stray field values obtained by the sensing coil is compared to the one measured by the compensation coils.

The operation of the BH-Loop is the following: The sample is placed in the center of two Helmholtz coils (90). An alternating current of frequency up to 100 Hz is applied to those coils. The latter is generating a uniform oscillating field in the region of the sample. To acquire the stray field stemming from the sample, a set of two pickup coils are placed at different positions. One is put below the sample and the other outside of the two Helmholtz coils. The sensing

²We thank H. Grimm for teaching us the use of the equipment.

coil submitted to an alternating magnetic field produces an alternating current. Similarly for the compensation coils, however, this one is not less submitted to the stray field of the sample. The compensation coils subtract the contribution from the Helmholtz coils to the generated voltage. An operational amplifier then acquires the voltage. From Faraday's law, we extract the stray field:

$$V = NA \frac{dB}{dt} \quad (3.1)$$

With N the number of loops that constitutes the sensing coil and A the cross-section area of the coil. Usually, a hall probe helps for the measurement of the voltage.

3.4.3 Magneto-optical Kerr effect microscopy

The Magneto-optical Kerr effect (MOKE), named after John Kerr (91) the English scientist who discovered the effect, sits at the origin of most of the magnetic imaging. Currently, most of the knowledge on magnetic domains is derived from measurements acquired with the technique, which in some sense proves its efficiency. It is mainly a qualitative, and useful for a basic understanding of magnetic domain directions. It hardly yields quantitative results on the magnetization properties. The MOKE is mainly due to Spin-Orbit coupling interactions and Exchange interactions mechanisms (20, 92). The optical characteristics of a solid are determined by the band diagrams, specifically the allowed transitions of the electrons from occupied to unoccupied states. The magnetic splitting of the energy bands at the Fermi level guarantees that the interaction with light is dependent on the orientation of the magnetic state. In fact, the magnetization direction can be imaged by choosing the polarization direction of the light. In a proper configuration of the microscope, a phase difference is induced between the right and left circular polarization upon reflection from the surface. We consider the MOKE effect for metallic magnetic systems. The penetration or skin depth for the reflection of visible light on metallic surfaces is around 50 nm (93), and the amplitude is dropping exponentially from its surface.

Semi-classical description of the Magneto-optical Kerr effect

We describe the interaction of the light beam with the essential components of the microscope. Fig. 3.7 displays the MOKE microscope's schematic and the light path. The light beam can be generated by arc discharge lamps used for their high radiance output levels (94). However, the high-pressure mercury arc lamps exhibit an inherent and significant arc instability, which is disadvantageous for MOKE imaging applications. During the project, the lamp was replaced by a state-of-the-art high power LED illuminator with a spectral irradiance similar or superior to high-pressure arc lamps, which exhibit high durability and a low noise level.

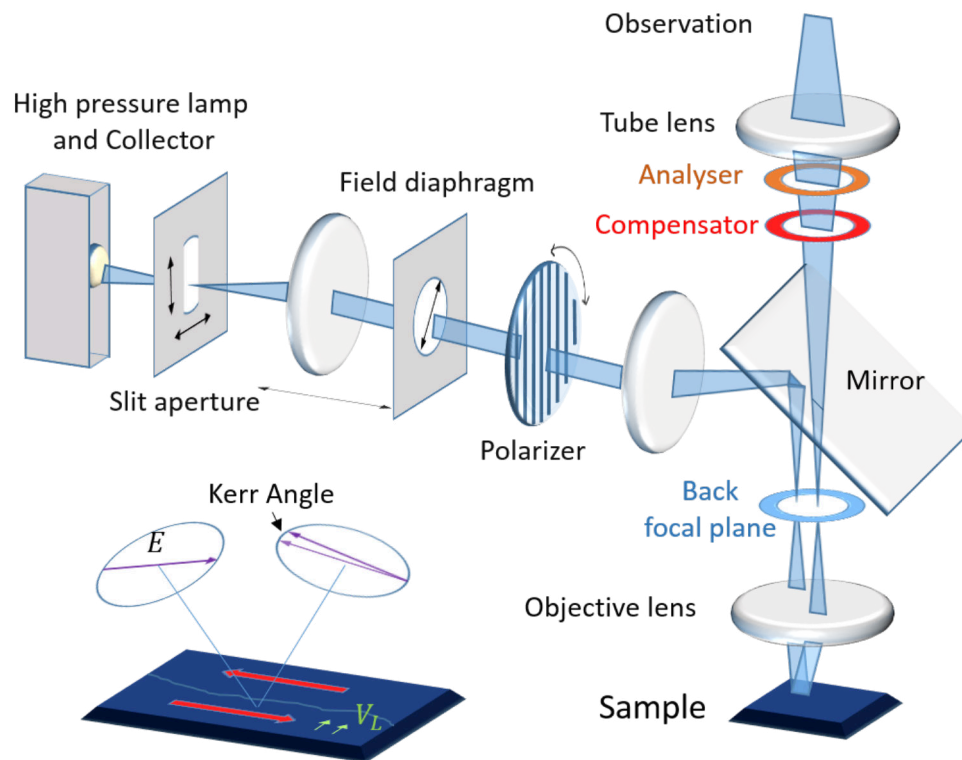


FIGURE 3.7: Schematic of the light path in a Kerr microscope. A cartoon indicates the effect of the magnetization on the electrical component of the light.

MOKE configurations The Kerr effect is characterized by the Kerr angle which is defined between the initial linear polarization and the one after reflection. The light is linearly polarized by traversing a quarter waveplate. We reference to used MOKE modes:

The polar MOKE where the magnetization is perpendicular to the plane of the sample and the wavevector of the sent ray of light is normal to the surface. This configuration is yielding the most substantial effect because the polarization is continuously orthogonal to the magnetization since the wavefront is normal to the magnetization.

In the longitudinal configuration, the magnetization is in the plane of the sample. MOKE is observable if the light is incoming at an angle with the normal of the surface of the sample. The light can be of both p-type or s-type. The p-type is represented on the cartoon (Fig. 3.7).

The imaging configuration can be selected by using slits in the back-focal plane resulting in the views in Fig. 3.8. With the use of LEDs, the selection is

more convenient as switching off some of the LEDs allows the selection of the configuration.

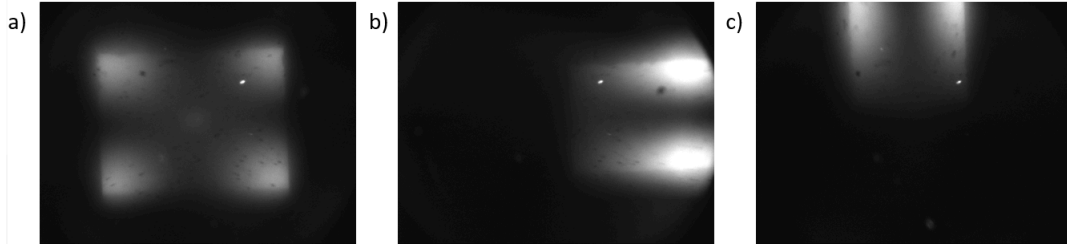


FIGURE 3.8: (a) Picture of the back-focal plane in the polar MOKE configuration. (b) Longitudinal Kerr effect configuration. (c) Longitudinal Kerr effect configuration with the magnetization rotated by $\pi/2$ as compared with the case (b).

Interaction with the sample: The beam propagates and hits the sample at a particular angle and is partially reflected, transmitted and/or absorbed. The optical properties of the metallic solid are regrouped in a dielectric tensor. In optics, the electromagnetic wave is characterized by an electrical and magnetic component being orthogonal and proportional to each other. The polarization is by convention represented by the electric field of the light. From a semi-classical approach, when a linearly polarized light beam interacts with the sample it induces a difference of potential created by the electrical component. The media is polarized, and the electrons start oscillating in the plane of the electric field. The relaxation of such electrons is going to produce photons with the same type and direction of polarization. The characterization of the process is obtained by projecting the state of the light beam on the dielectric tensor and comparing with the initial state. The dielectric tensor yields:

$$\epsilon = \epsilon \begin{bmatrix} \epsilon_1 & 0 & 0 \\ 0 & \epsilon_2 & 0 \\ 0 & 0 & \epsilon_3 \end{bmatrix} \quad (3.2)$$

For the case of a non-magnetic and optically isotropic material, the dielectric tensor is diagonal and with real coefficients. For a total reflection, the coefficients are equal to 1, and no MOKE effect is observable. A phase shift of π is induced by reflection due to the difference in refractive indexes of the two media. For a magnetic sample, the electrons that are oscillating with the linearly polarized light also experience a force created by the magnetization of the sample. The Lorentz force $\mathbf{v} \times \mathbf{M}$ (with v the motion induced by the electric field) leads to a deviation of the linear trajectory of the electron for non-collinear configurations of the trajectory and the magnetization vector. In this case, a new current orthogonal to the original one is induced thus yielding photons with a different polarization. The photons created by electrons affected by the Lorentz force are added to the non-modified ones generating the magneto-optical Kerr effect. This effect is

incorporated in the dielectric tensor as off-diagonal imaginary coefficients. The magnitude of the effect is usually 100 times smaller than the regular reflection (23). From (20), the dielectric tensor yields:

$$\epsilon = \epsilon \begin{bmatrix} 1 & -iQ_v m_3 & -iQ_v m_2 \\ iQ_v m_3 & 1 & -iQ_v m_1 \\ -iQ_v m_2 & -iQ_v m_1 & 1 \end{bmatrix} + \begin{bmatrix} B_1 m_1^2 & B_2 m_1 m_2 & B_2 m_1 m_3 \\ B_2 m_1 m_2 & B_1 m_2^2 & B_2 m_2 m_3 \\ B_2 m_1 m_3 & B_2 m_2 m_3 & B_1 m_3^2 \end{bmatrix} \quad (3.3)$$

with Q_v the Voigt material constant describing the magneto-optical rotation of the plane of the polarization of the light. The constants B_1 and B_2 describe the Voigt effect. The first effect with Q_v is linear with the saturation magnetization while the second exhibits a quadratic dependence. For an absorbing media, the diagonal components are also imaginary. Only a non-absorbing media gives a real diagonal and imaginary off-diagonal. The reflected wave is described by the scheme in Fig. 3.7.

Contrast The formulation of the contrast or Kerr rotation that is received by the camera at the end of the path is now possible. The polarizer setting is defined as the angle ψ as observed in Fig. 3.9. The reflected light off the sample re-emits the amplitudes A_s and A_p in a perpendicular and parallel direction, respective to the plane of incidence. The reflected Kerr component is then passing through the analyzer set at an angle α , being taken off the normal to the plane of incidence of the light beam.

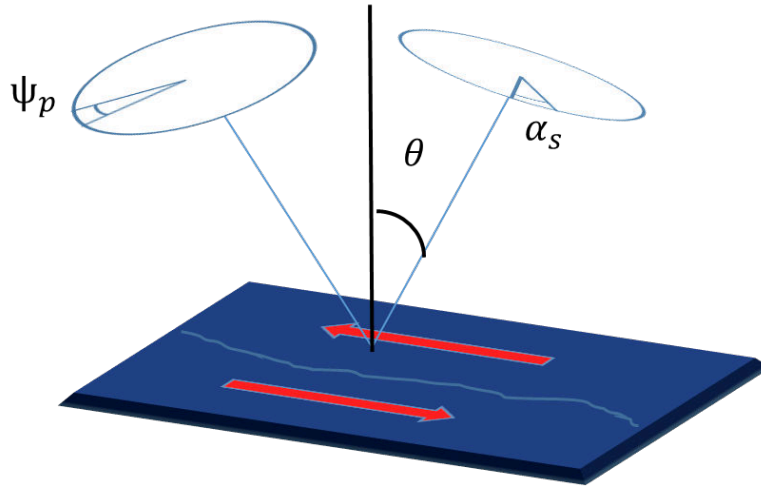


FIGURE 3.9: Schematic of a reflection of a polarized wave on a magnetic sample. The circles give the wavefront containing the electrical component with the angle ψ_p identifies the angle of the polarizer. The subscript identifies a p-type incoming wave. The second circle represents the reflected wave with the angle α_s for the analyzer setting, the subscript s being for an s-type. θ is the angle of the beam with surface's normal.

The amplitude obtained for the Kerr effect derived in (20) is:

$$\begin{aligned}
A_{tot} = & -A_p \cos(\psi_p) \sin(\alpha_s) + A_s \sin(\psi_p) \cos(\alpha_s) \\
& + A_{pol} \cos(\alpha_s - \psi_p) m_{pol} + A_{lon} \cos(\alpha_s + \psi_p) m_{lon} - A_{tra} \cos(\psi_p) \sin(\alpha_s) m_{tra}
\end{aligned} \tag{3.4}$$

where A_{pol} , A_{lon} and A_{tra} are the polar, longitudinal and transverse Kerr amplitude, respectively. The desired magnetization component is indicated by a subscript associated to m . From the analysis of the formula, both a small polarization angle and analyzer angle provide a substantial effect. In all cases, the total amplitude can be rewritten as the sum $A_{tot} = A_R \pm A_K$ where A_R is the regular part, not affected in the reflection process and A_K the Kerr amplitude. The Kerr rotation is defined as the ratio of the amplitudes:

$$\psi_K = \frac{A_K}{A_R} \tag{3.5}$$

We assume $\alpha_s = \psi_K$ and $\psi_K \ll 1$. If the phase of A_K and A_R are also equal, they are real amplitudes, and the 'lower intensity' domain has for intensity:

$$I_D = A_R^2 \sin^2(\alpha_s - \psi_K) + I_0 \approx (A_R \sin(\alpha_s) - A_K \cos(\alpha_s))^2 + I_0 \tag{3.6}$$

with I_0 the background intensity. For the 'higher intensity' domain:

$$I_B = A_R^2 \sin^2(\alpha_s + \psi_K) + I_0 \approx (A_R \sin(\alpha_s) + A_K \cos(\alpha_s))^2 + I_0 \tag{3.7}$$

The magneto-optical signal obtained is the difference between the two intensities:

$$I_{MOKE} = I_B - I_D = 2 \sin(2\alpha_s) A_K A_R \tag{3.8}$$

The MOKE intensity is then linear with the Kerr amplitude and the amplitude of the non-affected reflected light. We notice that theoretically if the analyzer angle α_s enlarges, the signal should increase. However, in practice, the total signal is mainly determined by the Kerr amplitude and the background intensity. The latter being affected by the imperfections in the optical system (polariser), the surface and the actual illumination. For all imaging equipment, it is essential to consider the signal-to-noise ratio. The sources of noise in optical microscopes are:

- The thermal drift of the sample, particularly relevant for small structures below the diffraction limit where the intensity is already weak.
- The electronic noise that depends on the electronics used for the detection. Both are to be improved for better resolution. Finally, a phase difference between the regular amplitude A_R and the Kerr amplitude A_K can be introduced upon reflection. The compensator element provides a way to correct the possible induced ellipticity.

MOKE setup

In this paragraph, we describe the different steps necessary for the imaging of the samples using a Kerr microscope ³. The microscope was provided by the company Evico magnetics (95) along with a software controlling the components.

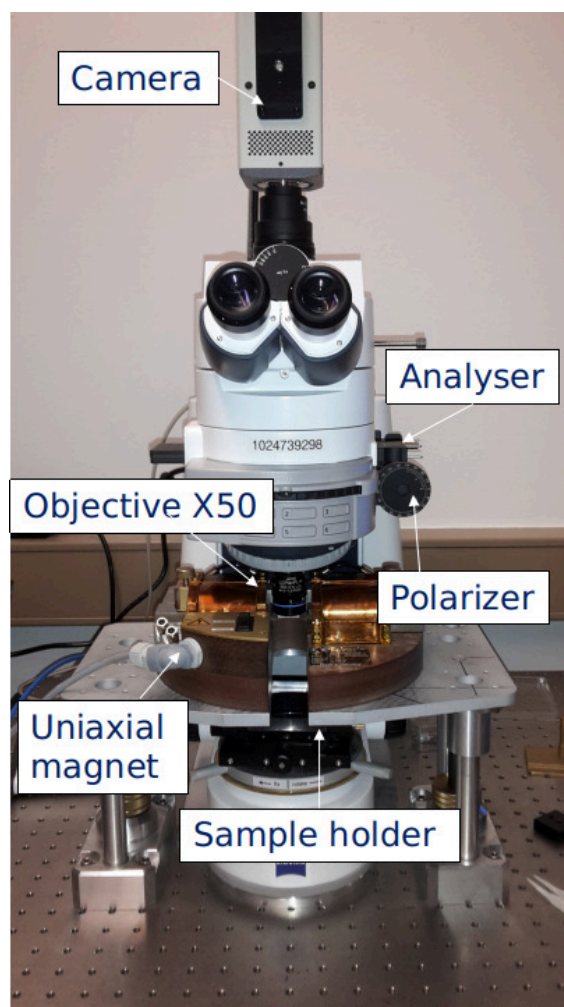


FIGURE 3.10: Described picture of the MOKE microscope.

Before imaging with the microscope, the samples are placed on a sample holder. Initially, the samples were fixed with epoxy glue which resulted in a strong drift of the sample until the solvent in the glue was evaporated. The process could be as long as 2 hours, so we decided to only position the sample on the holder. A 50-times magnification lens is mounted on the support and placed in the central position. Two in-plane magnets can be utilized to apply a magnetic field. The first is made of two in-plane Helmholtz coils (called Uniaxial magnet in Fig. 3.10), the second is an in-plane vector magnet (not shown) ⁴. The uniaxial magnet allows

³We warmly thank R. Lo Conte for teaching us the usage of the MOKE setup.

⁴We thank D. Heinze for helping with the realization of the vector magnet

the application of 300 mT, while the vector magnet can provide up to a 100 mT in any direction of the plane. The vector magnet also enables rotating fields. The sample is brought under the microscope's objective and placed at equidistance from the magnet's poles. The light beam is focused on the surface of the sample. The back-focal plane is then imaged, and the slit aperture is set to perform longitudinal MOKE measurements as pictured Fig. 3.8. From formula 3.4, in the longitudinal mode configuration, the polarizer angle as well as the analyzer angle need to be as small as possible to obtain a high contrast. Preferentially, they also should have opposite sign. A recently published article (96) describes the optimization of the MOKE contrast by setting the correct angle of the polarizer and the analyzer. After those steps, the parameters in the software need to be modified to the maximum contrast available. The imaging is then performed by the camera. The images are acquired in two steps; a background image is saved then this picture is subtracted to the currently obtained image. The resulting image is then grey, and any change in the gray scale indicates a different intensity than the saved image. This subtraction significantly improves the observed contrast. Furthermore, the background intensity is usually so prominent that the Kerr effect cannot be observed. The following formula

$$(A_B + A_K) - (A_B - A_K) = 2A_K \quad (3.9)$$

where A_B and A_K respectively represent the background reflected intensity, and the Kerr reflected intensity. With a careful configuration of the microscope, structures smaller than 200 nm lateral dimension can be imaged, which is already below the diffraction limit. The latter remains challenging due to the reduced reflected light intensity and the thermal drift occurring at room temperature.

3.4.4 Giant magneto-resistance effect

The discovery of the Giant magneto-resistance effect or GMR was a key enabler of Spintronics. It is a transport effect that is observable in alternating ferromagnetic and non-ferromagnetic layers. It manifests in the form of a change of the resistance of the stack depending on the relative magnetic orientation of the different layers. In the initial discovery by A. Fert (2) and P. Grünberg (3), the ferromagnetic layers were coupled anti-ferromagnetically because of the RKKY exchange mechanism (97). With the application of an external magnetic field, the anti-parallel layers to the field were switched, and a giant drop in resistance was measured. Hence, the name Giant Magneto-Resistance.

Generale description of the GMR

The GMR effect is used in different configurations. The first of which is the Current Perpendicular to the Plane (CPP) geometry (98) performed in multilayers with a current driven from top to bottom electrode or vice versa. The second configuration is the Current In Plane (CIP) where the current flows parallel to

the layers. The GMR effect is of the same magnitude whether the CIP or CPP configuration is chosen (99). For the study of magneto-resistance, two fundamental parameters are needed: the spin density and the momentum scattering time of conduction electrons at the Fermi level. In a multilayered system, the current passing through different layers is defined by a transmission and a reflection coefficient at the interfaces and in the bulk. Those features are related to the band structure at the Fermi level, the quality, and nature of the interfaces. For magnetic systems, the coefficients also entail a spin dependence; consequently, spin-up electrons exhibit a different transmission coefficient than spin-down. The figure 3.11 represents a basic schematic of the GMR effect.

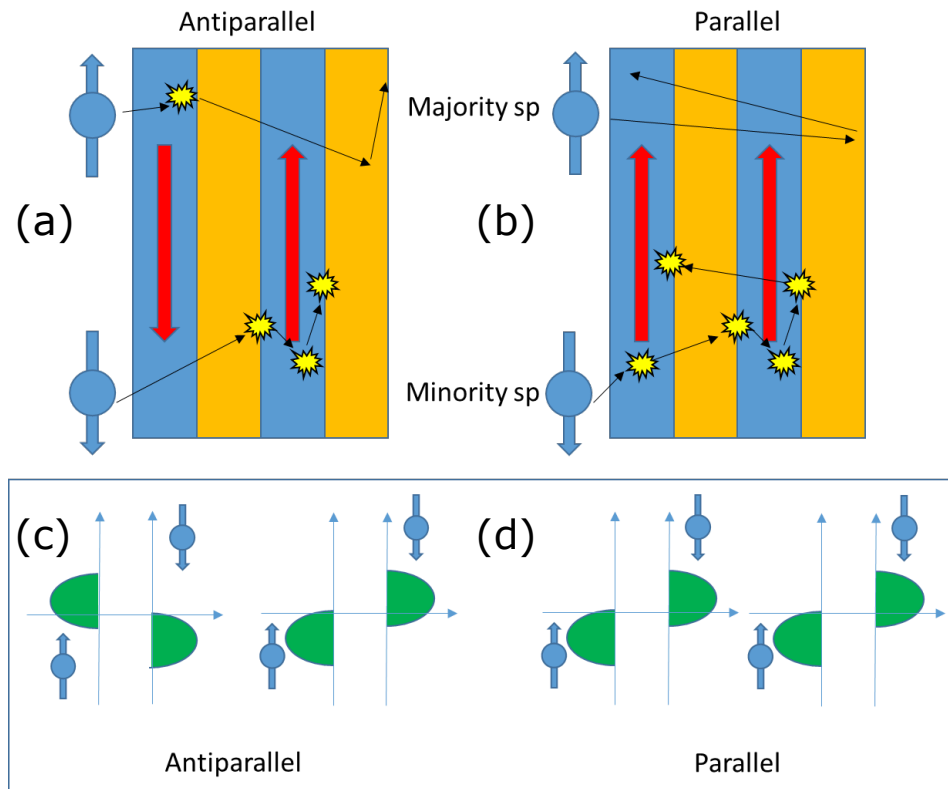


FIGURE 3.11: (a) Schematic of the electron scattering in the bulk of the layer in an anti-parallel configuration of the magnetization state. (b) Schematic of the electron scattering in the bulk of the layer in a parallel configuration of the magnetization state. (c) Representation of the spin d-bands in the anti-parallel configuration. (d) Representation of the spin d-bands in the parallel configuration. Note that the scattering arises due to the large density of state in the d-minority band, allowing the electron spins from the sp-band to change orientation. Consequently, most of the electrical conduction is carried by the spin majority electrons experiencing less scattering events.

We consider that our system is composed of four layers as depicted in Fig. 3.11. The blue layers being ferromagnetic and the yellow ones are non-magnetic metallic layers. The layers share the same thickness t . We also depict the two

different spin orientations for the d-band near the Fermi level (Fig. 3.11 (c and d)).

Non-magnetic layers Concerning the band diagrams of noble non-magnetic metals, the sp-bands are located at the Fermi level while the d-bands are filled with electrons and are way lower in energy. We choose Cu as a non-magnetic metal. In those metals, the spin diffusion length (distance traveled by a spin before flipping) is long (500 nm in Cu (100)). Thus the electrical conduction of the two spin channels is the same. The spin-up and spin-down conduction channels do not interfere.

Ferromagnetic layers In the case of the ferromagnetic 3d-metals, the Stoner model described previously bounds us to a splitting of the spin d-band at the Fermi level. The d-bands being split, one of them contains more electrons than the other, so the density of states at the Fermi level is different for up electrons and down electrons. For ferromagnetic materials, the sp-electrons are also split at the Fermi level, but due to the parabolic shape of the band, the difference in DOS is not as significant as in the d-band. Depending on the material, the density of states of 3d-minority electrons can be much higher than the density of states of the majority electrons at the Fermi level. The result is an increase in the number of scattering events for the sp-electrons with the minority spin direction in the d-band. The mean free path is then remarkably reduced for the minority electrons which increases the resistance. We first develop a simple model based on the Mott's two current model (101) and closely related to the derivation of the Boltzmann transport in (99).

Mott's two current model

To give a semi-quantitative description of the effect, we derive the 4-resistors model (Fig. 3.12). In the CIP configuration, the resistor model delivers a fast, physical understanding of the GMR effect. The 4-resistors consist in a double alternation of ferromagnetic and non-ferromagnetic. The spin quantization axis is taken as the magnetization direction. The majority spin resistivity times the contact area is defined as $\rho_{\uparrow\uparrow}$ and the minority is $\rho_{\downarrow\downarrow}$. In this model, we assume that the mean free path of the electrons is long compared to the thickness of the layers meaning that there are no spin flips considered. The bulk and interface resistances are discussed separately. For a single spin channel, all the resistances are connected in series, and the sum of it gives the total resistance of the stack for this spin channel. The resistance of the bilayer system, ferromagnetic plus non-ferromagnetic layer is then defined as:

$$R_{\uparrow\uparrow(\downarrow\downarrow)} = \rho_{NM}t_{NM} + \rho_{\uparrow\uparrow(\downarrow\downarrow)}t_{FM} \quad (3.10)$$

with ρ_{NM} and t_{NM} being the resistivity times the contact area and the thickness of the non-ferromagnetic metal, respectively. The term t_{FM} straightforwardly

represents the thickness of the ferromagnetic metal. We assumed perfectly transparent interfaces, so the interfacial resistance is dropped from the equations. The electric scheme can be seen in Fig. 3.6.

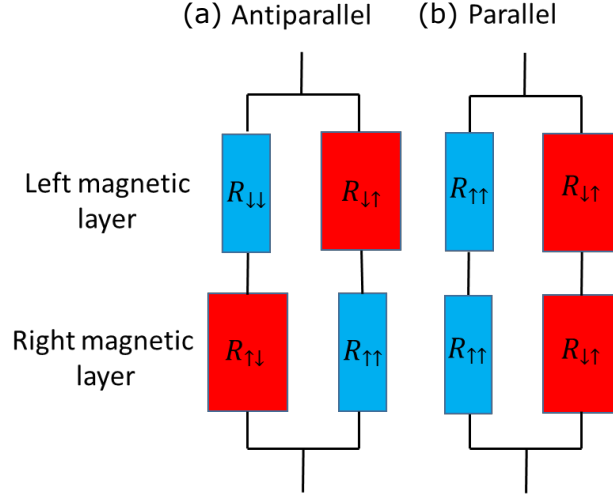


FIGURE 3.12: (a) 4-resistors model for the anti-parallel case. (b) 4-resistor model for the parallel case.

Using the previous formula for the resistance, we can formulate an expression for the total resistance of the stack. In the parallel magnetization case:

$$R_P = 2N \frac{R_{\uparrow\uparrow} R_{\downarrow\uparrow}}{R_{\uparrow\uparrow} + R_{\downarrow\uparrow}} \quad (3.11)$$

with N the number of iterations of the bilayer system. For the anti-parallel case:

$$R_{AP} = N \frac{R_{\uparrow\uparrow} + R_{\downarrow\uparrow}}{2} \quad (3.12)$$

The GMR ratio can be determined by the subtraction of the resistance in the two cases.

$$\frac{\Delta R}{R} = \frac{R_{AP} - R_P}{R_P} = \frac{(R_{\downarrow\uparrow} - R_{\uparrow\uparrow})^2}{4R_{\downarrow\uparrow}R_{\uparrow\uparrow}} \quad (3.13)$$

The GMR ratio is normalized to the parallel resistance. It is a convention in the literature, and we adopt it. We assume that the resistance of the noble metal to be minute as opposed to the resistance of the ferromagnetic layers. It is then possible to express the effect just regarding the resistance of the spin majority and minority in the ferromagnets. We define the parameter $\alpha = R_{\downarrow\uparrow}/R_{\uparrow\uparrow}$ as the ratio of the minority resistance and the majority resistance. A reformulation is then straightforward.

$$\frac{\Delta R}{R} = \frac{(\alpha - 1)^2}{4\alpha} \quad (3.14)$$

Naturally, in the case where there is no difference between spin-up and down resistances, $\alpha = 0$, there is no GMR effect. In that picture, the GMR effect is represented in a simple model, and the central consequences are easily visible. Recently, Mott's two current model was assessed by the measurement of the spin density and momentum scattering time of conduction electrons at the Fermi level. The measurement was performed via terahertz spectroscopy in the 100 fs regime (102). The latter was allowed by the possibility of measuring the electric conductivity of a spin-valve under applied field without spin accumulation effects.

Valet-Fert model

We now present a more accurate model based on the Valet-Fert Drift-Diffusion model (103), (104) to discuss the limitations of the 4 resistor model. In the Valet-Fert model, in the CPP configuration, more than the volume spin-dependent scattering, an interface spin-dependent scatterings due to the spin accumulation at the interface is also taken into account. In the CIP configuration, no interface spin-dependent scattering is necessary since there is no net spin current across the interfaces. In the 4-resistors model, one of the significant assumptions is that $l_{sf} \gg \lambda$, the spin diffusion length is much larger than the mean free path of the electron, we develop in the appendix A the VF-model with the same assumption, here we just expose the main conclusions of the calculations. The spin scattering at the interfaces is of importance in this model. This macroscopic model successfully treats a multilayer case with spin accumulation at the interfaces. This model is unfortunately not incorporating any spin relaxation in bulk in the case where the mean free path is of the order of the spin diffusion length or even when it is larger. The latter case manifests quite often because of the introduction of defects or because the thickness of the layer is large. The two models also fail to describe GMR values obtained for room temperature measurement because the spin relaxation through magnon scattering is not taken into account due to the assumption of a system at 0 K.

GMR setup: The transport measurement setup for the GMR effect is located at the company Sensitec. The sensor is constituted of a spin-valve stack which allows the measurement of the magnetization direction in the stripe. The general composition of the stack is made of a SAF described in 3.1.1 and a free layer of 30 nm of $\text{Ni}_{81}\text{Fe}_{19}$ between which a Cu nonmagnetic spin conduit is used. The direction of the pinning layer is defined during the stack deposition, and the arrow in the center of the sensor 3.13 indicates the direction. The GMR measurement requires the contacting of the gold pad with needles for the acquisition and the application of the voltages.

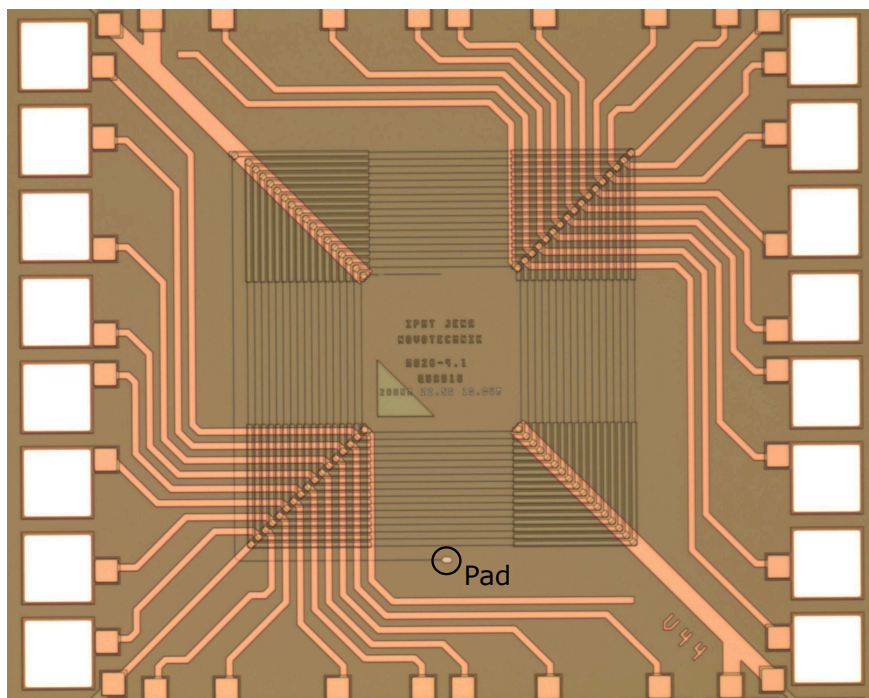


FIGURE 3.13: Optical microscope image of the MULTITURN sensor designed by Novotechnik and manufactured by Sensitec GmbH. The orange connections are representing the electrical contacts while the white pads at the end are required to connect the sensor to the outer electronic. The dark loops are representing the 16 magnetic loops of the sensor. Finally, the triangle, in the center, indicates the direction of the pinning layer of the spin-valve below the free layer of the sensor.

The contacting is the following: The ground is connected to the bottom right corners while the positive potential is applied to the top left corners. The measurement is performed on the two other corners.

3.4.5 Atomic Force Microscopy

The Atomic Force Microscopy or AFM was invented in 1985 by G. Binnig, C. Quate and C. Gerber at IBM Zurich (105). This idea opened the field of visualization of nanometric structures in 3 dimensions. It is a scanning technique, so the sample is analyzed point after point. The tip can scan at a speed of $40 \mu\text{m/s}$ and lower. The AFM uses the forces in between the last few atoms of a tip and the surfaces of the sample to acquire the topography of the structures. There exist different types of AFM: piezoelectric force microscopy, magnetic force microscopy, magnetic resonance force microscopy. In all the configurations, the tip ends with atoms of particular elements which allows the detection of specific forces. The AFM can also enable the imaging of nanostructures of polymers or in liquid compared to other nano-imaging techniques such as the Scanning Electron Microscopy 3.4.6, which cannot. In the present study, we only used a regular AFM Bruker (106) in the tapping mode. About the physics of the techniques, the

force that the tip is experiencing is the Van der Waals force, which is an electrostatic force of the form (107):

$$E_{VanderWaals} = -\frac{1}{r^6} \left[\frac{\mu_1^2 \cdot \mu_2^2}{3(4\pi \cdot \epsilon_0 \cdot \epsilon)^2 \cdot k_B \cdot T} + \frac{\mu_1^2 \cdot \alpha_2 + \mu_2^2 \cdot \alpha_1}{(4\pi \cdot \epsilon_0 \cdot \epsilon)^2} + \frac{3 h \nu \cdot \alpha_1 \cdot \alpha_2}{4 (4\pi \cdot \epsilon_0)^2} \right] \quad (3.15)$$

Where ϵ_0 is the vacuum dielectric constant, h is the Plank constant, k_B is the Boltzmann constant, T is the temperature in Kelvin, r is the distance between the molecules, μ is the dipolar momentum, ν the electronic frequency of absorption and α the electronic susceptibility. It decreases as $1/r^6$, so the forces are very located.

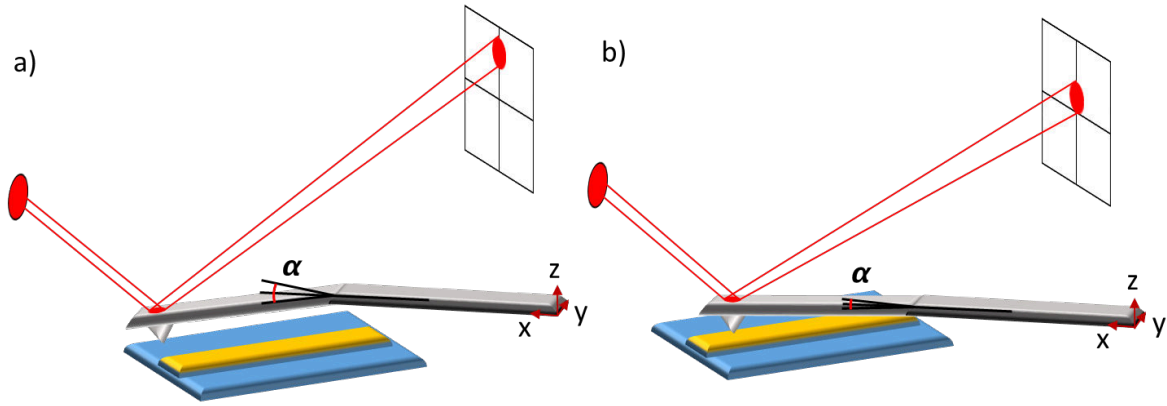


FIGURE 3.14: (a) AFM Setup displaying the deflection of the cantilever at its lowest point near the surface, the cantilever is vibrating with an amplitude described by the angle θ . The reflection of the laser on the cantilever and then on the photo-diode can be seen. (b) This configuration shows the cantilever positioned on top of the measured structure, the amplitude of the oscillation is reduced due to a change in the effective spring constant.

The tapping mode 3.14 consists in the oscillation of the cantilever at its resonance frequency (typically around 75 kHz) with a defined amplitude. When the tip starts to feel the repulsion or attraction forces due to the surface, the amplitude of the oscillations is modified. This effect is a consequence of the change of the spring constant of the cantilever. We used high-quality etched silicon tips for soft tapping mode imaging in air (FESP-V2 from (108)). A laser is shone on top of the surface of the cantilever, and its deflection is detected by the position of the reflected laser spot on the four photo-diodes generating a quadrant in Fig 3.14. The tip is then scanning the sample line by line thus producing an image. Micrograph images were obtained for the wires of our investigated sensors to assess the cross-sectional shape. With this technique, we obtained the following plot and image:

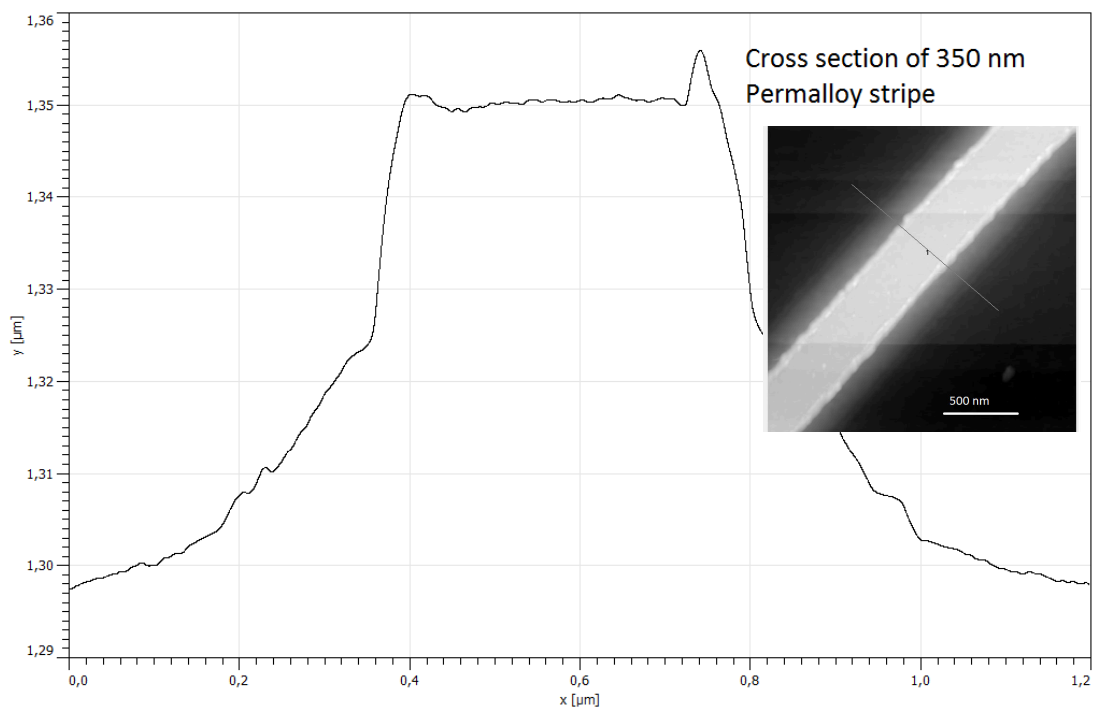


FIGURE 3.15: Plot of the height values as a function of the position. The plot is extracted from a section across the wire as shown in the inset.

3.4.6 Scanning Electron Microscopy

The Scanning Electron microscopy technique is capable of producing a high-resolution micrograph of the surface of a conductive sample down to a few nanometers in resolution. In microscopy techniques, the resolution is limited by the wavelength of the probing wave. The best optical microscopes on the market can reach up to 100 to 200 nm of resolution.

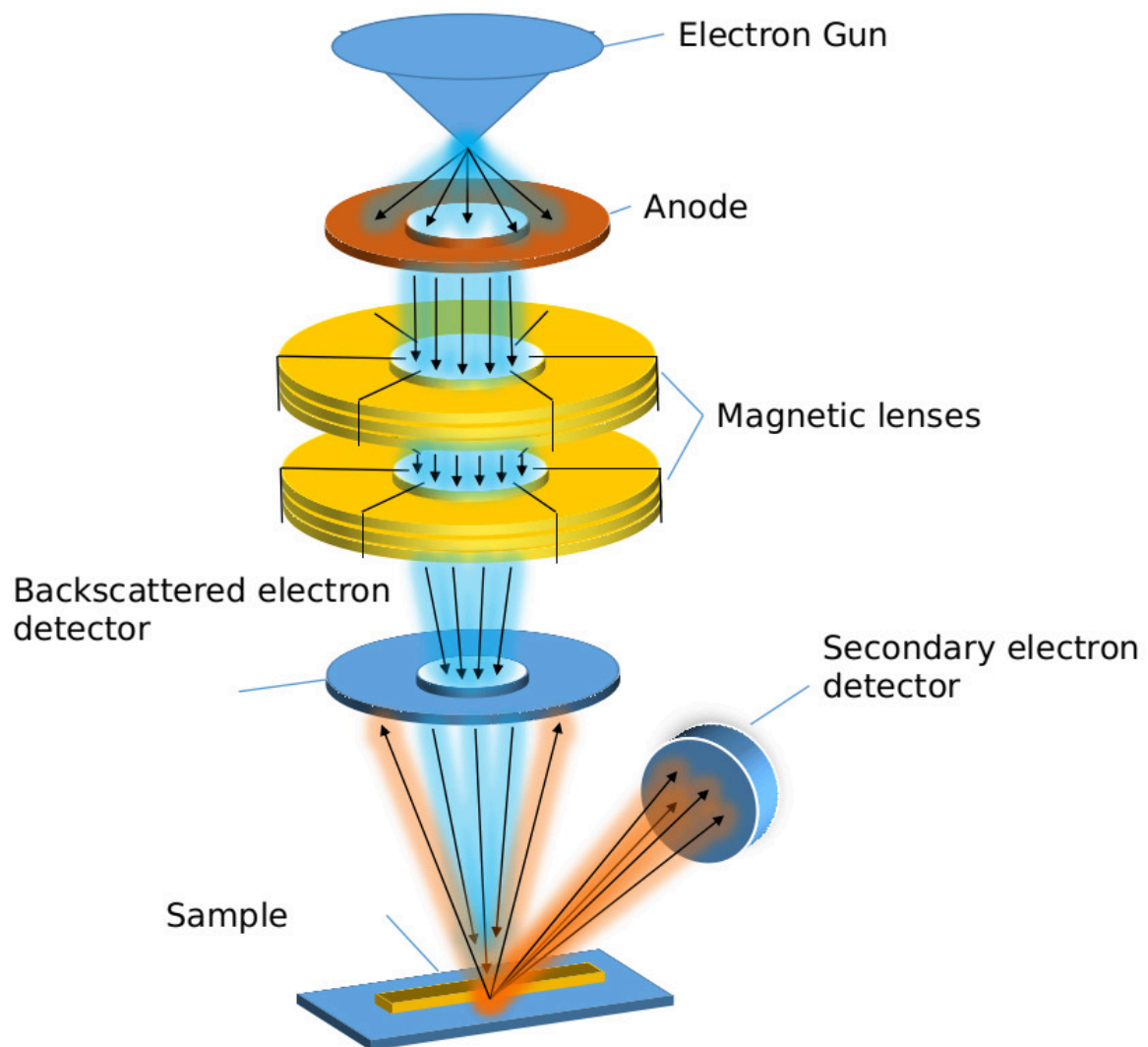


FIGURE 3.16: Schematic of the scanning microscope. The blue rays are picturing the electron beam incoming to the sample, the orange ones represent the electrons leaving the sample and colliding with the detectors.

The principle of the SEM (109) is the following: An electron gun is used to generate electrons in the microscope. A tungsten wire is heated up to the point of thermionic emission of electrons where the electrons obtain an energy superior to the work function. They are emitted from the wire and enter the column where they are accelerated and focused. At the end of the column, the electrons are shot into the sample and interact with the materials present. The primary electrons are then traveling until they generate secondary electrons, backscattered electrons, Auger electrons, and in some cases for high acceleration energies, X-rays. Each of the species carrying some specific information on the investigated sample. The detection of the expelled species can be performed with several sensors present in the chamber. A typical detector type is a scintillator-photomultiplier, where electrons are converted to photons further multiplied and converted back to an electrical signal. The magnitude of the voltage acquired depends on the distance

of the sample with the detector and the topography under the beam spot. Different species of emitted electrons (backscattered, secondary) can be differently detected by placing the sensors at particular locations. An evident requirement for the detection of the signal is the re-emission of the incoming electrons. Thus the sample needs preferably be conductive. Some of our samples possess a protective layer made of AlO_x , which requires a high acceleration voltage to traverse the oxide layer. In this case, the underneath metallic can still be imaged if the oxide layer is thin. In Fig. 3.17 are a couple of representative images taken with a Helios NanoLab 600i with 15 kV of acceleration voltage.

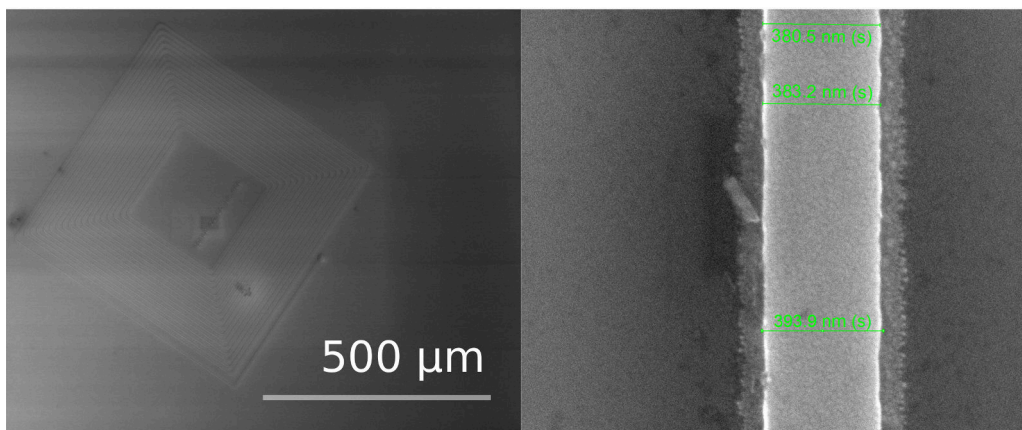


FIGURE 3.17: SEM micrographs of an open loop multiturn sensor structure on the left and a wire on the right.

With this technique, the detection of defects can be performed after every step of a patterning process. It can also serve for a fast characterization of the edge roughness and width of wires.

3.4.7 X-ray diffraction

X-rays are associated with a defined range of the electromagnetic spectrum. The X-ray photons possess a wavelength of the order of 1 to 100 angstroms, which is a similar dimension as the atomic inter-distances in the solid-state matter. The X-rays are then used to determine the crystal composition and orientations of solid compounds. For the X-ray diffraction method (110) to be performed the atoms should be organized in a lattice. The electrons of the atoms present in the planes of the crystals are then acting as scatterers. When an X-ray scatters off an atom, it is re-emitted in the three spatial directions due to the principle of Huygens-Fresnel (111, 112). However, due to the scattering of other X-rays at nearby locations, the waves tend to cancel out due to destructive interference. The X-rays add constructively solely in particular directions determined by Bragg's law (113). This array of outgoing X-ray yields a diffraction pattern and is then containing information on the crystal with which the primary X-ray beam interacted. Bragg's law reads as:

$$2d \sin \theta = n\lambda \quad (3.16)$$

with θ the angle of incidence as represented in Fig. 3.18, d represents the distance between diffracting planes, n is an integer and λ is the wavelength of the beam.

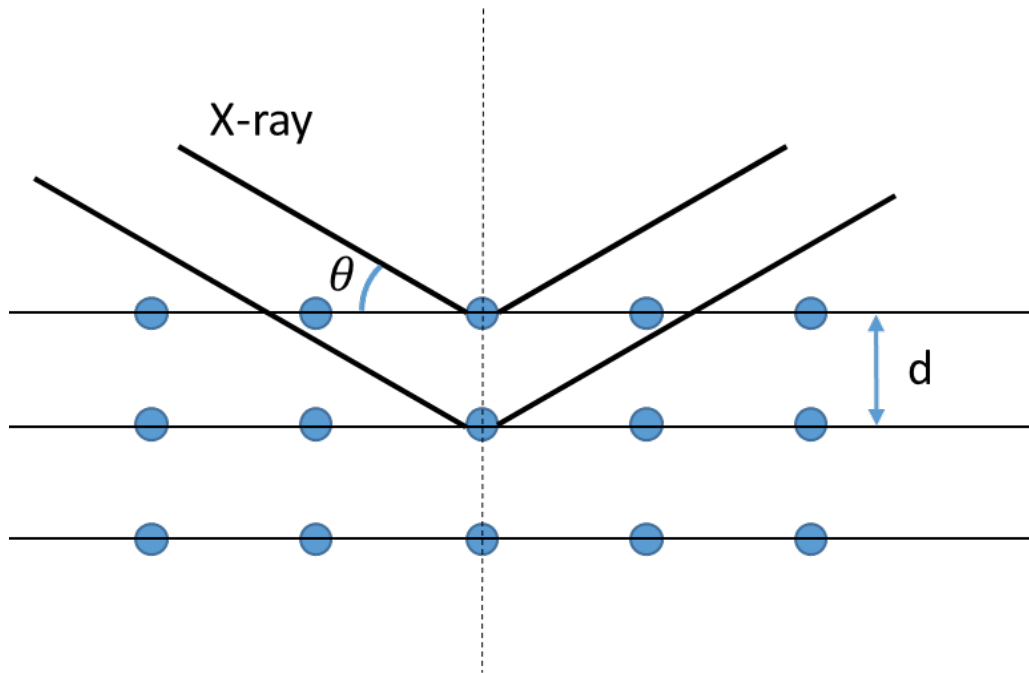


FIGURE 3.18: Schematic of an X-ray beam (black lines) interacting with the atoms of a crystal (blue circles). The angle between the plane of atoms and the angle of the X-ray beam is defined as θ . The distance between scattering planes is named d .

To extract crystalline information from a sample, it is then necessary to have an ordered lattice. Despite the latter, some information can still be obtained on the degree of crystallinity of a polycrystalline sample. However, quantitative data remain challenging to extract.

3.5 Sample fabrication

In this subsection ⁵, we describe the patterning process of the samples in chronological order. Some possible missing information is due to the confidentiality of some fabrication parameters. All the steps are performed in a clean-room environment at Sensitec GmbH (S), or the Institut of Physics at Johannes Gutenberg University (IPJGU).

⁵We first would like to thank the processing team of Sensitec who kindly provided some of the samples, and the company Singulus Technologies, which produced some of the sputtered stacks.

3.5.1 Lift-off method approach

We intend to describe a typical lift-off process in this subsection. For this purpose, the selected resist is positive. The resist is then exposed with one of the two methods presented in the patterning section 3.3. The exposed resist is then removed, and the furrows left in the sample are filled with a sputtering process. The nonexposed resist is then also removed, leaving the free-standing structures on the substrate.

3.5.2 Etching method

For this process, the thin layers of the materials are initially grown on the substrate using a deposition technique. A negative resist is then spin-coated and processed by one of the exposition techniques described in the patterning section 3.3. Further, the development of the resist removes all the nonexposed parts. Finally, the sample is etched leaving untouched the parts protected by the resist. The resist left is also removed at the end of the process.

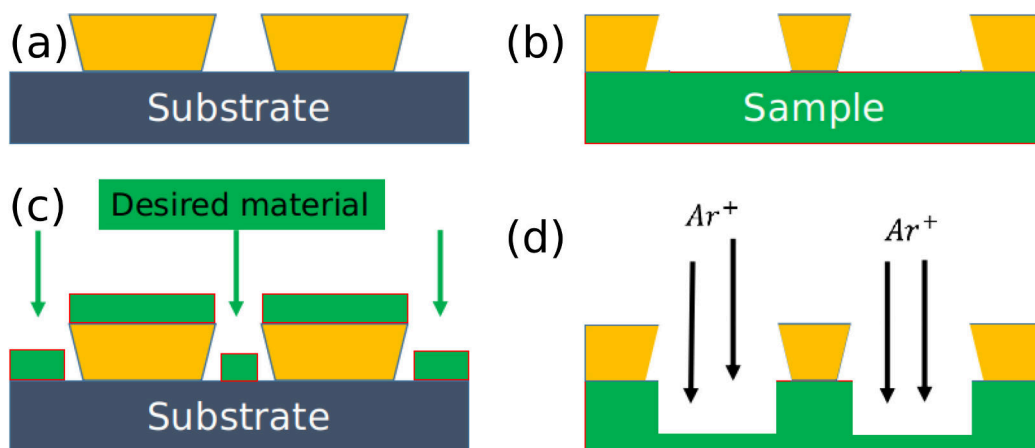


FIGURE 3.19: (a) Substrate with an exposed and developed positive resist. (b) Sample covered with an exposed and developed negative resist. (c) Deposition of the desired material in the furrows left in (a). (d) Etching of the sample not covered with resist.

1. Selection of the substrate The first step usually consists of choosing a substrate, in our case, a 5-inch wafer with a notch on the left side. The wafer is typically made of the materials described in 3.1. The notch helps to track the wafer's gross position and orientation while it is being handled by the processing machines.

2.a. Cleaning This cleaning is performed at (S). The wafers are first sponge-cleaned by hand for a rough removal of large adsorbed particles. They are then water-cleaned under a high-pressure water-jet, and exposed to an oxygen plasma

for 20 min. The plasma carbonizes all the organic compounds still present on the surface of the sample. Indeed, the sample in the plasma chamber is submitted to a flow of vacuum ultra-violet photons and oxygen ions, which are extremely effective for destroying most organic bonds (114). The ions strongly react with the carbon contaminants and form H_2O , CO and CO_2 molecules. Those light molecules under vapor are removed from the chamber during the process. At this point, the surface is considered as cleaned by industrial standards.

2.b. Soft cleaning If the cleaning is performed at University, the tools necessary for a similar cleaning than the one carried out at Sensitec are not present on site. The wafers are then directly submitted to a flow of Acetone, followed by a flow of Isopropanol, and finally deionized water. The substrates are dried under a Nitrogen gas flow.

3. Deposition of the thin layers The deposition of the active layers is performed using a magnetron sputtering tool. The deposition is either made at (S) using an applied field during growth, or with a Rotaris machine (provided by Singulus Technologies (ST)) present at the Institut of Physics of Johannes Gutenberg University (IPJGU). In the second case, no external field is applied during the growth.

4. Characterization of the thin active layers This step is exclusively performed at (S). The electrical characterization is performed using a four-point probe measurement set, and the magnetic characterization is acquired with a BH-Looper. The electrical measurement yields, in the case of a GMR stack, the GMR ratio and the sheet resistance. Naturally, for a single magnetic layer, only the sheet resistance is acquired. The magnetic measurements provide the saturation magnetization (M_S), the coercivity (H_c) and the remanence (M_0) of the stack or the single layer. Some characteristic hysteresis curves are plotted in Fig. 3.20.

The plateau indicates the M_S on the y-axis. The coercivity is related to the switching of the magnetization, which in the hysteresis curve is the field value (x-axis) necessary to nullify the saturation magnetization (4 Oe for the $Co_{90}Fe_{10}$ samples).

5.a. Photolithography After the deposition, the nano-patterning needs to be carried out. All the processes described in the section 'Photolithography' 3.3.1 are performed. Exposing 100 devices at the same time is possible using a stepper mask. The resist is then developed, and the wafer is ready for further processing. The photolithography was exclusively performed at (S).

5.b. Electron beam lithography This step is only carried out at (IPJGU). A positive or negative resist is used depending on the desired process, and the electron beam lithography is performed as described in 3.3. The resist is then developed (details, see the appendices B, E, F, and D).

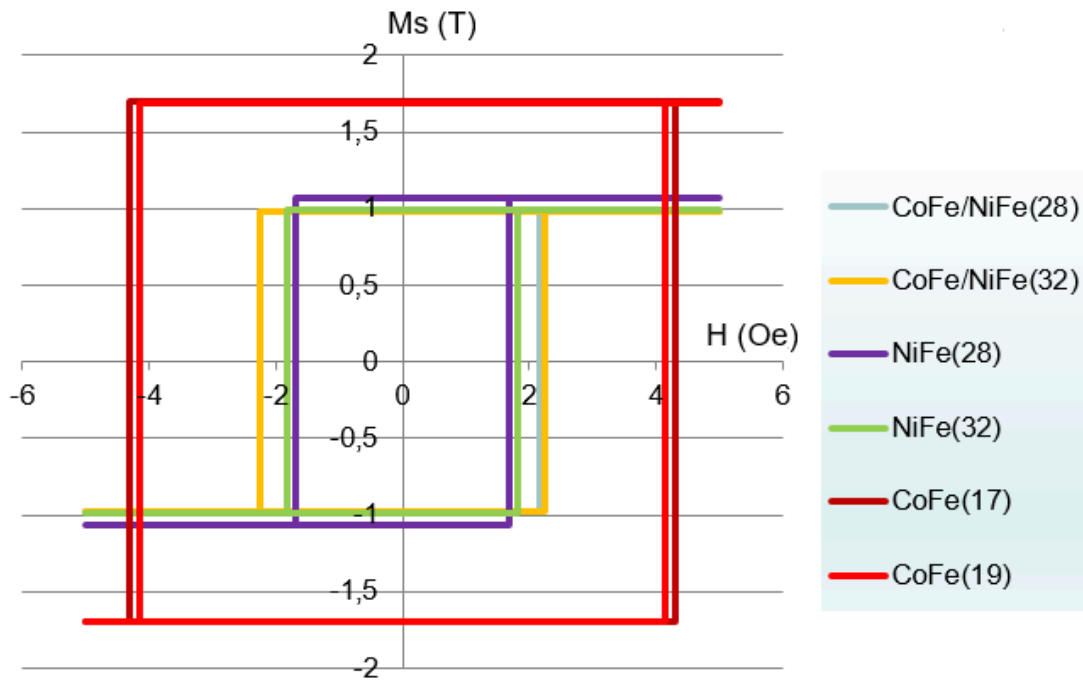


FIGURE 3.20: Hysteresis curves in the easy axis direction for various material stacks deposited in the presence of a magnetic field.

6. Ion milling For the standard ion milling performed at (S). The milling is realized under two different values of the angle of the beam with the surface normal. The latter avoids redeposition of the etched materials on the edges of the resist. This redeposition is called fencing, and it is a standard issue of the milling process. The ion milling performed at (IPJGU) was conducted under varying conditions of angles and power. All the methods are described in the appendices **B**, **D**, **E**, and **F**.

7. Cleaving After the structuring of the wafer, they are usually cleaved into smaller pieces to fit the sample holder of the different investigative tools. The cleaving is performed as follows: The samples are spin-coated with a protective resist. Then they are turned upside down and scribed with a diamond pen on the back. By bringing the wafer on the edge of a rectangular object and applying a uniform pressure on both sides of the scribed line, the wafer is cleanly cleaved. The same operation is reproduced until the desired size is achieved.

3.5.3 Standard manufacturing for the multiturn devices at Sensitec

We give the number indicating the processes performed in chronological order. The steps performed are the following:

- 1. Wafer selection

- **2.a.** Cleaning
- **3.** Material sputtering
- **4.** Electric and magnetic characterization
- **5.a.** Photolithography
- **6.** Ion milling

At that position in the process, the active layers are patterned, and the wafers where no transport measurement is performed are taken out of the process line. Typical, this applies to wafers with single magnetic layers. For wafers with a GMR stack, a contacting layer need to be added.

Contacting A second photolithography step is required to fabricate aligned contacts with a lift-off process. The typical material used for connections is Au.

Protection For all types of wafers, a protective layer can be deposited to avoid damages or oxidation. Usually, 60 nm of AlO_x or SiN are sputtered to cover the wafers.

Separation of the sensor elements For the separation of the sensor elements, the sample is brought under a high-pressure water-jet and is diced into squares of $2 \times 2 \text{ cm}^2$.

- **7.** Cleaving: This process is performed only if the wafer were not diced.

The packaging of the sensor element is required if the element is sold. However, since this step does not concern us, we decide not to describe it.

3.5.4 Processing at Johannes Gutenberg University

Etching

We give the number indicating the processes performed in chronological order. The steps performed are the following:

- **1.** Wafer selection: In this case, the bare wafers are provided by the company (S) to keep a similar substrate for the deposited materials. Furthermore, some of the university-processed samples are directly given by (S) with a single sputtered magnetic layer. In the manuscript, the deposition location is explicitly mentioned for the various samples.

- **2.b.** Soft-cleaning

- **3.** Material sputtering: The previous and current steps are only performed if the layers were not previously deposited by (S). Just single magnetic layers are deposited since all the samples processed at the University are then investigated by optical means (MOKE).

- 4. Magnetic characterization, only: The wafers are brought back to (S) for this step.
- 5.a. Photolithography or 5.b. Electron beam lithography: both processes were conducted on different wafers.
- 6. Ion milling with the tool at S and also with the machine at (IPJGU).
- 7. Cleaving

Lift-off

We give the number indicating the processes performed in chronological order. The steps performed are the following:

- 1. Wafer selection: In this case, the bare wafers are provided by the company Sensitec to keep a similar for the deposited materials.
- 7. Cleaving
- 2.b. Soft-cleaning
- 5.b. Electron beam lithography
- 3. Material sputtering

The different variations to the processes described are detailed in the appendix.

3.6 Micromagnetic simulations

Micromagnetic simulations serve as a tool for numerical calculations of complex problems in magnetism (115). As we outlined in the theory notion section, most of the micromagnetic energy terms are virtually impossible to derive analytically for nonconventional shapes or nonuniform samples. Up to now, all the micromagnetic software are tasked with solving the Landau-Lifshitz-Gilbert equation with effective fields arising from the conventional micromagnetic energy terms. We first describe here a nonexhaustive list of the various software available and their characteristics. The primary difference in between packages lies in the type of solver used either being finite difference method or finite element based. For solving micromagnetic simulations, partial differential equations need to be computed the latter can only be performed after discretization of the studied medium. The two discretization methods are evidently the finite difference and finite element.

Finite difference The finite difference method partitions the sample in cuboids to differentiate between facing boundaries. The cell is not required to be cubic and could be rectangular. Shapes that are well represented by cuboids are then well simulated with this method. For example, wires as opposed to spheres, which are poorly represented. Finite difference simulations also need less computer memory (RAM) than finite element methods. A finite difference software is OOMMF

(116) standing for Object Oriented Micromagnetic Framework. OOMMF was developed in 1988 by M. Donahue and D. Porter, and was and is still very popular in the community for its precision and its 'user-friendly' environment. OOMMF runs on CPUs. An alternative is Mumax3 (117), which is the software we mainly used. We describe this software in details further in the manuscript. An excellent micromagnetic package using the finite difference method is Micromagnum. This solver is precise and versatile; it can be computed on CPUs as well as GPUs. Unfortunately, this package suffers a lack of visibility and user-friendliness as compared to Mumax3.

Finite element The finite element method uses tetrahedra as a shape for the mesh elements. The form of the tetrahedra is allowed to vary across the computed region. Complicated geometries are better approximated with this method. Such geometries are spheres, torus, and curved regions in general. A finite element package is MagPar (magpar.net). The cell size in both cases needs to be kept below the exchange length to avoid wrong representations of the micromagnetic dynamics. A nonproper selection of the cell size can lead to significant spin angle in between cells yielding entirely unphysical results. The latter is the primary source of errors in micromagnetic simulations. A way to test against it requires to perform the same simulation with different cell sizes smaller than the exchange length and compare the results. If the results do not significantly change with the reduction of the cell, the simulation is relatively robust.

3.6.1 Mumax3

The coding language used for Mumax3 (118) is Go language. It was developed at the DyNaMat group of Prof. Van Waeyenberge at Ghent University, in Belgium. The code is written and maintained by Arne Vansteenkiste. The simulations are finite-difference based, and the computation is performed by Graphic Process Units which offers an incredible speed advantage compared with CPUs. It is also a script and Graphical -User-Interface based package being relatively user-friendly hence its latest growth of users in the past 5 years. The disadvantage is the precision of the stored results during the computation. Indeed, most of CPUs store data as float numbers and in a double precision type. So simulations such as OOMMF are not fast but reliable since a double can store up to 12 digits of precision. In the case of Mumax3, the precision is a simple float so only 6 digits. The difference in precision can cause troubles while simulating very small effective fields. Despite the latter, Mumax3 is believed to be 'sufficiently accurate for most practical applications (119).

3.6.2 Simulated system

A typical simulation script is provided in appendix G. The simulated framework in our case can be extended from hundreds of nanometers to systems of 25 μm

$\times 25 \mu\text{m}$ while still maintaining a cell size smaller than the exchange length of the desired material. These dimensions are limited by the internal memory of the GPU card used. Usual cell sizes are $4 \text{ nm} \times 4 \text{ nm} \times 4 \text{ nm}$, which lower than the exchange length of $\text{Ni}_{81}\text{Fe}_{19}$ being close to 5 nm . For the mesh, the discretization is made in powers of 2 or with 7-smooth numbers. The essence of such a choice comes from the calculation of the Fast Fourier Transform necessary to compute the demagnetization field and the generation of random numbers. It is essential to know that the demagnetization field is the most consuming regarding computational power, due to the double spatial integration required for non-local terms. During the initialization of the system, a vector representing the magnetization direction and magnitude is attributed to all cells. A drawing of the required shape which acts as a mask is applied to the whole frame. The later as for effect to nullify all the cells not comprised of the shape. The magnetization is initialized, for example, by placing a domain wall on the left side of a wire. To recreate a realistic system, boundary conditions are critical and can be deliberately selected. In fact, without them, the system will minimize the stray field produced by the magnetization and create magnetic volume charges at the edges of the simulated framework. Those charges are attracting the wall and are biasing the system. To suppress them, the demagnetization field is calculated and deleted at the edges. Another type is periodic boundary condition where the current framework is duplicated in the selected direction x -amount of times. When the system is prepared, the simulation starts and the solver is computing the LLG equation for a time step, which can be fixed or dynamic depending on the requirements. Two types of stopping conditions are generally used to finish the computation. The first of which is a time constraint defined in the script (e.g., 20 ns) and the second one is a relaxation condition more precisely a bottom limit to the integral of the torque on the complete system. The second method tends to yield results faster as the interest is only placed on the equilibrium of the system and not the dynamics.

Chapter 4

The open-16-loop structure

Most of this chapter has been published in (14, 16), the text was adapted, and the figures were directly taken or little modified to fit the present manuscript. A few figures were added for a more complete explanation of data.

4.1 The open-loop sensor device

Magnetic domain walls (DWs) in soft thin nanostructured films (43) are interesting quasi-particles for numerous applications such as logic (5) and memory devices (1). Furthermore, several sensor ideas based on DWs have been developed and reported in the literature (12, 120, 121). The first such device to be implemented (12) was designed a few years ago by Novotechnik (122) and is now produced by Sensitec (123). The purpose of this sensor is to count the number of 360°-rotations of a magnetic field. The sensor relies on the Giant Magnetoresistance (GMR) (2, 3) effect to generate a signal (details see chapter 3). The information of absolute rotation is stored by the use of a combination of determining the DW positions and their number within the device. This simple method provides an elegant and reliable solution, which enables a versatile sensor design as required by the application. The structure, under a rotating magnetic field, nucleates one domain wall every 180°-rotation, and hence by counting the number of DWs, the number of 360°-turn is extracted (see appendix H for the details on the functionality of the device). These magnetic domain wall devices exhibit two types of failure events, the pinning of DWs if a particular depinning field threshold (depinning field limit) is not reached and the undesired nucleation of DWs at too high fields. Those two critical fields ought to be as separated as possible to allow an extensive range of operating applied fields and consequently of industrial applications.

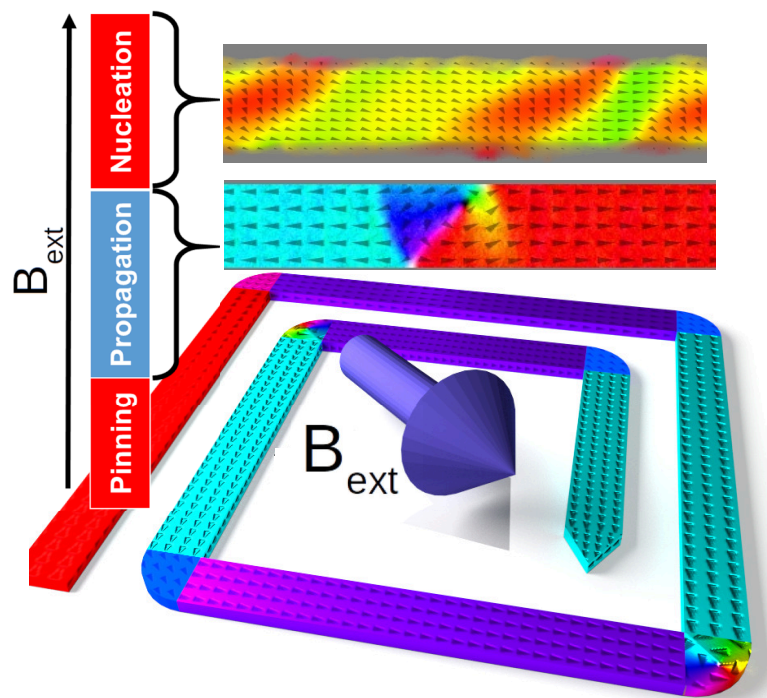


FIGURE 4.1: Schematic image of the concept of an open-loop sensor. At the top is a scale displaying the different possible magnetic states of the multium counter sensor device. At its side is the corresponding simulated spin structure for two characteristic states. At the bottom, is a schematic of the architecture of the device with magnetization direction indicated by various colors. This figure was published as a teaser for the manuscript (14).

4.1.1 Advantages of the technology

The potential of magnetic DW-based sensors is due to their many attractive attributes compared to other technologies. Magnetic DWs can be stable well above room temperature, making it a potential candidate to store data and be used for nonvolatile sensing and they can be displaced rapidly in application's relevant geometries (124). The second point of such technologies relies on the fact that no external power is required to create, stabilize or manipulate the storing element, meaning that a power failure in the system does not affect the functionality of the device. This stability ensures non-stop sensing even in cases where power is lost. Moreover, the only necessary power is that associated with the injected current that reads the state of the device, which can be applied during only a small part of the total operating time.

4.1.2 Disadvantages of the technology

A disadvantage of the open-loop structure is the limited number of counted turns. Indeed, the scalability of the technology is limited by the physical number of loops. The first commercialized concept could count 16 turns clockwise and back (122). The development of sensors with higher turn counts (40 turns) is expected, but it remains very challenging to implement, due to the more significant probability of defects for more extended structures. Thus the desired integrating system should perform a small number of rotations.

In this chapter, we describe the measurement scheme to study the field operating window of the open-loop structure by measuring the successful operations and errors occurring at different field strength values. We observe three essential regimes of the sensor: the pinning, the propagation and the nucleation field of DWs for several materials and varying geometries. We employ Magneto-Optical Kerr Effect (91) microscopy (see section 3.4.3) for the precise investigation of the position of DWs in the devices under various conditions and measure the GMR effect (see section 3.4.4) for high-statistics device characterization to obtain relevant information for the industry. The propagation field is identified as being affected by the edge roughness and the crystalline structure of the wires, while the nucleation field is dependent on the shape of the sample and the processing parameters. Simulations are used to identify the 2-dimensional variations of the magnetization close to the nucleation field and the expected nucleation field value. Furthermore, comprehensive statistics are obtained with the utilization of an automatized measurement using the GMR effect to compare with the MOKE microscopy results and determine a precise nucleation field for a significant number of devices.

4.2 The investigated system

The investigated materials were selected to acquire an understanding of the influence of material properties on the DW depinning and nucleation fields. The samples were deposited in a magnetron sputtering system employing a seed layer (details, see chapter 3). The investigated systems are two single layers of $\text{Ni}_{81}\text{Fe}_{19}$ (28 nm and 32 nm) (see Table 4.1),

Nominal Width (nm)	Ni ₈₁ Fe ₁₉ (28 nm)	Ni ₈₁ Fe ₁₉ (32 nm)
	Average Width (nm)	
200	205±9	240±15
250	264 ±10	288±15
300	328±6	342±9
350	372±18	391±9

TABLE 4.1: Summary of the measured widths for the two single layers Ni₈₁Fe₁₉(28 and 32 nm). The average width is determined from the average of 15 width measurements from Scanning Electron Microscopy micrographs of the wires.

two single layers of Co₉₀Fe₁₀(17 nm and 20 nm)(see Table 4.2),

Nominal Width (nm)	Co ₉₀ Fe ₁₀ (17 nm)	Co ₉₀ Fe ₁₀ (20 nm)
	Average Width (nm)	
200	211±6	NaN
250	266 ±6	NaN
300	323±9	NaN
350	357±19	NaN

TABLE 4.2: Summary of the measured widths for the two single layers Co₉₀Fe₁₀ (17 and 20 nm). 'NaN' indicates that the width was not determined, the same width as Co₉₀Fe₁₀ (17 nm) is used. The average width is determined from the average of 15 width measurements from SEM micrographs of the wires.

and two bilayers of Co₉₀Fe₁₀(1 nm)/Ni₈₁Fe₁₉(28 and 32 nm) (see Table 4.3).

Nominal Width (nm)	Co ₉₀ Fe ₁₀ (1 nm)/ Ni ₈₁ Fe ₁₉ (28 nm)	Co ₉₀ Fe ₁₀ (1 nm)/ Ni ₈₁ Fe ₁₉ (32 nm)
	Average Width (nm)	
200	235±10	209±8
250	290 ±10	264±8
300	356±6	327±15
350	409±9	364±20

TABLE 4.3: Summary of the measured widths for the two bilayers Co₉₀Fe₁₀ (1 nm)/Ni₈₁Fe₁₉(28 and 32 nm). The average width is determined from the average of 15 width measurements from SEM micrographs of the wires.

All the samples were capped with a 4 nm Ta layer. For the GMR measurement, a complete GMR stack with a free layer of Co₉₀Fe₁₀(1 nm)/Ni₈₁Fe₁₉(32 nm) was used. The GMR ratio was measured with a four-point probe technique (see section 3.4.1) under an applied magnetic field. A resist was spin-coated on the as-deposited wafers and patterned with photolithography in the shape of the structures (see Fig. 4.2). After the development of the resist, the material was then etched away by an Ar⁺ ion etching process. To fabricate electrical connections, part of the batch went through a second lithography followed by Au deposition

and lift-off processing. The latter allows for the measurement of the GMR effect in the devices (see measurement scheme detailed in appendix H). The materials used are magnetically soft and exhibit a full film coercivity of 2 Oe for the Ni₈₁Fe₁₉ films and bilayers, and 4 Oe for the Co₉₀Fe₁₀ films. Both materials were selected for their softness. Nonetheless, Co₉₀Fe₁₀ also exhibits an increased saturation magnetization ($M_s = 1334$ kA/m) compared with Ni₈₁Fe₁₉ ($M_s = 795$ kA/m) and the bilayer Co₉₀Fe₁₀/Ni₈₁Fe₁₉ ($M_s = 779$ kA/m). These values were measured using a BH-looper set-up (125). The films are polycrystalline, with an expected crystallite size of 10 nm (126). The individual crystallites of Co₉₀Fe₁₀ can be expected to exhibit a large magneto-crystalline anisotropy constant ($K = 45 \cdot 10^4$ J/m³ for pure Co (127)) compared with Ni₈₁Fe₁₉. The bilayer was selected to demonstrate that the addition of a thin Co₉₀Fe₁₀ does not yield significantly different magnetic results. The latter is necessary to compare the magnetic switching measurement results obtained on single layers with the one received with the GMR effect where a thin layer of Co₉₀Fe₁₀ (1 nm) is always added at the bottom of the free layer to enhance the GMR signal. We readily observe that the bilayer system exhibits similar coercivity and saturation magnetization values as the single Ni₈₁Fe₁₉ layer. Thus showing that the addition of the Co₉₀Fe₁₀(1 nm) does not drastically modify the magnetic results of the thicker Ni₈₁Fe₁₉ layer. As a consequence, if differences are measured between a single layer of a magnetic material and a GMR stack with a free layer of the same material, the difference is then attributed to the influence of the underlying stack of the GMR.

4.3 The structure and its shape characterization

A scheme of the used architecture is depicted in Fig. 4.2. The structure starts with a nucleation pad to introduce DWs in the looping wires (128) and finishes with a tapered tip to prevent nucleation on that end. The devices are designed with 16 loops (i.e., the complete length of the device is 31 mm from the nucleation pad to the tapered tip end). This structure can contain a maximum of 33 DWs (i.e., 2 DWs per loop plus 1 in the wire following the nucleation pad), this allows for the sensing of 16 360°-turns clockwise of the applied field. The sensing stops at 16 since one more rotation of the applied field leads to the annihilation of 2 DWs and the introduction of 2 new DWs from the nucleation pad. The state of the sensor is then the same at turn 16 and 17, and the GMR transport measurement yields the same result. This open-16-loop structure is chiral due to the position of the nucleation pad on one side and the tip at the end. This chirality requires that the integrating application possesses some designed sequences to use the 16-turn characteristic fully. Namely, an empty sensor could not sense a counter-clockwise rotation since no DW can be introduced in that direction. From an empty sensor, 16 turns clockwise, and 16 turns counter-clockwise can be detected, and only in that order. To allow a customer to start the rotation in any desired direction the sensor needs be half-filled, and be in state 8 out of 16. A starting rotation in the clockwise direction yielding state 9/16 and a starting rotation in the anti-clockwise direction giving state 7/16, which are distinguishable. In that case, only half of the turn count can be utilized. The quality of the processing in an

industrial environment can provide large structures compared to the typical dimensions encountered for DW-based devices in the literature (89, 129–131). The large size is advantageous for the assessment of devices reliability since the DW needs to cover a sizeable distance. The DW has thus a high probability of encountering the full distribution of geometrical and structural variations induced by the fabrication. Furthermore, the inner loops of the devices are far away from the starting nucleation pad and the end of the sample which could otherwise provide an unwanted extra source of device variability (reduction of the nucleation field due to flux closure at the edges). In order to investigate the influence of variations of the cross-section, four different devices widths were compared (200, 250, 300 and 350 nm). The width is not decreased further since 200 nm lies at the limit of the lateral resolution of the photolithography tool that Sensitec uses.

4.3.1 Characterization of the cross-sectional shape

After processing, a subset of the devices was characterized under Scanning Electron Microscopy (SEM, see section 3.4.6) and Atomic Force Microscopy (AFM, see section 3.4.5) to study the topography of the wires and assess the pattern transfer of the geometrical shape. From the acquired images (see example in Fig. 4.2), we observe a variation of the widths compared to the nominal widths. Furthermore, the AFM profiles reveal a trapezoidal shape instead of a square shape which is a consequence of the etching process being unable to transfer precisely the photolithographically defined structures for all depths. Such variations are caused by shadowing effects during the ion milling and might affect the dynamics of the DW propagation as well as the nucleation process (130–132). Due to the ion milling process and more precisely, the chosen angle for the etching of the stack, some of the already etched material is redeposited on the edges of the protected structures. Material redeposition is seen on the images as side bumps on top of the wire. The redeposition is expected to be composed of all the materials constituting the stack. It, therefore, remains difficult to determine the effective 'magnetic' width of the effective magnetic layer. In our case, we define the width as the distance between the two bright lines in the SEM image, corresponding to the bump regions of the AFM profile. In Tab. 4.1, Tab. 4.2, and Tab. 4.3 are referenced the average measured widths for the different investigated stacks. Some of the sample exhibit much larger widths than the nominal one, i.e., the nominal 350 nm width for the bilayer with $\text{Ni}_{81}\text{Fe}_{19}$ (28 nm) is in fact 409 ± 9 nm wide. It is observed that the width can vary up to 60 nm between devices and a further 60 nm between the top and the bottom of the wire due to the shape of the wire profile. This effect results from the inhomogeneity of the resist thickness over the wafer and the difficulty in controlling photolithography dimensions on length scales below the diffraction length.

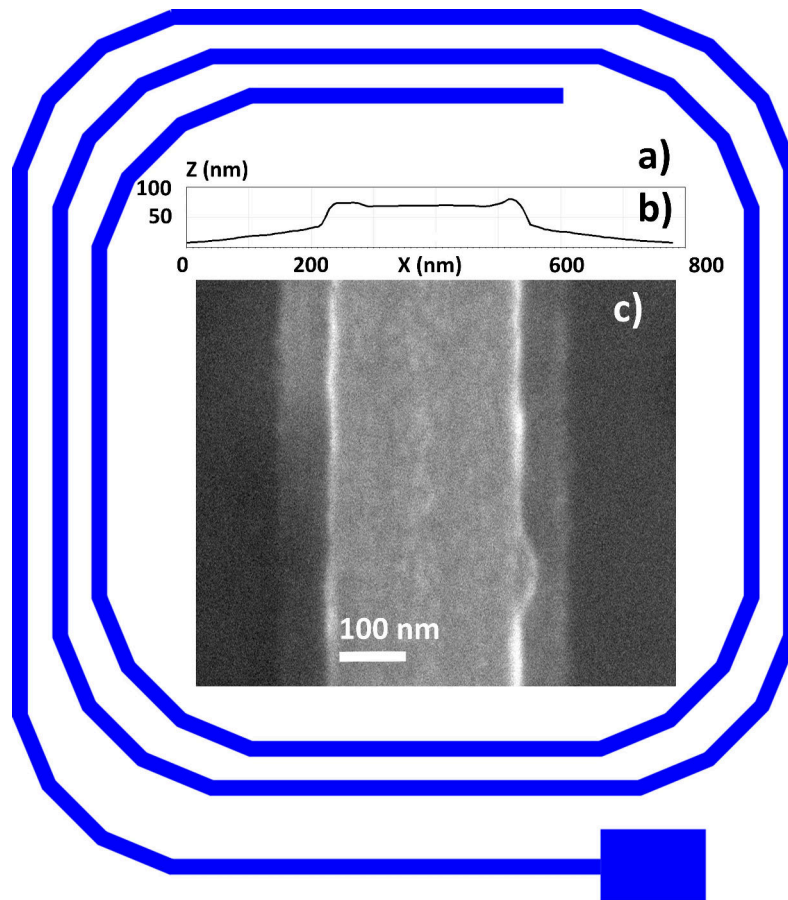


FIGURE 4.2: (a) Schematic of the structure, 3 loops are represented. (b) Atomic Force Microscopy image of a $\text{Ni}_{81}\text{Fe}_{19}$ wire of 300 nm nominal width. (c) Scanning Electron Microscopy image of a $\text{Ni}_{81}\text{Fe}_{19}$ wire of 300 nm nominal width. Adaptation from (14).

Finally, we do not provide data for the average width of the single layer of $\text{Co}_{90}\text{Fe}_{10}$ (20 nm) sample since it received a 60 nm covering layer of AlO_x for protection during the dicing process (the other samples were cleaved and thus did not need the protective layer). The oxide layer is hindering the measurement of the $\text{Co}_{90}\text{Fe}_{10}$ (20 nm) sample in the SEM we are then unable to provide the width of the wires. However, it is safe to assume that the average width is not too distinct from the other samples.

4.4 Sensor operation conditions

4.4.1 MOKE investigation

We now start the magnetic investigation of the described structures. There are two main failure events of magnetic devices, namely unwanted DW nucleation at too high fields and DW pinning as a result of too low fields being applied

to allow for DW propagation. For this section, the aim is to obtain the width dependence of the limit between pinning and propagation (depinning field limit) and the limit between propagation and nucleation (nucleation field limit). The measurement set-up is the following:

The Magneto-Optical Kerr Effect microscope set-up used is described in the section 3.4.3. The wires of the sensor are positioned parallel to the camera's field of view to provide a reference for the angle of the applied field. A vector magnet is utilized for the application of a rotating field of up to 100 mT. To detect a switching event, a differential contrast method is used. A background image is saved and subtracted to the current field of view thus yielding a clear contrast even for widths as small as 200 nm, which is lower than the diffraction limit of our light source.

Depinning field limit

The depinning or propagation field limit is the lowest field value, at which any DW freely propagates and is not pinned at any point in the whole structure. Since DW pinning is a highly stochastic phenomenon (133, 134) a significant amount of statistics is required to characterize it reliably. In our scheme, for a single measurement to be successful, all the 33 possible DWs must propagate along the entire device without anyone experiencing a failure event. If a failure (pinning of a wall) occurs, it necessarily leads to it being annihilated with the subsequent wall when the latter also reaches the pinning site, thus destroying the information carried by the walls. The measurement scheme depicted in Fig. 4.3(a)-(d) is the following: the sensor is in an unknown state at the start of the experiment (DWs can be present or not without constraining the measurement scheme). The starting field strength is 1 mT, and the rotation is launched at a frequency of 1 Hz. At least 33 complete rotations of the field were performed in the clockwise direction, and every DW probed 31 mm of wire for a pinning event. In total, 10 structures were examined for a combined length of more than 10 m of magnetic materials. The data are shown by the discs in Figure 4.4. In Fig. 4.4, the data points demarcate the transition between lower fields yielding a pinning event for one of the DWs and higher field strength providing a reliable propagation of all DWs in the complete structure. All the depinning field values for the $\text{Ni}_{81}\text{Fe}_{19}$ samples are located between 5 and 25 mT, similarly for the bilayers. Despite the variations in width and thickness, all the $\text{Ni}_{81}\text{Fe}_{19}$ samples, exhibit similar depinning fields. The shape of the wire is thus not entirely governing the DW depinning. The depinning field is mainly affected by the irregularities of the shape and the material. However, due to the redeposition on the wires, it is difficult to directly ascertain the relevant magnetic roughness of the wires, which might be different from the topographical roughness. A priori, this is not very surprising as for perfect wires the propagation field would be close to zero and independent of the wire geometry, since uniformities in the anisotropy are pinning the DW. Consequently, in real wires, defects and edge roughness play the role of governing mechanisms for the propagation field, and these effects are not strongly geometry dependent (width, thickness). The small increase with decreasing wire width can be explained by

the influence of the edge roughness becoming relatively more important for narrower wires (the edge roughness is mostly wire width independent).

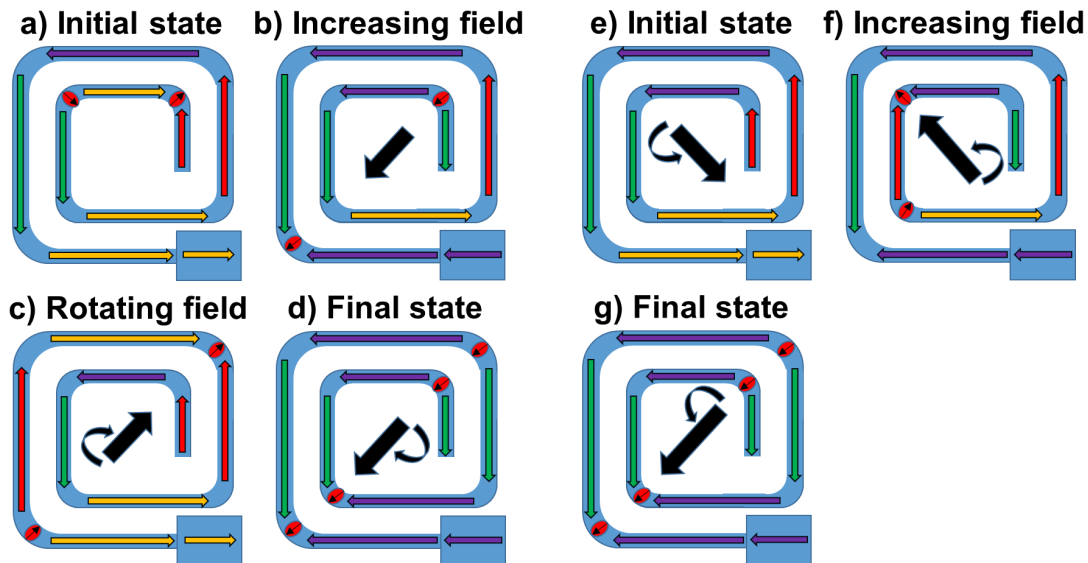


FIGURE 4.3: Schematic representation of the field sequences for the measurement of the depinning and nucleation fields for a simplified device based on two turns. (a)-(d) Depinning/propagation field - (a) The sensor is in the initial state with a pair of domain walls in it. The propagation field measurement can be carried out for any state of the sensor (filled with DWs or empty). (b) The field is rotated clockwise and increased to inject DWs from the nucleation pad at each 180° turn. (c) The nucleated DW should continue to propagate around the corners and further into the device as the field rotation continues. As long as the wall continues to propagate, the field is kept constant, however, if pinning is detected the field is increased to sustain the propagation. (d) The device is entirely filled up with DWs at all alternate corners in the structure. (e)-(g) Nucleation field measurement. (e) Empty state for the initial configuration is obtained by rotating the field counter-clockwise with a field higher than the propagation field value. (f) The field is increased and rotated counter-clockwise until a nucleation event occurs. (g) The final state with a full sensor. Adaptation from (14).

The $\text{Co}_{90}\text{Fe}_{10}$ samples have propagation fields that are two times higher than the ones for the $\text{Ni}_{81}\text{Fe}_{19}$. We attribute the latter effect to the magneto-crystalline anisotropy of each $\text{Co}_{90}\text{Fe}_{10}$ crystallite generating an energy landscape which increases the pinning of the DWs. Another exciting aspect is the decrease of the depinning field with an increase of the thickness, which could be exploited to reach similar depinning values as for the $\text{Ni}_{81}\text{Fe}_{19}$ layers. Furthermore, the samples with a thin layer of $\text{Co}_{90}\text{Fe}_{10}$ (1 nm) below the $\text{Ni}_{81}\text{Fe}_{19}$ layer do not exhibit significant differences between the samples with and without the thin layer, which thus plays only a minor role for the magnetic properties.

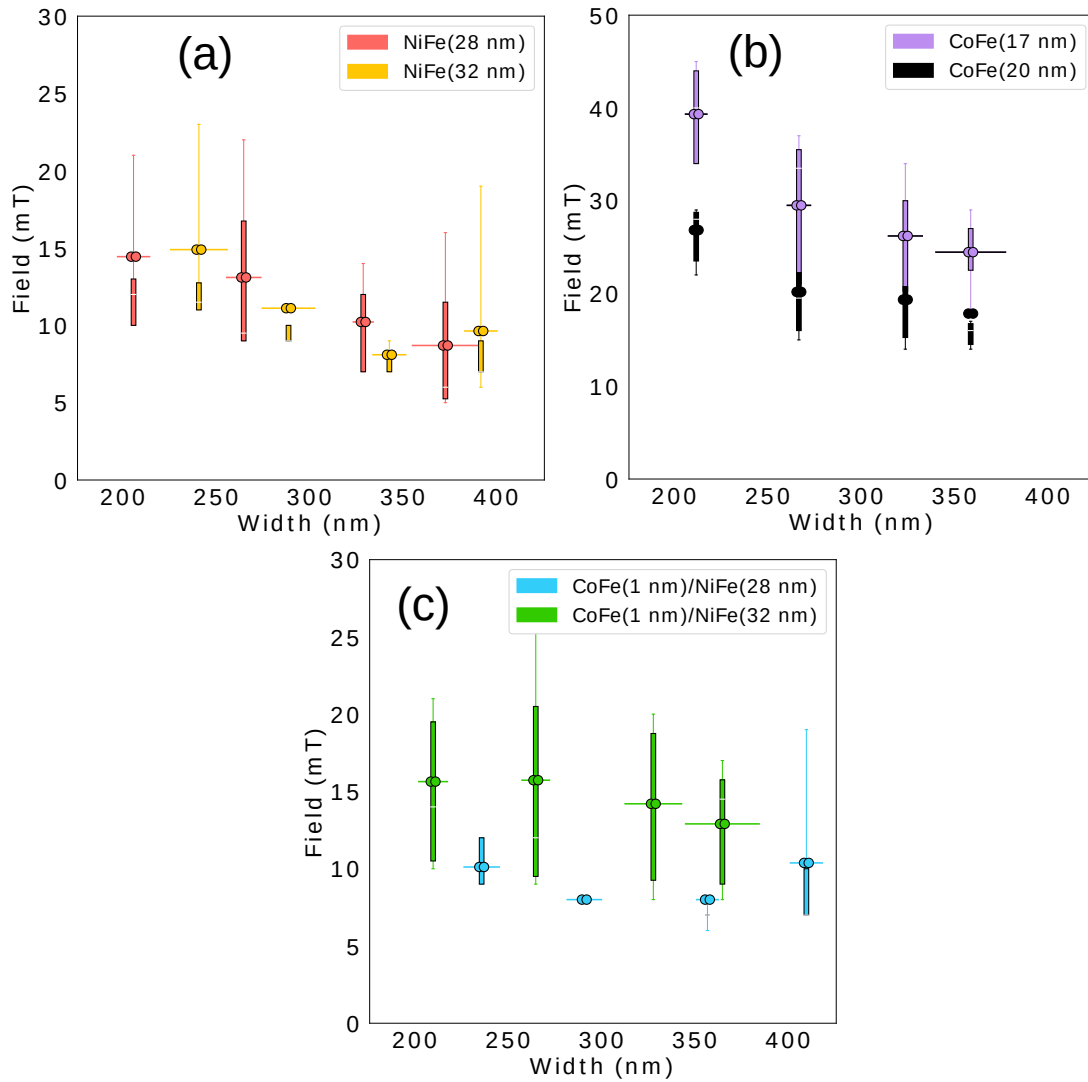


FIGURE 4.4: Plots of the limit (depinning field) between the pinning of DWs at lower field values and propagation of DWs at higher field values. The boxes associated with the data points in the plot represent 25% (first quartile) to 75% (third quartile) of the distribution. The whiskers or dashed lines represent 5% to 25% and 75% to 95%. In this manner, the plot represents the key features of the entire distribution. The mean value of the distribution is represented by 2 disks. (a) Depinning fields for the samples $\text{Ni}_{81}\text{Fe}_{19}$ (28 and 32 nm). (b) Depinning fields for the samples $\text{Co}_{90}\text{Fe}_{10}$ (17 and 20 nm). (c) Depinning fields for the samples $\text{Co}_{90}\text{Fe}_{10}$ (1 nm)/ $\text{Ni}_{81}\text{Fe}_{19}$ (28 and 32 nm). Adaptation from (14).

In summary, for devices, it is therefore desirable to avoid materials with strong magneto-crystalline anisotropy and limit processing variability to ensure the reliability of DW propagation. The propagation field appears then as a characteristic materials parameter that is not strongly dependent on the wire width and thus cannot be easily tailored by the geometry to improve the operational reliability. For the field values presented here and with the dimensions of the cross-section, we are above the Walker breakdown limit. The dynamic of the DW is expected

to be chaotic and endorsing the generation of several point vortices during the propagation process. Each of the vortices has a probability of being pinned by defects thus rendering a theoretical analysis of the process difficult. Due to this stochasticity, we require a large count of iterations of the measurement to obtain the complete distribution of depinning fields. The automotive industry needs millions of trials of the process to assess that the sensor will work without failure. The latter not being possible with the MOKE effect we stop the study at this point.

Nucleation field

We next investigate the other boundary of the field operating window of the open-16-loop devices, namely the nucleation field of the devices. At high fields, instead of DW nucleation only occurring in the pad region of the device, undesired DW nucleation takes place in the wires. For the tapered end of the device, it is expected that the shape anisotropy, in this part, is too high for the nucleation of a new DW for the probed field range. We are then investigating the transition of the devices from the propagation region above the depinning field up to the nucleation region. The measurement scheme described in Fig. 4.3 (e)-(g) is the following: Having established the depinning field, we can rotate the applied field counter-clockwise to empty the device completely of all the DWs by annihilating them in the nucleation pad. The resulting magnetic state is the initial state, which we term the vortex state due to its resemblance to the one for ring structures (43) as seen in Fig. 4.3 (e). By continuing to rotate the field in this direction with incrementing field strength, we selectively detect DW generation through spontaneous nucleation somewhere within the wire, as depicted in Fig. 4.3 (f). The lowest field value promoting this event is termed the nucleation field and is of interest since it yields the field at which the measured information can potentially be lost in a failure scenario. From the Fig. 4.5, the propagation region located between the nucleation field and the depinning field is clearly visible. The sensor device can operate in this region. Concerning the nucleation boundary, we find that the scaling of the nucleation field follows a power law as a function of the width. This dependence arises from the fact that the nucleation field for DWs in nanopatterned soft magnetic materials is mainly determined by the cross-sectional shape of the system (width and thickness). For a closed system such as a ring or a loop, the only boundaries are the two side edges, which can be approximated as infinitely long. Furthermore, if the radius of curvature is much larger than the width of the wire, then no lowering of the nucleation field value is expected at corners. Such effects are usually provoked by a flux closure spin configuration at the ends of the wire. This reduction of the nucleation field has been observed in the case where a wire relaxes into an S or C state (135). Since our materials are relatively thick and soft, the magnetization is lying in the plane in the direction of the wire length due to a dominant magnetostatic energy contribution. The expectation is that the shape anisotropy is playing a primary role in the determination of the nucleation field value.

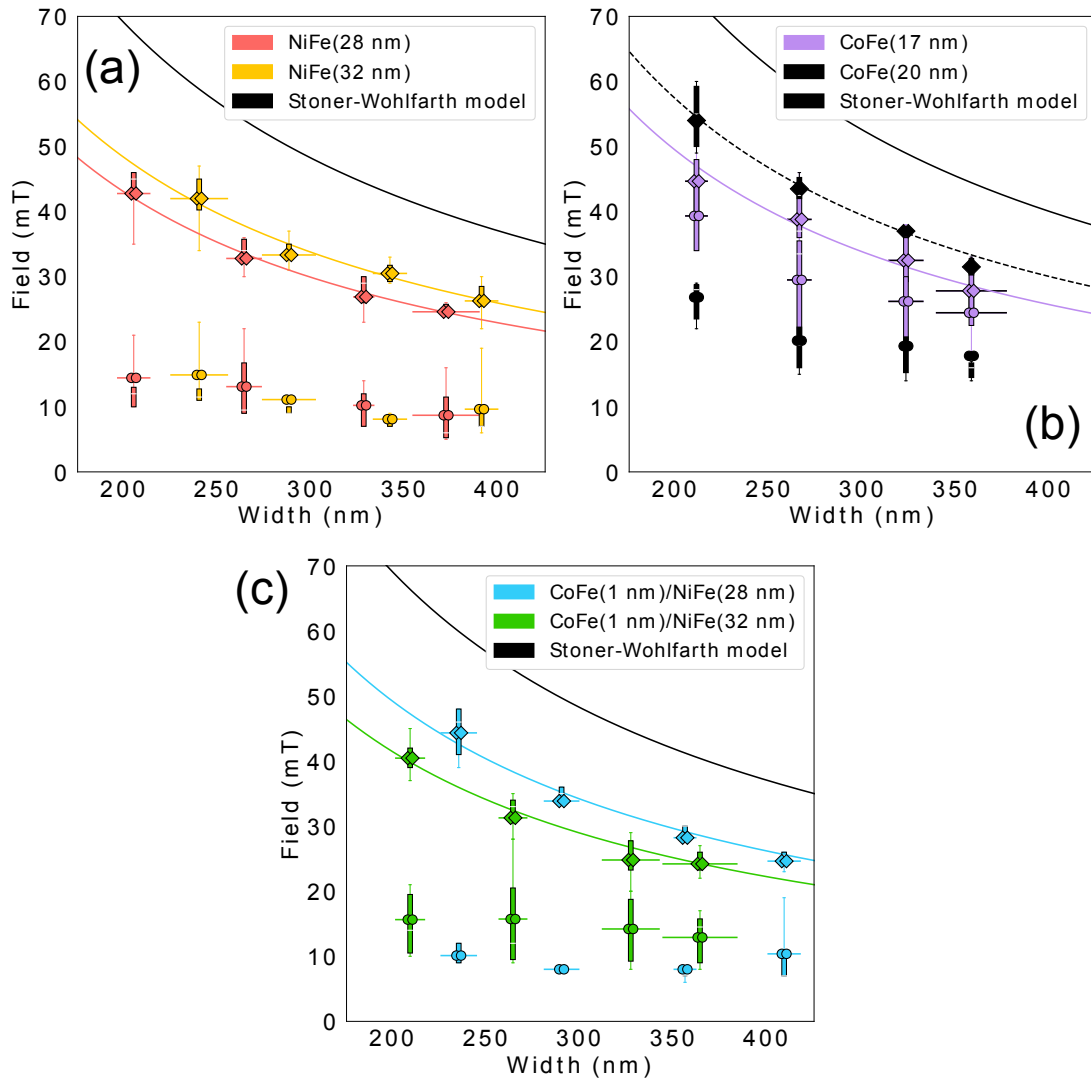


FIGURE 4.5: Propagation and nucleation fields for the investigated samples. The round points represent the average value of the depinning field limits while the diamonds represent the nucleation fields. (a) Plot of the nucleation and depinning field values as a function of the width of the wire for the $\text{Ni}_{81}\text{Fe}_{19}$ (28 and 32 nm). The black line is the pure Stoner-Wohlfarth behavior for $\text{Ni}_{81}\text{Fe}_{19}$ (32 nm). The red and orange lines are the adapted model fitted with a scaling constant $C = 0.7$. (b) Similar plot as (a) for $\text{Co}_{90}\text{Fe}_{10}$ (17 and 20 nm). The full black line is the SW model for $\text{Co}_{90}\text{Fe}_{10}$ (20 nm). The dashed black line and full purple line are the adapted model fitted with a scaling constant $C = 0.75$. (c) Similar plot as (a) for the bilayers $\text{Co}_{90}\text{Fe}_{10}$ (1 nm)/ $\text{Ni}_{81}\text{Fe}_{19}$ (28 and 32 nm). The black line is the SW model for $\text{Ni}_{81}\text{Fe}_{19}$ (32 nm). The turquoise and green lines are the adapted model fitted with a scaling constant $C = 0.8$ and 0.6 , respectively. Adaptation from (14).

Within the framework of the Stoner-Wohlfarth model (34), for a particle with dimensions smaller than the exchange length (5 nm in $\text{Ni}_{81}\text{Fe}_{19}$), the magnetization is approximated with a macrospin and is expected to rotate coherently during the switching (details, see section 2.3.2). In the most simplistic version

of the model, this particle is only subject for instance to a uniaxial anisotropy of the form $K \cdot \sin^2(\theta)$, in our case, K being mainly the shape anisotropy. For larger systems that are not fully described as a macrospin, one can expect an activation volume, located for instance at the point of lowest anisotropy, to rotate coherently (34). Mathematically, this can be described as follows 2.3.2:

$$E = E_{Zeeman} + E_{Demag} = -\mu_0 H M_s V + \frac{1}{2} \mu_0 N_y M_s^2 V \quad (4.1)$$

with M_s being the saturation magnetization, V the activation volume and N_y the demagnetizing factor described in (42) for an infinitely long wire:

$$H_n = \frac{1}{2} \frac{t}{t+w} M_s \quad (4.2)$$

With t the thickness and w the width of the sample. In this simple formula, the nucleation field is then determined by the geometry as well as the saturation magnetization, which is a material constant. As plotted, in Fig. 4.5 with full black lines, such a calculated curve for the pure Stoner-Wohlfarth behavior does not reproduce the obtained data quantitatively.

Simulation of the magnetization configuration right below a nucleation event: To understand the magnetization behavior close but below the nucleation field, micromagnetic simulations (details, see section 3.6) are performed with the software Mumax3 (118). AFM profiles are used as the simulated shape, and periodic boundary condition serves to extend the length of the wire. To realize the latter, a python program (see the source code in appendix I) inputs an AFM micrograph processes it and outputs slices of a regular thickness. In an AFM micrograph, the intensity of the pixel encodes the measured height of the structure. The first performed task of our python framework is the analysis of the intensities and the averaging over the length of the wire. From the latter, an average profile is extracted in which the highest plateau represents the average height of the top of the wire. From this height, the program descends 4 nm to avoid the Ta capping to consider the shape of the magnetic material solely. At that point, the height value is saved, and the original micrograph is loaded. Starting from the saved height, the original micrograph is sliced every 2 nm, and an image is generated for every slice (see a stack of created slices in Fig. 4.6 (b) from the AFM profile in (a)). The blue region is encoding the presence of magnetic material and the black one its absence. At that point, the work of the python framework is done. To create the simulation, the bottom image is loaded in the software, then a cube of $2 \times 2 \times 2 \text{ nm}^3$ is attributed to every blue pixel (representing the magnetic material, see Fig. 4.6 (b)). During the conversion processes from the AFM micrograph to the simulation, all the dimensions are kept constant. Then the second image is loaded, and the cubes generated by this image are stacked on the previous ones. The process is repeated until the complete shape has been rebuilt in the simulation software.

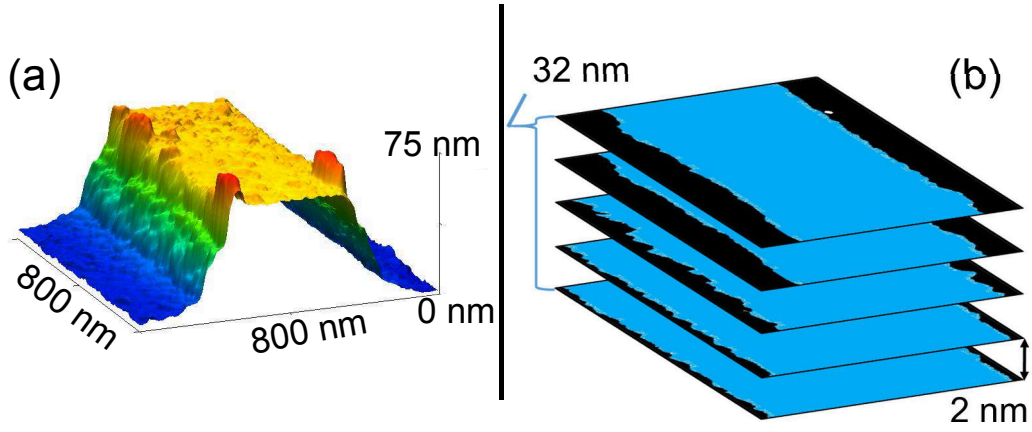


FIGURE 4.6: (a) Atomic force micrograph expanded in 3 dimensions by using the intensity value of a pixel as the height. (b) A stack of slices taken in the AFM micrograph's intensity and cutting every 2 nm of height. For a 32 nm thick wire, 16 slices are generated. Here only 5 of them are shown.

We mainly used this method of slicing to study the influence of the side edge roughness. Indeed, the roughness can be quite accurately represented up to a 2 nm resolution. The latter value being limited by the processing power of the current Graphics Processing Unit cards and the resolution of the AFM tool (see chapter 4). This method can yield even better results by allowing the top surface roughness. Finally, the study of the implantation of magnetic and nonmagnetic defects can be performed by randomly selecting pixels in the images and changing their color, which can be translated to a different material in the simulation software. Our framework discretization with cells of volume $2 \times 2 \times 2 \text{ nm}^3$ also respect the limit of the exchange length for a physical representation of the magnetization dynamics. After setting the simulation framework, the magnetization is initialized along the length of the wire and left to relax. A field is then applied for 20 ns following an equation of the form:

$$B = \left(-\frac{\sqrt{2}}{2} B_{ext} (1 - \exp\left(\frac{-t}{4 \cdot 10^{-9}}\right)), -\frac{\sqrt{2}}{2} B_{ext} (1 - \exp\left(\frac{-t}{4 \cdot 10^{-9}}\right)), 0 \right) \quad (4.3)$$

to avoid artifacts due to an instantaneous applied field. A bisection method was then used to determine the nucleation field within 1 mT precision. The results are presented in Fig. 4.7. A snapshot of the magnetization in Fig. 4.7 represents the relaxed state of the wire at an applied field value that is just 1 mT below the nucleation field value. The spin structure and the subsequent dynamics show that the reversal mode of our stripes resembles an in-plane curling mode. The latter is expected for large systems with inhomogeneities in the anisotropies (36). As compared to the Stoner-Wohlfarth model 2.3.2, the rotation of magnetization is not coherent in the whole structure and exhibits a 2-dimensional variation along the wire (136). A pure curling mode would not yield nucleation field values significantly different from the Stoner-Wohlfarth model (137). Furthermore, our

data also show that despite the trapezoidal shape and the included edge roughness, the nucleation field at 0 K is on average 90 % of the expected one from the Stoner-Wohlfarth model.

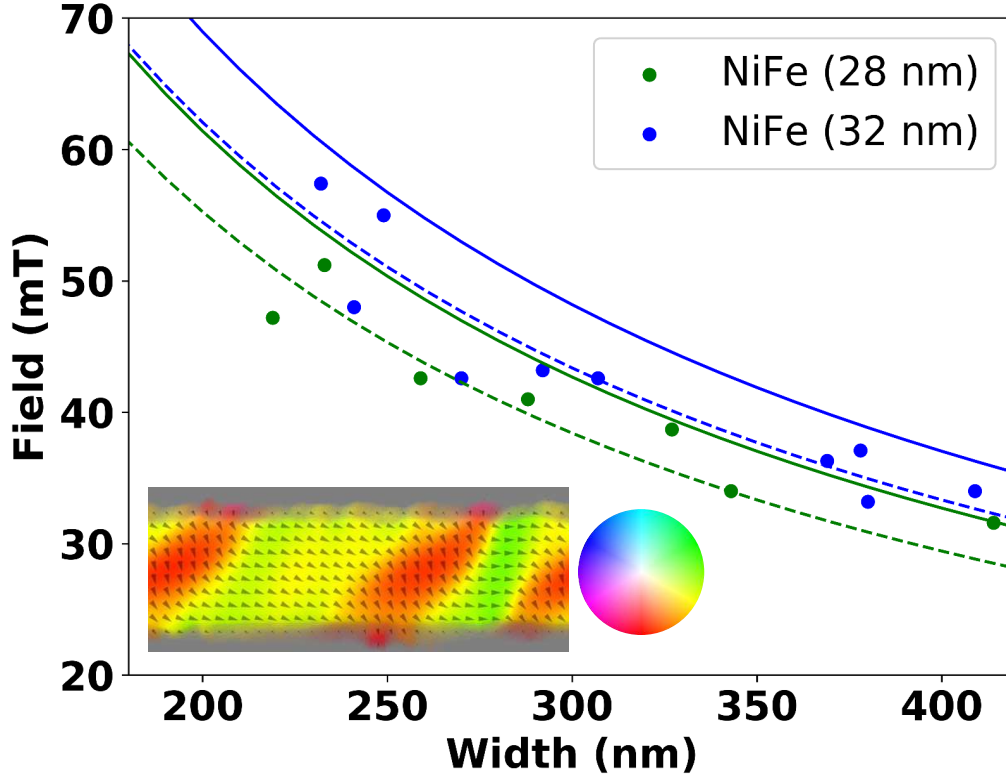


FIGURE 4.7: Simulation results of the nucleation field as a function of the minimum width of the wire. The green and full blue line represent the SW model for the $\text{Ni}_{81}\text{Fe}_{19}$ (28 nm) and $\text{Ni}_{81}\text{Fe}_{19}$ (32 nm), respectively. The dashed lines are the SW model with a scaling factor $C = 0.9$. A simulation snapshot of the magnetization was taken at a field just 1 mT below the nucleation field value of a 200 nm wide wire of $\text{Ni}_{81}\text{Fe}_{19}$ (32 nm). Adaptation from (14).

However, wire irregularities are expected to yield a lowered nucleation field as seen from the inhomogeneous spin configurations shown in the simulation results in Fig. 4.7. In the real system, further effects can lead to a reduction of the nucleation field. For example, damage from the ion milling causing a change of crystallization at the edges and a decrease of the saturation magnetization (138) or a doping of the wire due to material implantation can lead to a locally reduced shape anisotropy due to a reduced saturation magnetization (139). Finally, thermal activation is also having an impact not considered in the Stoner-Wohlfarth model. In order to account for such effects in the simplest manner, we include a scaling factor C to the demagnetization factor as follows:

$$H_n = C \frac{1}{2} \frac{t}{t+w} M_s \quad (4.4)$$

By fitting the data in Fig. 4.7, we find that the two samples with a single layer of $\text{Ni}_{81}\text{Fe}_{19}$ (28 and 32 nm) can be fitted with the value $C = 0.7$. The two single layers of $\text{Co}_{90}\text{Fe}_{10}$ (17 and 20 nm) are fitted with $C = 0.75$. Finally, the bilayer $\text{Co}_{90}\text{Fe}_{10}$ (1nm)/ $\text{Ni}_{81}\text{Fe}_{19}$ (28 nm) is fitted with $C = 0.8$ and $\text{Co}_{90}\text{Fe}_{10}$ (1nm)/ $\text{Ni}_{81}\text{Fe}_{19}$ (32 nm) with $C = 0.6$. Several effects can be at the origin of this value thus its interpretation remains tricky, the value of $C = 0.7$ provides good agreement with the results of the samples. Overall, the observable variations of the nucleation field with the geometry provide a handle to tailor the characteristics of the device thus the operation condition and the reliability.

4.4.2 GMR investigation

In the present subsection, we investigate samples with a GMR stack to perform transport measurements. Transport measurements can be fully automatized and are thus quite quick at providing a substantial amount of statistics in a short period. Nevertheless, the results obtained are often confusing to analyze due to the contribution of many external factors to the magnetization dynamics. The most important ones are originating from stray fields created by the layers located below the free layer. The comparison between the results obtained with single layers with the MOKE effect and the results achieved with the transport measurements is then not at all straightforward.

Measurement algorithm

Despite the latter, and to investigate the nucleation limit further, we measure a considerable number (3200) of open-16-loop devices. The majority of the possible geometrical variations are going to be encountered, generating a clear idea of the maximum deviations still enabling a working device. For the measurement of the GMR effect, in the presented architecture, the Vcc and GND electrode are positioned on opposite sides of the looping structure as shown in Fig. 4.8 (a). The measurement points are placed at the other corners of the structure. The blue triangle indicates the reference direction (direction of the last layer of the SAF 3.1.1) for the GMR effect. An example of the resistance values obtained for a magnetization configuration is presented in Fig. 4.8 (b). An entire wafer was prepared with the previously mentioned GMR stack structures and contacted to measure the resistance of the wires (A scheme of the device with all the electrical connection can be found in the chapter 3). The resistance in the initial state (no domain walls) is probed and compared to the case where a domain wall is inside. An algorithm also using a bisection method (see Fig. 4.9) is used to define the exact nucleation field value.

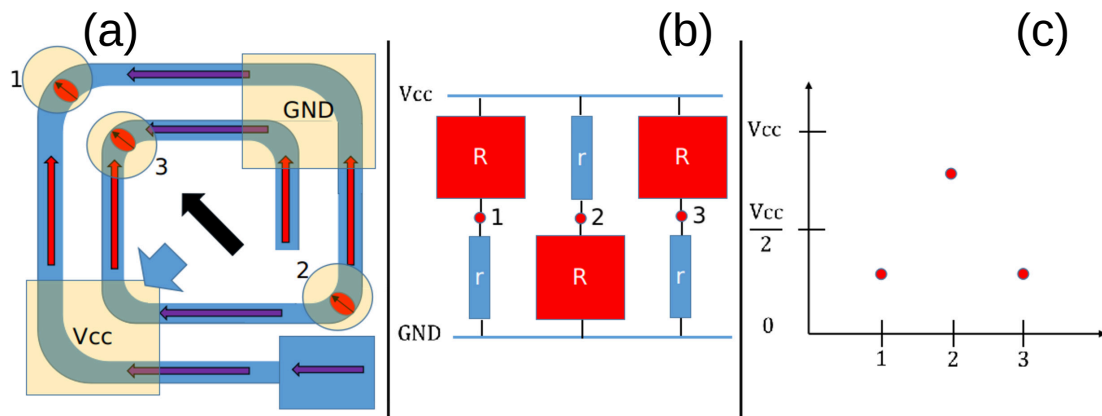


FIGURE 4.8: (a) Schematic of the multiturn counter with two loops and containing 3 DWs (red ovals containing a black arrow). The applied field is represented by a black arrow and the direction of the fixed layer of the GMR stack by a blue arrow. For the measurement of the GMR effect, the V_{cc} potential is applied in the bottom left corner and the ground at the top right corner. The voltage measurement points are located at positions 1, 2 and 3. (b) Schematic of resistance values obtained when the magnetization is in the configuration presented in (a). (c) Plot of the resistance values at the different measurement positions, the measured resistances correspond to the magnetization pattern in (a). Adaptation from the appendix in (14)

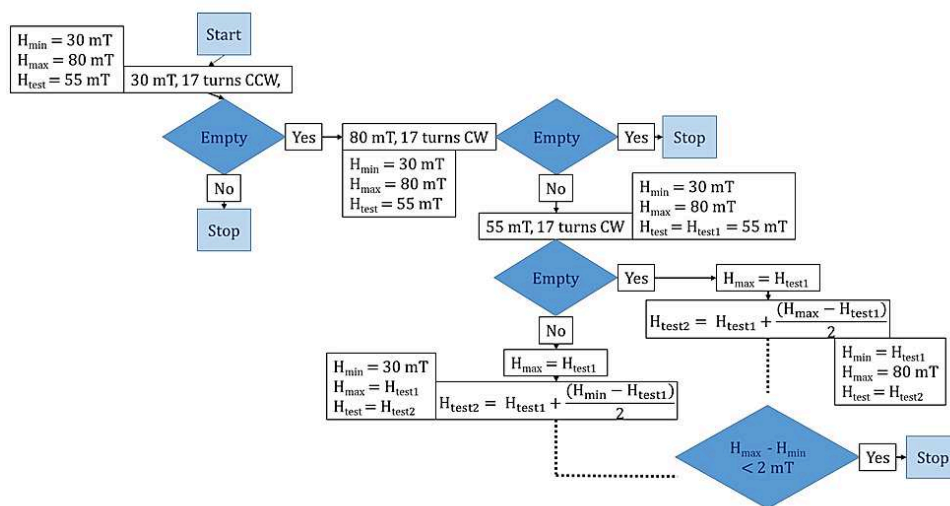


FIGURE 4.9: Flowchart of the algorithm for the automatic measurement of the exact value of the nucleation field of the sensors using a GMR transport measurement.

The applied field rotation sequence is made of 17 full rotations clockwise then 17 full rotations counter-clockwise followed by an electrical measurement. We call this type of rotation sequence a 2-17 turn sequence. After the 17 full turns counter-clockwise, the device is expected to be empty if the nucleation field is

higher than the tested value, and the depinning field is lower than the tested value. We describe the standard measurement scheme for a working element, any failure in the following steps result in the device being counted as defective. A starting value of $\mu_0 H = 30$ mT is applied for the rotation sequence since the depinning field limit was previously found to be lower than this value (4.4). After the rotation sequences, if the sensor is measured empty the applied field is increased to fill the sensor with DWs via the nucleation process. A field of $\mu_0 H = 80$ mT is selected since we expect the nucleation field of all the structures to be lower, and the rotation sequence is applied. If no failures occurred, the next applied field value is taken as half of the difference of the previous ones added to the lowest value giving 55 mT. After the sequence, if the device is measured empty, then the following field is half of the difference between the highest (80 mT) and the middle value (55 mT) added to the middle value. The lowest value (30 mT) is replaced by the middle one (55 mT). If the sensor is filled, then half of the difference between the lowest (30 mT) and the middle value (55 mT) is added to the lowest value. The highest value (80 mT) is replaced by the middle one (55 mT). The algorithm continues until the difference between the lowest, and the highest field value is smaller than 1 mT.

Measurement results

The latter process serves to measure the exact nucleation field of 3200 structures. Approximately 800 measurements per wire width are performed. An electrical resistance of the complete device is measured between the V_{cc} and GND (as seen in chapter 3). Due to the connection layout, the number of wires connected is 33, and their length is 400 μm . Before this resistance measurement, the sensors were initialized with DWs in the whole device. Due to the looping structure and the DWs present, half of a wire is in a ‘high’ resistive state with the GMR and the other half is in a ‘low’ resistive state as seen in Fig. 4.8. Thus the measured resistance does not contain a GMR component (the DW has a negligible contribution). The resistance of every wire is then similar. We then apply the formula $r = R_s \frac{L}{w}$ for the resistance of a wire, with $R_s = 4.09 \Omega/\text{sq}$ being the sheet resistance, L the length and w the width of a wire. The wires are connected in parallel thus the resistance of the device is $R = \frac{r}{33}$. We notice that the absolute resistance value of the sensor, which is based on the geometry of the wires (width, thickness, and length) can be compared to the nucleation field also geometry related as it was pointed out in the previous section. We plug the latter equations in equation 4.4 to obtain:

$$H_n = \frac{1}{2} \frac{t}{R_s L + 33Rt} 33M_s R \quad (4.5)$$

with R being the resistance of the sensor, t the thickness, M_s the saturation magnetization and L the length of the wire. The previously described model with a constant $C = 0.7$ is plotted in brown in Fig. 4.10 while the Stoner-Wohlfarth nucleation field is in black. In the Fig. 4.10, a fixed reference value for propagation is

used (30 mT). Indeed, for the algorithm to work a starting propagation field value is needed, then no data points are obtained for lower field values. The expected theoretical resistances with a 200 nm (purple), 250 nm (red), 300 nm (green), 350 nm (blue) wire width are 247 Ω , 198 Ω , 165 Ω , 141 Ω , respectively. A circle represents the nucleation field of every single device as a function of its resistance. With our measurement sequence, the 350 nm width devices results are less reliable than the other width values due to the small number of measured points on the graph. The latter effect is just an artifact of the measurement sequence. Indeed, 350 nm width devices are expected to have a nucleation field limit lower than 30 mT.

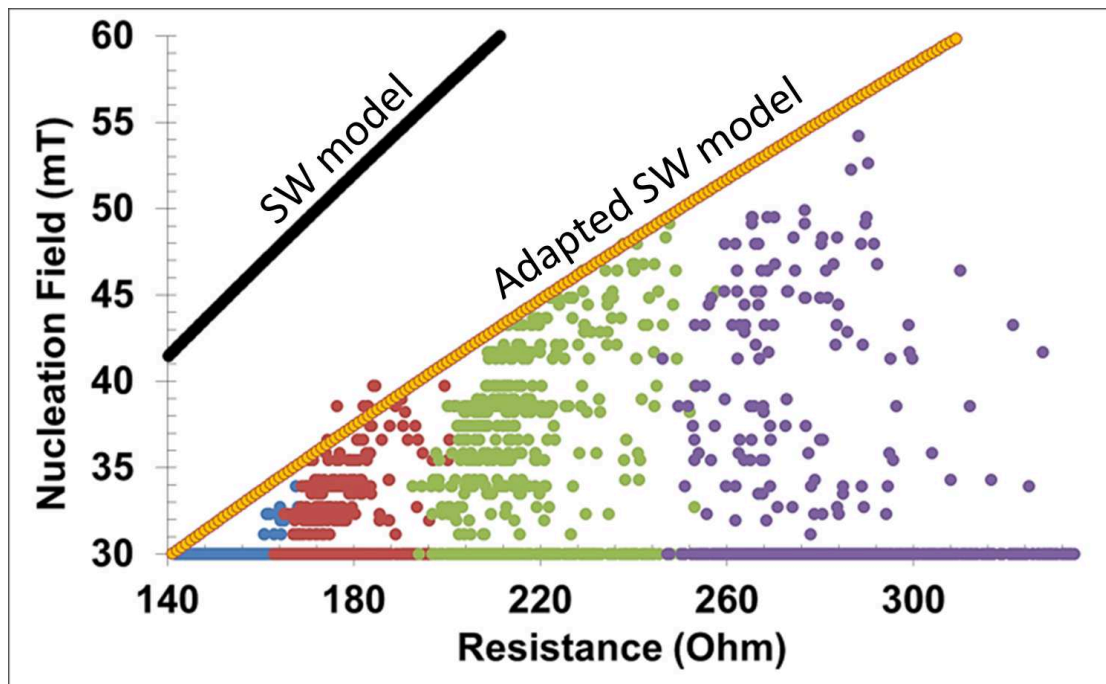


FIGURE 4.10: Nucleation field of the device as a function of the resistance. The different nominal widths are represented by different colors: 350 nm (blue), 300 nm (red), 250 nm (green) and 200 nm (purple). Adaptation from (14).

Consequently, the devices for which it is the case are discarded at the first step of the bisection method. These devices are probably correctly working but with an operating window outside of the desired one. Similarly, the 200 nm width device distribution also exhibit few data points possibly because the depinning field limit is higher than 30 mT, thus failing the first step of the bisection method. Despite the latter, the nucleation field values are observed to lie below the adapted model. Furthermore, we note that the resistance is always higher than the one expected from the nominal width. The latter is a confirmation that the measured width with the SEM is probably not the effective electrical width contributing to the magnetic and electrical signal and that most of the sides are covered with redeposited material thus generating an effectively larger topographical width.

Note that taking into account the multilayer nature of the GMR stack by calculating the resistance using the Fuchs-Sondheimer model (140, 141) does not significantly change the values as the conduction is dominated by the thick $\text{Ni}_{81}\text{Fe}_{19}$ free layer, which carries most of the electrical current. The limit shown by the adapted Stoner-Wohlfarth model demonstrates the impossibility for our current architecture (3-vertices corners and 16 loops) to reach the ideal Stoner-Wohlfarth model behavior. The latter is probably due to the long length of the structure and thus a large number of chances for a defect. Furthermore, the process does not yield a perfect cross-sectional shape, which can also induce some variability in the shape anisotropy and consequently the SW model. The model is expected to work for an infinitely long wire with a perfectly rectangular cross-section and no edge roughness. The fitting constant of 0.7 sets the maximum average nucleation field obtainable for these industrially produced devices in these geometries. These results are of primary importance for applications because a simple resistance measurement allows for the identification of a non-working device. As an example, if the requirements are that devices should not exhibit a nucleation field lower than 40 mT then any device with a resistance below 200 Ω can be discarded. These results provide a tremendous gain of time since the measurement duration for the characterization of a single device can be 1 minute.

4.5 Conclusion

To conclude the chapter, we have determined the critical fields for sensor operation based on DW propagation allowing us to gauge the limitations of the functioning of the devices. We find that both the materials and the geometry play a key role. Firstly, the origin of the geometrical dependence of the depinning field limit is difficult to pinpoint because a variety of factors contribute to the variation in depinning field limits and these are hard to characterize and quantify precisely. Compared to $\text{Ni}_{81}\text{Fe}_{19}$, the $\text{Co}_{90}\text{Fe}_{10}$ samples yield a drastically increased depinning field limit. This effect is attributed to the enhanced magnetocrystalline anisotropy in each crystallite compared to $\text{Ni}_{81}\text{Fe}_{19}$. For the nucleation field, the dependence on the geometry exhibits a geometrical scaling of the form that one expects if the shape anisotropy dominates. It can be described by an adapted Stoner-Wohlfarth model, despite the simulation not showing a coherent rotation of the magnetization in the complete stripe. However, the nucleation event exhibit a Stoner-Wohlfarth like scaling. Thus the nucleation field geometry dependence provides a handle for the improvement of magnetic DW sensors. For all the measured materials, the maximum expected nucleation value could be fitted by a corrected uniaxial anisotropy rectified by a constant accounting for the processing, the angle segmentation, and the geometrical scale. A measurement of a large number of devices is performed to allow for an accurate assessment of the fitting constant used for the MOKE measurement results. We can ascertain a definite limit by the previously mentioned maximum nucleation field value and find that this is related to the resistance of the sensor. This limit can be used as a tool for future fast analysis of magnetic sensors.

Chapter 5

Prospect for the improvement of the FOW of open-loop structures

Part of the chapter has been published in (14, 16). In the previous chapter, we described the field operating window (FOW) of an open-16-loop multiturn counter sensor device. The depinning or propagation field and the nucleation field generating failure to the operation of the sensor device are the two boundaries of this FOW. To provide a wide range of applications of the sensor device, we aim at the enlargement of the FOW, thus yielding a versatility of the operating field value and high reliability of the component.

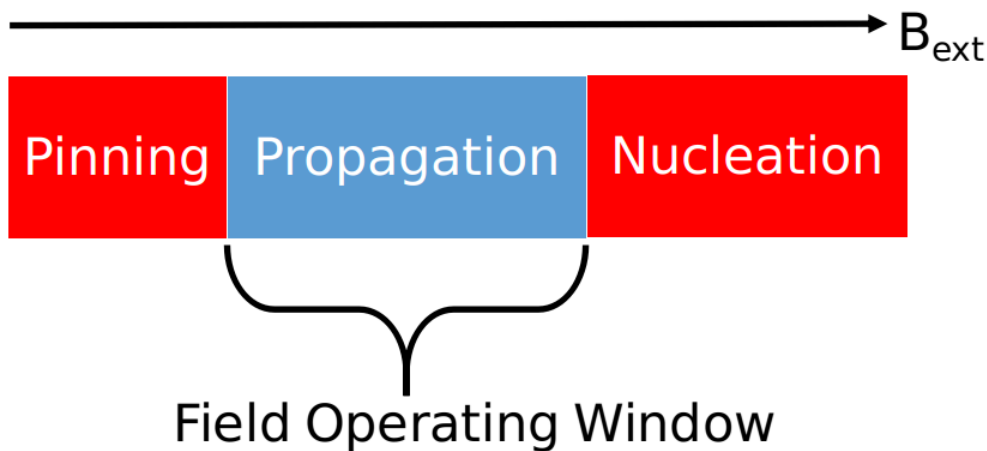


FIGURE 5.1: Scale showing the position of the field operating window in the propagation region of magnetic domain walls. The black arrow represents the applied field intensity scale of \vec{B}_{ext} .

From previously exposed results, we derived that the depinning field is difficult to understand since the effects leading to the pinning of a DW originate from local defects or local variations of the magneto-crystalline anisotropy. Detrimentally, these features are cumbersome to characterize for large structures such as the open-16-loop device. This difficulty is inherent to the limitations of the characterization techniques available. In fact, a scanning electron microscope and an atomic force microscope can resolve features in the range of a few nanometers but on a $1 \mu\text{m} \times 1 \mu\text{m}$ area. The imaging of a millimeters long structure with

the same resolution detail is impossible. In contrast, the nucleation field being mainly cross-sectional dependent provides a more practical handle for the improvement of the FOW. Its investigation is also potentially more accessible since solely imaging the cross-section of a single location on the device can already provide a significant amount of information on the expected nucleation field.

In this chapter, we first probe the depinning field and nucleation field of portions of open-16-loop devices with the MOKE microscope under a uniaxial applied field. From the results, we derive the uniformity of the patterning within a device, within devices and a sample. The obtained results call for improving the consistency of processing for the augmentation of the production yield. We then describe innovative designs created to replace the original open-16-loop device for faster investigation of modifications to the geometry of the structure and its cross-section. The influence of the alterations to the original design is then studied regarding the depinning/propagation field and nucleation field. From the obtained results, we identify the best structure for the investigation of the FOW. With these designs, we compare depinning-field distributions obtained with a large number of counted turns on a few devices opposed to distributions measured for a small number of turns for a significant amount of devices. After the investigation of the propagation field, we focus on the nucleation field. To test this limit, we apply changes such as increase of the thickness, or variation from a trapezoidal cross-sectional shape to a rectangular cross-sectional shape. Further on, the deposition conditions of the $\text{Ni}_{81}\text{Fe}_{19}$ are varied by selecting different sputtering systems, and the patterning method is also changed to ascertain if better-defined structures are obtainable via different lithography methods. These investigations, finally, yield explanations for the dependences of the nucleation fields and provide with a practical way to improve the field operating window.

5.0.1 Influence of the spatial spread over a wafer

The field operating window is expected to change with variations from device to device induced by a spatial nonuniformity of the processing methods. The two field limits, constituting the operating window, are compared within a device and then between devices to extract their spatial distributions. We then measure the depinning field and nucleation field of half loops of open-16-loop in a uniaxial field configuration (see Fig. 5.2 (a)) allowing to extract the influence of portions of the structure.

Nucleation field in a uniaxial applied field

We measured three spatially separated open-16-loop devices from the same wafer composed of a GMR stack with a free layer of 32 nm of $\text{Ni}_{81}\text{Fe}_{19}$. The experiment is carried out with the MOKE setup. A reference to the applied field direction is provided by positioning the wires of the device parallel to the sides of the camera

of the microscope's field of view (black rectangle in Fig. 5.2 (a)). For the measurement of the nucleation field, the initial magnetic configuration is obtained by applying a magnetic field of 80 mT opposite to the direction indicated by the black arrow in Fig. 5.2 (a). The field is then reduced to 0 mT, and the magnetization relaxes in the state shown in Fig. 5.2 (a). In this picture, the DWs are represented by the red ovals. This state constitutes the initial magnetization state. The field is then increased in steps of 1 mT in the direction shown by the black arrow, and due to the small torque applied by the external field on the DW, we expect to detect a nucleation event in the wires. The nucleation of the DWs is then followed by the propagation that reverses the current magnetization direction resulting in a contrast observable in the microscope. If in fact, a nucleation event occurs, we expect it to be located in the position indicated by the black circles in Fig. 5.2 (a). These locations for the nucleation are expected from the Stoner-Wohlfarth model (34) describing the lowest coercivity for a 135° -angle between the magnetization and the applied field. In real conditions, only the location with the lowest anisotropy of the four will experience the first nucleation followed by domain wall propagation. During the experiment, we retrieve the particular nucleation field value of every wire within the microscope's field of view.

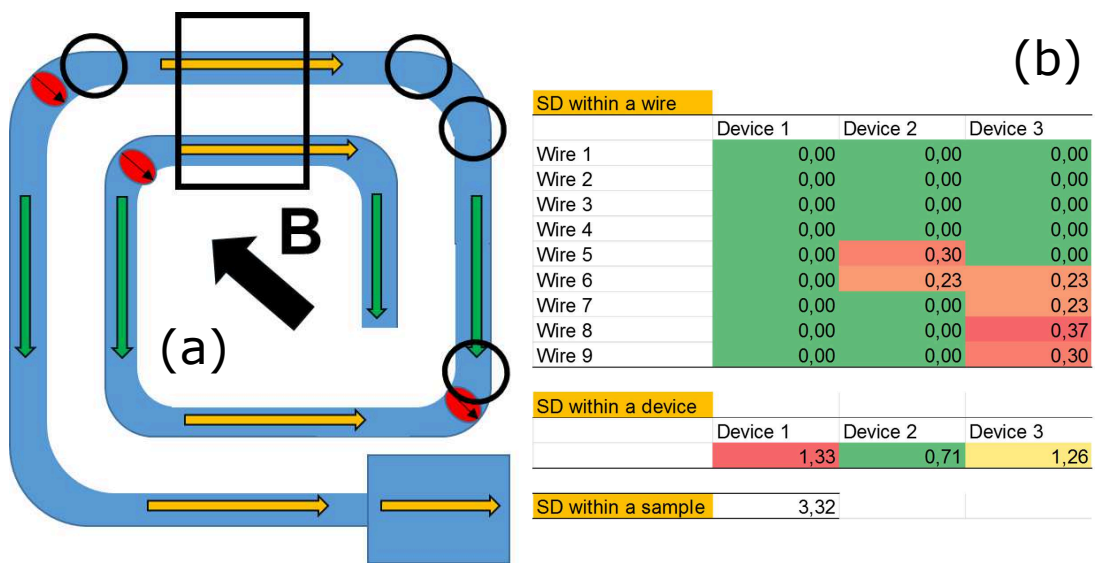


FIGURE 5.2: (a) Schematic representation of the measurement of the nucleation field limit with a uniaxial field configuration. The black arrow represents the applied field B . The black rectangle displays the position of the microscope's field of view, and the black circles are the expected position of nucleation of DWs for the half upper right loop. The magnetic configuration is the initial one. (b) Table regrouping the standard deviations (SD) of the gaussian distribution of the nucleation fields acquired in a uniaxial field configuration. The color code highlights the lowest to the largest standard deviation with a color scale ranging from green to red, respectively.

The present measurement is repeated 10 times for 9 wires of the same device.

From the obtained distributions, we extract the mean value and the standard deviation for each wire, then each device and finally for each sample. In Fig. 5.2 (b), a table references the mentioned standard deviations (SD). For single wires, the standard deviations are in 70 % of the cases equal to 0 limited by the field resolution and the number of measurements, and in the rest of the cases, it is not larger than 0.37 for a mean nucleation field limit close to 65 mT in all cases. These small standard deviations indicate the reliability of the nucleation field limit within a single wire over 10 measurements. The distribution of nucleation fields within the devices is obtained by summing the distribution of the nucleation fields measured in the individual wires. For this distribution, the standard deviations are more substantial than for the individual wires. Indeed, the devices n° 1, 2 and 3 exhibit respective SDs: 1.33, 0.71 and 1.26. These enhanced values indicate that the distribution enlarges. Finally, the distribution of nucleation field limits for a sample is generated from the summation of the distributions of all devices. The standard deviation of the sample is larger than the standard deviations for the devices indicating that variations between devices are more significant than within the devices. This result demonstrates that the variances in the distribution of the nucleation field limits built from measurements on different devices are originating from a characteristic more uniform within the device than in between devices. We know that with our processing techniques, the lateral accuracy of the patterning techniques (photolithography) is lower than the vertical one (sputtering). The characteristic change between devices is most probably primarily the width of the wires. The resistance of the devices is measured across the wafer to check the previous observations. During the lithography process, the intensity of the illumination originating from the UV lamp is varied from the top to the bottom of the wafer. We remind that the lithography machine is a stepper thus exposing the wafer in areas called flash-fields. One of these is highlighted by a black rectangle in Fig. 5.3. We note that within a flash-field, there are already variations of the resistance. We deduce that the larger resistance in the center of the flash-field is attributable to a stronger intensity of the light at this position yielding a lower wire width of the devices. This effect is even further enhanced as the intensity of the flash is increased. A spiraling pattern is as well observable starting from the center of the wafer and pursuing to the outer top of the wafer. This pattern results in highly resistive elements that are created by the chemical etching of the developer reducing the resist for a too long time. In fact, during the development process, the wafer is rotated, and the liquid is poured from the center thus remaining a longer time in the spiraling area and reducing the width of the structures. From these results, we conclude that the reproducibility of the nucleation fields is achievable for improved uniformity of the patterning process across the wafer.

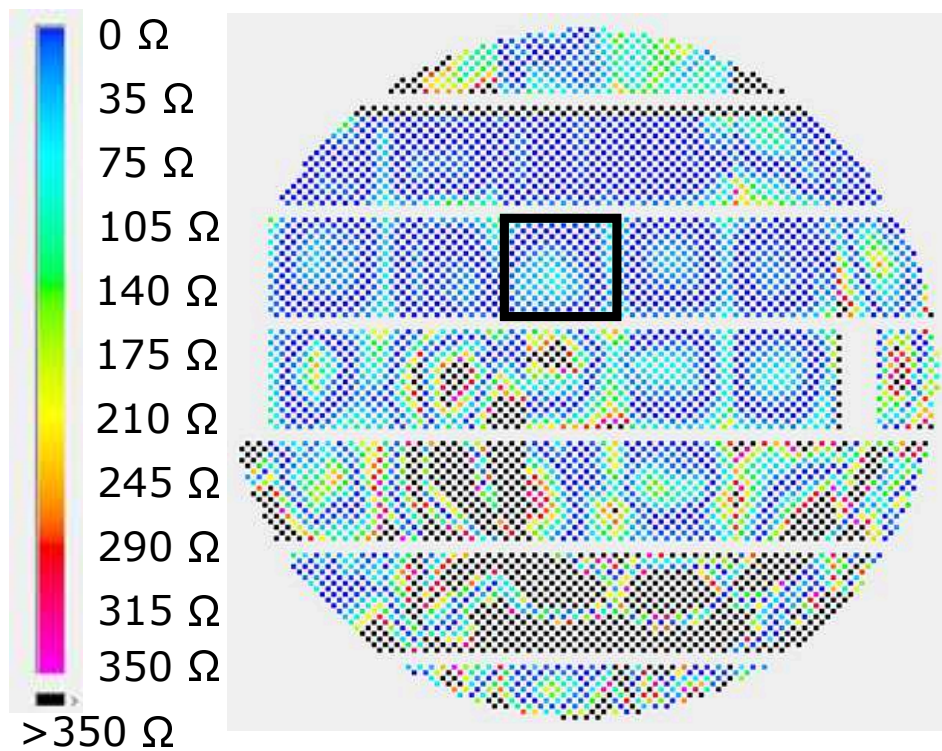


FIGURE 5.3: Spatial distribution of the resistance of open-16-loop devices across a wafer with varying exposition intensity from top to bottom. The rectangle indicates the area of a flash-field. On the left side, a color scale is provided, which shows the resistance values.

Depinning field in a uniaxial applied field

In a rotating field measurement configuration, the domain wall starts propagating at the lowest depinning field of the section where it is positioned. As it propagates through the structure, the DW is sampling the lowest depinning field of every part of the structure. The highest of these is the depinning field presented in chapter 4. In contrast, the depinning/propagation field limit can as well be investigated in a uniaxial configuration. In the present measurement, the initial magnetic configuration is the same as for the nucleation experiment, and it is also obtained similarly. The difference lies in the direction of the applied field. The magnetic field is increased in steps of 1 mT horizontally in the direction indicated by the black arrow to promote the DW depinning from the corner. In this case, due to the structure geometry (low number of vertices in the corners) and the position of the DW, the measured depinning field is dominated by the depinning from the section where the DW sits. Furthermore, it is not the lowest depinning field for this particular section (see details in (16)). The latter does not hinder the comparison of the depinning field from various devices.

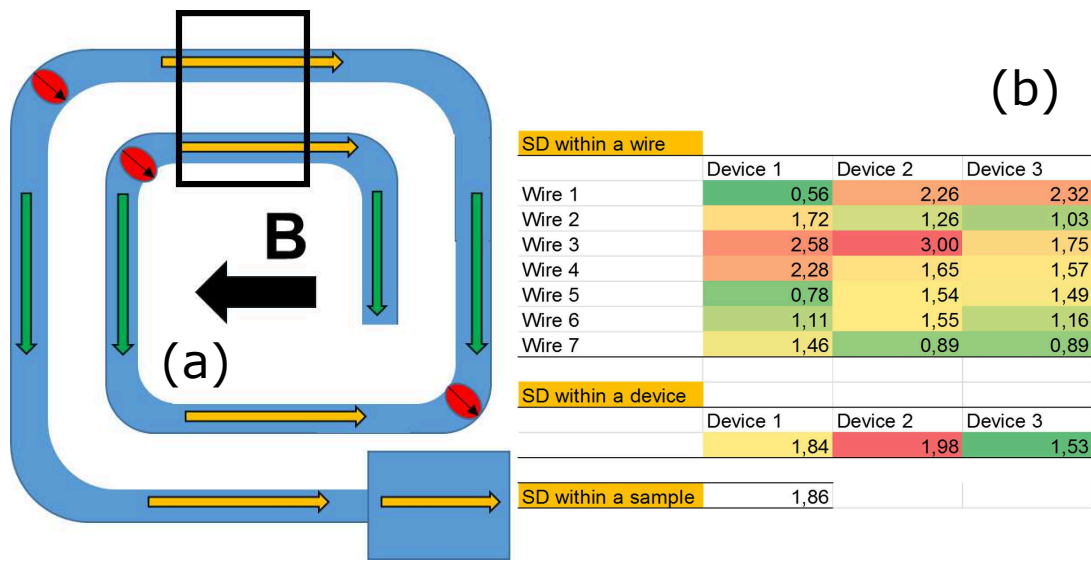


FIGURE 5.4: (a) Schematic representation of the measurement of the depinning/propagation field limit with a uniaxial field configuration. The black arrow represents the applied field B . The black rectangle displays the position of the microscope's field of view. (b) Table regrouping the standard deviations of the gaussian distribution of the depinning/propagation fields acquired in a uniaxial field configuration. The color code highlights the lowest to the largest standard deviation with a color scale ranging from green to red, respectively.

Interestingly, as compared to the nucleation field, the standard deviations for the individual wires are as significant as the deviations observed between devices (Fig. 5.4). The latter information describes that the distribution of pinning is the same within a device as compared to in between devices, indicating that the mean values of the distributions are grouped around the average depinning field of the sample. To summarize the considerable spatial variability of the nucleation field indicates a sensitivity to the uniformity of the patterning process across the wafer. In opposition, the depinning field is seemingly not affected by width variations across the wafer but by the local homogeneity of a wire.

5.1 The creation of innovative designs for an improvement of the FOW

The standard open-16-loop structure is composed of 3-vertices corners and 16.5 loops of magnetic material, the half loop containing the nucleation pad at the outer end of the structure (see Fig. 5.5 (d)). These type of structures are manufactured at the company Sensitec with the process described in chapter 3. In this process, the nanopatterning is realized with a photolithography stepper machine, which has the advantage of being fast thus suitable for mass-production.

However, an inherent issue with this photolithography process is the requirement of an expensive mask to transfer the designs to the resist. During a mass-production, the same design for one product is duplicated in a matrix that covers the whole surface of the mask. This 2D map is usually drawn in a tungsten layer on top of a glass mask. An industrial mass-production process line is then intentionally not adapted for the experimentation on innovative shapes for the structures as it is optimized for a massive throughput. For a research product such as the open-loop structure, a mask with 4 different widths was already present at the company at the beginning of the project. The latter is still very limited, and it was concluded that to conduct a more precise and faster investigation of the open-loop structure, a new mask with more variations to the original design needed to be manufactured. These designs can be found in the appendix J.

5.1.1 Modifications to the original open-16-loop device

The first significant change that we performed consisted in the reduction of the number of investigated loops. One of the primary constraints of the 16 loops is the time required for the investigation of the field limits. In fact, with a field rotation speed of 0.5 turns per second, it takes 17 seconds to make 17 full clockwise and 17 full counter-clockwise rotations (34 turn rotation sequence), which is a standard rotation sequence. For the measurement of only 2 field strength values, it requires $0.5 \times 17 \times 2 \times 2 = 34$ seconds per element. The reduction of the number of loops straightforwardly dramatically reduces this measurement time thus allowing to measure the field rotation sequence for a whole field range (e.g., from 5 mT to 80 mT) in a reasonable amount of time. A second modification is applied to the length of the loop, which is shrunk from 4 outer sides \times 400 μm to 4 outer sides \times 200 μm . This reduction of the area covered by an element permits to put 5 open-2-loop elements in the same footprint as 1 open-16-loop element (see Fig. 5.5 (a, b and c) for the innovative design and (d) for the original design). With this modification, 5 structures are simultaneously measured for the same rotation sequence rendering the testing 5 times faster. A disadvantage of the new elements as compared to the original one is the reduction of the probability to detect all defects because of the shorter investigated length. The innovative designs are also less covered by the Au connection layer. In the original design, close to 1/2 of the structure was covered with Au connections, which might be inducing stresses to the underlying magnetic layers potentially rendering the investigation of the field operating window more cumbersome. The measurement card to contact the sensor elements and the outer electronic is kept the same as for the open-16-loop, and only the measurement pins are changed. The same voltage is applied in between the V_{cc} and GND as in the case of the original scheme. Furthermore, the contacting layer of the innovative structures is designed in such a way that minimal modifications needed to be performed to the measurement setup. Finally, the pinning direction of the SAF (see section 3.1.1) was rotated by 90° in the new elements, which is inconsequential. So far the changes brought to the original design aim at a faster investigation of the open-loop structure. We as well require

an investigation of a broader range of wire widths to confirm the expected hyperbolic behavior of the nucleation field exposed in chapter 4. Different open-2-loop devices are then produced with a width varying from 200 nm to 1000 nm. The length of the structure is also varied from 4 outer sides \times 200 μm to 4 outer sides \times 800 μm to determine the influence of a more extended structure.

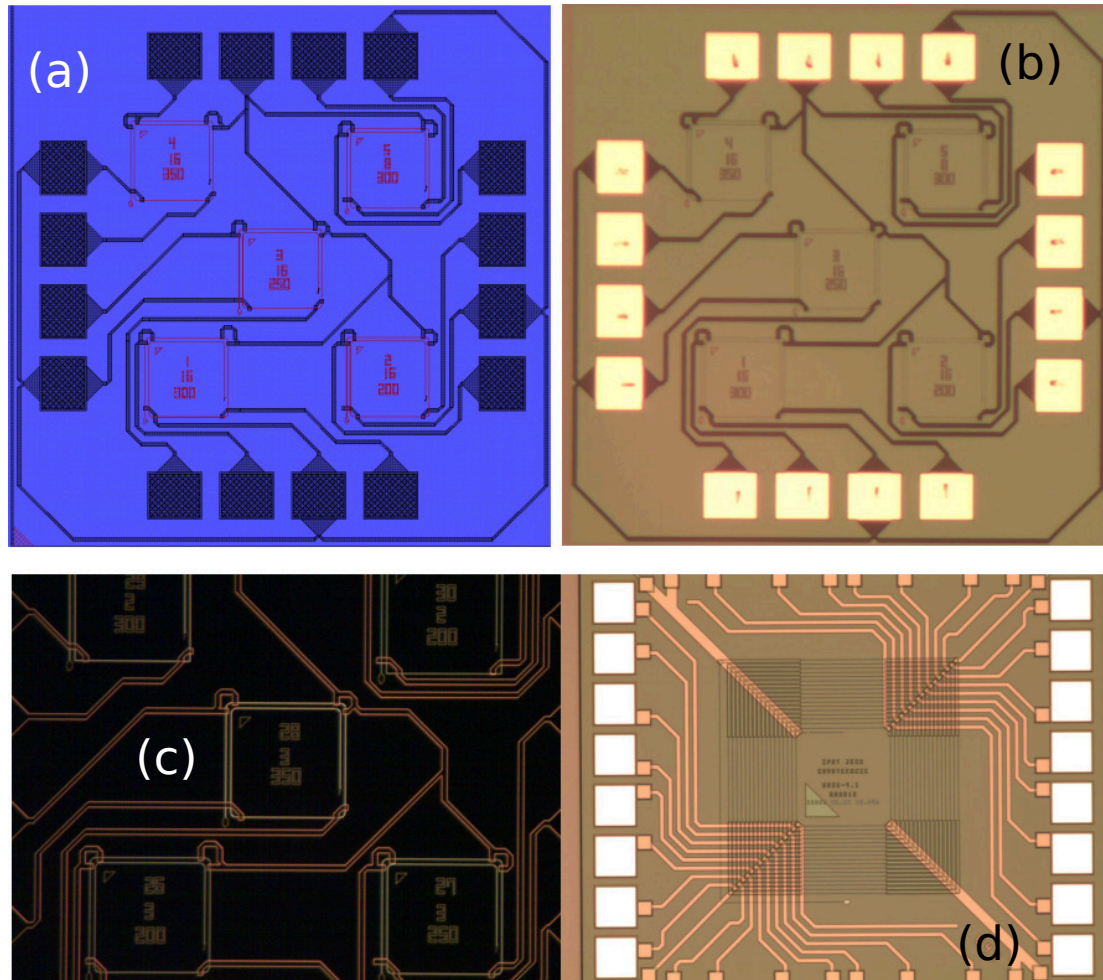


FIGURE 5.5: (a) Drawing of the innovative designs with electrical connections. The red color represents the patterned magnetic material, and the black designs represent the electrical connections. Here, 5 elements are represented with an inscription patterned in the magnetic layer to allow for a quicker identification of the measured element. (b) Optical microscopy image of the realized design shown in (a). In this microscope image, the barely visible wires are made of a GMR stack with a free layer of $\text{Ni}_{81}\text{Fe}_{19}$ represented in orange in (a). The bright yellow and the dark brown structures are the electrical connections made of Au. (c) Zoom in one of the new structures. The image is taken in a dark field configuration with an optical microscope. The yellow color, in this case, is the GMR stack and the orange color represent the electrical connections. (d) Microscopy image of the original concept. As in (b), the grey wires are the GMR stack with a free layer of $\text{Ni}_{81}\text{Fe}_{19}$, and the orange and white regions represent the electrical connections.

Some modifications are performed to the corners of the original design. The original corner is composed of 3 vertices, thus rotating a wire from 0° to 90° in steps of 22.5° . This corner shape is varied from 0 to 16 vertices to observe the influence of the change in the anisotropy due to the segments. Finally, the wire width is modulated along the length of the wire. A sinusoidal pattern is drawn on the edges of the wire. The wavelength of the sinusoid is varied as well. This pattern is investigated as it was demonstrated that the Walker breakdown could be suppressed in the case of periodic variation of the width (142). An exhaustive list and pictures of the innovative designs can be found in the appendix J. In this subsection, we describe the influence on the depinning and nucleation field limits of the changes made to the original design of the open-16-loop structure.

5.1.2 Influence of the length of the wire

In the open-loop structures, a single wire is patterned and looped. Its length can reach up to 31 mm in the case of the open-16-loop structure constituting a vast nanostructure. It is then of interest to obtain the influence of this length on the FOW. From a simple picture, the expectations are that measuring different lengths of magnetic wires will increase the depinning field as well as decrease the nucleation field, only due to a higher probability to encounter a defect resulting in a failure event. In order to observe such effect, the distributions of the nucleation fields of some of the already measured samples are plotted. We then represent the distributions of the nucleation field limit values obtained with the uniaxial field configuration with open-16-loop devices, and with a rotating field configuration with open-16-loop devices (left and middle column in Fig. 5.6). In the subsection 5.0.1 only the 200 nm nominal width is investigated, here we measured 4 various nominal widths, i.e. ,200 ,250 ,300 and 350 nm. In Fig. 5.6 in the left column, the distribution of the nucleation field obtained in the uniaxial configuration for different nominal wire widths are plotted (200 nm (purple), 250 nm (blue), 300 nm (green), and 350 nm (orange)). The distributions appear Gaussian and exhibit an enlargement of the standard deviation and an increase of the mean value with a decrease of the width. We then plot the distribution of the nucleation field for the devices measured in the GMR section of the chapter 4 (see Fig. 5.6 middle column). These devices were measured under a 2-17 turns rotating applied field sequence. The exact nucleation field plotted in the histograms of Fig. 5.6 (middle column) are obtained with the use of a bisection method with 30 mT of applied field as the starting bottom boundary. This limit is selected to ensure that our tested field value is larger than the depinning field allowing us to probe the nucleation field. The obvious drawback of this selection is that no nucleation field limit lower than 30 mT can be detected as seen by the absence of data below 30 mT in the middle histograms. For 200, 250, 300 and 350 nm widths, the percentage of devices with a depinning field limit lower than 30 mT and a nucleation field higher than 30 mT (passing the 30 mT test) are 4.6 %, 41.6 %, 57.6 %, and 22.2 %, respectively. Failures to the 30 mT test can be due to defective devices, or a propagation field larger than 30 mT (mainly for 200 nm width devices), or a nucleation field lower than 30 mT (mostly in the case of 350 nm width devices),

thus explaining the small number of devices successfully passing the bisection method for 200 nm and 350 nm. For open-16-loop devices, the loss of a part of the Gaussian distribution is unavoidable because to keep the measurement time low, the bisection method needs to be used, and a starting bottom boundary of the tested field window needs to be selected.

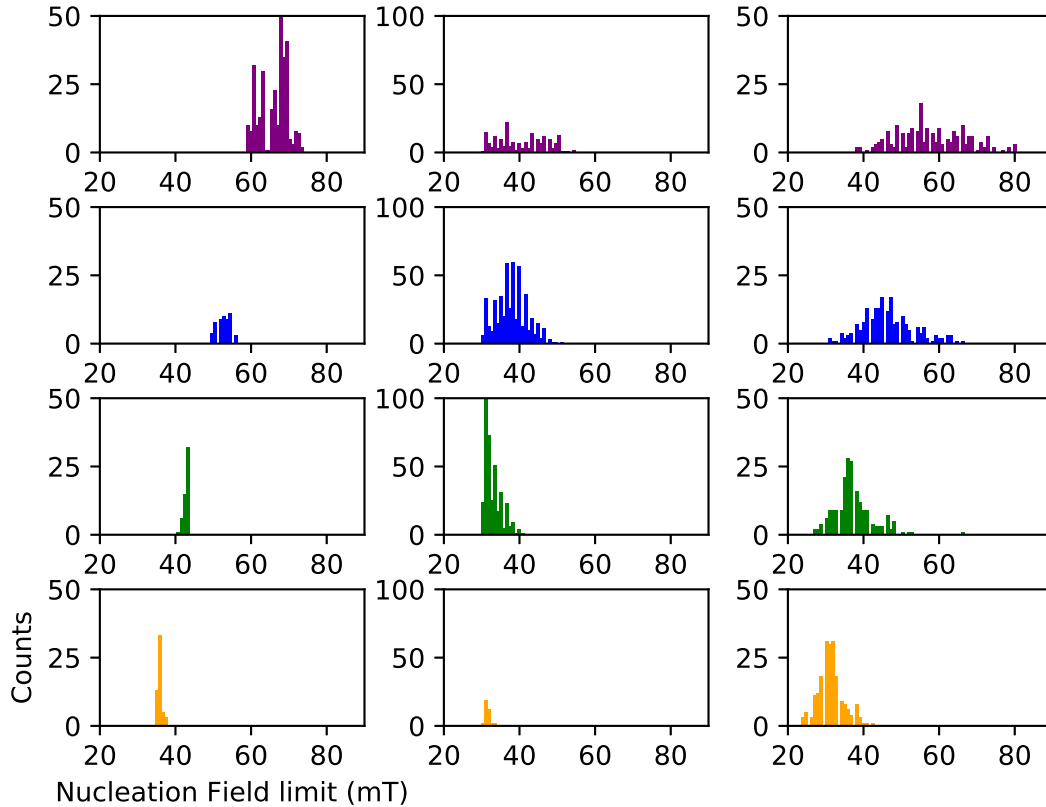


FIGURE 5.6: Histograms of the nucleation fields for GMR stack samples with a free layer of 32 nm of $\text{Ni}_{81}\text{Fe}_{19}$ for left and middle column and 30 nm of $\text{Ni}_{81}\text{Fe}_{19}$ for the right column data. The 200, 250, 300 and 350 nm wire widths are represented by the purple, blue, green and orange colors, respectively. The left column shows distributions obtained with a uniaxial field configuration on open-16-loop structures acquired with a MOKE microscope. The middle column shows histograms constructed from the distribution of the data represented in the GMR section of chapter 4. The nucleation fields are acquired via GMR measurement under a rotating field. The right-column data show the histograms of the nucleation field acquired with a GMR measurement in a rotating field for the open-2-loop design with 3-vertices corners. All the labels are similar to the ones shown at the bottom right.

Finally, we show the distribution of the nucleation field obtained with the innovative design of the open-2-loop in the right column of Fig. 5.6. The rotation sequence is 3 full rotations clockwise and 3 full rotations counter-clockwise (2-3 turns rotating applied field sequence). With the lower amount of loops on the device, we are able to measure the rotation sequence every 2 mT of magnetic

field strength. The latter is then less precise than the bisection method, which can provide a nucleation field with a 1 mT precision. Nevertheless, measuring a complete range of field has the advantage of not requiring a lower boundary for a tested field window, which as we have seen might yield an incomplete distribution. From the histograms in the right column, we retrieve a Gaussian distribution. The distribution obtained with uniaxial field value only represents the nucleation field of a very tiny portion of the device. Indeed, we just probe the entrance of the corners as compared with the open-16-loop and the open-2-loop devices, which are measured in a rotating field. In the rotating field measurement, the whole length of the open-loop structure is probed yielding the lowest nucleation field for the entire structure. We focus on the 250 nm width distributions (blue) as the Gaussian profile is well defined even for the measurement of the open-16-loop devices. The mean value of the Gaussian distribution in the uniaxial measurement configuration is 55 mT as compared to 45 mT for the open-2-loop and 37 mT for the open-16-loop. We observe that the mean value of the Gaussian distributions is correlated to the probed length. Thus the nucleation field of a structure is expected to reduce as the length of the device is increasing.

Various length of open-2-loop devices

To demonstrate the latter, two different sizes of the open-2-loop designs are investigated. The first one is the standard 4 outer sides \times 200 μm and the second is 4 outer sides \times 800 μm . The two lengths are investigated under the 2-3 turns rotation sequence, i.e., 3 full turns clockwise and 3 turns counter-clockwise. This sequence is tested every 2 mT starting from 1 mT up to 79 mT. From the results in Fig. 5.6 in the right column, the apparent Gaussian distribution allows us to display the results of the measurement performed on open-2-loop structures with the mean value and the standard deviation of the distribution. In Fig. 5.7, we observe the similar behavior as shown in Fig. 5.6 namely a reduction of the mean value of the distribution of the nucleation field with an increase of the length of the structure. The depinning/propagation field is also plotted, and in that case, a slight increase of the mean value is observable. The distribution is also widening, and more pinning events at higher field values are occurring. From the previous results, we conclude that the length of the devices needs to be kept as small as possible to enable the reliability of the sensor device. The latter finding is detrimental to the scaling of the device since every added loop yielding one more sensed turn will also reduce the field operating window. The 40 open-loop sensor currently in development is probably suffering from an even more reduced field operating window. For this device, we can speculate that the standard deviation from the nucleation and the propagation field are overlapping resulting in a difficulty to prove the reliability of the concept.

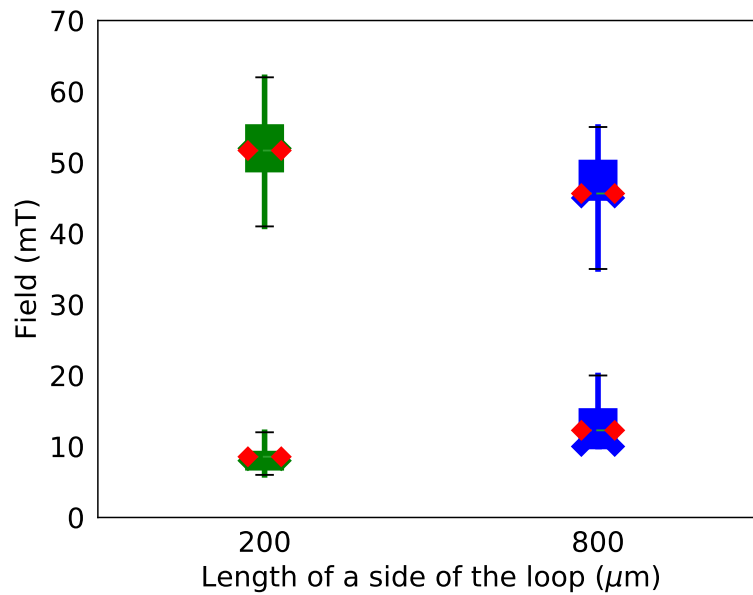


FIGURE 5.7: Box and Whisker plot presenting the comparison between open-2-loop devices with different length of loops. The boxes associated with the data points in the plot represent 25% (first quartile) to 75% (third quartile) of the distribution. The whiskers or dashed lines represent 5% to 25% and 75% to 95%. Red diamonds represent the mean value.

5.1.3 Influence of the reduction of the number of vertices in the corners

In the original design, the structure is composed of 3-vertices corners. In our recent work (16), we showed that the corners influence the propagation field limit of the DW due to the different directions of the segments with the applied field (16). In the present subsection, for the measurement of the open-2-loop structures, the field is rotated. Thus the different directions are expected to yield little difference for the depinning/propagation field. Furthermore, the increased width at the merging point of the segments is only of a few nanometers for a 200 nm nominal width. This slightly increased width is then not expected to reduce the nucleation field or increase the depinning field since few nanometers variation of the width is in the range of the changes already present due to the side edge roughness of the wires. To investigate the influence of the segmentation of the corners, we use a sample composed of a GMR stack with a free layer of 30 nm of $\text{Ni}_{81}\text{Fe}_{19}$. The designs that we utilize are the open-2-loop devices with a varied number of segments constituting the corners. After manufacturing the devices with the standard process of Sensitec (details, see chapter 3), they are measured with the GMR setup under a 2-3 turns rotation sequence. For the structures possessing corners with 0, 3 and 4-vertices, the field is increased in steps of 2 mT starting from 1 mT. For the 5, 6, 7, 8 and 16-vertices corners, the field was increased in steps of 5 mT due to time constraints. Furthermore, the most significant effects are observed for the 0, 3 and 4-vertices corners, which justify the choice.

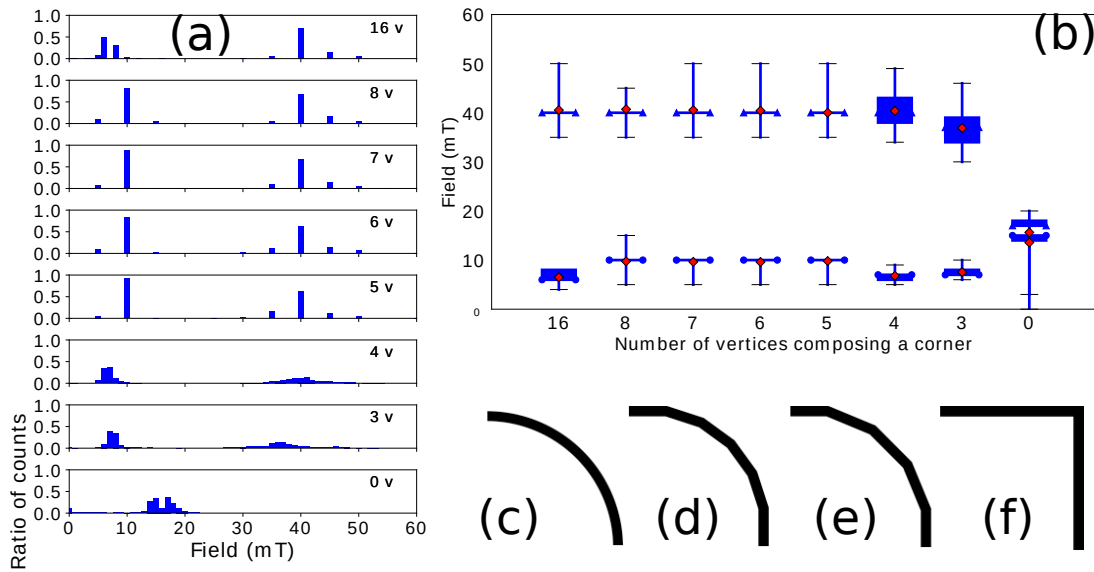


FIGURE 5.8: (a) Histogram of the depinning/propagation field at low field values and the nucleation field at larger field values for the 16 to 0 vertices. The number of vertices is decreased from top to bottom. (b) Box and Whisker plot represents the comparison between the different number of vertices present in the corners. The boxes associated with the data points in the plot represent 25% (first quartile) to 75% (third quartile) of the distribution. The whiskers or dashed lines represent 5% to 25% and 75% to 95%. (c) Schematic representation of a 16-vertices corner. (d) Schematic representation of a 4-vertices corner. (e) Schematic representation of a 3-vertices corner. (f) Schematic representation of a 0-vertices corner.

In Fig. 5.8, we observe a reduction of the mean value of the nucleation field for a lower number of vertices than 4. The depinning field appears unaffected up to the 0-vertices corner. In the case of the 0-vertices, the looping structure is directly square; the corner has 0 radii. For these elements, the field operating window is lost due to an increase of the depinning field and a decrease of the nucleation field.

Simulation of the nucleation for various vertices

In order to understand, this behavior we simulated structures that resemble the different devices. The 16, 3 and 0-vertices corners are represented by a circle, a hexadecagon, and a square, respectively. In the simulation, the initial state of the magnetization is a vortex state as it can be seen in Fig. 5.9. A magnetic field is applied along the direction indicated by the blue arrow following an increase of the form $1 - \exp(t/(4 \cdot 10^{-9}))$; the simulations are then run for 20 ns. A snapshot of the magnetization is taken every 10^{-11} s, and the nucleation is identified as a drastic local change of the magnetization direction. Practically, it is observable by a drastic change of the color as seen in Fig. 5.9. The identified nucleation fields are plotted alongside the experimental data in Fig. 5.9.

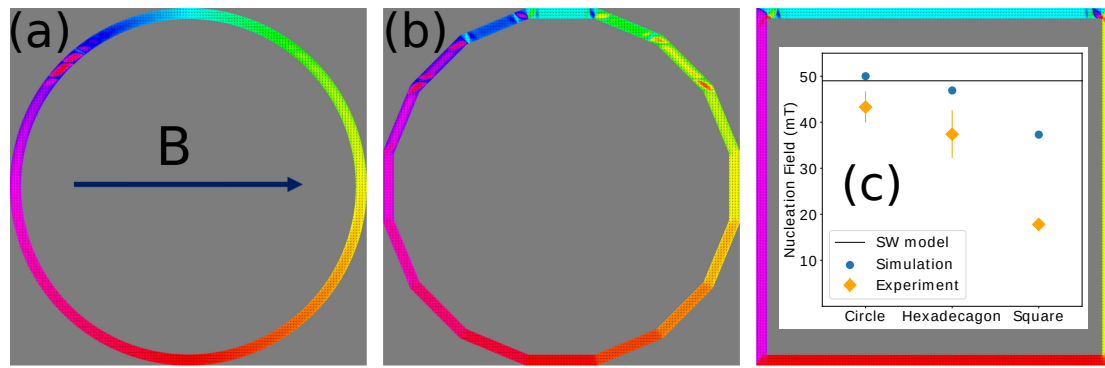


FIGURE 5.9: Snapshot of the magnetization right at the point of nucleation in the structure. The blue arrow indicates the applied field direction. The different simulated structures are (a) a circle of $15 \mu\text{m}$ diameter, (b) a hexadecagon of $15 \mu\text{m}$ diameter and (c) a square of $15 \mu\text{m}$ side length. In the square area is a plot of the nucleation fields obtained with simulations for the different presented structures. In the same plot, the experimental nucleation field of the structures with the 16, 3 and 0-vertices corners are presented with the circle, hexadecagon, and square, respectively.

The simulation results follow the same trend as the experimental data, namely as the number of segments decreases nucleation field as well does. We also note that in the simulations, the location of nucleation for the segmented structures is not always located at the point where the angle between the magnetization and the applied field is 135° , which is expected from the SW model. For the circle structure, it is the case, but for the 3 and 0-vertices structures, the nucleation is located at the merger of two following vertices closest to the 135° angle configuration. This observation already indicates that the use of segments decreases the shape anisotropy at the merger location being detrimental for a large nucleation field. However, the simulated nucleation field value is still very close to the expected nucleation field extracted from the Stoner-Wohlfarth model (black line in Fig. 5.9), thus not revealing the reason for the significant decrease of the nucleation field limit for the 0-vertices corner structures.

Structure characterization

We then perform scanning electron microscope micrographs of the 0-vertices structures to observe the shape of the wires. The micrograph is obtained under a 30° angle between the electron beam and the sample's surface normal. We find a substantial increase in the width at the corner position as seen in Fig. 5.10.

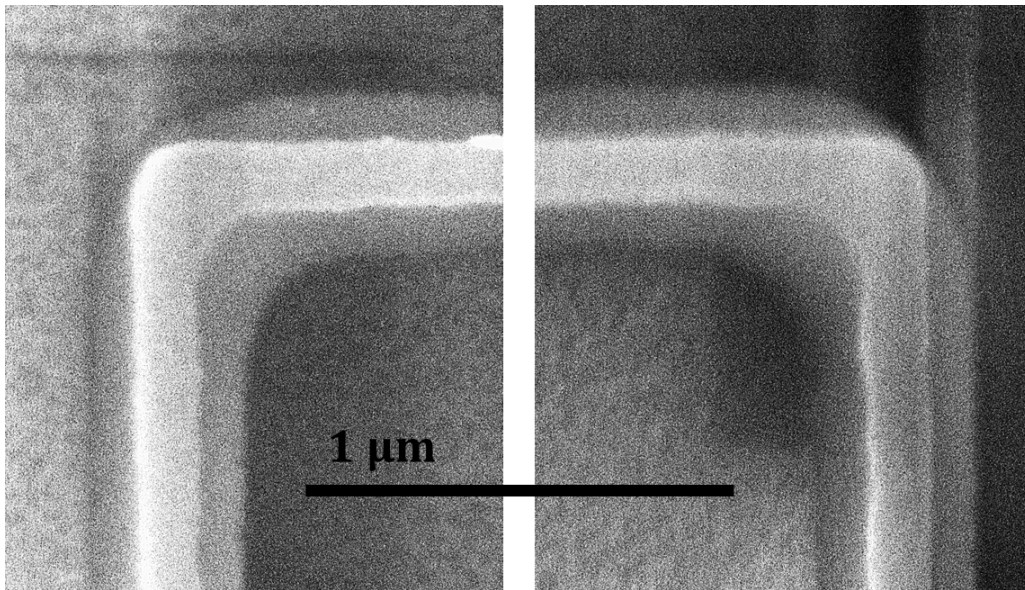


FIGURE 5.10: Scanning electron microscopy micrograph of two corners of a 0-vertices structure. The micrograph is obtained by tilting the sample and positioning the electron beam at 30° with the surface normal. This procedure allows acquiring scans that show more details of the side edges of the wires.

The severe increase in width is attributed to shadowing effects occurring during the etching of the material stack combined with proximity effects. The shadowing effects (143) arise from the fact that the etching is performed at an angle with the surface normal. Indeed, the thick resist projects a shadow in the direction of the beam preventing the etching in the shaded area. As the sample rotates during the etching process, both close sides of the wires are etched at a different rate, while the further sides are etched simultaneously. This effect results in the darker slanted edges observable in Fig. 5.10. On the other hand, proximity effects (144) occur when structures are spatially close to each other. The energy intended to expose one structure also exposes the nearest ones. These effects are less dominating as the angle between segments is opening thus describing the decrease of the nucleation field limit due solely to a more significant width in the corners. To conclude using smooth corners reduces the increase of the width due to the processing and allows a larger nucleation field. For the following subsections, we thus use the structures with 16-vertices corners.

5.1.4 Influence of an oscillatory width and pad geometry

The influence of an oscillatory width was already investigated in the literature (142). This study, however, mainly focused on the DW depinning and not on the nucleation field. We designed structures with an oscillatory width of amplitude 12 nm on both edges. At specific positions, the width is reduced by 24 nm, and half a period further it is increased by 24 nm. The wavelength of the variation

is chosen to be 500 nm, 1000 nm or 2000 nm. In the same, experiment we investigated the influence of modifications to the nucleation pad. In contrast to the diamond shape usually used, we designed a pad in the form of a lemon to try to decrease the depinning at the escape of the pad.

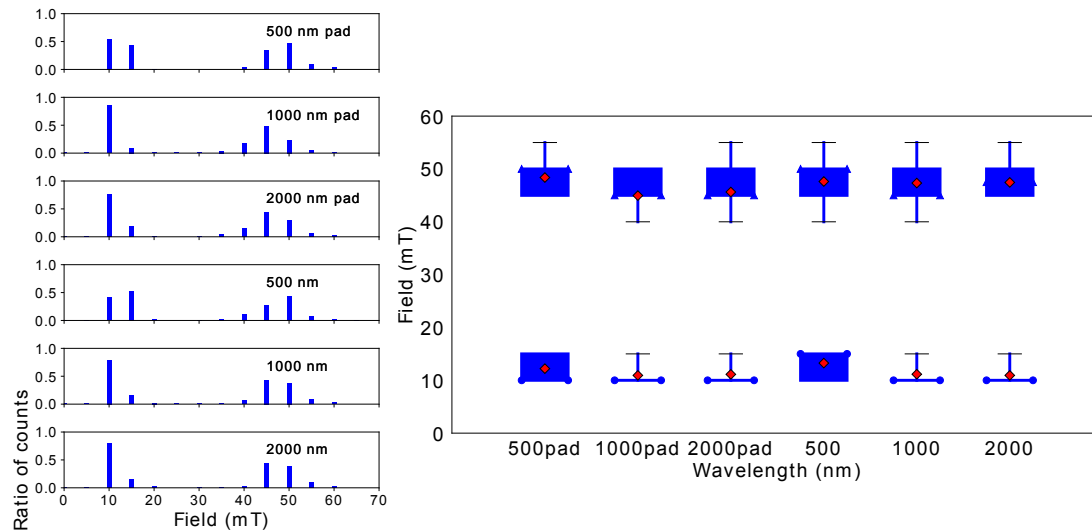


FIGURE 5.11: Left side: Histogram of the depinning/propagation field at low field values and the nucleation field at larger field values for the various wavelengths. The three histograms at the top show the distribution obtained for structures possessing the lemon-shaped nucleation pad, and the three at the bottom starting with the original diamond-shaped pad. On the right side: Box and Whisker plot represent the comparison between the different structures. The boxes associated with the data points in the plot represent 25% (first quartile) to 75% (third quartile) of the distribution.

The whiskers or dashed lines represent 5% to 25% and 75% to 95%.

The samples are made of a GMR stack with a free layer of 30 nm of $\text{Ni}_{81}\text{Fe}_{19}$. The selected designs are the open-2-loop devices with an oscillating width. The devices are measured with the GMR setup under the 2-3 turns rotation sequence. The rotation sequence is tested every 5 mT of an applied magnetic field. The distributions are plotted in histograms on the left-hand side in Fig. 5.11, on the right-hand side, the distributions are represented with box-whisker plot. It appears that neither the oscillating width nor the use of a new pad shows a strong influence. It is possible that the 12 nm changes were not appropriately transferred due to the limitation of the photolithography. Concerning the nucleation pad, we do not observe a variation of the depinning field whether the lemon or diamond-shaped pad is used. The latter is probably because the depinning process is defined by defects and irregularities in the looping structure. In fact, the width being smaller than in the pad then changes brought to the shape anisotropy due to for instance edge roughness of the wire would yield a more significant pinning potential.

5.1.5 Conclusion

In this section, we presented the influence of the modifications on the original open-16-loop structure. We have achieved a much faster rate of testing by shrinking the dimensions and reducing the number of tested loops. We also investigated the key elements of the structure, namely the nucleation pad, the straight wires and the corners. We find that minute variations to the two first do not significantly modify the characteristic of the device and that a smoother corner would yield an increased FOW.

5.2 Depinning field under large count of turns versus large number of elements

In the previous section, we described the effects of the modifications of the original open-16-loop structure regardless of the failure mechanism (pinning or nucleation). In this section, we aim at the improvement or, the very least, at a detailed description of the depinning field as one limit. To perform the latter, we conduct experiments to compare the changes of the depinning field in the case of the increase of the number of measured turns and the increase of the number of measured sensor elements.

5.2.1 Measurement for a large number of sensor elements

The samples used are two GMR stack with 25 and 35 nm thick $\text{Ni}_{81}\text{Fe}_{19}$ as a free layer. The wafers are patterned using the innovative designs previously presented. The measurement is limited to the structures with 16-vertices corners and 2 loops. This choice is motivated by the results shown in the previous section showing a larger FOW for this type of structures. The rotation sequence is composed of 3 full turns clockwise and 3 full turns counter-clockwise. The range of measured field values starts from 1 mT and ends at 79 mT, and in between the field is tested every 2 mT. This method is slightly more time consuming than the bisection method used in chapter 4, but less difficult to implement. The width of the innovative designs being varied from 200 to 350 nm, the depinning field limit of the 200 nm wires might be higher than the nucleation field limit of the 350 nm wire. This issue is described in the previous section, where a large number of data points are lost due to the selection of the lower boundary (30 mT) of the window used for the bisection method. Furthermore, this choice would not be necessary if solely one physical effect were investigated, but the inability to distinguish between a pinning or a nucleation event with the GMR effect leads to the change from the bisection method.

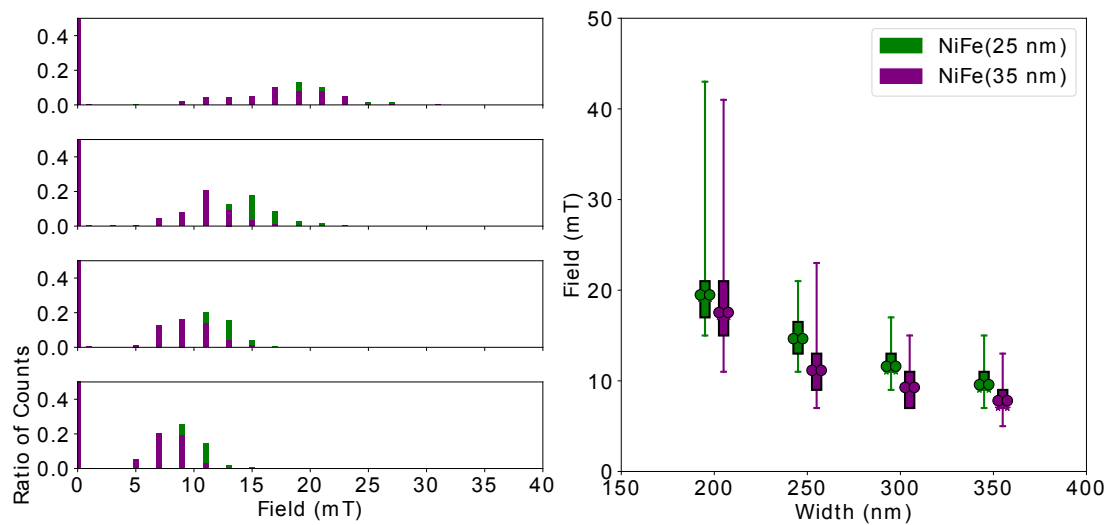


FIGURE 5.12: (a) Histogram of the depinning field limit for a wafer with a GMR stack with a free layer of 25 nm of Ni₈₁Fe₁₉ (green) and 35 nm of Ni₈₁Fe₁₉ (purple). (b) Box and Whisker plot of the depinning field limit for the same samples as in (a). The boxes associated with the data points in the plot represent 25% (first quartile) to 75 % (third quartile) of the distribution. The whiskers or dashed lines represent 5% to 25% and 75% to 100%. The disks represent the mean value.

In Fig. 5.12 (a), the histogram of two samples with a GMR stack with a different thickness of the free layer is represented. In (b), a box-whisker plot is shown of the distribution in (a). The distribution is built from 100 measured elements. We observe that despite the different thicknesses, the trend showing an increase of the depinning field limit with decreasing width is similar for the two thicknesses. The distributions appear mainly Gaussian, and an enlargement of the distributions at lower widths is attributed to the increasing influence of the edge roughness, whose absolute value is not too dependent on the width. The considerable increase of the maximum depinning limit at 200 nm seems to indicate that substantial defects are being introduced due to the limit of the process at this width. In the histogram, plenty of elements display a 0 mT depinning field. These points only represent devices that failed the test due to improper contact between the needles of the contact card and the electrical connection pads.

5.2.2 Measurement for a large number of turns

After the investigation of a large number of devices, we measure a large number of turns for a few devices. The setup required for this measurement is more complicated than with the permanent magnet rotating on top of the sensor device. In fact, some engineering is usually required to achieve rotations faster than 100 Hz due to unwanted mechanical vibrations. A system of two Helmholtz coils is assembled to obtain a 2D vector magnetic field. The magnet is driven by two amplifiers 'Takasago 40-15' and the signal is acquired with a National instrument

card. This electronic provides the necessary elements to rotate the field at 100 Hz and measure in parallel the state of the sensors. Such a rotation speed constrains the maximum applied field strength to 30 mT due to troublesome induction for more considerable field strengths. In that case, the coils tend to rise in temperature.

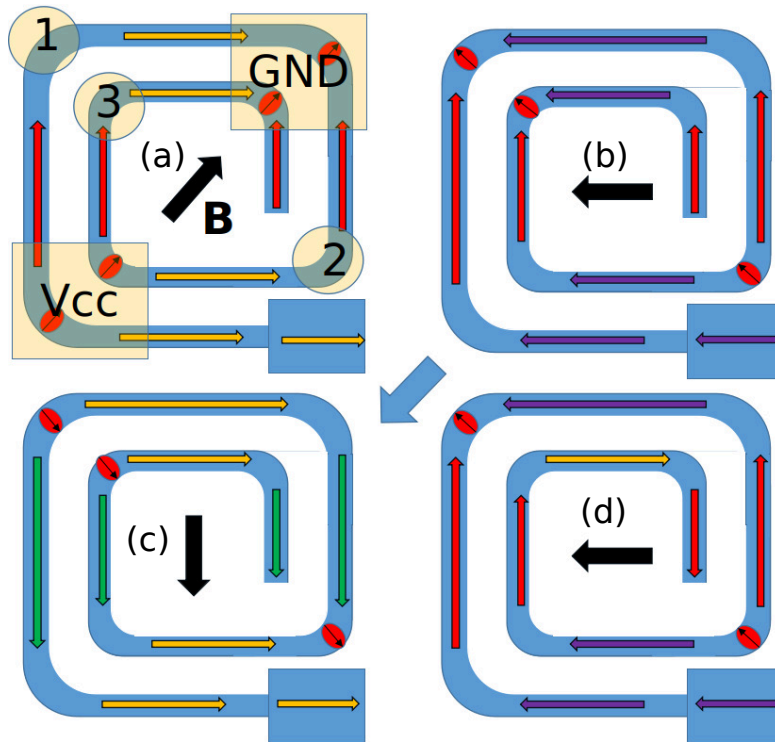


FIGURE 5.13: (a) Schematic representation of the device with the electrical connections in yellow and the magnetization in arrows of various colors. The ovoids in red represent the DWs. The numbers reference the contact points, and the black arrow represents the direction of the applied field. In this experiment, the represented field direction is considered as 0° . (b) Magnetization configuration after a rotation of the applied field of 135° counter-clockwise starting from configuration (a). (c) Magnetization configuration after a rotation of the applied field of 270° clockwise starting from configuration (b). (d) Magnetization configuration after a rotation of the applied field of 270° counter-clockwise starting from configuration (c). The direction of the exchange-bias is indicated by the blue arrow in the center of the figure.

The measurement scheme is the following: The devices are connected to the PCB card to acquire the GMR signal. The field is applied in a direction indicated in Fig. 5.13 (a) with a magnitude of 60 mT. The field is then rotated 135° counter-clockwise (b) and from there 270° clockwise (c), and then 10 times oscillating between 270° clockwise (c) and counter-clockwise (d). After this sequence, DWs are renucleated at the starting position (a), and the sequence is repeated. A failure is detected by the annihilation of a pair of DWs due to one of the DWs being strongly pinned and annihilating with the coming one. Depending on the

number of rotations performed, we can extract a failure rate for a certain applied field strength. The measurement is then repeated by changing the starting position from 0° (see Fig. 5.13 (a)) to 90° . The initial rotation direction is also modified from counter-clockwise (b) to clockwise.¹ With this measurement technique, it is possible to obtain the depinning field limit for 100 000 turns in 5 devices simultaneously. The latter being in general a minimum requirement for the automotive industry since reliability is essential. For this measurement, the device-fields (a device-field contains 5 different structures measured simultaneously) are separated by dicing the wafers presented in the subsection 5.2.1. A particular device-field (device-field n° 1 in appendix J) is investigated in the present experiment. On this device-field, 4 of the present elements are present with different wire widths (200, 250, 300, and 350 nm) and 16-vertices corners, and the last element possesses a 300 nm width and 8-vertices corners. According to the previous results (see 5.8), this element is not expected to yield differences with the 300 nm width and 16-vertices corners element. In Fig. 5.14, the measured curves are only obtained from the 300 nm width devices. The general trend followed by the curves is a plateau of the failure rate at low fields, and a drastic drop in failure rate as the field is increased. However, in a few cases, the failure rate drops and plateaus again as it is observable in Fig. 5.14 (b) to finally fall again at much larger field strengths. The initial drop is attributed to a very high rate of pinning events with weak pinning field. The latter seemingly originates from the pinning generated by the side edge roughness.

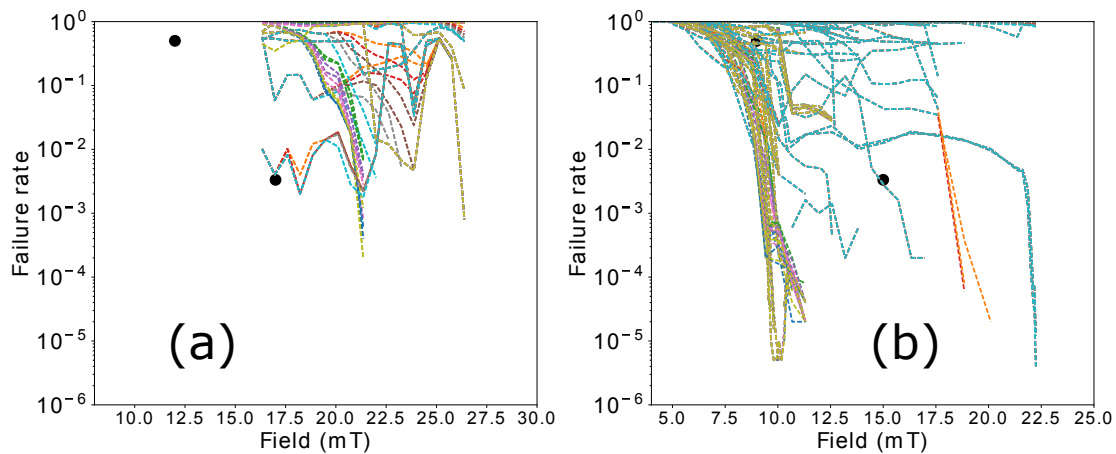


FIGURE 5.14: (a) Failure rate measured on 3 devices with a free layer thickness of 25 nm of $\text{Ni}_{81}\text{Fe}_{19}$ and 300 nm width. The black dots represent the failure rate extracted from the high volume data. The top left one being the taken at half the median of the data and the bottom right one is 1 failure out of 600 (100 devices performing 6 turns, 3 clockwise and 3 counter-clockwise.) (b) Failure rate measured on 6 devices with a free layer thickness of 35 nm of $\text{Ni}_{81}\text{Fe}_{19}$ and 300 nm width. The black dots represent the same data as for (a) only with the layer of 35 nm.

¹We thank the ITHP Jena and particularly D. Diegel and R. Mattheis for providing the measurement tools and helping for the acquisition of the data presented in this section.

However, it remains challenging to correctly identify the reason for the behavior of the failure rates. Indeed, the dynamic of the DW can be drastically changing as the applied field is increased. Furthermore, as the field increases the failure rate is mainly dominated by the stochastic behavior of the DW. In the literature, at least three regimes of distinguishable dynamics occurring during the propagation of the DW are reported. The Walker breakdown (46) at low fields, then the multi-core propagation (145) and finally, the propagation via Bloch wall formation (146). During the Walker Breakdown below 10 mT (see Fig. 5.15 (a)), the DW is propagating by changing its spin configuration from a transverse DW to a vortex DW. In the multi-core propagation between 10 and 30 mT (see Fig. 5.15 (b)), several vortex cores are nucleated and annihilated during the propagation process. Finally, above 30 mT, the propagation occurs with the formation of Bloch walls (see Fig. 5.15 (c)). A pair of vortex-antivortex is nucleated at the front of the DW that moves toward the edges and annihilates. A movie of the three processes is available in the appendix. We readily acknowledge that the dynamic of the DW is complicated for variously applied field strengths without the introduction of defects, thus the difficulty in the analysis of the obtained results without a direct observation of the DW.

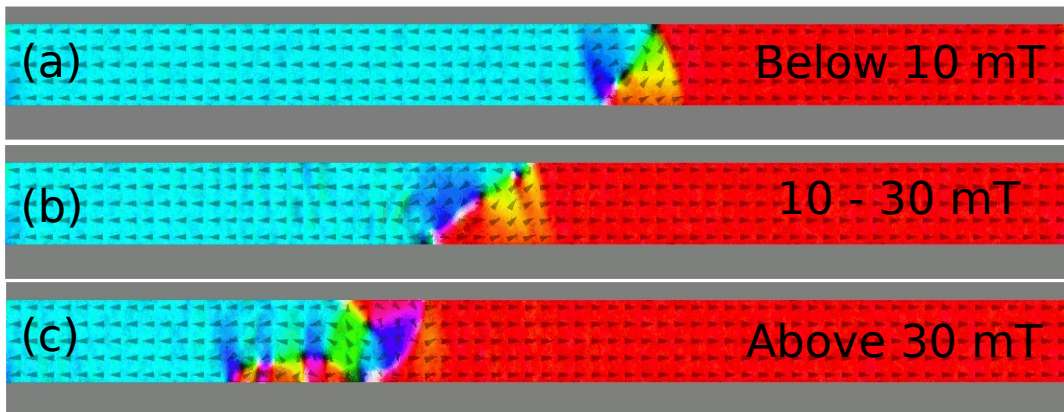


FIGURE 5.15: Simulation snapshot of different dynamics occurring during the propagation of a DW for various applied fields. The simulation parameters are the common ones used for $\text{Ni}_{81}\text{Fe}_{19}$ 4. The thickness and the width of the wire are 30 and 200 nm, respectively. The snapshots appear blurred due to the introduction of a random field simulating the application of temperature. (a) Snapshot of the Walker Breakdown occurring for an applied field smaller than 10 mT for our material parameters and geometry. (b) Snapshot of a DW propagating experiencing the multi-core process for an applied field in between 10 to 30 mT. (c) Snapshot of the propagation of a DW in the Bloch wall propagation regime, which occurs for applied fields larger than 30 mT.

5.2.3 Comparison between large number of element and large count of turns

In Fig. 5.14 in both subplots, the black dot on the top left represents the field where half the sensor devices (50 devices) failed for the experiment with a large number of measured elements. The black dot at the bottom right represents the highest depinning field measured for a large number of items. The latter corresponds to a failure rate of 1 out of 600 since 100 devices are measured with the 2-3 turns rotation sequence. We see that for both experiments, the increase of the depinning field with the decrease of the thickness is respected. However, in the case of the 25 nm thickness, the large count of turns experiment yields significantly increased depinning field limits. The latter is unexpected since the devices measured in a large number of turns experiment are part of the ones measured in a large number of elements experience. We would then expect in the case of the large count of turns to exhibit a larger depinning field limit only at lower failure rates. It is, however, not impossible that the devices were damaged in the dicing process thus yielding a high failure rate at higher applied field values. For the 35 nm thickness, both experiments appear to produce more consistent results, but still, some high failure rates are experienced at large applied fields for a large number of count experiment.

5.2.4 Conclusion

We conclude that there is a significant difference between measuring a single device at a high number of turns and several elements for a small count of turns. In fact, in some instances, measuring a single device for 600 turns yields more failures than measuring 100 devices for 6 turns, at the same applied field strength. There is then a clear need to measure the maximum amount of devices for a large number of turns to assess the reliability of the depinning field limit. This measurement then requires close to a complete day for the investigation of a single device. Furthermore, as described previously, the analysis of the reason for a failure remains cumbersome to pinpoint. The depinning field limit is then probably much higher than the one observed in the chapter 4 since it drastically increases for a large count of turns. However, the control of this limit appears difficult, thus not looking like a natural handle for the tailoring of the field operating window.

5.3 Improvement of the nucleation field of the open-loop structures

The depinning field being not easily controlled as discussed in the previous section, the strategy is to try to tailor the nucleation field. We experienced already that the nucleation field limit follows a similar trend as the Stoner-Wohlfarth model mainly dependent on the cross-sectional shape of the wires measured. In

this section, we then focus on tailoring the parameters present in the equation of the nucleation field derived from the Stoner-Wohlfarth model (34).

5.3.1 Influence of the thickness of the magnetic layer

Historically, at the company producing the open-16-loop device (Sensitec), the nucleation field was plotted as a function of the width. This choice is motivated by the fact that on a single mask several designs with varying widths can be placed. Thus a unique mask and a single wafer are required for the investigation of width variations while a single mask but several wafers are needed for the study of the thickness variation.

In this subsection, we present the results on the influence of the varied thickness of a single $\text{Ni}_{81}\text{Fe}_{19}$ layer or the thickness of the free layer in the case of a GMR stack. For the single layers, the thickness is chosen as 20, 30, 40, 70 and 100 nm, and the thickness of the GMR free layer is selected as 20, 25, 30, 35, 40 nm. The thickness of the free layer is kept below 40 nm since the GMR signal was observed to decrease with increasing free layer thickness, resulting in the impossibility to measure a signal for much larger thicknesses.

Single layer thicknesses

The single layers are deposited at the company Sensitec and patterned with a photolithography process exposed in the chapter about experimental techniques (see chapter 3). The designs imprinted on the wafer are the ones presented in the section about innovative designs 5.1. For the present experiment, only the devices with 16-vertices corners and 2 loops are measured. The measurement for the single layers is conducted with a MOKE microscope in the longitudinal contrast configuration. The measurement scheme is very similar to the one described in chapter 4, in the MOKE measurement section. The principal difference is the number of rotations effectuated to determine the depinning and the nucleation field. As described previously, the latter is merely a consequence of the reduced number of loops. The devices are then measured with the 2-3 turns rotation sequence that is tested every 1 mT. The measurement is performed for a minimum of three elements per thickness and width. In Fig. 5.16, the depinning field, and nucleation fields are plotted for all the investigated thicknesses as a function of the width in the range between 200 to 1000 nm. Every point represents the value obtained for an individual device. Both field limits are expressed as a function of the nominal width and not the effective width as in chapter 4. As expected from the previous results, we observe minimal variations in the depinning field with a change in thickness as it is mainly not dependent on the cross-sectional shape. Focusing on the nucleation field (diamonds), the hyperbolic behavior observed for the single layers in chapter 4 is as well visible for the thicknesses lower than 40 nm. Furthermore, as the thickness increases the nucleation field reaches higher

values. For a 200 nm width with a 20, 30 and 40 nm thicknesses, the maximum measured nucleation field limits are 61, 66, 77 mT, respectively.

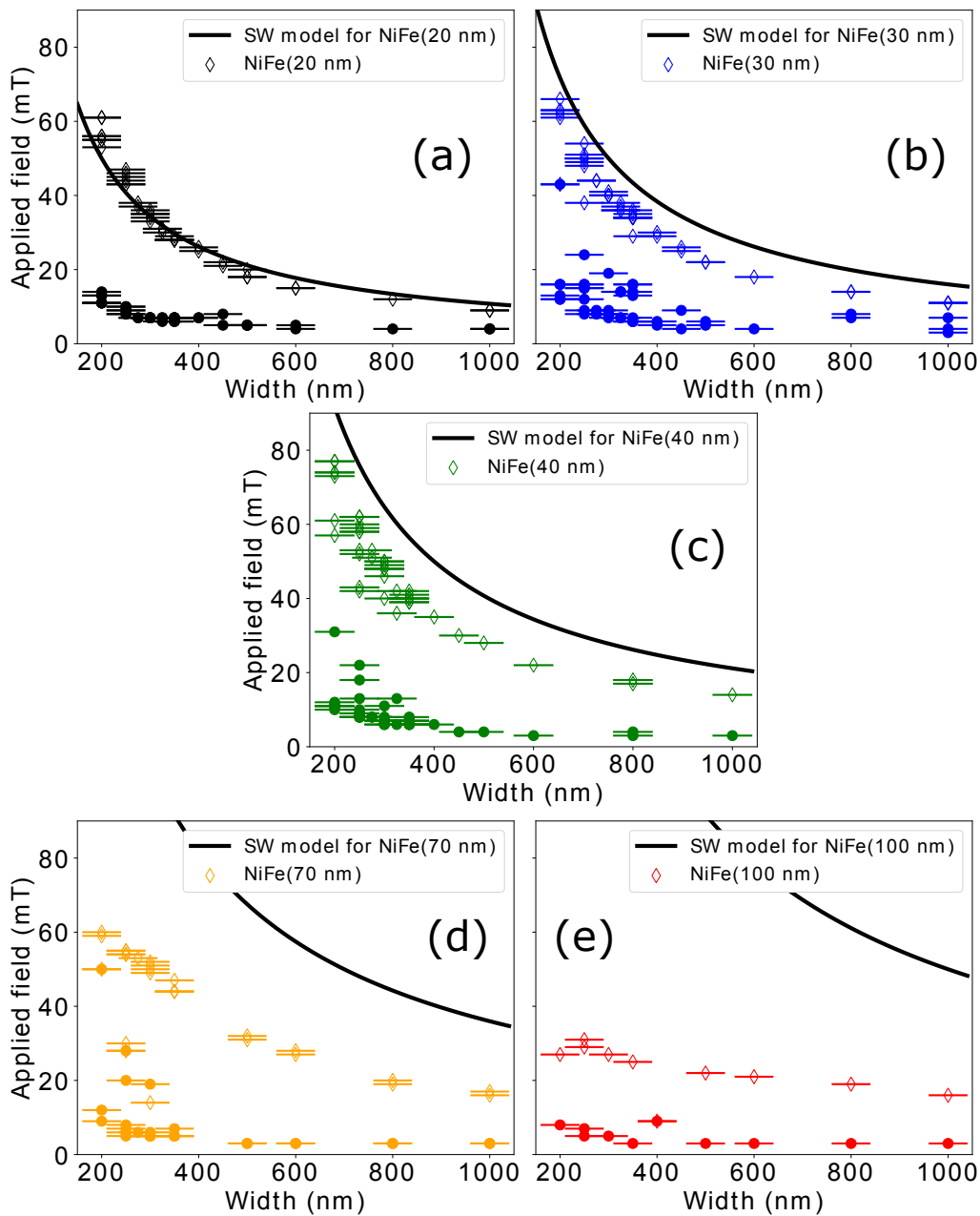


FIGURE 5.16: (a) Plot of the depinning field (full circles) and nucleation field (unfilled diamonds) for the thicknesses 20 nm (black). The full black line is representing the Stoner-Wohlfarth model for a thickness of 20 nm. (b) A similar plot as (a) for a thickness of 30 nm (blue). (c) A similar plot as (a) for a thickness of 40 nm (green). (d) A similar plot as (a) for a thickness of 70 nm (orange). (e) A similar plot as (a) for a thickness of 100 nm (red) of $\text{Ni}_{81}\text{Fe}_{19}$. The error bars in the y-direction contains only the systematic error on the applied field strength. This error was measured and is of the order of 1 mT, the data points being larger than the error bars, they do not appear.

In fact, the demagnetizing factor $N_y = \frac{t}{w+t}$ present in the nucleation field formula exposed in chapter 4 predicts a quasi-linear increase with the thickness. Interestingly, for the 70 nm thickness, the hyperbolic increase with decreasing width is lost at a width of 350 nm, and the trend becomes linear with the decreasing thickness. Similarly, for the 100 nm thickness, the hyperbolic increase is lost for widths lower than 700 nm, probably due to change in the easy-plane shape anisotropy.

Simulations of the nucleation field To understand such behavior, we focus on the 200 nm width and simulate the expected nucleation field. The simulations are performed with the software Mumax3. The simulated system is composed of a wire of dimension $2000 \times 200 \times \text{thickness nm}^3$, which is duplicated 4 times along the x-direction using periodic boundary conditions. At the very beginning of every simulation, the magnetization is initialized along with the x-direction. A field is then applied at an angle of 135° with this direction, thus yielding the lowest nucleation field value for the investigated geometry (see SW model). The first simulations performed were realized with an instantaneous applied field meaning that desired strength is imposed directly at the beginning of the simulation. Furthermore, no temperature effects are included, and various out-of-plane field (OPF) strengths are tested (out-of-plane direction is in the direction of the thickness). The detection of the nucleation field uses a bisection method, and the thickness is varied in steps of 2 nm. A condition is applied to the average magnetization value in the x-direction to detect a nucleation event. In simple words, if the average x-magnetization switches sign then a nucleation event occurred for the simulated parameters. The simulation results for 0, 1, 5 and 10 mT of OPF strength are represented in Fig. 5.17 (a) in green, turquoise, blue and purple, respectively. In the absence of OPF, the simulated thickness was extended to 200 nm. For the other cases, we stopped at 100 nm due to time constraints. In Fig. 5.17, the field values that have lesser strength than the limit only yielded a tilting of the magnetization away from the x-axis while more substantial field strengths triggered a nucleation event. We directly observe a deviation from the Stoner-Wohlfarth model (black curve) at 60 nm of thickness. Furthermore, the behavior of the nucleation field limit with increasing thickness does not appear utterly trivial. Looking first at the simulation without OPF, an increase is visible up to 95 nm thickness where a maximum nucleation field is achieved for 147 mT. After the peak, a decrease follows up to 170 nm thickness where the limit plateaus until the 200 nm thickness. The other simulated curves exhibit similar behavior. However, the application of an out-of-plane field reduces the maximum nucleation limit and the position of the peak. For 1 mT OPF strength, the maximum nucleation field is 140 mT for a 92 nm thickness, while for a 5 and 10 mT OPF strength, it provides 132 mT for a 90 nm thickness and 126 mT for an 82 nm thickness. From these simulation results, we deduce that the nucleation field is not adequately describable by the SW model for larger thicknesses than 60 nm. Furthermore, a process is involved that decreases the nucleation field above this thickness value, and this process is OPF dependent. We know that the demagnetizing factors evolve as the thickness is changing. If the OPF is opposed to the generated demagnetization field, then its influence is decreased, and the nucleation event occurs at a lower applied

in-plane field. To push the research in this direction, we simulate the nucleation limit for a differently applied magnetic field. This field obeys the equation:

$$B = \left(-\frac{\sqrt{2}}{2} B_{ext} \left(1 - \exp\left(\frac{-t}{4 \cdot 10^{-9}} \right) \right), -\frac{\sqrt{2}}{2} B_{ext} \left(1 - \exp\left(\frac{-t}{4 \cdot 10^{-9}} \right) \right), 0 \right) \quad (5.1)$$

Such a change is motivated by the fact that the generated demagnetization field during the dynamic of the magnetization is field-increase-rate dependent. In fact, with a slow increase of the applied field, the system follows a relaxation path different than if the field were to be applied instantaneously. The simulation results are then expected to be different. The field is then increased for 20 ns to reach the desired value. In Fig. 5.17 (b), the nucleation field simulated without OPF and with such a field increase is plotted in red. The nucleation field is lowered as compared to the ones simulated with the instantaneous field. We attribute the latter to the slower increase of the applied field generating a smaller out-of-plane demagnetizing field. The maximum nucleation field limit is 110 mT for a 59 nm thickness. Interestingly, the nucleation field prior to 60 nm is not influenced by the application rate nor by the OPF. A possible explanation is that below 60 nm, the out-of-plane demagnetization field is very large whether the field is applied instantaneously or not, thus not generating differences to the nucleation field limit.

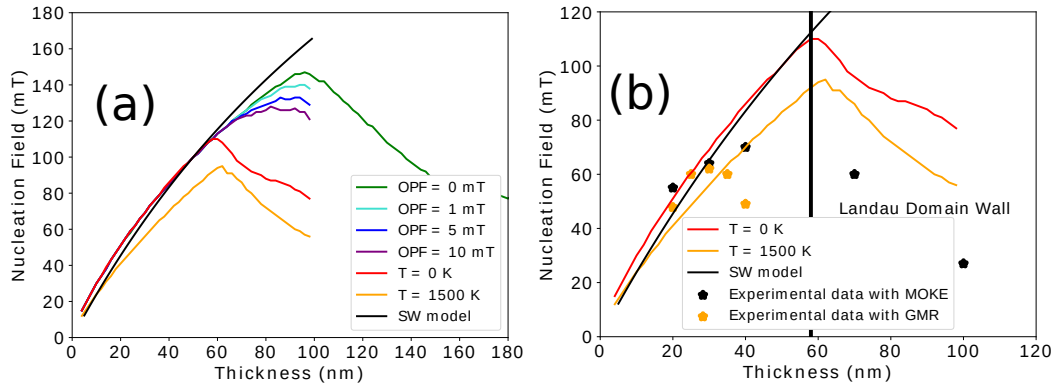


FIGURE 5.17: (a) Plot for the simulations and theory of the nucleation field as a function of the thickness with a wire width of 200 nm. The full black line represents the SW model. The simulated limit of the nucleation field at 0 K for an instantaneous applied field and 0, 1, 5 and 10 mT out-of-plane field are in green, turquoise, blue, purple, respectively. The red, orange full lines represent the nucleation field limit simulated at 0 K, 1500 K, respectively, and for a 20 ns applied field increase. (b) Zoom into the plot in (a). The simulated data for an instantaneous applied field are removed. The experimental data for the single layers of $\text{Ni}_{81}\text{Fe}_{19}$ (black stars) are added and called (MOKE data), and the experimental data for a GMR stacks (orange stars) are also added and called (GMR data).

Finally, some simulations are performed at finite temperature. In the software Mumax3, the temperature is generated following the equation found in (118):

$$\mathbf{B}_{therm} = \vec{\eta}(step) \sqrt{\frac{2\mu_0\alpha k_B T}{B_{sat}\gamma_{LL}\Delta V\Delta t}} \quad (5.2)$$

with α is the Gilbert damping parameter, k_B is the Boltzmann constant, T is the temperature, B_{sat} is the saturation magnetization in Tesla, γ_{LL} is the gyromagnetic ration (1/Ts), ΔV is the cell volume, Δt is the time step used for the computation of the Landau-Lipshitz-Gilbert equation and $\vec{\eta}$ is a random vector changed every time step. Since the time step and the cell size enter in the computation, the use of 300 K as input parameter does not accurately generate the effect as 300 K in reality. The latter is mainly due to the cut-off of short wavelength magnons because of the discretization of the system (147). To simulate a more realistic 300 K temperature influence, we measure the saturation magnetization as a function of the temperature using a SQUID (148). From the measurement results, we extract that at 300 K, the saturation magnetization is decreased by 5 % as compared to its value at 0 K. With this knowledge, the simulation is performed with a temperature yielding a similar decrease in the saturation magnetization. The temperature we use is then 1500 K as the input parameter in the simulation to reproduce the effect of 300 K in reality. For these simulations, an apparent decrease of the limit for all thicknesses is observable. The latter is due to a more significant probability to switch the magnetization at a higher temperature (thermal activation of the nucleation process) and a lower energy barrier due to the decreased saturation magnetization. In Fig. 5.17 (b), we also represent the measured nucleation field limit of the single layer samples (black stars). In this case, a similar decrease of the nucleation field occurs between 40 nm and 70 nm thickness, thus fitting the simulation results (red and orange lines). Deviations from the simulation regarding nucleation field values are attributed to a non-square cross-sectional shape, the edge roughness and an incorrect intrinsic representation of thermal effects in the micromagnetic model.

Investigation of the two nucleated DWs At this point, the physical process causing the saturation of the SW model with increasing thickness is still unknown. A closer investigation of the nucleation event for various thicknesses is lead to answer this question. All the data can be found in the appendix K. At the nucleation event, two DWs are created and propagated from the center of the wire to the edges. In Fig. 5.18 (a) and (c), a snapshot of the magnetization at the nucleation point is acquired for a wire of 30 nm and 100 nm thick, respectively. In the two cases, we observe a clear difference in the magnetic spin textures. To obtain more insight, we divided the computation region in half, the top half and the lower half, with the aim to analyze both DWs separately. The average magnetization values in both regions are collected, and the results are plotted in Fig. 5.19.

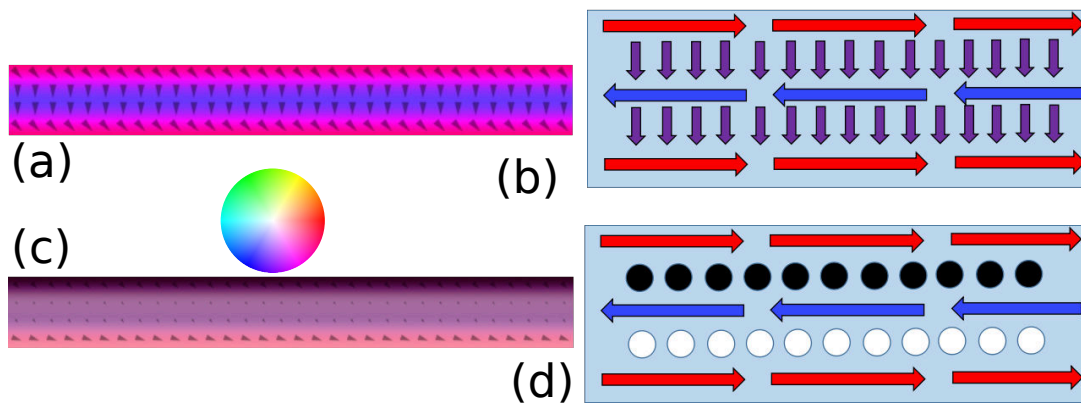


FIGURE 5.18: (a) Simulation snapshot at the exact moment of the nucleation of two DWs, the thickness of the wire is 30 nm. (b) Schematic representation of the magnetization in (a). The wire contains 2 Néel DWs of opposite chirality. The arrows represent the magnetization direction. (c) Simulation snapshot at the exact moment of the nucleation of two DWs, the thickness of the wire is 100 nm. (d) Schematic representation of the magnetization in (c). The wire contains 2 Bloch DWs of opposite chirality. The up magnetization is represented in white and the down magnetization in black. The color wheel shows the in-plane magnetization direction.

In this figure, we represent the data for two wire thicknesses (30 nm, top row, and 100 nm, bottom row). In both cases, the average x-component of the magnetization starts at the +1 value since the magnetization is initialized to the left. After a certain time and due to the applied field, DWs are created, propagated and annihilated at the edges observable by the oscillating average x, y, and z-component of the magnetization. If we take a closer look at the data for the two different regions, the region 0 and 1 for the 30 nm thick wire yield the same data. Thus describing that the same DW is generated and propagated toward the opposite edges. Since there is a large negative average y-component, the DWs are Néel with the chirality shown in Fig. 5.18 (b). Interestingly, for the 100 nm thick wire, there is a difference between the average x, y, and z-component of the magnetization in region 0, and 1. Especially, the z-component exhibits two opposite directions of the magnetization suggesting the creation of 2 Bloch DWs with the same chirality as represented in Fig. 5.18.

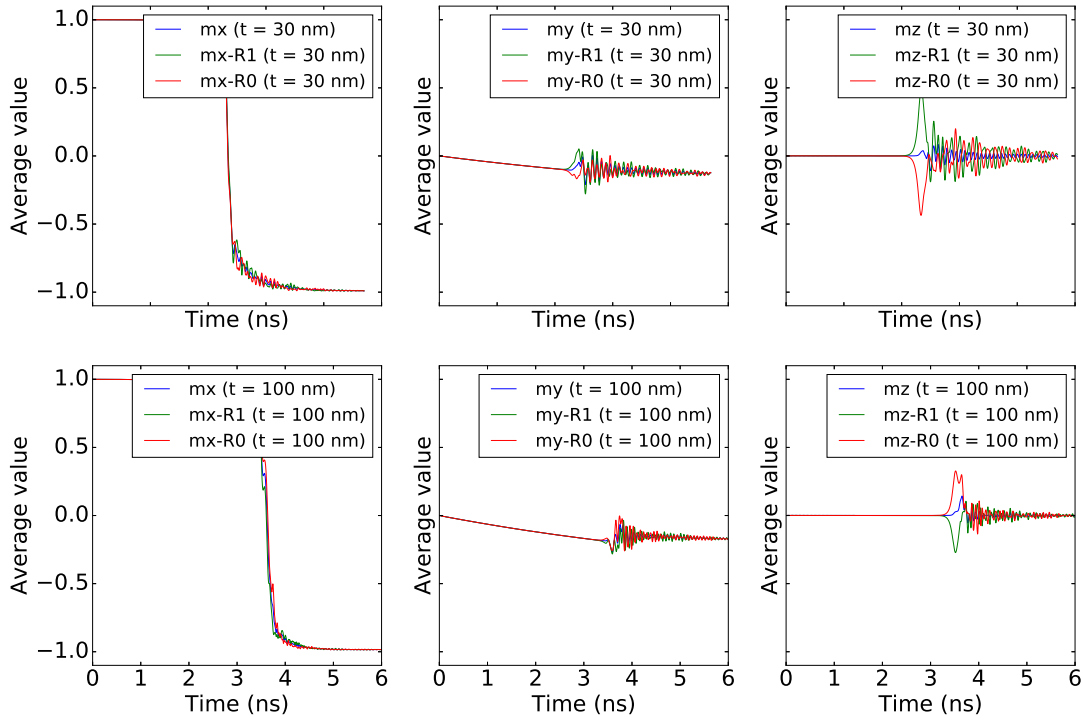


FIGURE 5.19: Plot showing the average magnetization of each three spatial components for the whole computation region (blue), the upper half part (R1 in green) and the lower half part (R0 in red) of the computation region. The top row provides the data of a 30 nm thick wire and the bottom row, the data of a 100 nm thick wire. Both wires exhibit a 200 nm wire width.

In order to make the last observation clearer, we represent the average z -component of the magnetization of region 0 and 1 and their difference in Fig. 5.20. The plots of the right column display the lack of difference between region 0 and 1 for 30 nm and the large difference for the 100 nm. We note that the y -component of the two Néel DWs is similar, an explanation to this effect originates from the necessity to lower the demagnetizing field. In this configuration, there is a better flux closure and more reduced Zeeman energy than if one of the two DWs exhibited the opposite y -direction. Similarly, it explains the fact that the Bloch walls exhibit opposite z -component, which also leads to a lowered demagnetizing field. The latter observation is then investigated across thicknesses and in Fig. 5.21 is shown the results.

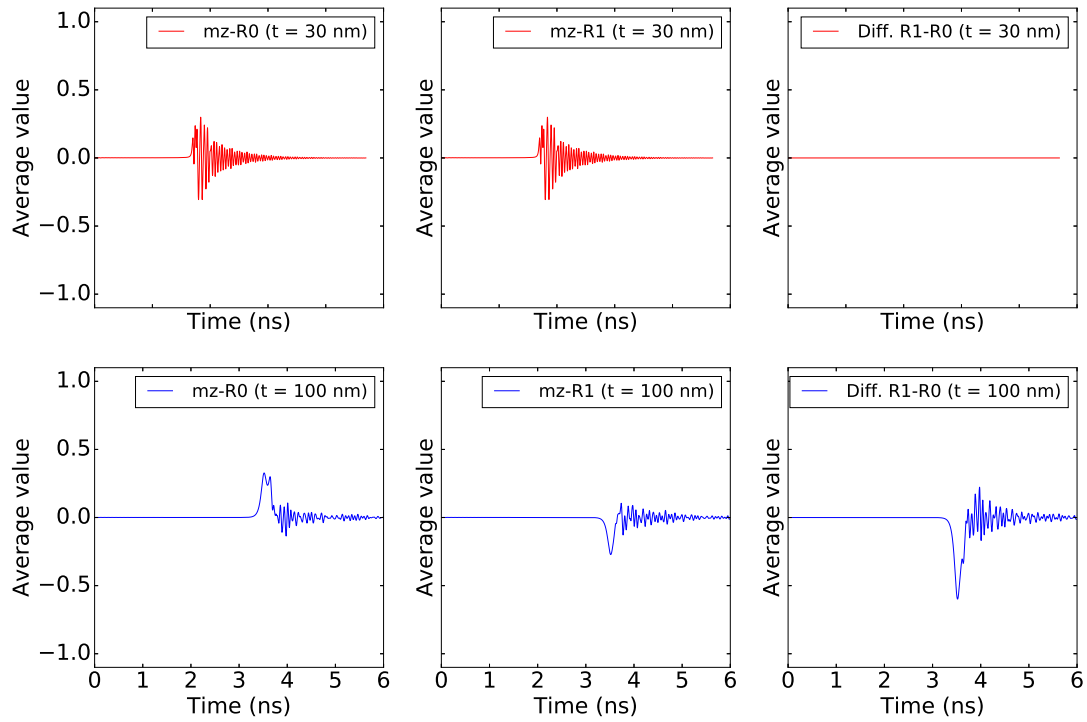


FIGURE 5.20: Plot showing the average z-component of the magnetization of region 0 (left column), 1 (middle column), and the difference between the two (right column). The top row provides the data of a 30 nm thick wire and the bottom row, the data of a 100 nm thick wire.

In this figure, we plot the maximum and minimum value of the difference between the region 0 and 1 for various thicknesses. Interestingly, the first noticeable difference occurs for thicknesses larger than 60 nm, which is the value we obtained earlier for the saturation of the scaling of the SW model. We notice that the energy density also decreases after that point. We deduce that below 60 nm thickness, the switching of the magnetization is realized with the creation of two Néel DWs propagating toward the edges and annihilating. In contrast, for a thickness larger than 60 nm, the switching of the magnetization results from the generation of two Bloch DWs propagating toward the edges and annihilating. This effect is a consequence of the more efficient reduction of the demagnetization energy density with the spin structure generated from the two homochiral Bloch walls as the thickness increases as seen in Fig. 5.21.

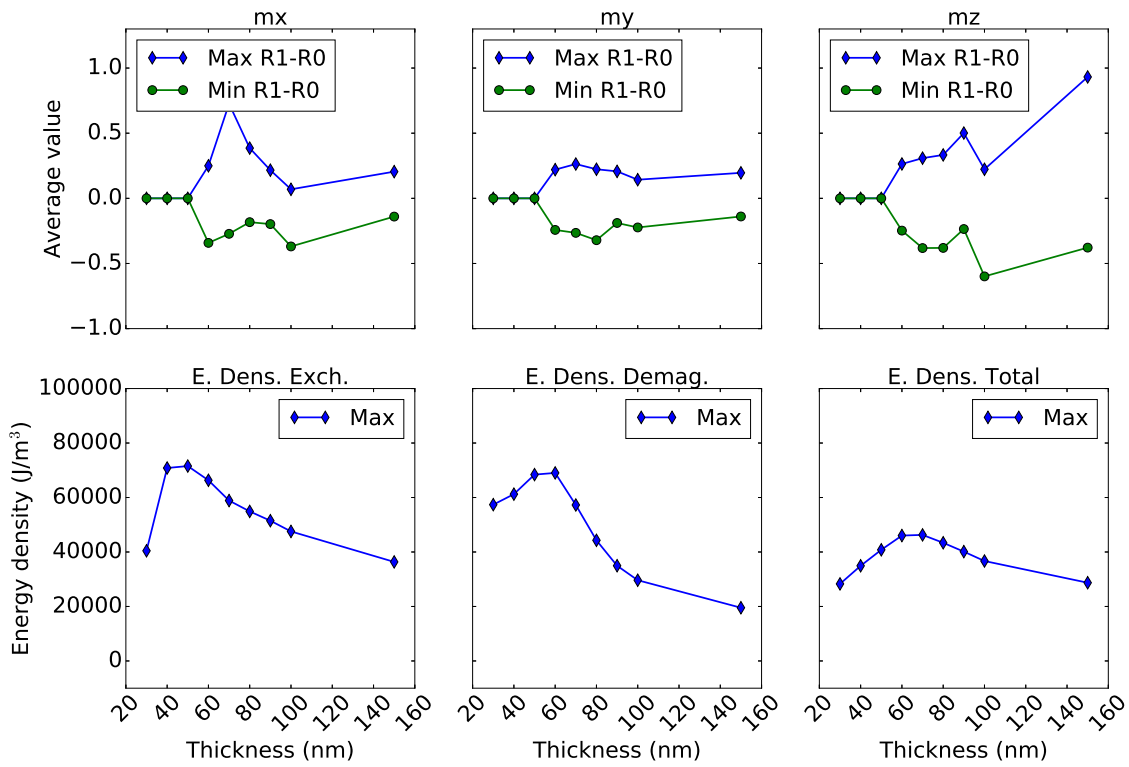


FIGURE 5.21: (Plot showing the max and min values of the difference between region 0, and 1 of the x, y and z-component of the magnetization as a function of thickness. The bottom row shows the max and min value of the exchange energy density (left), the demagnetization energy density (middle), and the total energy density (right) as a function of thickness.

In the literature, we also find reference to a transition between two types of DWs at 60 nm thickness of $\text{Ni}_{81}\text{Fe}_{19}$. Below 60 nm, the vortex DW is stable, while above a Landau-type DW (149) is the stable spin structure. The Landau DW exhibits a Bloch wall in its center, which demonstrates the lowered out-of-plane anisotropy allowing out-of-plane spin structures to be meta-stable. Finally, we conclude that the Stoner-Wohlfarth model is applicable as long as Néel DWs are initially nucleated.

GMR stacks with changing free layer thickness

For this experiment, the nucleation field limit is obtained for varying free layer thicknesses. The chosen thicknesses are 20, 25, 30, 35 and 40 nm. As in the single layer experiment, the structures used are the innovative designs with 16-vertices corners. The nucleation field is determined by measuring the results of the previous exposed 2-3 turns rotation sequence. The results of the experiment are plotted in Fig. 5.22. The deviation from the hyperbolic behavior is already observed from thicknesses between 35 to 40 nm. Despite using $\text{Ni}_{81}\text{Fe}_{19}$ in both the free layer and the single layers, the thickness yielding the maximum nucleation field limit is drastically different (see Fig. 5.17). This discrepancy is unexpected and is not

fully understood. It is possible that the underlying stack generates a stray field, which reduces the nucleation field limit as experienced for the application of the OPF. However, the latter is still an unproven speculation. This effect could be checked via simulations since it is possible to simulate a stack of magnetic materials in Mumax3. The simulations were not performed due to time constraints.

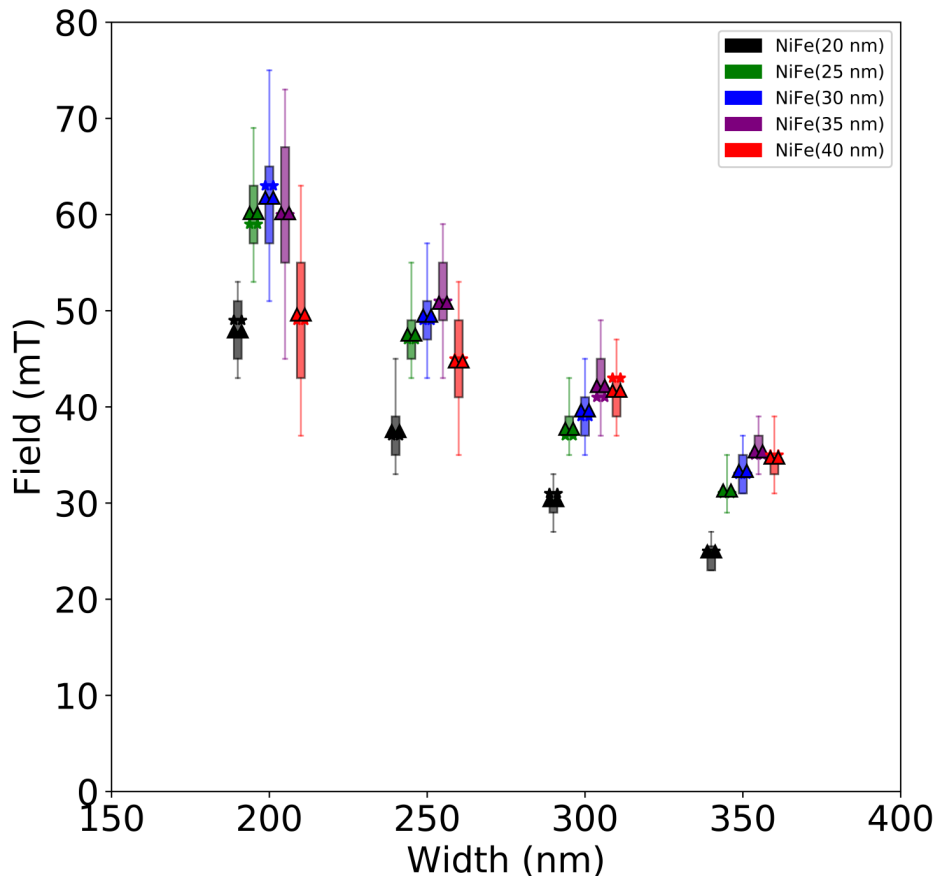


FIGURE 5.22: Nucleation field as a function of the width of the wire constituting the device. The thickness varies between 20 and 40 nm. The box-whiskers are plotted aside for enhanced visibility. The nominal width for all thicknesses being the one shown for the 30 nm of $\text{Ni}_{81}\text{Fe}_{19}$.

Conclusion

To summarize the results highlight the influence on the nucleation field of thickness variations. The scaling of the Stoner-Wohlfarth model is saturating at the transition between the nucleation of 2 Néel DWs and 2 Bloch DWs, due to a more efficient reduction of the energy density of the system in the latter case. For our material $\text{Ni}_{81}\text{Fe}_{19}$, the transition occurs at 60 nm thickness. However, this transition is material dependent, thus needs to be determined again if different material is used as a free layer. Furthermore, the discrepancy between the results

yielded by the GMR stacks and the single layers remains unexplained. Finally, with the identification of a maximum nucleation field for a particular thickness value, we conclude that the selection of the highest theoretical nucleation field can be calculated. The latter can be performed by selecting the thickness yielding the transition between DW types and selecting the smallest width fabricable by the patterning tool.

5.3.2 Cross-sectional Shape modifications

After modification of the two most-easily-modified parameters (width and thickness) of the nucleation field equation, we investigate the scaling factor C used to fit the data in the chapter 4. The present subsection aims to determine the origin of this scaling factor and thus modify the wires in consequence to reach the nucleation field values predicted by the Stoner-Wohlfarth model.

Desentanglement of the contributions to the scaling factor

We start by realizing micromagnetic simulations for different cross-sectional shapes. In the present case, we select a sample with a single layer of 32 nm of $\text{Ni}_{81}\text{Fe}_{19}$ covered with a 4 nm Ta layer. The sample is patterned into open-2-loop devices with 16-vertices corners and varying width. The exact nucleation field is acquired for 20 devices with the MOKE microscope. The applied field sequence consists in performing the 2-3 turns rotation sequence every 1 mT of the applied field. A contrast appearing in the microscope signals a nucleation event at the tested field strength.

Following the magnetic measurement, the cross-section of a wire of each of the investigated devices is acquired with the AFM tool. From each micrograph, an average height along the y-axis (Fig. 5.23 (a)) and an exact AFM profile (Fig. 5.23 (b)) is extracted. After this extraction, the first simulations are created by conforming the shape of the simulated wires to the average height profiles shown in Fig. 5.24 (a) and (d). The simulations are initialized by saturating the magnetization in the direction of the length, and after relaxation, a field is applied at 135° with the magnetization. A nucleation field is obtained for these average-profiled wires using a bisection method, and the green circles in Fig. 5.25 represent these results.

After the simulation of the average-profiled wires, we simulate wires with a realistic shape by loading the slices of the AFM profile as described in chapter 4 (Fig. 5.24 (b) and (d)). The simulations are then initialized and run in the same way as for the average-profiled ones. The nucleation field is also obtained with a bisection algorithm, and the results are now shown by the orange disks in Fig. 5.25. The motivation behind the simulations is that the comparison between the nucleation fields obtained for the average-height profile and the realistic shapes allows to potentially derive the influence of the shape profile separately from the

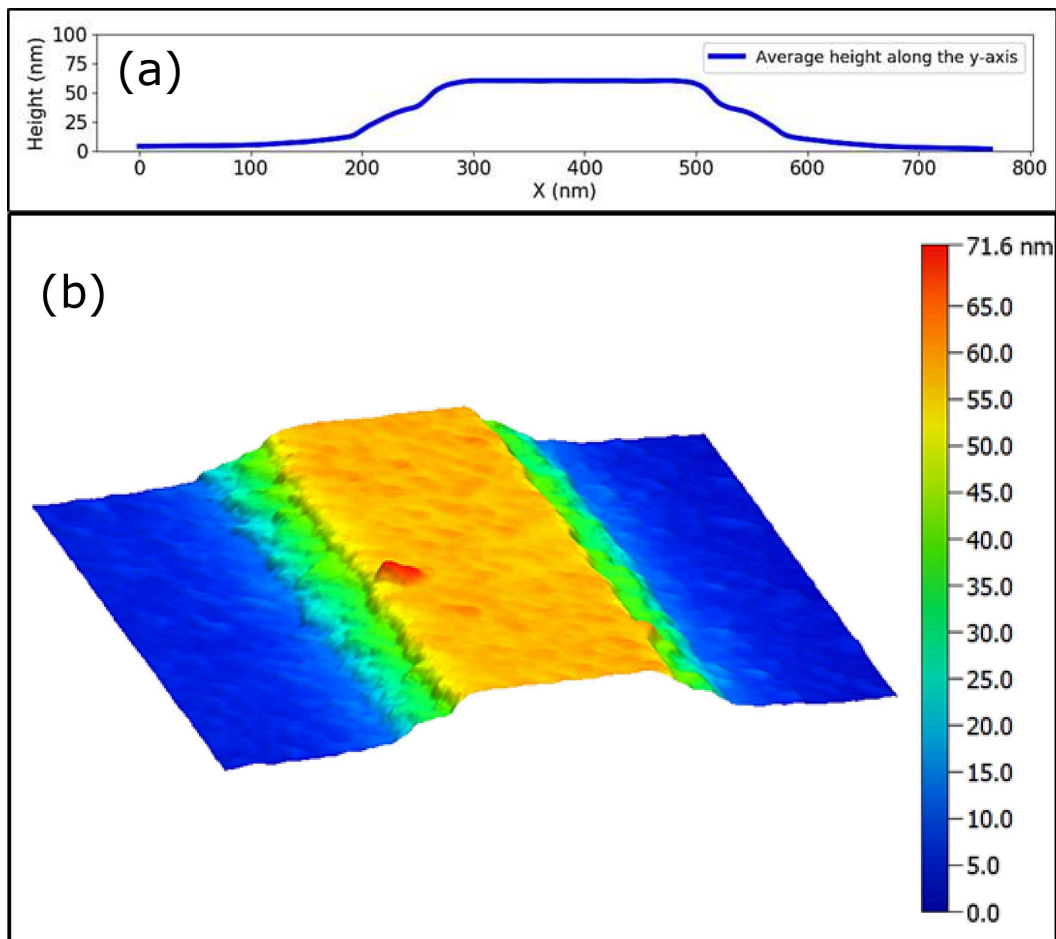


FIGURE 5.23: (a) Average height of wire along the y-axis direction. (b) AFM micrograph expanded in 3 dimensions and colored depending on the pixel height.

edge roughness. Further-on, simulations are performed including temperature effects together with the realistic shapes. The selected temperature is 1500 K as an input parameter for reasons described in the subsection 5.3.1. Finally, the nucleation fields measured experimentally are as well plotted with black diamonds and are fitted using the Stoner-Wohlfarth model with a scaling factor $C = 0.7$ (red line). As an initial observation, the results of the nucleation field obtained with only the average height already reproduce very well the experimental data. Notably at lower widths, where the shape anisotropy is more affected by a trapezoidal shape than at 1000 nm widths. Despite the different spin textures as seen in Fig. 5.24 (c) and (d), we note that the introduction of the roughness does not yield an extreme reduction of nucleation field as compared to the simulations with the average-height profile. The decreases are contained in between 2 mT and 4 mT for rough wires, probably because the edge roughness does not drastically change the shape (see Fig. 5.24 (a) and (b)). The nucleation field appears then rather insensitive to very local variations of the shape anisotropy. Finally, the introduction of the temperature in the simulations reproduces the experimental results even

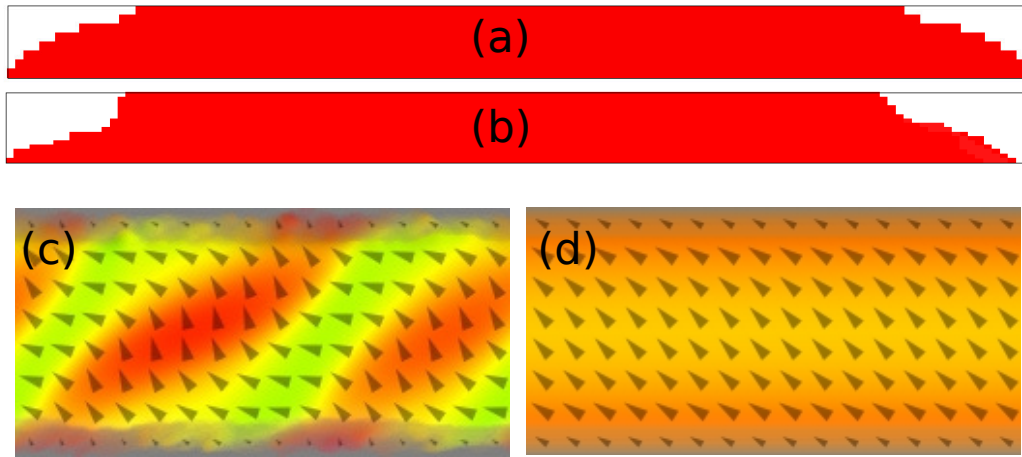


FIGURE 5.24: (a) Cross-section of the simulated wire extracted with the algorithm performing a discretization of the average of height profile. (b) Cross-section of the simulated wire extracted with the algorithm slicing the AFM image. The cut for the cross-section is taken in the middle of the wire. (c) Snapshot of the magnetization right before the nucleation event. This wire is generated from the slicing algorithm, similar to (b). (d) Snapshot of the magnetization right before the nucleation event. This wire is generated with the discretization of the average height profile algorithm similar to (a).

for very large widths such as 1000 nm. The thermal activations being more probable at low energy barriers (larger widths yield lower N_y demagnetizing factor) thus resulting in a more substantial decrease for larger widths.

Experimental realization of cross-sectional shape modifications

After the numerical investigation of the influence of various parameters on the scaling factor used to fit the Stoner-Wohlfarth model, we experimentally realize wires with a different cross-sectional shape. To achieve a change of the cross-section, we varied the parameters of some of the fabrication steps, namely 3 wafers were processed with varied ion-milling times resulting in different etched thicknesses. The SiO_x wafers received a single layer of 32 nm of $\text{Ni}_{81}\text{Fe}_{19}$ and 4 nm thick covering Ta layer. A resist is then spin-coated and exposed with the photolithography stepper tool to transfer the innovative designs (details, see chapter 3). After the development, the ion milling was performed differently for all the 3 wafers; the first was milled for a thickness of 46 ± 5 nm, the second for 53 ± 5 nm and the last for 76 ± 5 nm. This milling is performed under a 30° -angle between the beam direction and the surface's normal. The various milling depths/thicknesses were achieved by milling for various time lengths. Furthermore, the wafer milled for 53 ± 5 nm was etched in steps with a 30 s cool-down period in between them. The different milled thicknesses were measured with the AFM tool to obtain the cross-section of the wires in the various samples. In

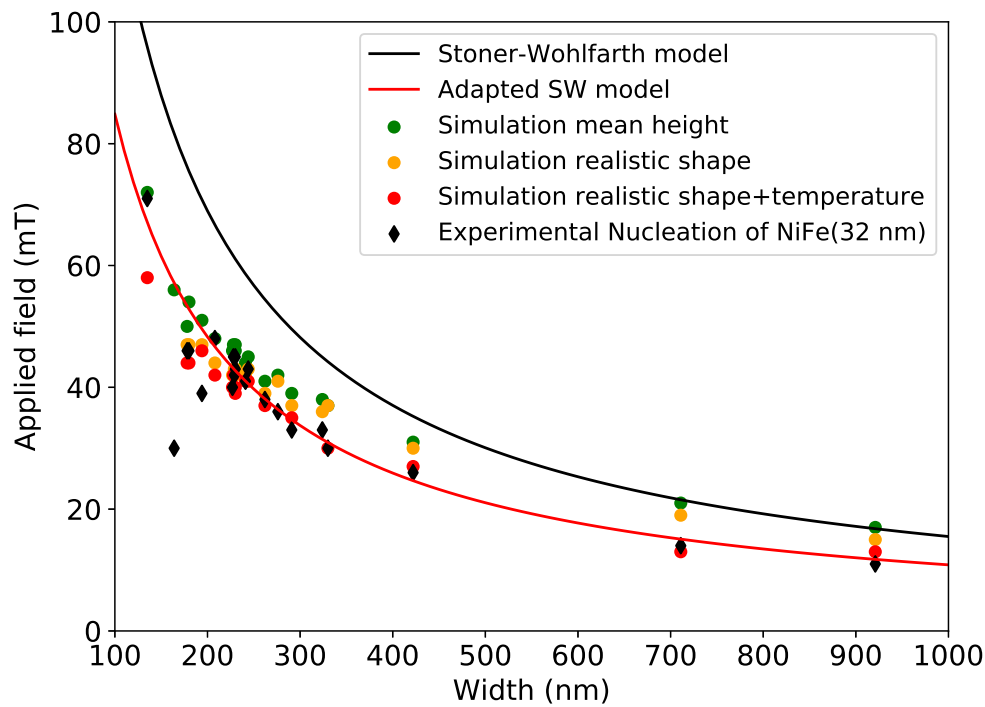


FIGURE 5.25: Plot of the nucleation fields for experimental data (black diamonds) compared to simulated data only using the average height profile (green circles), using a realistic shape of the wire (orange circles), and including temperature to the realistic-shape simulations (red circles). The full black line represents the Stoner-Wohlfarth model while the full red line represents the adapted Stoner-Wohlfarth model with a scaling factor $C = 0.7$.

Fig. 5.26 (b-d) is depicted some representative 3D-AFM micrographs of wires selected on the various samples. We observe that the cross-sectional shape of the sample etched for 76 nm is well defined and square-like. The $\text{Ni}_{81}\text{Fe}_{19}$ layer being only 32 nm thick, it is well contained within the 76 nm milled. Thus the shape of the magnetic layer is close to a perfect rectangular shape. For the samples etched for a lesser time, the roughness on the edges of the wires is apparent.

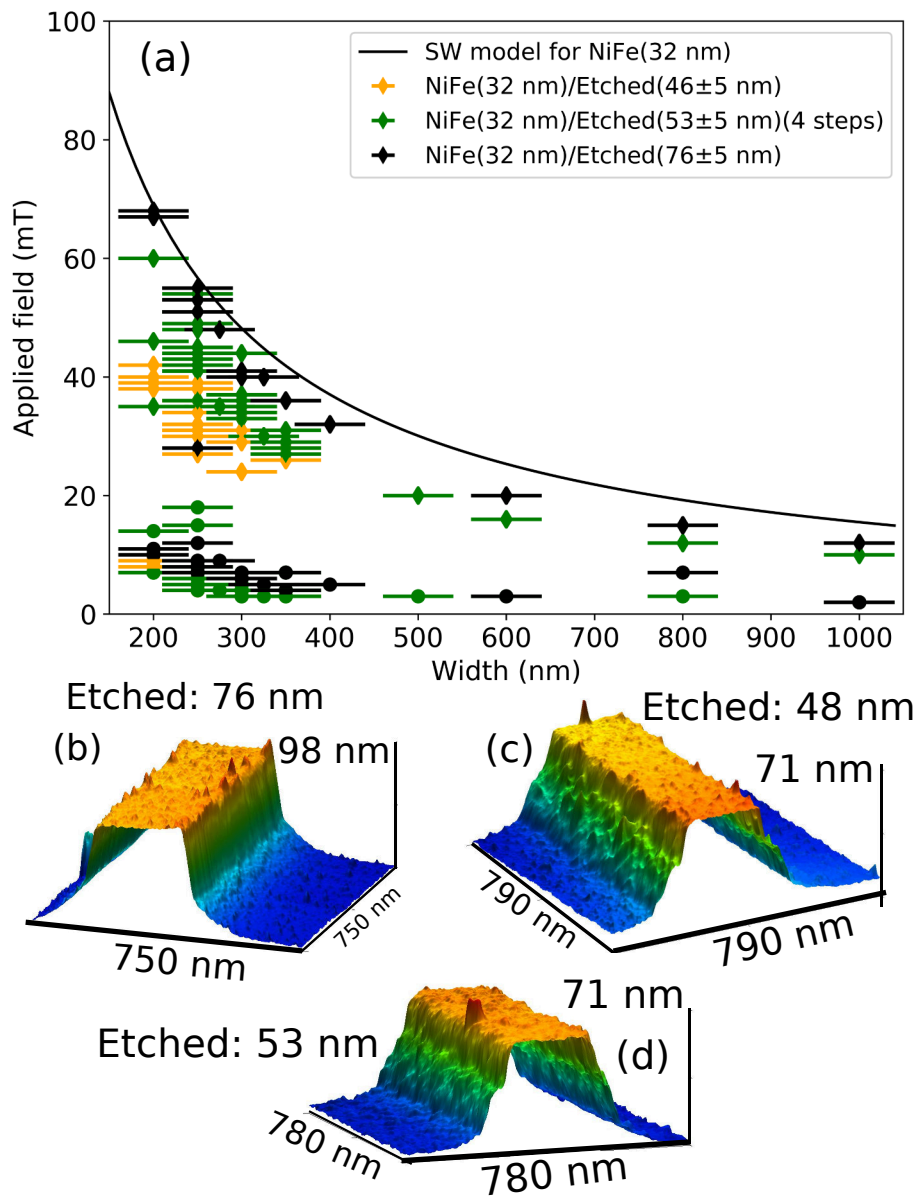


FIGURE 5.26: (a) Plot of the depinning/propagation field (circles) and nucleation field (diamonds) limit. For three samples, etched for different times thus yielding a different etched thickness. The first sample is etched for 46 ± 5 nm (orange), the second one for 53 ± 5 nm in four steps (green), and finally, the last sample is etched for 76 ± 5 nm. (b) 3D-AFM micrograph of a wire on the sample that etched for 76 ± 5 nm. (c) Similar to (b) for the sample etched for 53 ± 5 nm. (d) Similar to (b) for the sample etched for 48 ± 5 nm. The representation is different from the micrograph in Fig. 5.23 (b) since in that figure the scale for the three axes is the same. In the current figure, in order to highlight the side edges, the scale of the z-axis is different from the one of the x and y-axis.

For the wire etched for 53 nm, the cross-sectional shape is rectangular and smooth for 30 nm at the top and rough further down. Furthermore, the wires etched 48 nm show some side edge roughness almost reaching the top of the

wire. From that point, we can already conclude that changing the etching conditions alters the cross-sectional shape, and the longer the stack is etched, the more defined the shape becomes. Looking at the magnetic results, the nucleation field (diamond) is increasing with the increasing etched thickness, and especially at smaller widths where the contribution from the cross-sectional shape is more important. At 200 nm width, the difference between the nucleation fields is as significant as 30 mT. Indeed, the 76 nm etched wires show a nucleation field of 70 mT while the 46 nm etched ones only provide 40 mT. The distribution of the nucleation field is as well shrinking for a deeper etched thickness. The latter consequence is of extreme importance for the industry as the reliability of a sensor device needs to be extensively tested before sold. From the conclusions drawn from the simulations, we attribute the decrease of the nucleation field not to the edge roughness but to the fact that the wire width is increasing with a non-perfect rectangular shape wire. This conclusion is furthermore emphasized by the fact that the almost perfectly rectangular shape of the sample etched for 76 nm yields 95 % of the nucleation field expected from the Stoner-Wohlfarth model with a thickness of 32 nm of $\text{Ni}_{81}\text{Fe}_{19}$. Finally, we again observe that the propagation field (disks in Fig. 5.26) is very little influenced by the modification of the shape of the wires.

Conclusion

To conclude, we first investigated different cross-sectional shapes with the use of a micromagnetic simulation tool. The comparison between an average-height profile and a realistic shape helped us distinguish between the influence of the profile shape and the influence of the edge roughness to the nucleation field. Finally, the experimental results are modeled with the inclusion of temperature effects in simulations. After the simulations, experiments are performed, and different samples are fabricated with selected etched thicknesses thus yielding various cross-sectional shapes. The results of the simulations, as well as the experimental ones, indicate that the cross-sectional average profile is the main contributor to the scaling factor. We also find that the nucleation field is improved by milling for a large enough time yielding a defined cross-sectional shape. The latter is, however, cumbersome as many other problems arise when the etching time is increased, such as crystallization of the wires due to a rising temperature, damages or implantation of the atoms used for the etching process. The creation of magnetic domain wall devices is then relying on a compromise between the improved cross-section and the damages induced during prolonged etching.

5.3.3 Modification of $\text{Ni}_{81}\text{Fe}_{19}$ deposition conditions

For the present subsection, the aim is to investigate the influence of changes to the deposition conditions of the single layers of $\text{Ni}_{81}\text{Fe}_{19}$. For the purpose of the experiment, wafers are processed at different locations.

Processing at Sensitec

Several wafers were produced at the company Sensitec. The standard wafers made of Si/SiO_x constitute the substrates for the deposition. For the present experiment, two kinds of stacks are investigated, the first of which is NiFeCr(4 nm)/Ni₈₁Fe₁₉(x nm)/Ta(4 nm), and the second is Ni₈₁Fe₁₉(x nm)/Ta(4 nm) with x representing a variable thickness. The order used here is from bottom to top, so the first layer at the left is the first deposited on the substrate. In the first investigated stack, we used a seed layer of NiFeCr (4 nm) since this layer is used in stacks that aim at measuring a GMR or an Anisotropic Magnetoresistance (AMR) phenomenon. In fact, the seed layer helps for the enhancement of the magnitude of the effect ($\Delta R/R$) (150). In fact, NiFeCr exhibit very little magnetoresistance and weak paramagnetism (151). Furthermore, the crystalline structure of NiFeCr is very close to the one of Ni₈₁Fe₁₉ thus promoting the growth of large grains. The texturing of Ni₈₁Fe₁₉ on top of NiFeCr also yields a smooth interface between the two materials at the origin of the sizeable Magnetoresistive effect (150). This seed layer is still employed in the produced GMR stacks. In this subsection, we then investigate the difference brought by the texturing of Ni₈₁Fe₁₉ on the domain wall properties. The samples are deposited by magnetron sputtering under ultra-high vacuum conditions. During the deposition, an in-plane field is applied to texture the film. The top Ta layer aims to protect the Ni₈₁Fe₁₉ layer from oxidation. After the deposition of the stacks, the coercivity in the hard and easy axis directions, as well as the saturation magnetization, are measured using a BH-Looper tool 3.4.2. The samples are also investigated using an X-ray diffraction method to obtain the crystalline structure present in the sample.

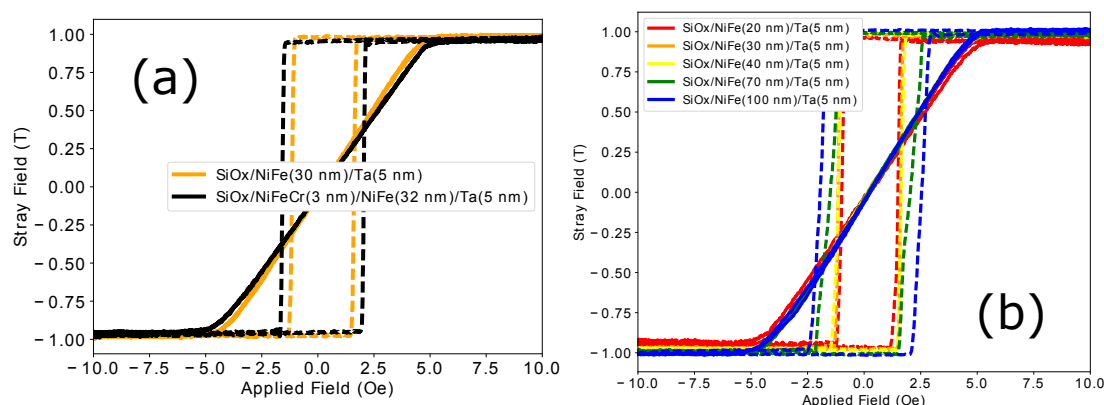


FIGURE 5.27: (a) Hysteresis loops measured with the BH-Looper setup on samples grown at Sensitec. A comparison between a sample with and without a NiFeCr seed layer is displayed. (b) Hysteresis loop measured with the BH-Looper setup on samples with different Ni₈₁Fe₁₉ layer thicknesses (20 nm (red), 30 nm (orange), 40 nm (yellow), 70 nm (green) and 100 nm (blue)) grown at Sensitec.

The measured hysteresis curves for a sample with stack constituted of NiFeCr(3 nm)/Ni₈₁Fe₁₉(32 nm)/Ta(5 nm) (black) and with stack constituted of Ni₈₁Fe₁₉(30

nm)/Ta(5 nm) (orange) are plotted in Fig. 5.27. The hard axis is represented by a full line while the easy axis is with a dashed line. We observe the consequences of the applied field during the deposition in the difference between the hard and easy axis curves. The strong anisotropy favoring the easy axis is seen in the rectangular shape of the curve, which indicates an abrupt switching of the magnetization at the coercivity field. The coercivity for the sample without the seed layer is 1.2 Oe, while it is 1.7 Oe for the sample with the seed layer. Oppositely, the change of magnetization direction following the hard axis appears linear, and the two samples exhibit a similar anisotropy field (H_k). The increase in coercivity for the sample with the seed layer is probably originating from the larger grains present. In Fig. 5.27 (b), hysteresis loops for samples with various thicknesses are plotted. The easy and hard axis show the same behavior as in (a). We observe an increase of the coercivity with increasing thickness of the $\text{Ni}_{81}\text{Fe}_{19}$ layer. The coercivity is similar for the 20, 30, and 40 nm thicknesses and it is equal to 1.2 Oe. In between the 40 and 70 nm thickness, the coercivity starts increasing and sits at 1.5 Oe for the 70 nm thick and 2 Oe for the 100 nm thick layer. The latter can also be attributed to an enlargement of the crystallite size as the thickness grows (Fig. 5.27).

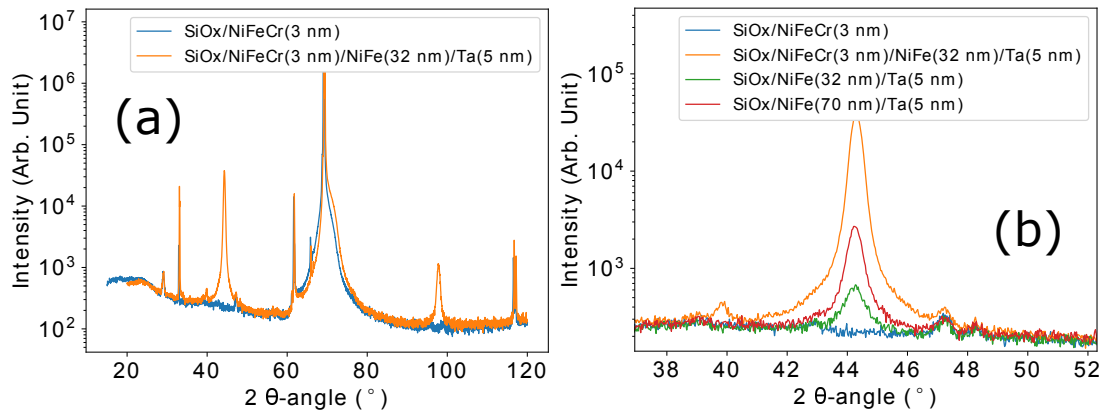


FIGURE 5.28: (a) Plot of X-ray diffraction measurement data performed on samples grown at Sensitec. The scan is acquired between $2\theta = 15^\circ$ and 120° . The contribution from the seed layer alone is in blue, and the data from a stack containing a layer of 32 nm of $\text{Ni}_{81}\text{Fe}_{19}$ is in orange. (b) Zoom in the peak related to the 111-orientation of $\text{Ni}_{81}\text{Fe}_{19}$. The two samples presented in (a) are plotted, and two other samples are added. These samples do not possess a seed layer but a single layer of 32 nm (green) or 70 nm (red) of $\text{Ni}_{81}\text{Fe}_{19}$.

To confirm the previous assumption on the material features, we measured the various stacks with the X-ray diffraction method. The diffraction measurement can yield the amount of texturing of a stack. In Fig. 5.28 (a), we present the results of X-ray diffraction scan taken between the $2\theta = 15^\circ$ and 120° for a sample with only the seed layer of NiFeCr deposited on the substrate and the stack of NiFeCr(3 nm)/ $\text{Ni}_{81}\text{Fe}_{19}$ (32 nm)/Ta(5 nm). Since the interest is to extract information about the $\text{Ni}_{81}\text{Fe}_{19}$ layer, we identify the peaks that are providing a

large intensity in the stack containing the material and no intensity for the other stack with the seed layer solely. We observe a clear difference in the angle $2\theta = 44.3^\circ$, which according to the literature is the peak of the 111-direction of $\text{Ni}_{81}\text{Fe}_{19}$ (55, 152). The difference is as well seen at $2\theta = 97.7^\circ$, which we expect to be the 222-orientation for $\text{Ni}_{81}\text{Fe}_{19}$ (153). These data show a texturing of the $\text{Ni}_{81}\text{Fe}_{19}$. In Fig. 5.28 (b), we zoom in the 111-peak and add the X-ray diffraction measurement data from two samples without seed and a single layer of 32 nm and 70 nm thick $\text{Ni}_{81}\text{Fe}_{19}$. Interestingly, the crystallization of the samples with a seed layer yields a signal which is at least 10-fold more substantial than the signal provided by the single layers. Furthermore, the crystallization is as well enhanced in the case of an increased thickness as depicted by the 5-fold more significant signal for the 70 nm thick sample. These results confirm that the crystallization is enhanced by the seed layer and by an increased thickness, thus suggesting that our interpretations of the hysteresis curves are correct. However, we find that, in all cases, the coercivity remains very small and that the samples are still extremely soft. Furthermore, the significant signal obtained in the XRD measurement for the sample with the seed layer does not result in the proportional increase of the coercivity. In fact, the increase is only of 0.5 Oe for a sample with similar $\text{Ni}_{81}\text{Fe}_{19}$ thickness. Despite a lower XRD signal of the 70 nm film than the one with the seed layer, the coercivity is still 1.5 Oe. The major conclusion that can be extracted is that more crystals grow in the 111-direction with a seed layer and an increased thickness.

Processing at Singulus

We next present films grown by a sputtering tool manufactured by the company Singulus Technologies. We already thank them here for their contribution. The samples are as well grown in ultra-high vacuum conditions. The main difference other than the fact the deposition system is different is that no field is applied during the growth of the samples. With this machine, several samples are deposited among which are also single layers with varying thicknesses (20, 30, 40, 70, 100 nm seen in Fig. 5.29 (b)) and samples with a seed layer of NiFeCr(4 nm).

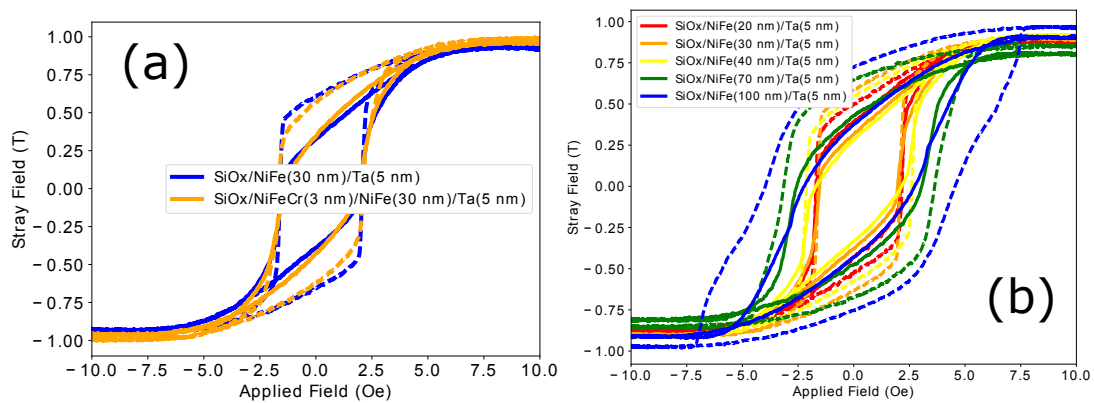


FIGURE 5.29: (a) Hysteresis loop measured with the BH-Looper setup on samples grown at Singulus. A comparison between a sample with and without a NiFeCr seed layer is displayed. (b) Hysteresis loop measured with the BH-Looper setup on samples with different Ni₈₁Fe₁₉ layer thicknesses (20 nm (red), 30 nm (orange), 40 nm (yellow), 70 nm (green) and 100 nm (blue)) grown at Singulus.

Looking at the hysteresis curves of Fig. 5.29 (a), the hard (full line) and easy axis (dashed line) data are similarly shaped. The anisotropy is, however, still slightly stronger in the easy axis direction. Furthermore, the sample with a seed layer exhibits a similar hysteresis as the one without it. These results appear to contradict the ones obtained with the Sensitec deposited wafers. Concerning the samples with various thicknesses, the coercive field of the 20 and 30 nm are similar and equal to 1.6 Oe. Then for the 40, 70 and 100 nm samples, the coercivities are 2, 3.2, and 3.5 Oe, respectively. In the present case of the samples deposited at Singulus, the larger thicknesses as well yield a larger coercivity.

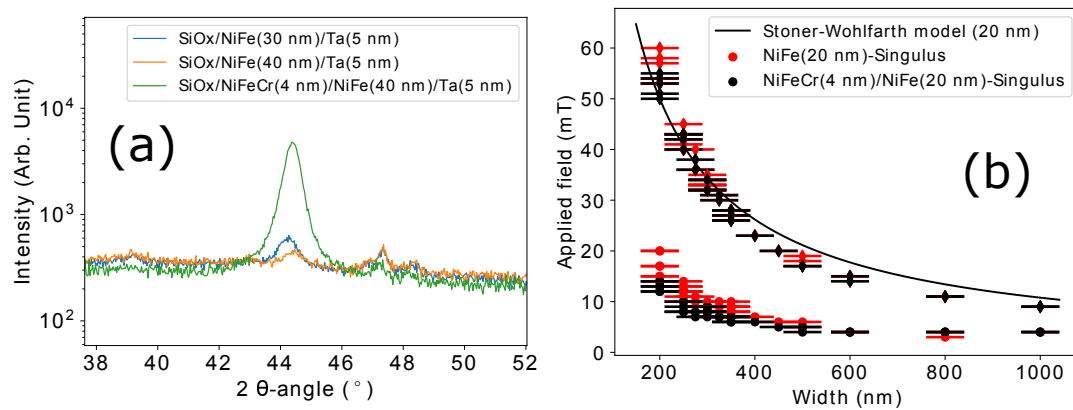


FIGURE 5.30: (a) Plot of X-ray diffraction measurement data performed on samples grown at Singulus. The scan is performed between $2\theta = 38^\circ$ and 52° . Two single layers with thicknesses 30 (blue) and 40 nm (orange) are plotted next to the data obtained for a sample with a NiFeCr seed layer with a 40 nm $\text{Ni}_{81}\text{Fe}_{19}$ on top. (b) Plot of the depinning/propagation field (circles) and nucleation field (diamonds) limits for a sample with 20 nm $\text{Ni}_{81}\text{Fe}_{19}$ thickness (red) and a sample with a seed layer of 4 nm of NiFeCr below a 20 nm $\text{Ni}_{81}\text{Fe}_{19}$ layer. All the samples are grown at Singulus.

In Fig. 5.30 (a), the peak signal associated with the 111-direction of $\text{Ni}_{81}\text{Fe}_{19}$ is shown. As for the samples deposited at Sensitec, the sample with a seed layer displays an enhanced crystallinity with a signal which is 10-fold larger than the ones provided by the single layers. Interestingly, with these stacks, the increased thickness does not necessarily lead to an increase in the measured intensity. The intensity, in fact, decreases from the 30 to 40 nm thick layer. Furthermore, the peak for the 40 nm thick sample is displaced from $2\theta = 44.3^\circ$ (30 nm of $\text{Ni}_{81}\text{Fe}_{19}$) to 44.4° which can be due to a relaxation of a strain in the sample. Finally, in Fig. 5.30 (b), the depinning field and nucleation field are plotted for a single layer as compared to a stack with the NiFeCr seed layer with a $\text{Ni}_{81}\text{Fe}_{19}$ layer on top. To obtain these data, the full films presented previously are patterned using the photolithography tool at Sensitec. Here, we provide data only obtained on designs of the 2-loops 16-vertices corners devices measured with the MOKE microscope. The measurement rotation sequence is 2-3 turns rotation sequence between 1 mT and 80 mT with the applied field stepped by 1 mT. We readily observe that as for the coercivity the nucleation and depinning fields yield very similar results. The small discrepancies can be attributed to slightly different widths of the investigated wires. The latter confirms that the enhancement of the crystallinity of the sample by adding a seed layer does not yield changes to the FOW of the sensor devices.

Comparison between the Sensitec and Singulus processed wafers

Next, we present a direct comparison between the results provided by the two different deposition conditions. In Fig. 5.31 (a), hysteresis curves are shown for

two nominally similar samples deposited at the two locations. In orange is the 40 nm thick $\text{Ni}_{81}\text{Fe}_{19}$ sample deposited at Singulus and in blue is the one made at Sensitec. The same color code is used throughout the subsection. As observed in the previous section, the hysteresis curves are different in shape from each other. We attribute this effect to the field applied during the growth of the material at Sensitec leading to an anisotropy. Interestingly, the coercivity of the sample made at Singulus is 2 Oe as opposed to 1.2 Oe for the sample made at Sensitec. The texturing of the material during growth appears to reduce the switching field at least in the easy axis direction. The saturation magnetization is also slightly different which can be attributed to a deviation from the expected 40 nm thickness. The XRD plot in Fig. 5.31 (b) shows that the application of the field that creates the easy axis is promoting the texturing of the $\text{Ni}_{81}\text{Fe}_{19}$ layer in the 111-direction. The peak position is also slightly displaced, which can be a consequence of a different strain in the samples.

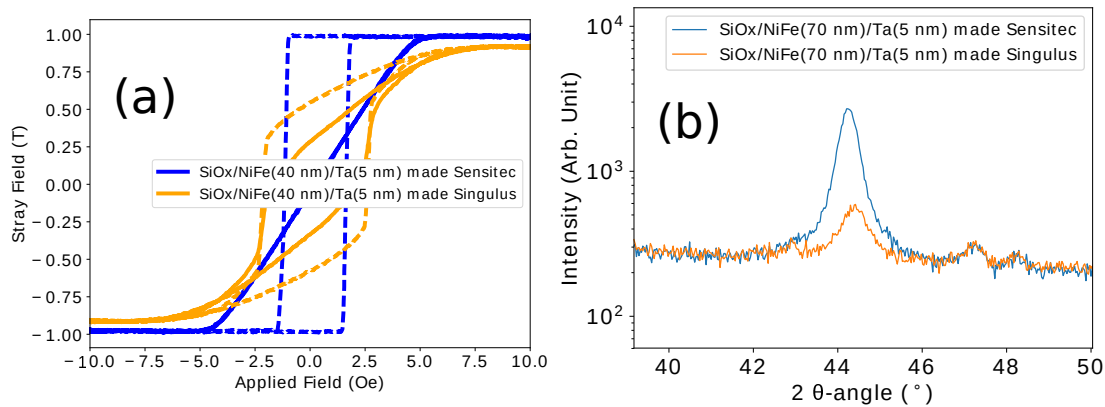


FIGURE 5.31: (a) Hysteresis loop measured with the BH-Looper setup on samples grown at Singulus (orange) and Sensitec (blue) for the same nominal layer thickness (40 nm). (b) Plot of the X-ray diffraction measurement data performed on a sample made at Sensitec (blue) and the other at Singulus (orange) for similar thickness of 70 nm of $\text{Ni}_{81}\text{Fe}_{19}$.

Finally, in Fig. 5.32, we compare the depinning/propagation field and nucleation fields for various thicknesses of $\text{Ni}_{81}\text{Fe}_{19}$ deposited with the two different machines. The samples are patterned as described in the previous subsection and measured with the MOKE setup. The 20 nm thick samples (Fig. 5.32 (a)) yield similar results for the two deposition conditions. For a large width where the shape anisotropy is less dominating, the most substantial influence on the FOW from a change to the crystallization should be observed. However, the data are as well very similar at that point. For the 30 nm thickness, the nucleation fields are also very similar to an increase of 2 mT is not significant and can be attributed to a variation of the effective width of the wire or a slight inaccuracy in the deposited thickness. In fact, if the original width in the Sensitec sample is 500 nm then the expected nucleation field for a 30 nm thick sample is 28 mT. If the width is reduced to 470 nm for the Singulus sample, the predicted nucleation field is 30 mT. Thus the change of 2 mT can be the result of a 30 nm variation of the width solely,

which is a feature already observable within the same flash-field of the same sample. Furthermore, a change of layer thickness from 30 nm to 29 nm with a 300 nm wire width is also expected to provide a 2 mT difference between the nucleation fields. Finally, the 40 nm thick samples also exhibit the same depinning field and nucleation fields.

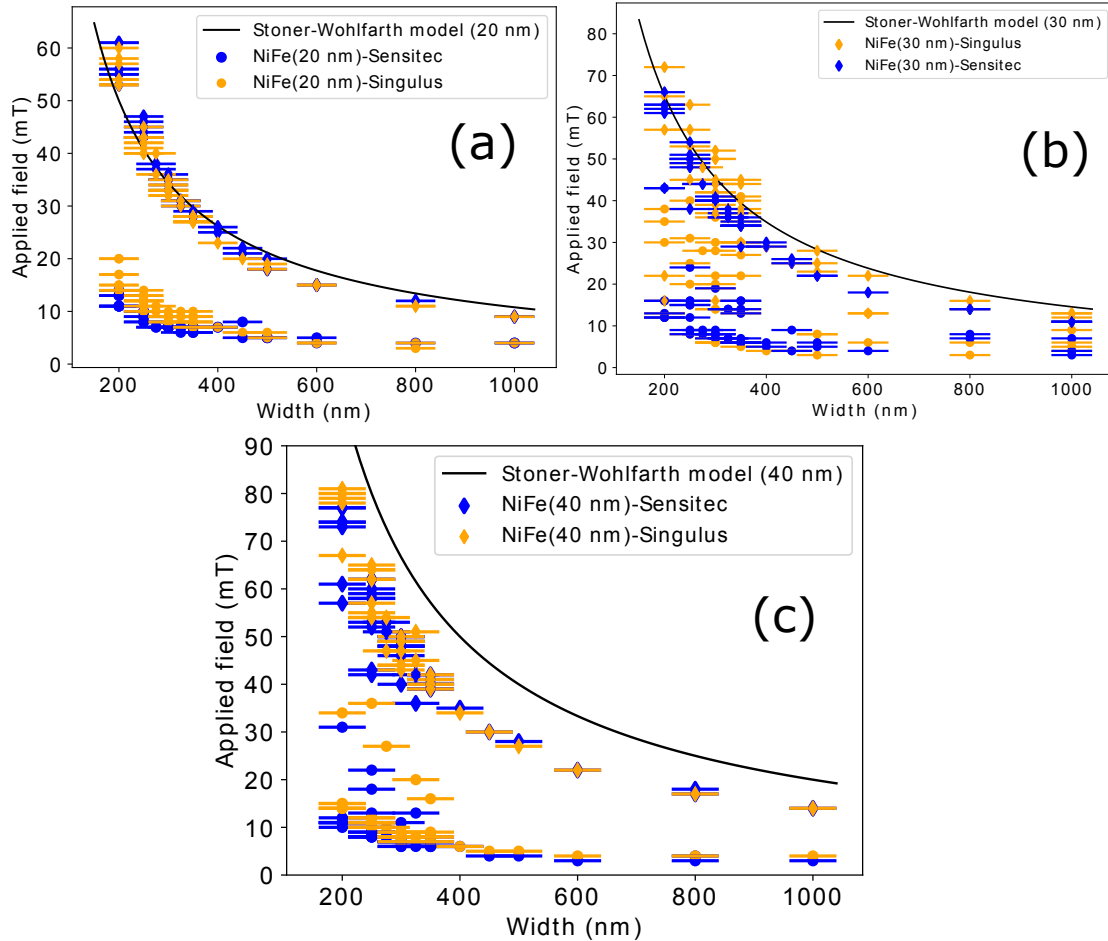


FIGURE 5.32: (a) Plot of the depinning/propagation fields (disks) and nucleation field (diamonds) for a sample grown at Sensitec (blue) and grown at Singulus (orange) for a 20 nm thickness of $\text{Ni}_{81}\text{Fe}_{19}$. (b) Plot of the depinning/propagation fields (circles) and nucleation fields (diamonds) for a sample grown at Sensitec (blue) and grown at Singulus (orange) for a 30 nm thickness of $\text{Ni}_{81}\text{Fe}_{19}$. (c) Plot of the depinning/propagation fields (circles) and nucleation fields (diamonds) for a sample grown at Sensitec (blue) and grown at Singulus (orange) for a 40 nm thickness of $\text{Ni}_{81}\text{Fe}_{19}$. The black line represent the Stoner-Wohlfarth model for the respective thicknesses.

Conclusion

To summarize, we see that using different deposition conditions and various machines are yielding clearly distinguishable stacks as visible in the hysteresis curves and the XRD measurement data. These differences related to the field applied during the growth of the sample resulting in a different texturing. Despite the latter, the field operating window seems virtually unaffected. This lack of influence is due probably to the fact that the shape anisotropy is dominating enough to mask any of the effects of changes in crystallization. The DWs are however less affected by this when confined in the wires. This result is essential for the production of the sensor device because it reveals a certain robustness concerning deposition variations and thus a reliability in that matter. However, no other deposition techniques were thoroughly investigated during the project. Some samples were deposited with a molecular beam epitaxy technique, but the results did not yield conclusive insights after the patterning of the samples.

5.3.4 Influence of the patterning process

Finally, we investigate the influence of the patterning process used. In the past, the open-16-loop structure was always patterned using a photolithography stepper for the transfer of the designs onto the resist. With this technology, the photon wavelength limits the minimum lateral dimensions of the structures, and thus the resolution of the technique. A possible approach for the reduction of the wavelength of the particle exposing the resist, nests in the usage of an electron beam lithography system. Such a tool generates electron beams that enable the patterning of structures down to a few of nanometers in lateral precision. The standard recipes used for the patterning with the electron beam are described in the patterning section of the experimental chapter, all the detailed recipes can be found in the appendix.

Issues encountered

At the beginning of the electron beam (ebeam) patterning, we faced some issues: The encountered problems concern the merging of different geometrical sections of the structures in the software of the tool. While drawing the designs, the different elements (e.g., the corners, straight lines of the loops, and nucleation pad) are created separately, we then merge them to obtain a complete structure. The latter is performed because the software displacing the electron beam treats merged structures as a single entity. After the writing of an entity (e.g., corner), the software chooses the following object, processes again and selects a starting position. So in the case of unmerged structures, we could end up with disconnected elements in the same structure due to the lack of precision of the writing software, which is what happened (see Fig 5.33 (a))

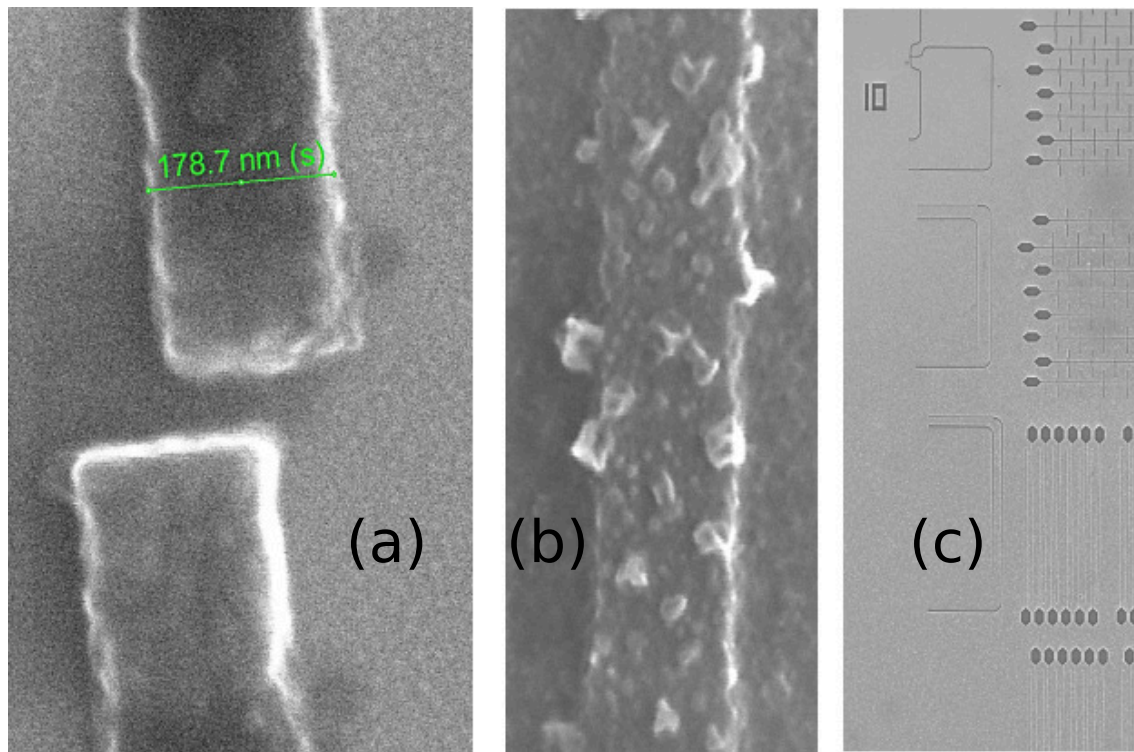


FIGURE 5.33: (a) Scanning electron microscope micrograph of two wire drawn in the resist being unconnected. (b) SEM micrograph of particles appearing on the sides of the wire made of resist, which appears to be some contamination. (c) SEM micrograph representing half of the structures being drawn after development of the exposed resist.

Furthermore, the software possesses two possible writing modes, one being the meander mode where the structures are drawn using a meander pattern and a line mode where it straightforwardly follows a line. The software appeared to overload when large and complicated structures similar to ours are drawn in a meander mode, thus yielding half drawn structures (see Fig. 5.33 (c)) The line mode could handle this type of structures, but the computation necessary to draw them would take a humongous amount of time. The only possibility for us to use the ebeam lithography was to unmerge all the structures, which forces us to teach the software to obtain a close to perfect precision to avoid stitching errors. Finally, contamination needed to be avoided to achieve well-defined structures (see Fig. 5.33 (c)).

Patterning using ebeam lithography with various negative tone resists

In this subsection, we present the results of the measurement of the depinning field and nucleation field limits obtained, for structures processed with an electron beam machine with various exposure doses and resists. We chose to use a negative tone resist to allow the ion milling of the material stack. The latter was motivated by the necessity of providing a patterning process that could still be

included in the production line of Sensitec. The material stacks are deposited at Sensitec in a magnetron sputtering tool. The stack constitutes in the substrate on which a single layer of Ni₈₁Fe₁₉ of selected thickness and 4 nm Ta capping layer is deposited.

AR-N 7520.073 The first selected resist is called AR-N 7520.073. It is a negative tone and non-chemically amplified resist. It also exhibits an excellent sensitivity, a very high resolution (< 30 nm) and a remarkable process and plasma etching stability (154). In our process, the resist has a thickness of 100 nm after spin-coating on the surface of the sample. Before patterning, some of the described innovative designs were coded for the ebeam machine to use. The samples are then patterned using an ebeam Raith Pioneer machine (155). Various acceleration voltages from 10 to 30 kV, various step sizes of the beam as well as exposure doses were tried. Following the exposure, the development is necessary to wash away the unexposed resist from the surface. Over the trials, we identified the extreme sensitivity of this particular process for this resist. In our conditions and for our samples, the development is successful after 24 s. Other times were tried never yielding as good results. This time is also very sensitive to the previous baking and the dose used during the exposure. For this resist, the best conditions for the processing of 200 nm wire widths are an exposure dose in between 125-140 $\mu\text{C}/\text{cm}^2$ and a development time between 23-25 s. At this step, the resist is then often imaged with the SEM to assess the proper transfer of the dimensions and structures. After the development, we etched the structures with an ion beam etcher machine. Despite the described good stability of the resist when submitted to an ion milling process, the etching of the material stack for a time of 4 x 1 min with a break of 30 s in between would yield structures of the quality displayed in Fig. 5.34 (b). The quality refers mainly to the side edge roughness of the wire. This induced edge roughness is attributed to the damage induced to the resist. In fact, local heating and etching of the resist sides is an issue for the transfer of the pattern to the material stack. The resist is, in theory, etched 3 times slower than our magnetic metal. However, the sides of the resist, which are attacked by the chemicals during the development process and might not be entirely exposed, are fragile and tend to break under the ion etching. The consequences are the creation of uneven sides and then edge roughness. The heating of the material during the ion etching is also potentially harmful. In fact, despite the sample being mounted on a backside-cooled sample holder, the temperature might locally increase thus curing the sides of the resist and further damaging. The combination of the processes yields very rough wires if the resist thickness is too little as compared to the thickness that we wish to etch. In our case, for a 40 nm depth of etching the 100 nm resist appeared challenging to handle. Despite these issues, we pushed the optimization of the mentioned resist. For the improvement of the process, we used a less harmful ion etching by rotating the angle of the beam with the surface normal. Indeed, the milling is ordinarily performed at 10° with the surface normal, thus reducing ion implantation in the wires but increasing the fencing (redeposition of the etched material) on the side edges of the resist. The etching procedure is then sequenced in the following way: An etching of 12 s is performed at 0° with the surface normal, and then the beam is blanked for 2 min. Then the etching is performed for 21 s while the sample rotates from the 0°

angle to 90° and the beam is blanked for 2 min. Finally, the sample is etched at 90° for 36 s, and the beam is blanked for 2 min. The sequence is repeated until the desired etched thickness is reached. The time values given here were phenomenologically determined and are material dependent. The times are powers of 3 because it takes 3 s for the sample holder to complete a full rotation. Using this sequence, and a properly selected exposure dose and development time, we achieved wires of the quality shown in Fig. 5.34 (c).

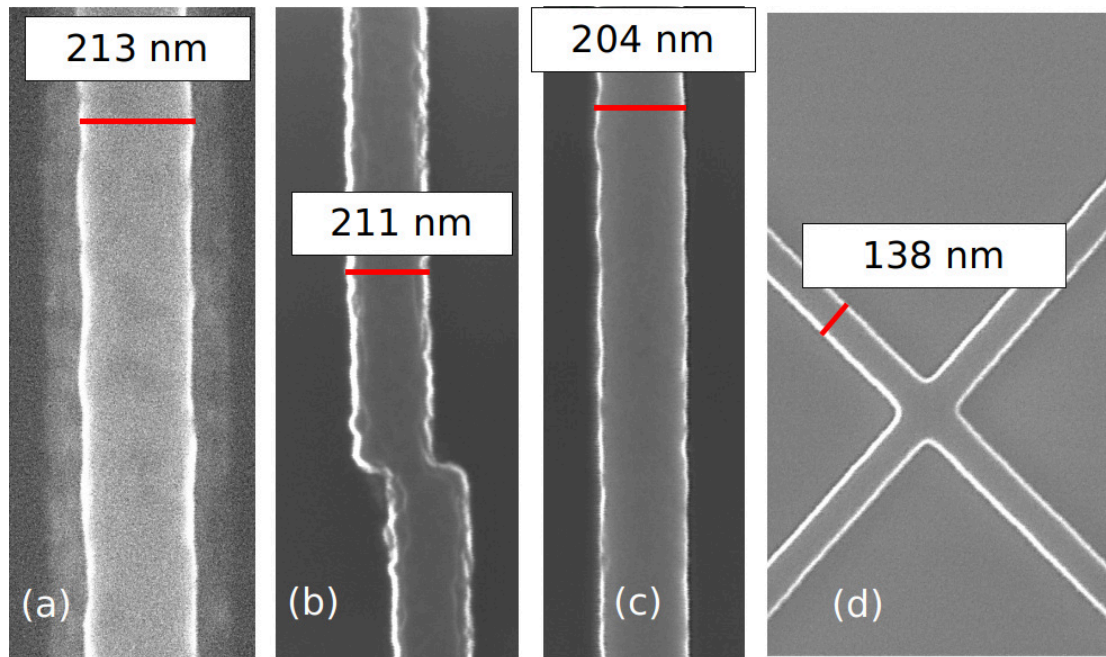


FIGURE 5.34: (a) SEM micrograph of a 200 nm nominal width wire patterned with photolithography followed by etching at the company Sensitec. (b) SEM micrograph of a 200 nm nominal wire width patterned with the resist AR-N 7520.073 with the electron beam lithography system at the Johannes Gutenberg University followed by etching. (c) SEM micrograph of a 200 nm nominal wire width similarly processed as in (b) but after optimization of the parameters. (d) SEM micrograph of a 150 nm nominal wire width pattern with the HSQ resist.

HSQ resist mixed with methyl isobutyl ketone or MIBK After the optimization of the AR-N 7520.073, the edge roughness is in the range of 10-15 nm. These values constitute a significant improvement from the edge roughness of the wires patterned at Sensitec (Fig. 5.34 (a)). Furthermore, the trapezoidal cross-section in Fig. 5.34 (a) appears more rectangular as observable by the lack of tails alongside the edges. Despite the improvement, the ebeam lithography is expected to yield a better wire quality. The resist is changed for the Hydrogen silsesquioxane resist (HSQ), which is as well a negative tone resist. It is, however, an inorganic resist. The resist sold under the name FOX-15 and after XR1541 allows the patterning of impressively detailed structures. In fact, the minimal feature size indicated by

the manufacturers are 6 nm and 3.3 nm of edge definition (156, 157). Furthermore, the resist has the property to turn into an amorphous silicon oxide after the exposition or baking rendering a very solid and sharp edge. The process recipe is described in the appendix. The resist is significantly easier to handle for our purpose. The etching does not damage the wires as much due to the increased thickness of the resist (200 nm), and its amorphous composition yields a very smooth edge. The dose used for the processing is, however, more significant, i.e., $3000 \mu\text{C}/\text{cm}^2$. Structures as small as 30 nm were achieved with the present recipe. In Fig. 5.34 (d), the wire width is 138 nm, and the edge roughness is less than 10 nm. The samples were etched following the rotation of the etching beam sequence.

AR-N 7520.017 After the use of the HSQ resist, we changed to a resist requiring a lower exposure dose. Structures with a 200 nm nominal width were patterned using the AR-N 7520.017. It is a much thicker resist than the previous ones (400 nm thick after spin-coating), thus allowing a smooth etching process. The advantage of this resist as compared to the others is its high sensitivity. The dose used for the exposure was only $50 \mu\text{C}/\text{cm}^2$ with a 30 kV acceleration voltage. After the etching of the structures, the wires were imaged with a SEM, and the wire width is found to be slightly larger than the nominal 200 nm width. The side edge roughness is the same as the one presented for the wire processed with the resist AR-N 7520.073 (see Fig. 5.34).

Comparison between the different processing methods The measurement of the depinning fields and nucleation fields are performed on the samples previously described. The measurement is performed with the MOKE microscope with the 2-3 turns rotation sequence. Astonishingly, the field operating windows of the sample processed at Sensitec are better than for the others. Furthermore, the topographically best-defined structures processed with the HSQ resist yielding the worst results. The latter is unexpected as a better edge roughness should yield a lower depinning field and a higher nucleation field. It should be pointed out that the cross-sectional shape is similar for all the samples that were measured and are displayed in Fig. 5.35. In fact, the sample processed at Sensitec were etched for a large enough thickness to obtain similar results as the best exposed in the subsection concerning the cross-section shape 5.3.2. Thus the geometry of the cross-section should have no influence.

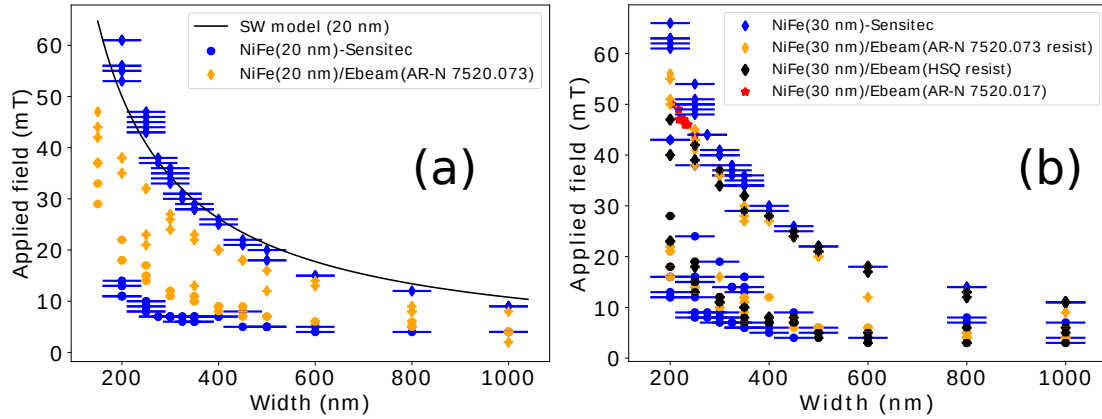


FIGURE 5.35: (a) Plot of the depinning (disks) and nucleation field (diamonds) for a 20 nm thick $\text{Ni}_{81}\text{Fe}_{19}$ layer patterned with optical lithography (blue) and with e-beam with the resist AR-N 7520.073 (orange). (b) Plot of the depinning (disks) and nucleation field (diamonds) for a 30 nm thick $\text{Ni}_{81}\text{Fe}_{19}$ layer patterned with optical lithography (blue) and with e-beam with the resist AR-N 7520.073 (orange), HSQ (black), and AR-N 7520.017 (red).

In Fig. 5.35 (a), we observe the difference in both the depinning field and nucleation field for the photolithographically or ebeam patterned wires. With the ebeam patterning, 150 nm width wires were processed that yielded a substantial enhancement of the depinning field and reduction of the nucleation field. An explanation of such an effect can arise from the energy that is put in the material stack during the processing. In fact, the ebeam patterning tends to deposit more energy into the stack than the photolithography just due to the more substantial energy transported by the electrons. This energy can contribute to the heating of the system and trigger the crystallization or the damaging of the stack. In Fig. 5.35 (b), we present all the resist used for the patterning of the open-2-loop structures. Focusing on the 200 nm width, we observe the decrease of nucleation field with an increase of the energy provided to the system. Using photolithography offers much better results than the ebeam lithography only due to the less amount of damages performed by the patterning process. Despite showing a massive enhancement of the edge roughness, the ebeam lithography does not provide a better operating window. Furthermore, the reduction of the exposure dose for the resist AR-N 7520.017 (red stars in Fig. 5.35) and thus the reduction energy applied to the stack also does not yield improved results.

Conclusion

We demonstrate the possibility of the creation of well-defined wires with the use of an ebeam lithography process. Thanks to the HSQ resist, an edge roughness lower than 10 nm is achieved for wires with a 200 nm width. Despite the latter,

the FOW is not enhanced and is even reduced as compared to the structures processed with photolithography. The ebeam lithography remains a fantastic process for its versatility and the possibility to investigate a large variety of patterns, but it does not yield the best operating window for magnetic structures. Optical lithography with a phase shift mask or lift-off with ebeam lithography should then be considered for the largest possible operating window.

5.4 Conclusion

In the present chapter, we explored the limits of the field operating window of open-loop devices. We first demonstrated that the non-uniformity of the current process used for the open-16-loop dramatically influences the nucleation field of the open-loop structures. The propagation field is, however not strongly affected by the latter. Innovative designs and a new setup are created for the faster investigation of the limits of the field operating window. We observe that the number of vertices used for the corners tends to influence the nucleation field. The latter is attributed to an increased width at the connection between the segments introduced by the processing. The 3-vertices corners present in the original design of the open-16-loop should then be changed for 16-vertices corners or more. Furthermore, we observe the drastic decrease of the field operating window with increasing length of the structure or number of loops. This effect is detrimental to the scaling of the technology. We then probe the propagation field with a large number of turns and observe that to obtain the correct propagation field, measuring a large number of devices is not sufficient. This limit remains cumbersome to study without better imaging tools, it, furthermore, is mainly affected by the quality of the processing and not by geometrical parameters. We then study the nucleation field hoping to find a more comfortable handle for the improvement of the FOW. We first modify the thickness of the magnetic layer and observe a saturation of the scaling of the nucleation field. This saturation is located at the transition between the nucleation with 2 Néel DWs and the nucleation with 2 Bloch DWs. We then modify the shape of the cross-section and identify the little influence of the edge roughness and the massive one from the trapezoidal cross-section. This cross-section appears as the main contributor to the scaling factor used to fit our data with the Stoner-Wohlfarth model. The $\text{Ni}_{81}\text{Fe}_{81}$ deposition conditions are then varied by depositing the material with two different sputtering systems. The application of a field during the growth of the use of a NiFeCr seed layer does not modify the field operating window thus showing some robustness in that matter. Finally, the patterning process is modified to try to reach a perfect rectangular cross-section with very little edge roughness. For the latter, we used the electron beam lithography, and despite the much-improved shape, the FOW is decreased. This puzzling result is attributed to the damage induced by the electron beam during the processing that exceeds the gains from the improved shape.

As a conclusion to obtain the largest FOW, our opinion is that the focus should be on the nucleation field. A large nucleation field is reached for a rectangular cross-sectional shape without edge roughness. Furthermore, the structures need

to be patterned with a 'soft' technique such as photolithography or by using a lift-off technique. The architecture of the structure should as well be as smooth as possible to avoid pinning points or enlargements of the width.

Experiment	Propagation field	Nucleation field	Figure
Decreased Width from 200 nm to 1000 nm	Increase: +10 mT	Hyperbolic increase: +60 mT (SW model)	Fig. 5.16
Increased Side-length from 200 μm to 800 μm	Increase: +3 mT	Decrease: -7 mT	Fig. 5.7
Increased Thickness from 20 nm to 100 nm	No clear difference	Large increase up to saturation	Fig. 5.16
Decrease in number of segments in corners 16 to 0 vertices	Increase: +9 mT	Decrease: -23 mT	Fig. 5.8
Increase in Edge roughness	Slight increase	Slight decrease: -3 mT	Fig. 5.25
Trapezoidal shape	Slight decrease: -6 mT	Decrease: -27 mT	Fig. 5.26
Change in deposition conditions and texturing of the magnetic layer	No clear effect	No clear effect	Fig. 5.32
Ebeam lithography	No clear effect	Decrease: -21 mT	Fig. 5.35

TABLE 5.1: Table summarizing the effect of the various modifications to the wires on the propagation and nucleation field. An indication of the appropriate figure is provided.

Chapter 6

The closed-loop structures for the unturn sensor concept

Most of the results presented in this chapter were published in (15). The text and the figures were adapted for this manuscript.

6.1 Introduction

In the previous chapters, we introduced the first industrial device realization of a magnetic domain wall based sensor and the research performed for its improvement. Despite, DWs having been under investigation since the mid-1960s (1, 5, 10–13, 21, 43, 158–163) and the open-loop is the only multi-turn counter, which can sense and store the number of turns with a true-power-on functionality. This sensor can count from 0 to 16 and back, it is manufactured by Novotechnik and already commercially available [RSM-2800 Multiturn and RMB-3600 Multiturn (164)]. The concept of this kind of sensors is the generation and movement of 180° DWs along Giant Magnetoresistance nanowires in an open-loop-spiral-like geometry (see Fig. 6.3 (a)). However as described in the previous chapter 5, the scaling of this particular geometry remains limited, and only a maximum of 40 turns can be counted. However, many industrial applications require a significant number of counts (from hundreds up to millions). A different approach was recently proposed based on using closed loops with a different number of cusps (see Fig. 6.1) directed toward the center of the loop (13). However, an issue inherent to the cusp geometry is the double width caused by the merging of two nanowires at this position. This characteristic imposes a reduction of the maximum sensed field before unwanted and uncontrolled random nucleation is initiated on this broader part. The cusp geometry thus narrows the field operating window (FOW) of the sensor, which is defined by the difference between the maximum magnetic field above which unwanted DW nucleation occurs and the minimum field necessary for a reliable transport of the DW throughout the whole structure. Compared to a perfect straight stripe, the minimum field necessary for propagation through a cusp is also significantly increased. Thus the FOW is narrowed by an increased minimum and reduced maximum operating field, making this device geometry challenging for real use.

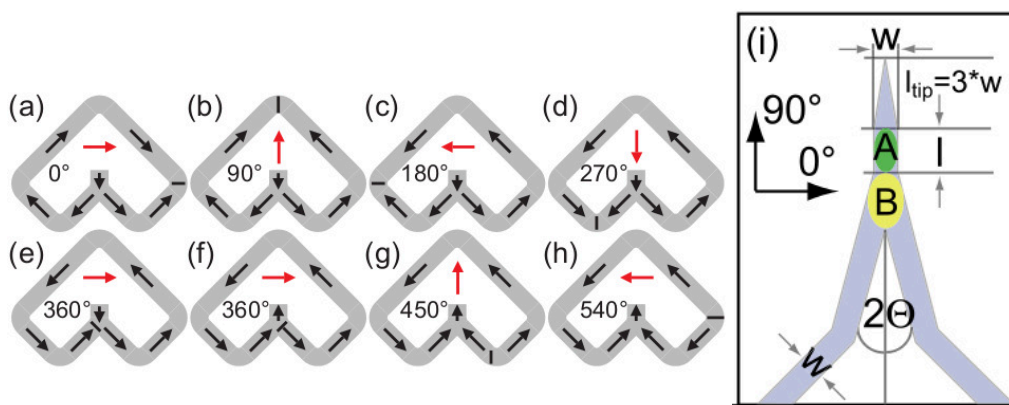


FIGURE 6.1: (a)-(h) Movement of a DW through a loop with one cusp for the rotating magnetic field in the CCW direction in steps of 90° . The magnetization state in the loop and the DW position is indicated by black arrows and a black line, respectively. The field angle of the rotating external field is given as number and illustrated with the red centered arrow. (i) Schematic representation of a cusp. Adapted from (13), more details can be found in it.

Due to the limitations imposed by the reduced FOW, there is a need for the development of alternative concepts. A possible different idea uses the combination of intersecting closed loops capable of counting coprime numbers of turns. This concept includes a distinct geometrical feature, namely a cross of nanowires to allow the intertwining of loops (Fig. 6.3 (b))(165). This geometry fundamentally provides for a much improved multi-turn counter. We name such a structure a n -CL, where n is the number of closed loops. For example, Fig. 6.3 (b) shows a 3-CL device with 3 closed loops and 2 crossings that can count 4 turns. Every n -CL contains a minimum of 2 and a maximum of $2n-2$ of DW for sensing. An intrinsic characteristic of the closed loop structure (Fig. 6.3 (b)), and arguably an essential one, is the possibility to automatically reset back to counting from 0 after achieving the maximum number of turns offered by the architecture. Using this resetting mechanism with the concept of coprime number counting permits to achieve counting of a much more significant number of turns. This type of counting is allowed by positioning several n -CLs next to each other. For example, with $n = 3, 4, 5$, and so forth with n being the coprime number. The results of individual structures are combined to enable counting to large numbers. The simultaneous use of a 3-CL, a 4-CL and a 5-CL (see Fig. 6.2) yields different sequences of output states allowing a maximum count of $3 \times 4 \times 5 = 60$ turns (Table 6.1), which is already more than any open-loop structure (Fig. 6.3 (a)) could ever do. The method is scalable and with 7 different n -CLs ($n = 5, 7, 9, 13, 16, 17$, and 19), the number of turns available is already $5 \times 7 \times 9 \times 13 \times 16 \times 17 \times 19 = 21 \cdot 10^6$ turns.

Maximum number of turns	3-CL	4-CL	5-CL
State of the device after 1 turn	1	1	1
2 turns	2	2	2
3 turns	3	3	3
4 turns	1	4	4
5 turns	2	1	5
6 turns	3	2	1
31 turns	1	3	1
61 turns	1	1	1

TABLE 6.1: Table summarizing the output of the devices for different count numbers. Adaptation from (15).

This closed loop multiturn sensor thus opens up additional fields of applications where the open multiturn counter would be inefficient, such as, for example, highly sensitive angle detection via pole wheels.

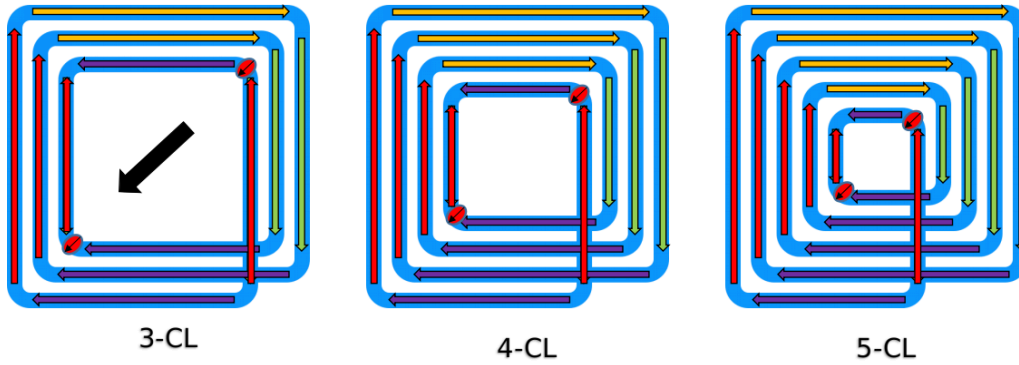


FIGURE 6.2: Schematic representation of 3 closed loops with $n = 3, 4,$ and 5 . The black arrow represents the applied field direction. The red ovals represent a DW and the arrows with various colors represent the magnetization direction.

However, a fundamental problem for this sensor operation arises at the eventuality that a DW does not propagate straight through the cross but takes a turn and thereby changes its path leading to a counting failure event. This event is particularly likely if the external field direction that drives the DW through the cross is not well controlled. Therefore, more sophisticated device geometries than the one shown in Fig. 6.3 (b) are needed for reliable device operation, robustness and fault tolerance.

In this chapter, we present a novel sensor architecture that can conceptually reliably count large numbers of complete turns of a rotating applied magnetic field. The structure is designed to comprise a new syphon shaped element in addition to the cross-shaped intersections of nanowires (166). This allows for the desired control of the propagation direction of the DW under the application of a rotating field. First, we introduce the different possible states that can be present in the cross structure and explain the necessity for a syphon structure. Second, the

angular dependence of the crossing and the syphon are separately simulated to extract the critical points of the two geometries. We also present different possible architectures for the cross and their individual advantages. Finally, the results are combined to observe the expected behavior of a complete structure. We identify the three key parameters that allow us to gauge the reliability of the structure, and optimized devices are demonstrated for further improvements of the concept.

6.2 Concept for a DW based multi-turn counter with crosses and syphons elements

To overcome the limitations caused by the cusp geometry, we propose the new concept, schematically shown in Fig. 6.3 (b). Here the inner and outer end of the spiral of Fig. 6.3 (a) are connected via a nanowire generating a cross-shaped intersection. As demonstrated in the previous chapters, in magnetically soft wires, the nucleation field for a DW follows a simple Stoner-Wohlfarth like model (14), and it is thus an inverse function of the wire width. A cross leads to only a $\sqrt{2}$ -fold increase of the width of the nanowire in its diagonal as compared to a 2-fold increase with the cusp geometry (13). Quantitatively, with a 30 nm thick and 300 nm wide stripe of $\text{Ni}_{81}\text{Fe}_{19}$, in the framework of the SW model, the nucleation field is improved by at least 40% by utilizing a cross structure as compared to a cusp structure.

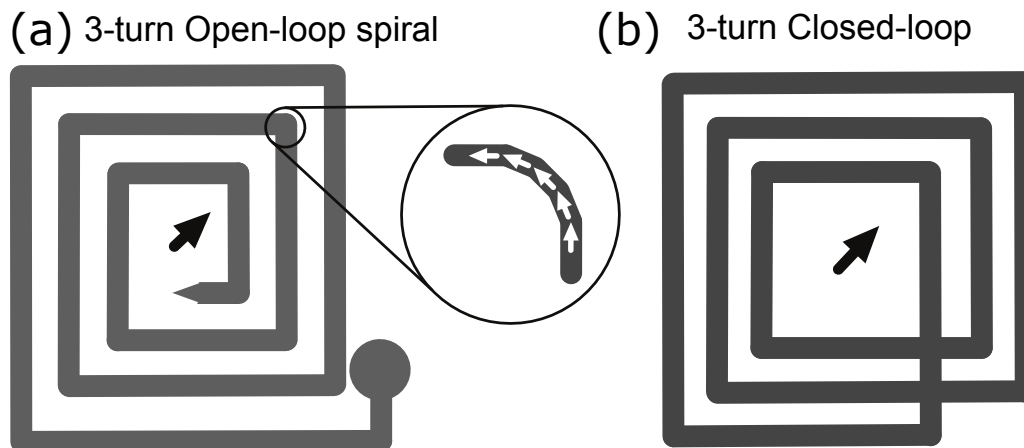


FIGURE 6.3: (a) A 3-open-loop spiral with DW nucleation pad and a pointed end. The enlargement shows the polygon-shaped corner with 22.5° kink angles usually used (164). (b) A 3-closed-loop structure with two cross-shaped intersections. Note that, in a real device, the distance between two crosses is expected to be much larger than the wire width effectively decoupling the crosses. Adapted from (15).

The propagation of DWs in straight and curved wires is well established (43), and the motion of a DW through the cross has been studied (167, 168). However, the details of the reliability of this process are still under active investigation due

to the complex dynamics involved in the process. In this section, dedicated to the explanation of the concept of the sensor mechanism, we used a transverse domain wall type as a simple representation of a DW. The quasi-static states before and after traveling through the cross are represented in Fig. 6.4. They illustrate the process of a moving DW in the horizontal arm from the left to the right side under conditions where the magnetization of the vertical arm is in the energetically favored state, i.e., parallel to some component of the applied field (see Fig. 6.4 (a)). Since both branches have the same width, the magnetization structure in the cross is stray-field free. When the DW is to the left of the cross (Fig. 6.4 (a)), there is a continuous magnetic flux from bottom to left and from right to up. The magnetization is along a 135° direction in the core of the cross. When the DW has moved through the cross, the core magnetization is rotated by 90° in the clockwise direction forming a stray-field-free state (Fig. 6.4 (b)) again.

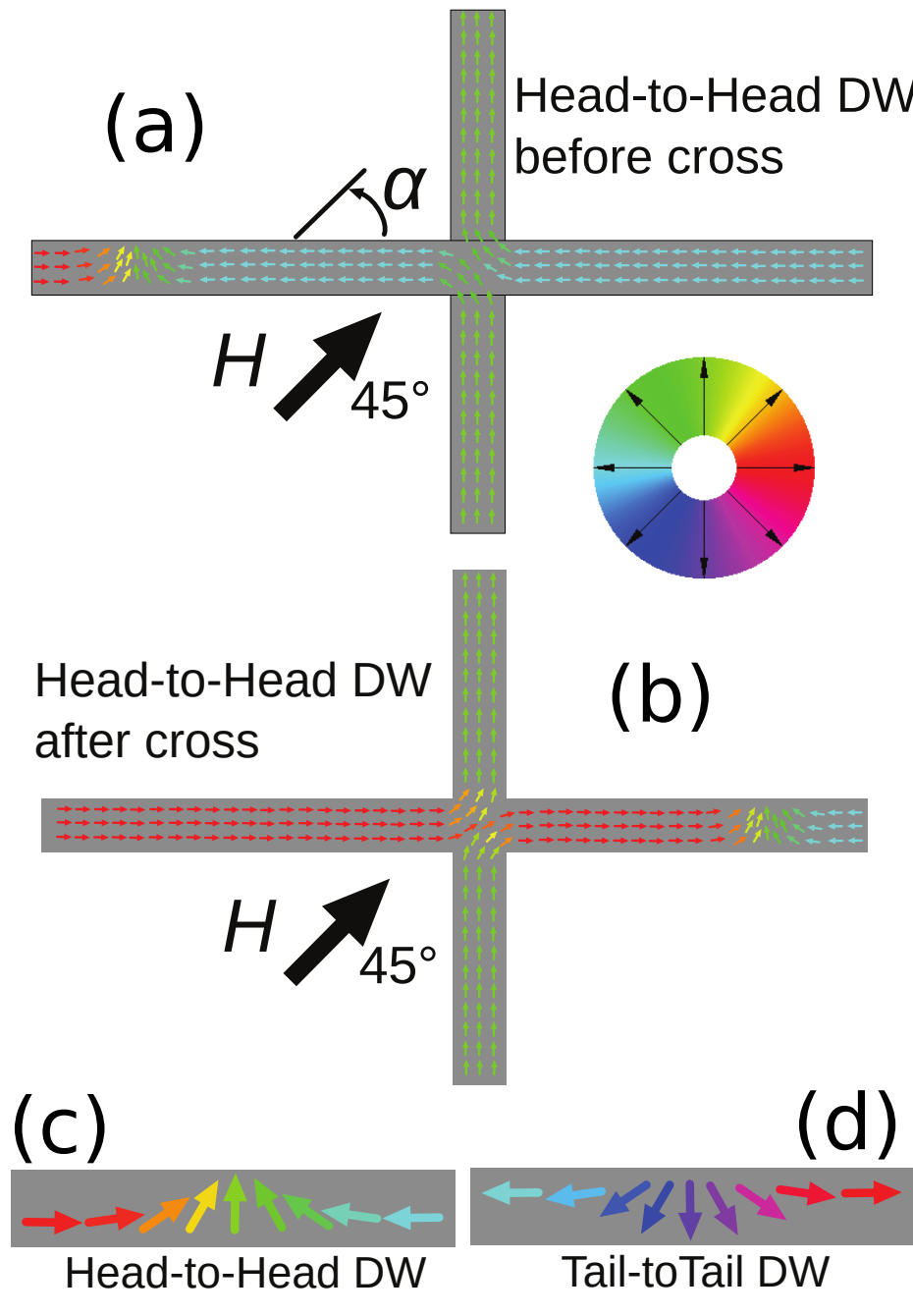


FIGURE 6.4: Sketch of a DW configuration before and after moving across a cross with an energetically favored magnetization state of the vertically oriented arm. α is the angle between the applied field direction and the horizontal direction. (a) DW positioned before the cross in the left arm. A field H at $\alpha = 45^\circ$ moves the DW towards the cross. (b) DW positioned in the right arm after moving through the cross. (c) Schematic representation of a Head-to-Head DW, and (d) a Tail-to-Tail DW. The color code indicates the in-plane magnetization direction as shown by the color wheel. Adapted from (15).

In Fig. 6.5, we present the second possible starting configuration. In this case,

the magnetization of the vertical arm is in a high energetic state as the magnetization is anti-parallel to some component of the applied field. Nevertheless, the magnetization pattern of the cross is stray field free, and the core magnetization is directed in a 225° direction as shown in Fig. 6.5 (a). As a result of this configuration, the magnetization in the top, bottom, and right arm are in a higher energetic state. Therefore the DW could travel horizontally or vertically (up or down) resulting in the three states shown in Fig. 6.5 (b), (c), and (d). Only the movement in the horizontal path (Fig. 6.5 (b)) yields a stray field free configuration (switching of the core magnetization by 90° from 225° to 315°). Any propagation of the DW into the up or down arms results in a magnetization structure with a 180° DW (Fig. 6.5 (c)) or an Anti-Vortex state (Fig. 6.5 (d)) in its center. From an energetic point of view, the energy barrier to overcome in the final states in Fig. 6.5 (c) and d is higher than in the sole horizontal depinning in Fig. 6.5 (b). This is due to the required energy to create an additional DW at the cross. From this simple picture, we intuitively expect a preferred DW motion in the horizontal direction toward the stray field-free state in Fig. 6.5 (b) instead of the more energetic states in Fig. 6.5 (c) and (d). Despite those different energy barriers for the various final states, if the applied field exhibits a significant component along the vertical direction, the DW is likely to move vertically resulting in a failure of the operation of the sensor device. Therefore, it is desirable to constrain the DW propagation to angles around $\alpha = 0^\circ$ respectively 180° . However, in a simple closed-loop multi-turn counter, the DWs are moved by a rotating magnetic field. We consider in this case a clockwise rotation of the field. The motion in the horizontal nanowire starts depending on the natural pinning strength for a Head-to-Head DW in the wires at field directions around $\alpha = 70^\circ - 80^\circ$ because the horizontal component of the applied field is sufficient to depin. Under these conditions, the DW would not reliably travel from the left arm to the right arm as desired, but instead into one of the vertical arms as depicted in Fig. 6.5 (c) and (d), resulting in a counting error of the sensor. To prevent this failure, we introduce a novel syphon-like geometry (Fig. 6.6). This syphon has the aim to pin the DW in its arms until the field angle is favorable for a propagation only in the horizontal direction. For example, in Fig. 6.6 (a), with $\alpha = 45^\circ$ and $\theta = 45^\circ$ (syphon arm angle), β the angle with the perpendicular to the syphon arm is 0° thus the applied field is perpendicular to the syphon arm, and the DW is pinned in the arm. In Fig. 6.6 (b), with the applied field angle $\alpha = 30^\circ$, the angle $\beta = 15^\circ$ thus there exist a component of the field along the syphon arm and the DW can depin. At field angles lower than $\alpha = 45^\circ$, a larger torque is provided in the horizontal direction than in the vertical thus favoring horizontal propagation through the cross as depicted in Fig. 6.6 (b).

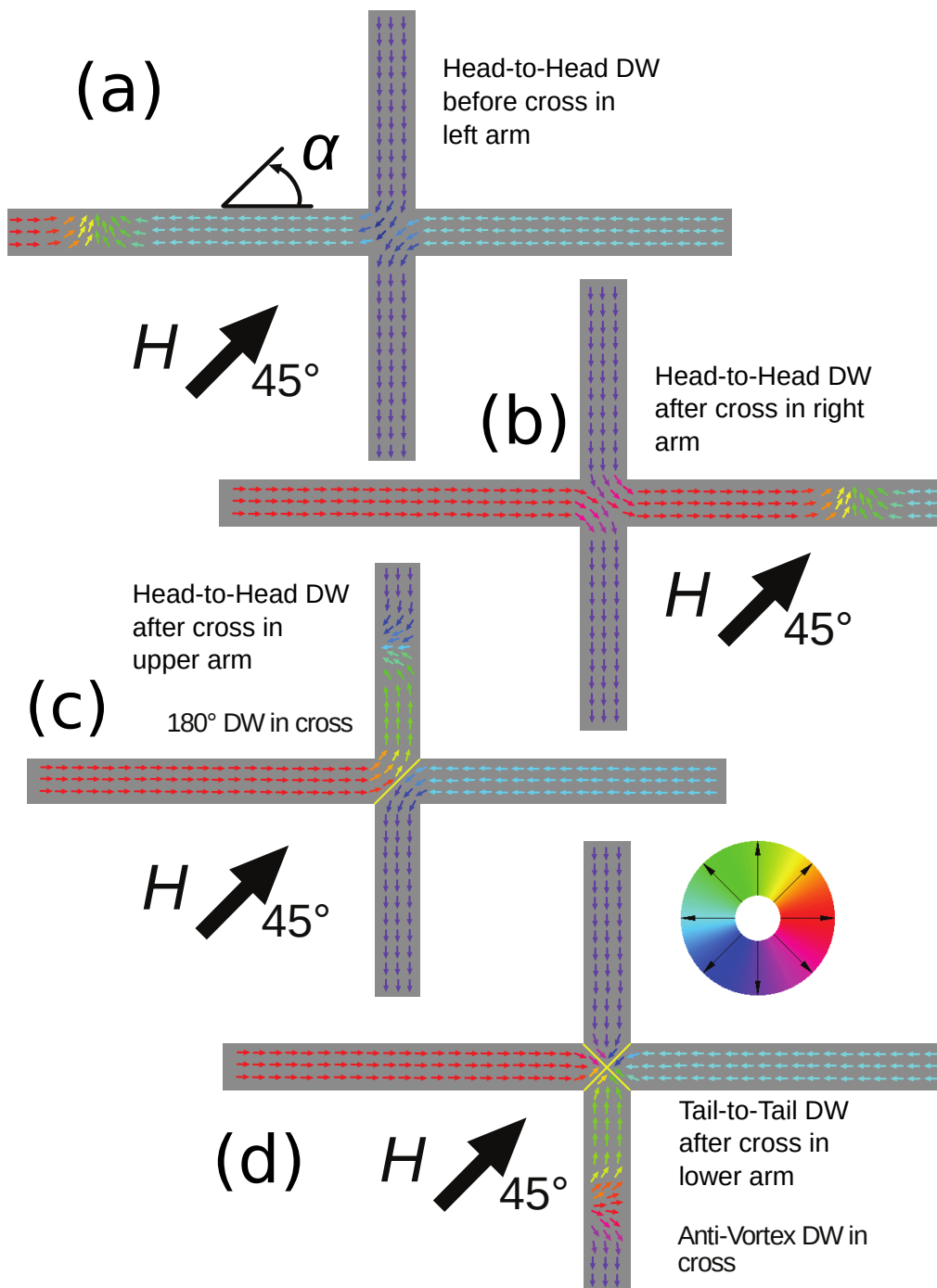


FIGURE 6.5: Sketch of the DW configuration before and after moving through a cross with the possible resulting magnetization structures. α is the angle between the applied field direction and the horizontal direction. The applied field can remagnetize the horizontal arm or the vertical arm. (a) The DW is positioned before the cross in the left arm. A field H inclined at 45° moves the DW towards the cross. For $\alpha = 45^\circ$ the DW can be positioned in any of the three arms after moving through the cross: (b) DW placed in the right arm. (c) DW placed in the upper (wrong) arm and (d) DW positioned in the lower (wrong) arm. In (a) and (b), the cross is DW-free. In (c), a 180° DW and in (d) an Anti-Vortex DW is located in the center of the cross. Additionally, in (d) the Head-to-Head DW must transform into a Tail-to-Tail DW during the movement through the cross. The in-plane magnetization direction is indicated by the color code visible on the color wheel. Adapted from (15).

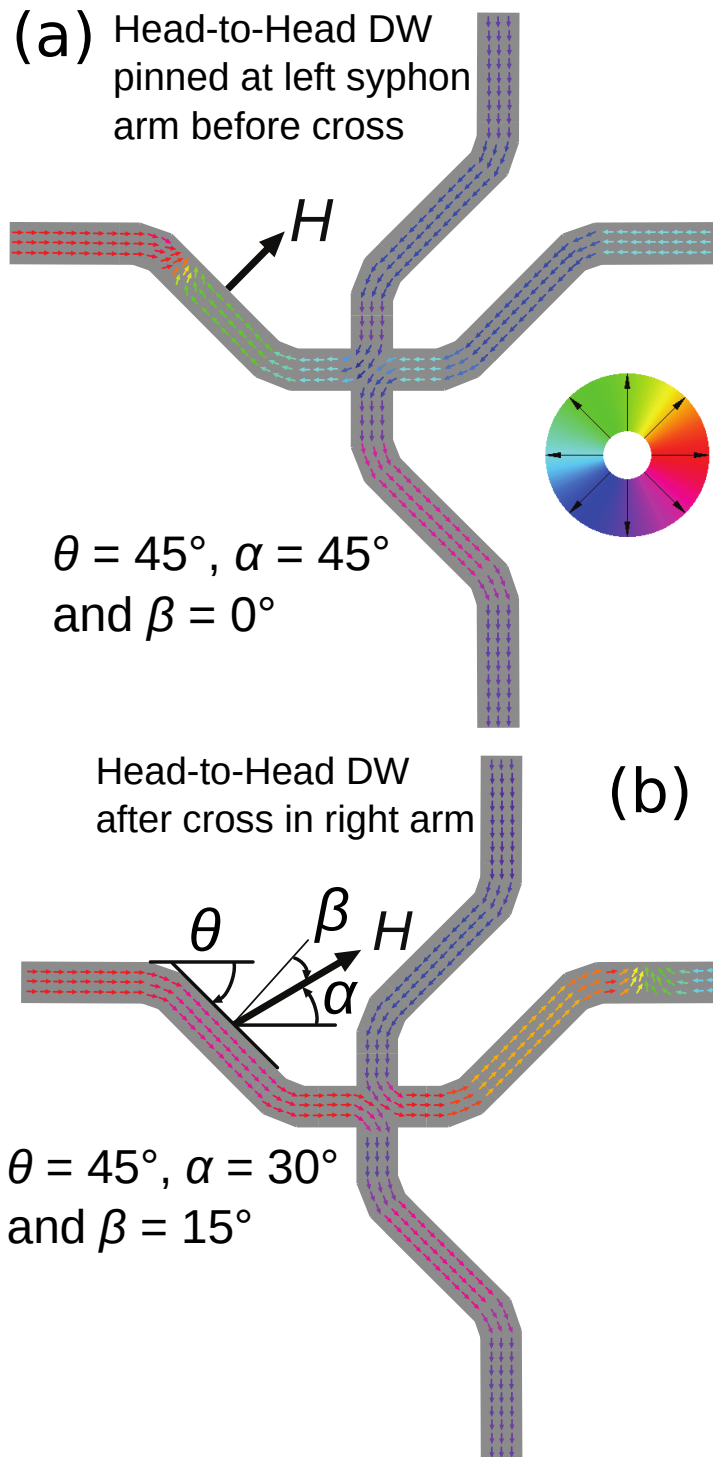


FIGURE 6.6: Sketch of the DW motion through a cross combined with a 45° syphon. θ is the angle of the syphon arm with respect to the horizontal direction, α is the field angle with respect to the horizontal direction, and β is the angle between the perpendicular direction with the wire containing the DW and the applied field direction. (a) A DW is pinned at the beginning of the syphon in the left arm for H inclined at 45° , resulting in no longitudinal component to move the DW into the syphon ($\beta = 0^\circ$). (b) The DW moved through the cross with H inclined at 30° ($\beta = 15^\circ$). Adapted from (15).

So far this conceptual discussion compares quasi-static states. The complexity of the DW motion under an applied external field can also yield other transitions. Therefore extensive micromagnetic simulations need to be performed to study the influence of the syphon geometry on the DW motion through the cross (see a snapshot in Fig. 6.7). The latter is then the key step to finding parameters that minimize failure and optimize reliability.

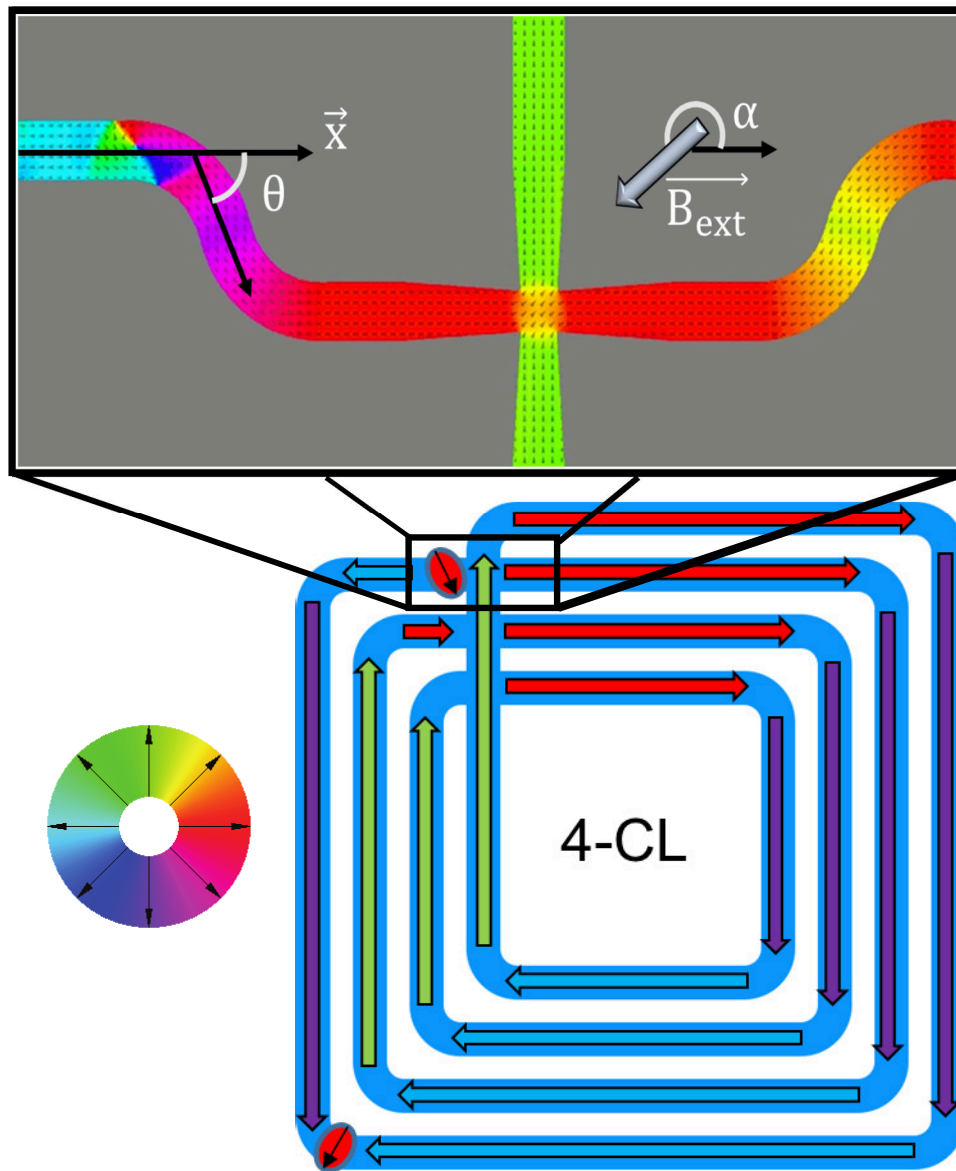


FIGURE 6.7: 4-Closed loop with a snapshot of a micromagnetic simulation in the inset. The various colored arrows represent the direction of the magnetization, and the red ovals represent the DW. In the inset, the syphon angle is θ and the angle of the applied field B_{ext} is α . The in-plane magnetization direction is indicated by the color code visible on the color wheel. Adaptation from (15).

All the previous discussion was based on an analysis of a Head-to-Head DW with α being between 90° to 0° and 0° to 270° . By symmetry, this is equally applicable to a Tail-to-Tail DW with α being between 90° to 180° and 180° to 270° .

6.3 Micromagnetic simulations

All the simulations are performed with the free software Mumax3 (119) on GPUs¹. The materials parameters used for $\text{Ni}_{81}\text{Fe}_{19}$ are: Saturation magnetization $M_s = 860$ kA/m, the exchange constant $A = 1.3 \times 10^{-11}$ J/m, no magnetocrystalline anisotropy and a Gilbert damping of 0.01. The thickness of the material is 30 nm, the width of the stripe is 300 nm, and the cell size was kept below $5 \times 5 \times 15$ nm³. The different relevant parts of the structure (cross and syphon) were separately investigated. The separate analysis is possible since the pinning potential in the syphon due to the corners is sufficiently strong to mask any attraction from the center of the cross. The two elements are then effectively decoupled and can be investigated individually in detail. While we have used a transverse DW as a simple representation of a DW in the previous section, the cross-section, and material used in the experiments and the micromagnetic simulations will favor a vortex DW. All simulations are thus started with a vortex DW that corresponds to the experimentally expected wall spin structure.

6.3.1 Crossing of two magnetic stripes

So far, the poorly controlled nature of DW propagation through the cross without a syphon is an effect that limits the use of n-CL structures for sensors. Despite some studies on the propagation of the DW in split paths (167, 169–171), DW dynamics propagating through the center of the cross is not yet fully understood, particularly its behavior about the reversal of the vertical arm of the cross. A systematic study of the DW propagation has been performed changing both the applied field strength and orientation. An initial configuration was obtained by placing a Tail-to-Tail vortex DW on the left arm and letting the system relax under no external applied field. A field with a chosen direction and magnitude was then applied, and the system was left to relax. Different testing conditions were then probed to determine if the desired behavior was obtained, namely the motion from left to right through the cross without the reversal of a vertical arm. The orange circles represent the pinning of the DW in the center (Fig. 6.8 (b), and Fig. 6.9 (a) from which an access to a video is available), the red diamonds the reversal of the vertical arm (Fig. 6.8 (c), and Fig. 6.9 (c) from which a video is accessible), and the blue diamonds the successful propagation through the cross (Fig. 6.4, 6.5 (b), and Fig. 6.9 (b) from which a video is accessible).

¹We would like to warmly thank the University of Salamanca as part of the WALL project for allowing us to use their GPUs to perform the simulation. We particularly appreciate Michele Voto for helping with the realization of the simulations and the fruitful discussions.

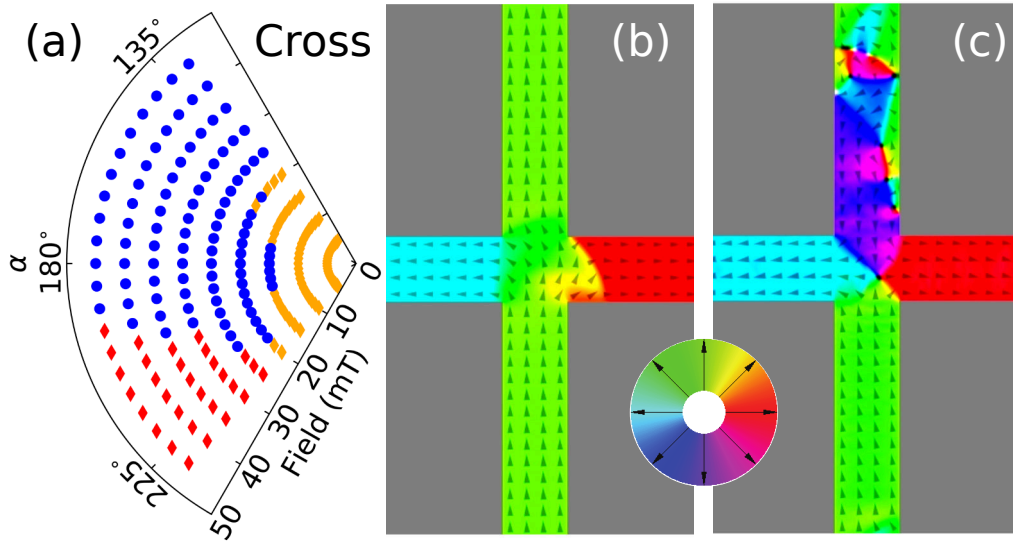


FIGURE 6.8: (a) Polar plot of the angular dependence of a Tail-to-Tail DW propagation with field orientation and magnitude represented as radius and angle respectively. The blue circles indicate successful propagation through the cross; the red diamonds represent a reversal of the vertical arm and the orange the pinning at the cross. (b) Spin structure of a DW pinned at a cross. (c) Snapshot of magnetization dynamics showing the splitting of the DW generating the reversal of the vertical arm in addition to the horizontal arm and thus representing a failure event. The in-plane magnetization direction is indicated by the color code visible on the color wheel. Adaptation from (15).

We notice that since the domain wall is Tail-to-Tail, the angular range for α is between 90° and 270° (centered around 180°) to be able to propagate the wall from left to right. The simulations are performed for the angle range between 130° and 230° which is sufficient to observe all the interesting switching behavior. The field amplitude is also kept below 45 mT, which is the nucleation field value of a wire in our system extracted from the Stoner – Wohlfarth model (34). Indeed, if the field reaches higher values, DWs can nucleate in the closed system, destroying the two studied spin structures. The applied field can be rotated clockwise or counter-clockwise in the device. However, from symmetry arguments, it is sufficient to scan one direction, and so we scan the plot starting from 240° towards 110° for different magnitudes of the field. At the first data points (230°), only failure events are encountered, i.e., pinning below 20 mT and vertical arm reversal above. The first propagation is reached for 20 mT at 220° . Regarding fields strengths, the first propagation occurs at 15 mT for a range of 10° centered around 180° denoting that the lowest depinning field is in between 10 and 15 mT (not observable due to our field step size). We observe an increase of the angular range of propagation as the field strength increases. In the case where the field is parallel with the vertical arm, no reversal can occur, however, in the opposite case it can. This effect results in a polar plot, which is not symmetrical around the 180° angle.

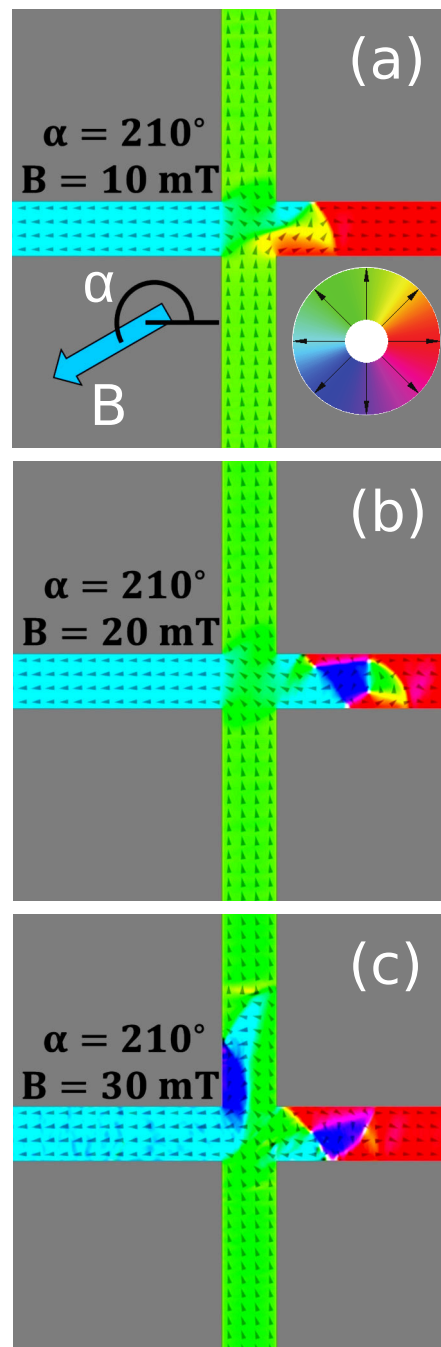


FIGURE 6.9: (a) VIDEO. 1. Snapshot of the magnetization with the DW is pinned in the center of the cross-shaped element under an applied field with $\alpha = 210^\circ$, and strength = 10 mT. The in-plane magnetization direction is indicated by the color code visible on the color wheel. The angle of the applied field B is α (b) VIDEO. 2. Snapshot of the magnetization dynamics showing the DW propagating through the center of the cross-shaped element under an applied field with $\alpha = 210^\circ$ and strength = 20 mT. (c) VIDEO. 3. Snapshot of the magnetization dynamics showing the DW reversing the vertical arm under an applied field with $\alpha = 210^\circ$ and strength = 30 mT. The in-plane magnetization direction is indicated by the color code visible on the color wheel.

This tendency continues until 25 mT, where the first reversal of the vertical arm occurs. The depinning dependence appears not symmetrical around the x-axis due to the smaller applied torque to the DW at lower angles while it is pinned in the center of the cross. At the entrance of the cross, the abrupt change in magneto-statics constitutes a potential well for the DW. The DW in the wire is confined to a pseudo-one-dimensional structure and keeps a well-defined vortex wall internal structure with two edge defects. At the cross, however, due to the lack of vertical confinement, one of the two edge defects annihilates and renucleates on the opposite side of the horizontal arm while the other $\frac{1}{2}$ -defect is spread across the vertical arm efficiently reducing the stray field (seen Fig. 6.8 (b)). The fact that the half edge defect present in the wire is always the one with the lower stray field thus supports our interpretation. Above 25 mT, the angular range decreases due to the significant vertical component of the applied field, which promotes the propagation along the vertical arm. At 45 mT, an angular range of 10° for the propagation is still present in the bottom quadrant. No reversal of the vertical arm is observed in the top quadrant because the vertical component of the applied field is parallel to the magnetization. Concerning the vertical arm reversal, the variety of spin configurations (46, 146) that the DW can acquire at high fields while interacting with the center of the cross makes the dynamics complex. The average magnetization and the energy density terms evolution across time is shown in Fig. 6.10 for the three characteristic events described previously. As expected, the average x-component is larger for the pinning case than for the two others due to the non-complete reversal of the horizontal arm. Similarly, a strong change of the average y-component is observable in the vertical reversal case. Considering the energy density terms, the total energy density is mainly driven by the Zeeman energy density of the system. In the three cases, an increase in the Zeeman energy density occurs first, due to the ramp-up of the applied field that follows a functional dependence of the form $B = (B_{ext}(1 - \exp(\frac{-t}{5 \cdot 10^{-10}})))\cos(\alpha), B_{ext}(1 - \exp(\frac{-t}{5 \cdot 10^{-10}}))\sin(\alpha), 0$. The following decrease is due to the DW movement switching the magnetization to a lower energy state. The magnitude of the Zeeman energy density at equilibrium is then directly proportional to the amount of magnetic material switched in the direction of the applied field. For the pinned case, half the horizontal wire switched, for the successful propagation, the whole horizontal wire switched, and for the vertical reversal the entire system switched.

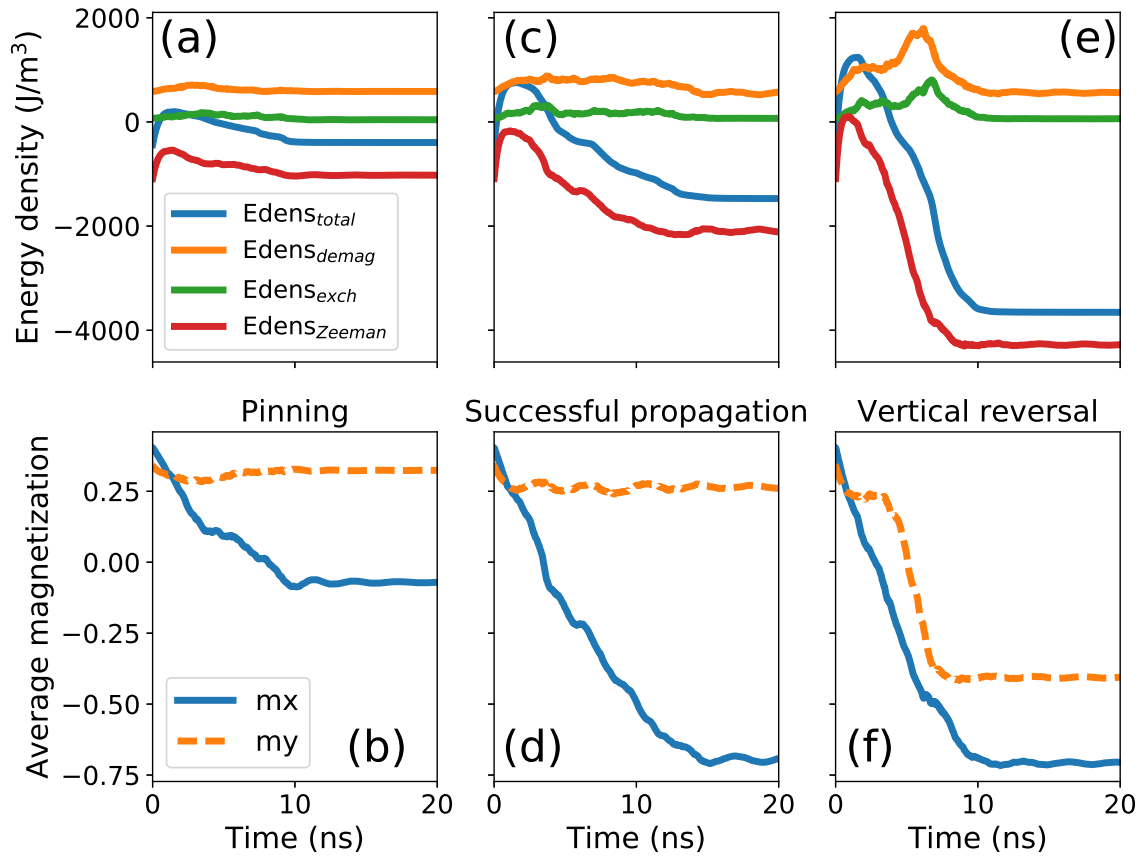


FIGURE 6.10: Time evolution of (a) the energy density terms and (b) x and y components of the magnetization in the case of the DW being pinned at the cross (Field: $\alpha = 210^\circ$, strength = 10 mT). Time evolution of (c) the energy density terms and (d) x and y components of the magnetization in the case of a DW propagating through the cross (Field: $\alpha = 210^\circ$, strength = 20 mT). Time evolution of (e) the energy density terms and (f) x and y components of the magnetization in the case of a DW inducing vertical arm reversal (Field: $\alpha = 210^\circ$, strength = 30 mT). Adapted from (15).

Variations of the initial chirality of the DW

The initial magnetic configuration used for the simulation in Fig. 6.8 is a vortex domain wall with an initial clockwise chirality (Fig. 6.8 (a)). With the present simulations, we investigate the influence of this initial chirality to the vertical arm reversal, the pinning, and the propagation region. The cross-system is slightly modified, and a notch is placed on its left side. The chirality is selected as a parameter in the simulation script, and the clockwise or counter-clockwise DWs are initially relaxed in the vicinity of the notch (see Fig. 6.11). The behavior of the DW is simulated for 20 ns under the constraint of an applied field with a selected configuration (strength and angle α). The final state obtained at the end indicates which of the three characteristic behavior the applied field yielded.

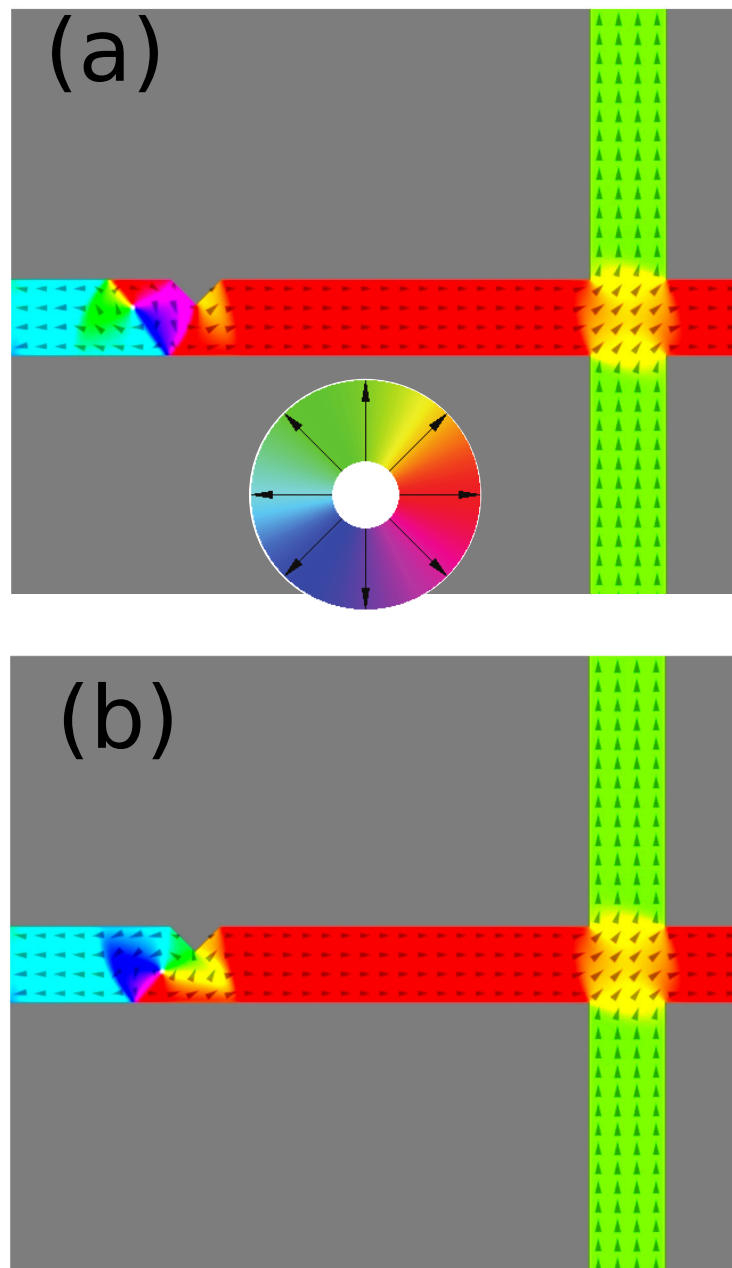


FIGURE 6.11: (a) Snapshot of the initial magnetic configuration in the simulations with a Tail-to-Tail clockwise DW. (b) Snapshot of the initial magnetic configuration in the simulations with a Tail-to-Tail counter-clockwise DW. The in-plane magnetization direction is indicated by the color code visible on the color wheel.

In Fig. 6.12, we represent the results for the initial clockwise DW (Fig. 6.12 (a)) and the initial counter-clockwise DW (Fig. 6.12 (b)). We notice that the only difference between the two chiralities is at low fields close to the depinning field limit. In the case of the CW DW, at 15 mT the angular range is 25° while for the CCW DW, the angular range at 15 mT is only 5° , thus showing that the pinning

field of the CW DW is lower than the pinning field of the CCW DW. From here, we already conclude that the depinning field from the center of the cross is chirality dependent. This kind of chirality dependent depinning field has also been observed in the literature for notches (172, 173).

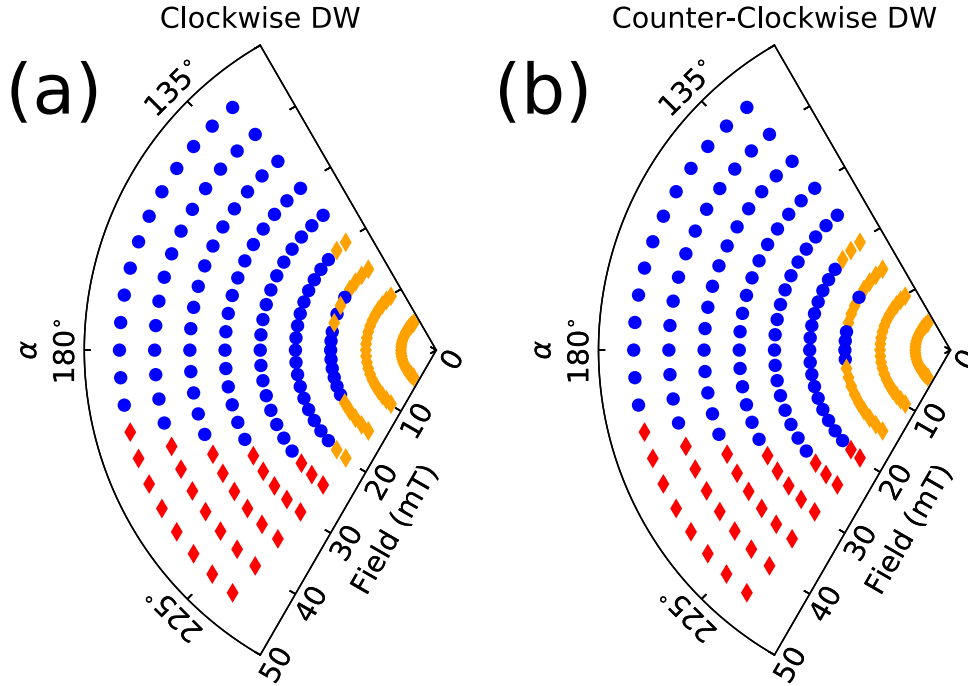


FIGURE 6.12: (a) Polar plot of the angular dependence of a Tail-to-Tail clockwise DW propagation with field orientation and magnitude represented as radius and angle, respectively. The blue circles indicate successful propagation through the cross; the red diamonds represent a reversal of the vertical arm and the orange the pinning at the cross. (b) Similar plot as (a) with a counter-clockwise DW.

To explain the latter effect, we observe the simulation before the entrance in the cross to identify the chirality of the DW, and also right after entering to observe the dynamic of the DW in the center. In Fig. 6.13 (a) and (b), the chirality is opposite. For a similar field strength, the dynamic right before the cross is different. The counter-clockwise DW in (a) smoothly merges with the vertical arm and directly yields a transverse DW like structure, seen in (c). In the case where the DW is clockwise at the entrance like in (b), the dynamic is different. A DW with this chirality does not simply merge with the vertical arm, and a vortex core is generated (see (d)) in the DW right before the DW enters the cross. As in the Walker breakdown (46), before transformation to a transverse DW, which is the stable configuration for the DW in the center of the cross, the vortex core travels from the center to the edge. In this case, the velocity of the DW is greatly reduced as compared to the case where the DW directly enters the cross, thus resulting in a difference of pinning field for various DW spin configurations. In our simulation, the fact that the CW DW configuration provides the lowest pinning field is fortuitous. Indeed, only the configuration of the DW right at the entrance of the

cross matters and since the propagation is turbulent, predicting it remains cumbersome. Despite the latter, it is clear that the depinning field required to escape the cross is chirality dependent.

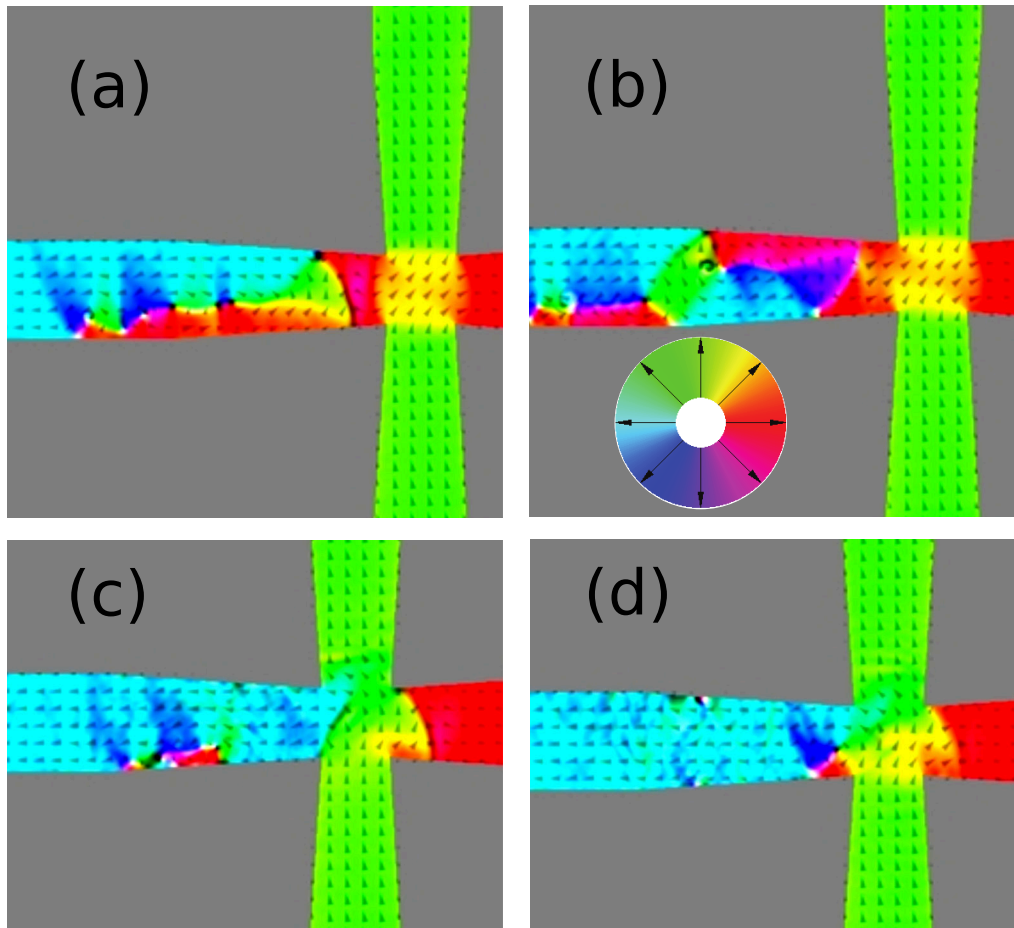


FIGURE 6.13: Snapshot of the magnetization configuration of (a) a counter-clockwise DW right before entering the cross, (b) a clockwise DW right before entering the cross. (c) Snapshot of the magnetization right after entering the cross starting from configuration (a). (d) Snapshot of the magnetization right after entering the cross starting from configuration (b). The in-plane magnetization direction is indicated by the color code visible on the color wheel.

Change of the geometry of the cross

After investigating the cross with $300\sqrt{2}$ nm center diagonal, we reduce this center dimension because the nucleation field is width dependent. We then expect to increase the vertical-arm-reversal field by reducing the dimensions of the cross diagonal.

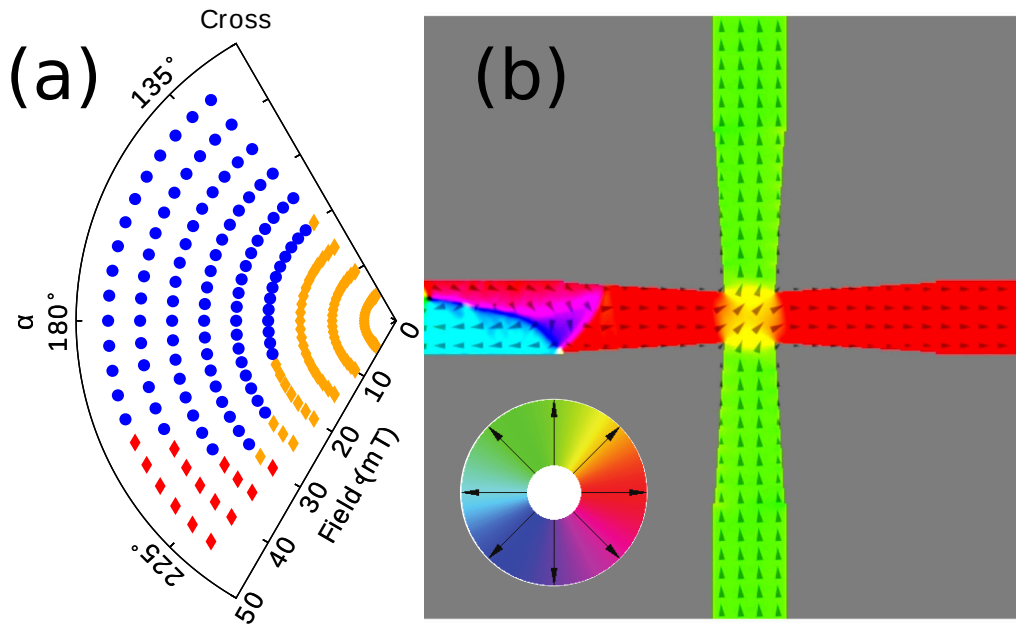


FIGURE 6.14: (a) Polar plot of the angular dependence of a Tail-to-Tail DW propagation with field orientation and magnitude represented as radius and angle respectively. The blue circles indicate a successful propagation through the cross; the red diamonds represent a reversal of the vertical arm and the orange the pinning at the cross. (b) Snapshot of the magnetization in a cross with a $210\sqrt{2}$ nm center diagonal. The in-plane magnetization direction is indicated by the color code visible on the color wheel.

In Fig. 6.14 (a), we present the results of the simulations performed with the $210\sqrt{2}$ center diagonal cross. The simulation is initialized with a Tail-to-Tail DW on the left side of the cross. A field configuration (strength and angle) is applied to the system, and the simulations are run for 20 ns. The depinning field is higher than for the cross with the $300\sqrt{2}$ nm center diagonal due to the more substantial constriction in the center. The angular range for the propagation area at 45 mT is also wider, i.e., 10° for the $300\sqrt{2}$ nm center diagonal as compared to 20° for the $210\sqrt{2}$ nm center diagonal. This effect originates from the increase of the nucleation field with the reduction of the center dimension. It is then probably interesting to reduce the center diagonal dimension for the optimization of the closed-loop device concept since the depinning field does not severely increase while the nucleation field does thus yielding a broader range of operating fields.

Issues with the cross in the sensor concept Due to the rotating field used in the actual sensor device concept, if the vertical arm has a magnetization anti-parallel to the applied field, the reversal of the vertical arm is likely to occur resulting in a failure event. For example, if a Tail-to-Tail DW is found to the left of the cross when a field of 40 mT is applied along 200° , according to Fig. 6.8 (a), its propagation will lead to a reversal of the vertical arm. To overcome this issue, we next

introduce additionally the syphon element, which will constrain the propagation through the cross at applied field angles close to 180° .

6.3.2 Syphon element

The syphon structure comprises of two horizontal wire segments connected by a tilted wire at an angle θ from the horizontal direction (Fig. 6.6). The goal is to limit the movement of the DW to field directions that lead to successful horizontal DW propagation without vertical DW propagation as represented by the blue area in Fig. 6.8 (a). The syphon arms are placed on each side of the cross to allow for the use of the device with a clockwise and counter-clockwise rotating field. In simulations, a DW is initialized at the top-left horizontal arm of the syphon and propagated towards the right. The two final configurations are the desired propagation shown in Fig. 6.15 (b) or the pinning of the DW in the center of the arm (Fig. 6.15 (c)). Different syphon angles (θ) were simulated. The results can be seen on the polar plot in Fig. 6.15 (a). In this figure, we present only the limit between pinning and propagation events. The circles are the simulation results while the lines are the fitting of the results for an angle of the syphon arm (Equation 6.1) with θ varying from 85° to 60° in steps of 5° (left syphon arm). The results for a syphon with $\theta = 60^\circ$, represented in purple, show that the domain wall will propagate through the syphon for field values between 7 mT and 45 mT and angle values between 180° and 205° (purple line). However, the domain wall will be pinned for applied fields at any angle higher than the limit marked by the solid line. The other syphon angles exhibit similar behavior but with different limits. We study the left arm of the syphon since all results can be applied to the right syphon by reflection symmetry along the vertical axis. Similarly, due to the symmetry of the system, if the angle of the applied field is smaller than $\alpha = 180^\circ$, the DW will propagate through the first syphon arm and the cross but not across the second syphon arm. Thus we are then only interested in the angles between $\alpha = 180^\circ$ and 220° . From the results, we find that the angular range increases with the magnitude of the applied field and the reduction of the syphon angle (θ).

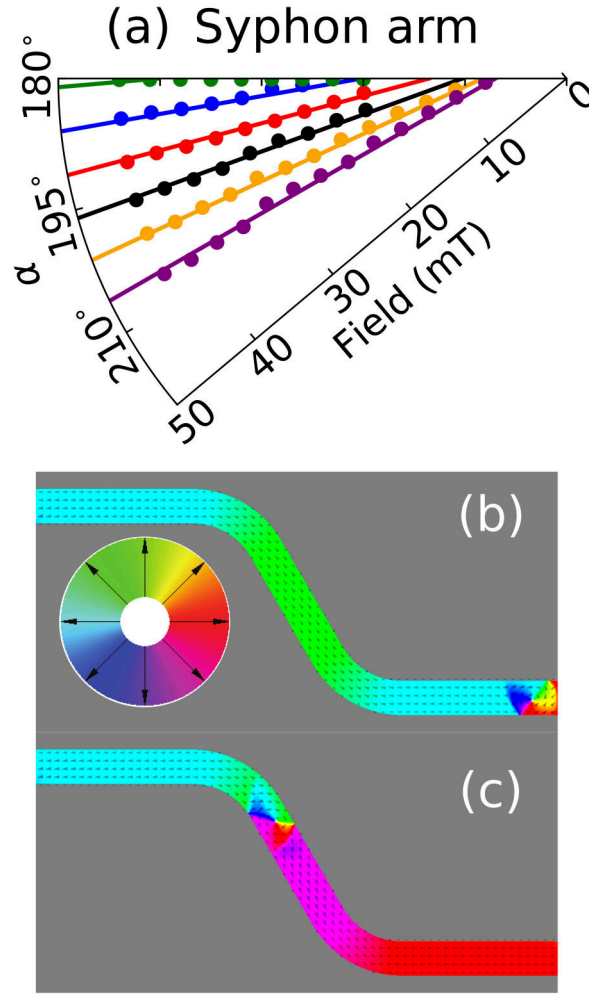


FIGURE 6.15: (a) Polar plot depicting the limit between pinning and propagation at the syphon arms. The circles are simulation results for the syphon angle $\theta = 85^\circ, 80^\circ, 75^\circ, 70^\circ, 65^\circ$ and 60° , respectively in green, blue, red, black, orange and purple. The lines are the fitting curves of the simulated data based on equation 1. Taking the results for $\theta = 60^\circ$ (purple), the DW pinning occurs for field angles larger than 205° , the propagation is allowed for field angles between 180° and 205° and field strengths larger than 7 mT. (b) Successful propagation of the DW through the syphon. (c) Pinning at the center of the syphon. The in-plane magnetization direction is indicated by the color code visible on the color wheel. Adapted from (15).

The propagation of the DW through the syphon element is described by a model of a DW in a straight wire under the application of a field with axial and transverse components (174, 175). In a 1D model (22, 176), the torque on the DW from the applied field can be approximated as $\mu_0 H_{ext} M_s \sin(\frac{3\pi}{2} - \theta - \alpha)$, and it is maximum when the applied field is parallel and opposite to the magnetization in the stripe. From the latter, we extract the depinning field in the arm:

$$H_{ext} = \frac{H_p}{|\sin(\frac{3\pi}{2} - \theta - \alpha)|} \quad (6.1)$$

With H_p the pinning field in the structure due to the corners geometry. For $H_p = 3.5$ mT, we notice the excellent agreement with the model. The syphon arm can thus prevent the DW from propagating for field directions outside the desired angular range. In a real device, the edge roughness might affect the propagation field in the syphon element. The result is likely to be a larger required longitudinal component of the field along the syphon arm to allow for the depinning of the DW. Although, we have not investigated the effect of edge roughness in our opinion the behavior at the cross will not be affected, and that of the propagation fields through the syphon might increase a little, but the angular dependence will remain.

6.4 Full device geometry

Finally, we now combine both syphon and cross elements for the creation of a reliable device geometry with the desired domain wall propagation properties. The creation of the angular dependence of a complete device is accomplished merely by merging the angular dependences of the two elements. This action is justified since the interaction between the elements is small due to the physical distance separating them. The results are shown in Fig. 6.16 where the following scheme has been chosen to represent the results: if the DW propagates across both elements as desired, field direction and strength are represented by a green diamond. If a vertical reversal can still occur then, the diamonds are red. The black diamonds represent the configurations where the DW would be pinned in the syphon arm but if released in the cross would still successfully propagate. We call this the buffer zone. All the irrelevant points of the cross-related effects are now colored with less intensity (faded). A device made of a particular cross and syphon is expected to function correctly if no red diamonds (vertical reversal) are seen and if the buffer zone is large enough to account for stochastic events due to thermal activation and irregularities, which would broaden the micro-magnetically computed operating field range boundaries.

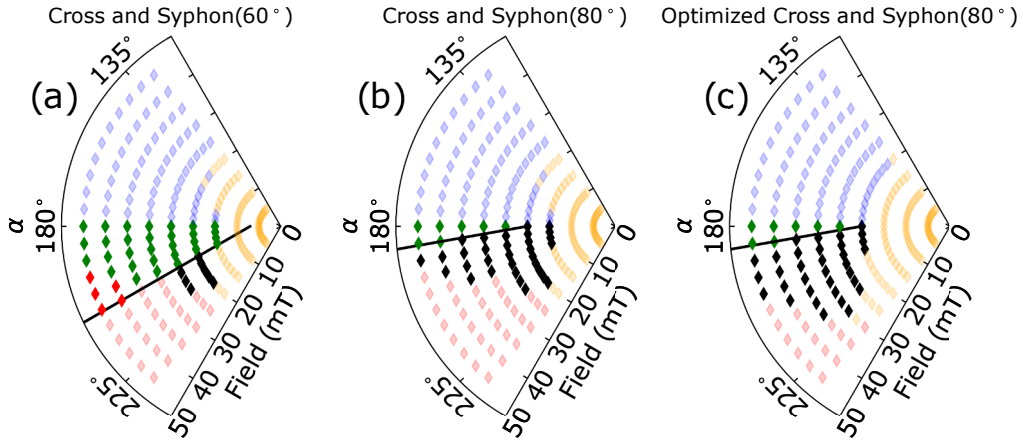


FIGURE 6.16: (a) Polar plot of the combination of a cross with a syphon arm of angle 60° (device $n^\circ 1$). The yellow color represents pinning of the domain wall due to a too low field strength. The green color represents the propagation through the full structure; the red circles are the reversal of the vertical arm, and the black region is where the device could potentially still be working if propagation through the syphon was facilitated. We refer to it as a buffer zone. (b) A similar plot for a device with syphon angle 80° (device $n^\circ 2$). (c) A similar plot for an optimized device with a cross center of 210 nm and syphon angle 80° (device $n^\circ 3$). The black line is the fitting limit expressed previously for the chosen syphon arm. Adapted from (15).

The merging of a cross with a $300\sqrt{2}$ nm center diagonal and a syphon arm with an angle $\theta = 60^\circ$ yields the polar plot in Fig. 6.16 (a) (device $n^\circ 1$). We note that the field is rotating and that all non-faded points need to be examined to assess whether a device is working or not. We notice that in the allowed range of device $n^\circ 1$, the application of a field more significant than 25 mT would lead to a reversal of the vertical arm since there is no buffer region above it. If we are to define an angle operating window (AOW) between the largest working angle 200° (at 25 mT) and 180° , device $n^\circ 1$ has an AOW of 20° . It is useful to define a field operating window (FOW) between the depinning field limit and the central arm reversal limit. For device $n^\circ 1$, the FOW is 10 mT (15 mT to 25 mT). Finally, the robustness of the structure to processing irregularities and stochasticity can be identified by the smallest black angular range. For device $n^\circ 1$, the robustness is of the order of 15° at 25 mT. We believe that for a device, the best parameters are met for a large FOW, a small AOW, and a wide Buffer zone or robustness to irregularities due to device fabrication. A summary of the values for those parameters are found in Table 6.2. The second plot (Fig. 6.16 (b)) represents the characteristics of device $n^\circ 2$. Device $n^\circ 2$ is created by merging the cross with a $300\sqrt{2}$ nm center diagonal to a syphon arm of 80° . This device has a passing field up to the theoretical nucleation field of the structure (no vertical arm reversal). The FOW of device $n^\circ 2$ is 25 mT (20 mT to 45 mT) which represents a substantial improvement to device $n^\circ 1$. The AOW is also reduced to 10° . However, the Buffer zone is only of 5° at 45 mT thus vulnerable to defects. The latter is due to the strong enlargement of the vertical-arm-reversal area as the magnitude of the

field increases.

	n°1	n°2	n°3
Angle Operating Window (°)	20	10	10
Field Operating Window (mT)	10	25	25
Minimum Buffer Zone (°)	15	5	15

TABLE 6.2: Summary of the three defining parameters of the n-CL device for the three presented architectures. Adaptation from (15).

We now investigate the cross with a $210\sqrt{2}$ nm center diagonal and the best syphon angle to enlarge the buffer region. We call this cross the optimized cross in Fig. 6.16. With this cross, the depinning event occurs at 5 mT higher field values, but the angular range at 45 mT is much larger. Due to the selection of the syphon angle the increase in depinning field has no impact on the performances of the device. The robustness of device n°3 is then drastically improved to 15° at 45 mT compared to n°2 with no loss of FOW thus providing the necessary reliability to the structure. Depending on the desired parameter range for the FOW, tailored combinations of a syphon and a cross structure allow for the creation of optimum conditions for maximum reliability operation.

6.5 Conclusion

To summarize, we present a new nonvolatile sensor concept based on magnetic DWs that will allow for counting to millions of turns of an applied external rotating magnetic field. The concept requires the use of the cross-shaped intersections of nanowires forming intertwined loops. We explore the DW propagation in this cross-shaped geometry and obtain different states of the cross while interacting with a domain wall. We find that with a simple cross, some configurations (applied field and magnetization in the vertical arm being anti-parallel) are generating the failure event for the sensor operation. Various chiralities and cross geometries are also checked, and the depinning field from the center appears to be chirality dependent, while a decrease of the center dimensions yields an increase of the nucleation field. We develop a syphon structure comprised of a tilted wire to overcome the problems leading to failure events. We simulate elements under fields of different strengths and angles to identify their operating conditions. The cross yields a complex DW behavior characterized by three physical mechanisms: the propagation through the cross, the pinning at the cross and the reversal of a vertical arm. The depinning field from the syphon arm for different syphon angles is modeled via a hyperbolic dependence on the angle of the applied field. The syphon structure successfully allows for the pinning of the DW in angular ranges where the applied field configuration in correspondence to magnetization state in the cross would yield a failure if the domain wall were to propagate into the cross region at these field directions and field strengths. Finally, the combination of the two elements allows for the identification an angular operating

window, a field operating window and a robustness factor; the three of them allow for an easy identification of a reliable structure, which is essential to design the geometries of reliable devices of this new generation of multi-turn sensor.

Parameter	DW interaction with the cross	DW interaction with the syphon	Figure
Decrease wire width	Increase of depinning field and of nucleation field	Increase of depinning field and of nucleation field	No data
Decrease of the cross center dimension from 300 nm to 210 nm	Increase of depinning field and of vertical-reversal field	No influence	Fig. 6.14
Reduced Syphon angle from $\theta = 85^\circ$ to 65°	No influence	Increase of the angular range of propagation field Reduction of the smallest depinning field	Fig. 6.15

TABLE 6.3: Table summarizing the influence of a change in the key parameters constituting the cross and the syphon element.

Chapter 7

Experimental realization of the closed-loop sensor device

Most of the results presented have been accepted for publication in Applied Physics Letters, at the time of writing of the manuscript the results are found at the following Ref. (177). The text and the figures were adapted for the present manuscript.

7.1 Introduction

As described in the previous chapter, an innovative approach is proposed based on the simultaneous measurement of several coprime-counting intersected closed-loop architectures (15). In contrast to the already studied open-loop DW based device structure (14, 165) (see chapter 4 and 5), this alternative concept includes a different geometrical feature, namely a cross-shaped intersection of nanowires, which has been investigated numerically and experimentally (15, 167, 169–171). This geometry ultimately enables a disruptive device that can count millions of turns. Despite the concept having been introduced theoretically and having been studied by micromagnetic simulations (15), no experimental realization has been reported in the literature. In this chapter, we identify the externally applied field configurations (strengths and angles) that result in a pinning, propagation or an unwanted splitting of the DW in the center of cross geometries that lead to a failure event for the sensor. We also present the effect of the change of the center diagonal dimensions on the performance of the device. We then develop a syphon structure and measure the field configurations that allow for the propagation through the syphon or the pinning in its arm for different syphon tilting angles. We then virtually merge the individual behaviors for DW propagation in a syphon and a cross thus generating the expected response of the complete device. We compare the latter to selected real device geometries measured under an applied rotating field thus yielding characteristics for the field regimes that result in a successful operation. By comparing the complete device and the individual constituents, we identify geometrical parameters that govern the device performance, which allows us to build an optimized sensor with a large field window for reliable operation.

7.2 Fabrication and characterization

For the fabrication of the structures, a stack of $\text{Ni}_{81}\text{Fe}_{19}$ (30 nm)/ Ta (4 nm) (bottom to top) is deposited on a substrate of SiO_x in a magnetron sputtering. The samples are then patterned by Electron Beam Lithography and Ar ion etching. The process is described in chapter 3. Scanning electron microscopy (SEM) reveals well-defined structures (Fig. 7.1). The polycrystalline material used ($\text{Ni}_{81}\text{Fe}_{19}$) is magnetically soft and exhibits a full film coercivity of 2 Oe with a saturation magnetization value of $M_s = 795$ kA/m.

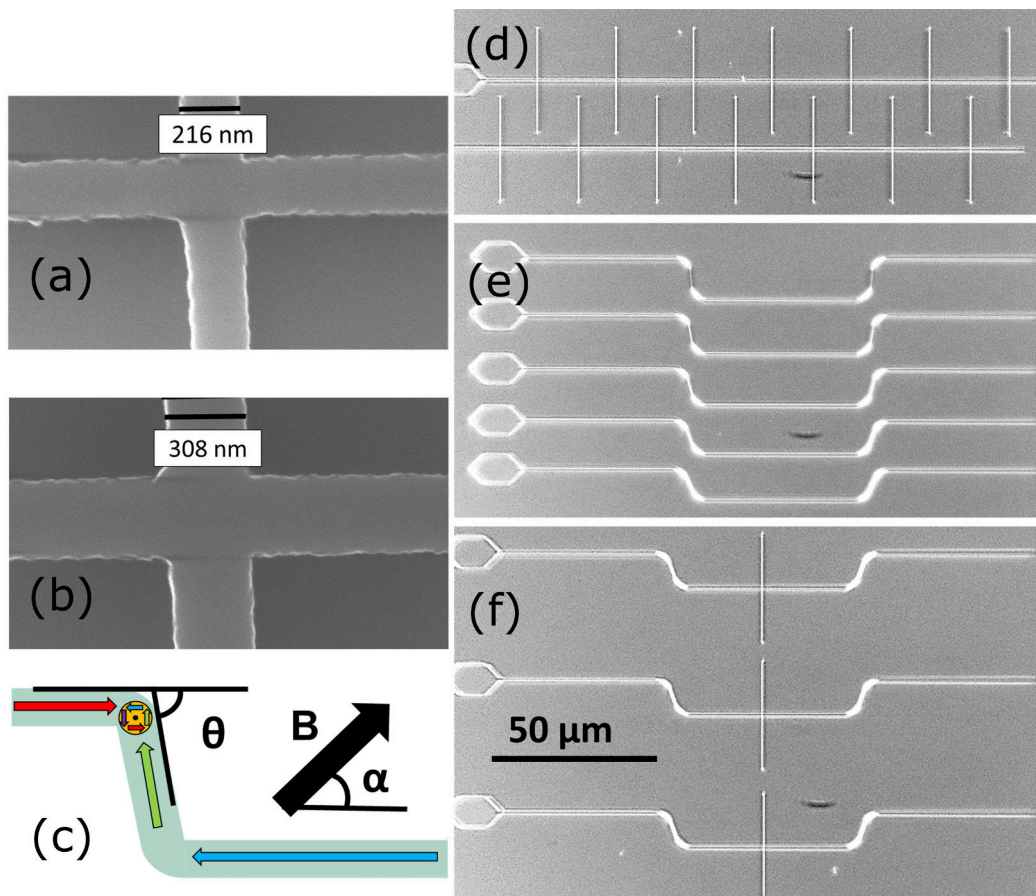


FIGURE 7.1: (a) SEM micrograph of a cross with center diagonal length equal to $210\sqrt{2}$ nm. (b) SEM micrograph of a cross with center diagonal length equal to $300\sqrt{2}$ nm. (c) Schematic of the syphon initial magnetization configuration. The orange disk with the arrows represents a vortex DW. The colored arrows represent the magnetization direction. The black arrow indicates the applied field with strength B and angle α . (d) Optical image of the cross structures with a center diagonal of $300\sqrt{2}$ nm for the top one and $210\sqrt{2}$ nm for the bottom structure. (e) Optical microscopy image of the syphon structures. The syphon angles θ (see (c)) are varied from top to bottom as $\theta = 85^\circ, 80^\circ, 75^\circ, 70^\circ$, and 65° . (f) Optical microscopy image of the complete structures with a syphon of angle $\theta = 70^\circ$ and a cross with center diagonal equal to $300\sqrt{2}$ nm. Adapted from (177).

The samples are patterned into cross-shaped element (Fig. 7.1 (a, b, and d)), the syphon elements (Fig. 7.1 (c and e)) and in a combination of the two (Fig. 7.1 (f)). A nucleation pad is located at one end of all geometries to allow for the introduction of DWs. Furthermore, wire ends are tapered to avoid DW nucleation at that point. In the designs, the nominal wire width is 300 nm for all structures as the nucleation and depinning fields for this wire width yield values that are useful for applications (14). In the center of the cross, the diagonal can be reduced down to $180\sqrt{2}$ nm. All experiments are conducted using a magneto-optical Kerr effect microscope (Evico Magnetics). Furthermore, rotating the plane of incidence of the light by 90° enables the observation of the magnetic switching of the structures in orthogonal directions. A vector magnet is utilized for the application of a rotating field up to 100 mT.

7.3 Cross-shaped intersection

The cross-shaped intersection of magnetic nanowires is the key element of the closed-loop DW based multiturn-counter sensor device. The results of the measurement of magnetic switching of the branches of the cross under an applied field of strength B and angle α are presented in Fig. 7.2 (a) and (b). To provide statistics, a system composed of 7 nominally identical crosses is measured for every geometry. At the beginning of all measurements, the system is initialized with a field magnitude of 70 mT oriented in the 225° -direction. This procedure leaves the cross in a similar state as the one shown in Fig. 7.2 (c), however, without the DW, i.e., the vertical arms magnetized downwards and the horizontal arm magnetized towards the left. In the experiment, we sense the reversing of the horizontal arms (Fig. 7.3 (a) and (b) for the MOKE images, and Fig. 7.2 (e) and (f) for the schematic explanation) by setting the MOKE sensitivity to a horizontal contrast. We then investigate a possible splitting of a DW (Fig. 7.3 (c) for the MOKE images, and Fig. 7.2 (e) for the schematic explanation) leading to the reversal of vertical arms by rotating the plane of incidence of the light by 90° yielding a sensitivity to a vertical contrast. In Fig. 7.2 (a) and (b), the results of the two measurements are represented by disks and diamonds, respectively. We interpret the data points as representing the boundaries between three characteristic processes. A schematic representation of these three possible outcomes is shown in Fig. 7.2 (d, e, and f) and the corresponding MOKE images can be seen in Fig. 7.3 (a, b, and c). The processes in Fig. 7.2 (d and e) are failures for the operation of the device. The pinning of the DW at one of the crosses is the first one, where no change of the horizontal contrast of the right horizontal arms was observed in the microscope (b). The second one is a switching of one or more of the vertical branches that we term here vertical arm reversal. This splitting of the DW as indicated in Fig. 7.2 (e) shows that one DW moves up or down a vertical arm thereby reversing it. Finally, the switching of the horizontal arm without a switching of the vertical arms shown in (f) is the desired behavior required for the functioning of the device concept.

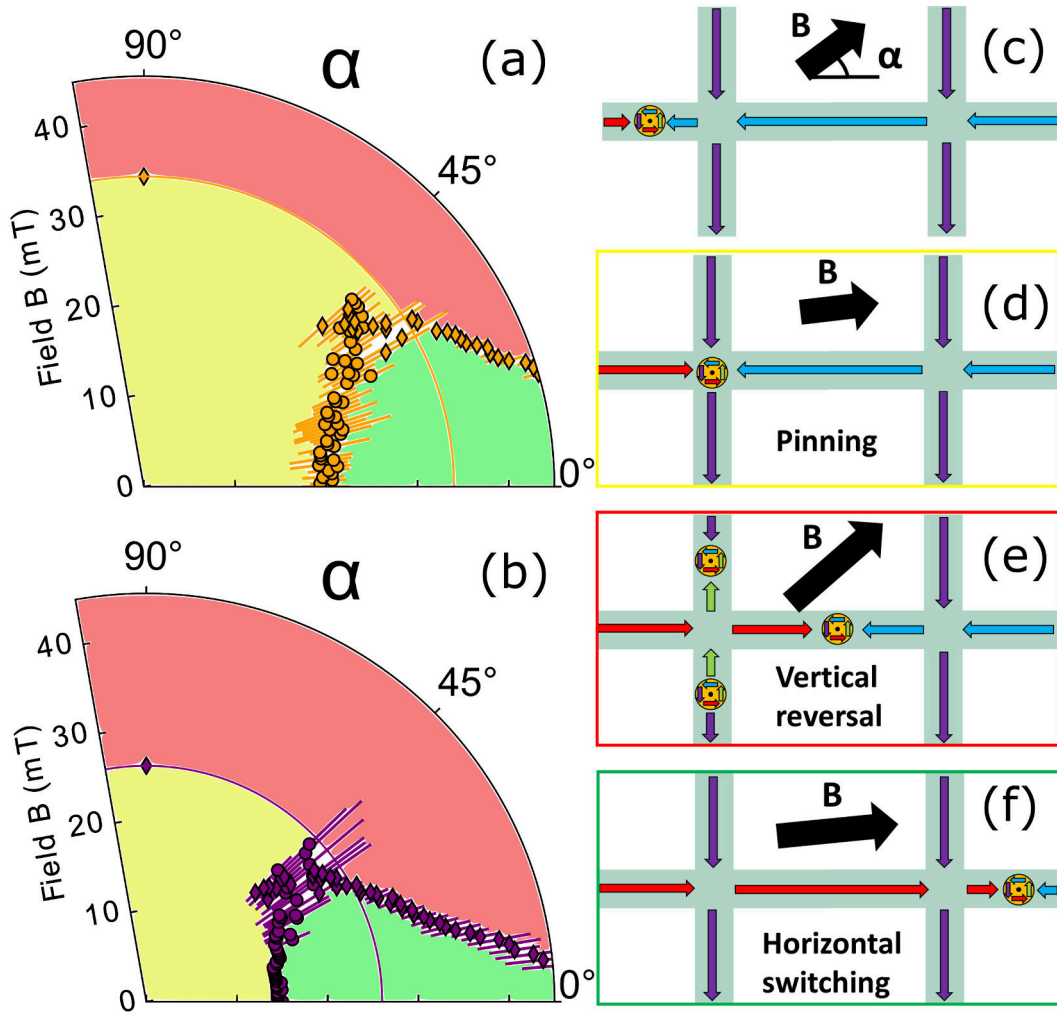


FIGURE 7.2: (a) Experimental results of the measurement of cross $n^{\circ}1$ (orange diamonds and disks) under an externally applied field. The colors of the areas in (a) correspond to the events depicted in (d)-yellow, (e)-red, and (f)-green. (b) A similar plot as (a) for cross $n^{\circ}2$ (purple diamonds and disks). (c) Schematic representation of the starting magnetization configuration. The orange disk with the arrows represents a vortex DW. The colored arrows represent the magnetization direction. The black arrow indicates the applied field with strength B and angle α . (d) and (e) Schematic representation of failure events, namely pinning of a DW in the cross and vertical arm reversal, respectively. (f) Schematic representation of the horizontal arm switching. Adapted from (177).

Two different cross geometries (see Fig. 7.1 (a) and (b)) are simultaneously measured and are plotted in Fig. 7.2 (a) and (b). The differently colored observable zones are each representing one of the three characteristic processes (red for vertical-arm reversal, yellow for pinning in the cross, and green for horizontal reversal solely). For cross $n^{\circ}1$, the center diagonal has the dimension $210\sqrt{2}$ nm, while for cross $n^{\circ}2$, the diagonal is $300\sqrt{2}$ nm. We find that qualitatively the same trend is followed for both geometries.

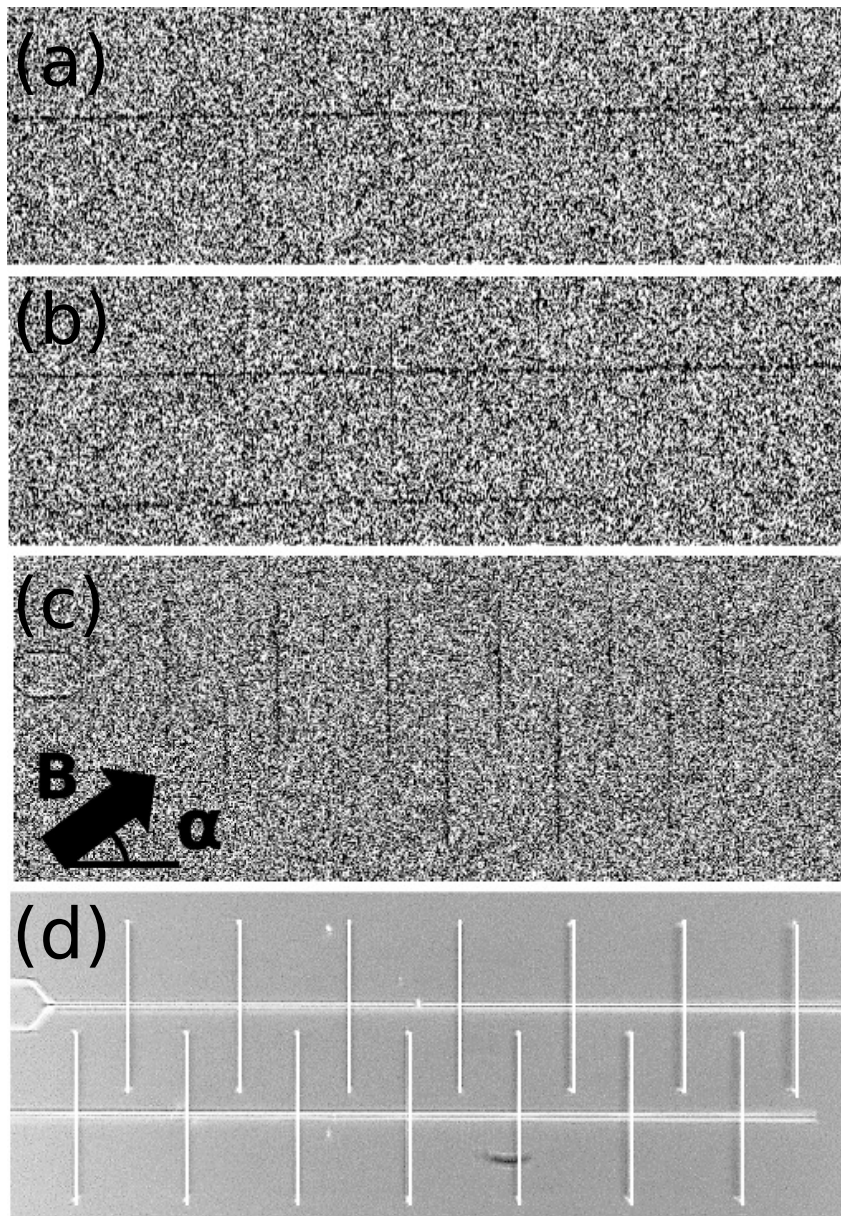


FIGURE 7.3: (a) MOKE differential contrast image of the horizontal arm reversal of the top system of crosses shown in (d). The field configuration is $B = 15$ mT and $\alpha = 0^\circ$. (b) MOKE differential contrast image of the horizontal arm reversal of the top system of crosses and uncomplete reversal of the bottom system. The field configuration is $B = 18$ mT and $\alpha = 0^\circ$. (c) MOKE differential contrast image of the vertical-arm reversal. The field configuration is $B = 32$ mT and $\alpha = 45^\circ$. (d) Optical microscopy image of two system of crosses already described in Fig. 7.1 (e)

At large angles, the distinction between the cross geometries is more obviously visible. This variation is attributed to the different nucleation fields inherent to the various cross diagonal lengths. In simple words, the narrower the diagonal, the larger the nucleation field due to increased shape anisotropy. Afterwards, measurements were performed with an angle $\alpha = 90^\circ$ to prevent horizontal DW motion. The obtained field strengths yielding a switching of the vertical

arm mark a delimitation in Fig. 7.1 (a) and (b) (orange and purple circular lines for cross $n^{\circ}1$ and 2, respectively). From this result, we conclude that for vertical-arm-reversal field values lower than the limit, the splitting of the DW leading to vertical-arm reversal is aided by the presence of a DW. The pinning of the DW in the center of the cross is represented by the yellow area. The depinning field is larger for cross $n^{\circ}1$ as compared to $n^{\circ}2$ due to the larger change in width while reaching the center of the cross. Finally, the green region represents the successful horizontal propagation necessary for the functioning of the device concept. The DW should reach the center of the cross solely for the field configurations (strength and angle) represented by this region.

7.3.1 Geometrical modifications to the center of the cross

Next, to probe the influence of the DW behavior on the cross-shape, we modify the center of the cross by adding some slanted corners. We realized this increase for the length values $d = 20, 40, 80, 120,$ and 200 nm as depicted in Fig. 7.4 (b). The aim for the latter is to observe the influence of the proximity effect in the center of the cross usually resulting in the geometry schematically represented in Fig. 7.4 (b).

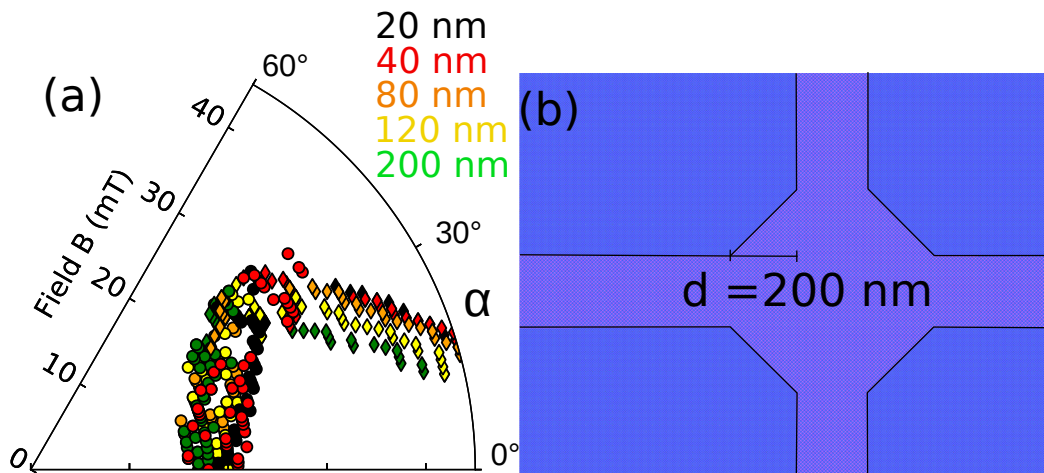


FIGURE 7.4: (a) Experimental results of the measurement of crosses with various increases of the diagonal as depicted in (b) under an externally applied field. The black diamonds and disks correspond to an increase of $d = 20$ nm. The red diamonds and disks correspond to an increase of $d = 40$ nm. The orange diamonds and disks correspond to an increase of $d = 80$ nm. The yellow diamonds and disks correspond to an increase of $d = 120$ nm. The green diamonds and disks correspond to an increase of $d = 200$ nm. (b) Schematic representation of the modifications brought to the center of the cross. The length d represent the increase from the original cross geometry.

The original center dimension of the cross diagonal are the ones of cross $n^{\circ}1$.

The results of the experiment are obtained in the same way as the ones in the previous subsection. We readily observe that the results of the horizontal and vertical arm reversal are similar for an increase of $d = 20$ and 40 nm. Furthermore, they are also identical to the results obtained for the cross n°1 thus revealing the small influence of an increase up to 40 nm. From the 80 nm and on, up to 200 nm, a decrease of the vertical-arm-reversal field values is shown, and the lowest values are attributed the most substantial increase of d . This effect is a consequence of the increased central dimension which decreases the nucleation field value as seen in the previous chapter 6. An increase of the horizontal reversal field value with the smallest increase of d is as well recognized. This effect is due to the enhanced constriction and thus more extensive pinning for the DW. Interestingly, the cross-shaped intersection shows a robustness to an enlargement of the type that could appear in the case of the occurrence of proximity effects during the patterning. This feature is essential for an industrial production, which usually encounters small variations and defects as compared to the original design.

7.4 Syphon structure

The critical problem of the closed-loop sensor concept is that a rotating field leads to the DW reaching the cross for values of α that lead to a vertical arm reversal. To overcome this problem and make sure that the DW only arrives at the cross for field angles that allow for a reliable horizontal propagation through the cross, we introduce a syphon element (see Fig. 7.1 (c and e)). This geometrical element is designed to block the propagation of a DW for particular field directions. We next present the measurement of the depinning/propagation fields of a DW in several syphon geometries for various field configurations (strengths and angles). The syphon structures are always initialized before every measurement with the application of a 70 mT field oriented along 180° -direction (see Fig. 7.1 (c)). The measurement is conducted as follows: the applied field strength was chosen, and the field was positioned at an angle of 45° , placing a head-to-head vortex DW at the position shown by the DW in Fig. 7.1 (c). The field was then rotated toward the horizontal direction (toward 0°) by reducing the angle in steps of 1° until the switching of the magnetization. After that, the field is increased by 1 mT, and the experiment is repeated. In Fig. 7.5, the measured values of 3 samples with different syphon angles are plotted together. The points separated from the rest of the distribution (i.e., around 45°) represent a nucleation in the wire. The equation $H_{ext} = \frac{H_p}{|\sin(\frac{3\pi}{2} - \theta - \alpha)|}$ with $H_p = 3.5$ mT describes the depinning of a DW in a wire submitted to a transverse and longitudinal field (16). The equation is plotted as a full line in Fig. 7.5 and the experimental depinning values fit the theoretical description. The points are scattered in the vicinity of the line due to the stochasticity of the depinning process inherent to thermal activations and edge roughness present at the side of the wire. Interestingly, the edge roughness does not significantly increase the pinning value H_p used in the equation, which is originally defined as a pinning field due to the curvature of the corners

in a device (16). The impact of the edge roughness is limited to the absence of a depinning point for a particular field strength value.

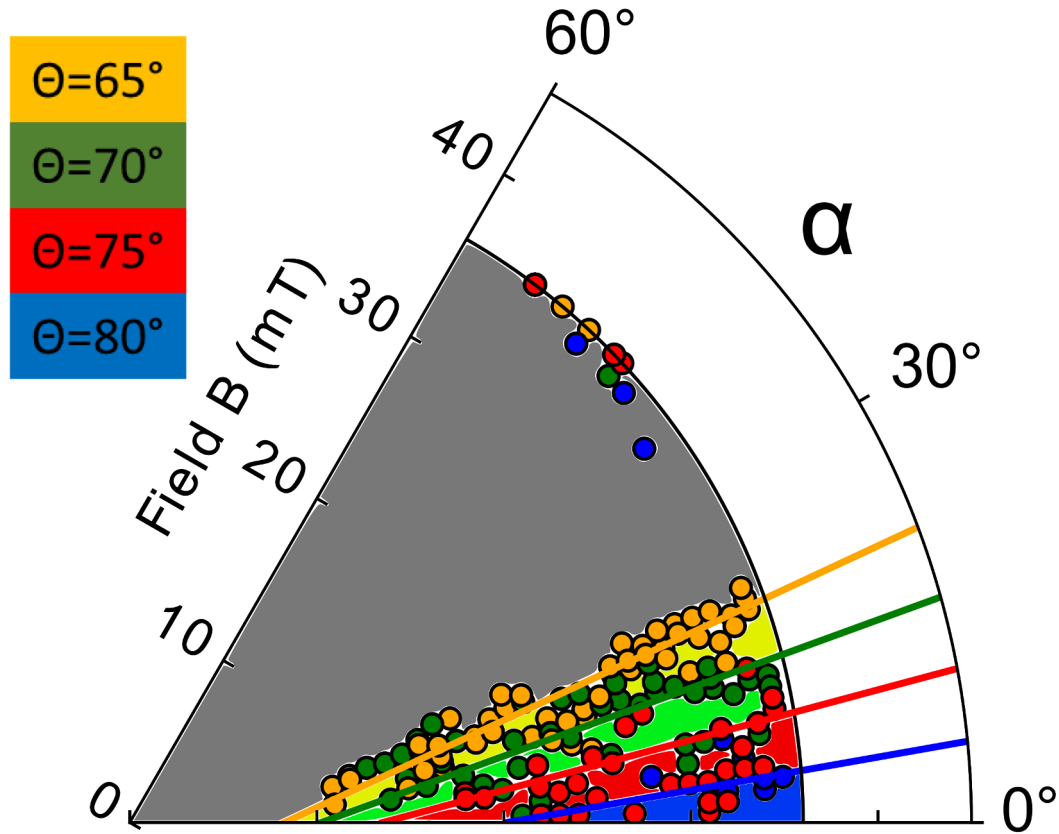


FIGURE 7.5: Polar plot of the angular dependence for different angles θ of the syphon arm under an applied field B with angle α . For $\theta = 65^\circ$ (yellow, green, red and blue is propagation while gray is pinning), for $\theta = 70^\circ$ (green, red and blue is propagation while gray and yellow is pinning), for $\theta = 75^\circ$ (red and blue is propagation while gray, yellow, and green is pinning), and for $\theta = 80^\circ$ (blue is propagation while gray, yellow, green and red is pinning). Adapted from (177).

For the syphon angle $\theta = 80^\circ$, some field strengths do not yield a depinning within the field range probed. We thus find a loss of reliability as the syphon angle is increased while the syphon operation is found to be reliable for angles of $\theta = 75^\circ$ (red) and less. The nucleation field value for all the structures is identified to be 36 mT (black circular line), which defines the absolute maximum value usable for the whole structure of the device and is governed by the shape anisotropy.

7.5 Combined and complete device

Finally, we measure complete devices and compare the response to what can be expected from the individual behavior of the cross and syphon. A device $n^{\circ}1$ is defined as containing cross $n^{\circ}1$, similarly for $n^{\circ}2$. In a combination plot (Fig. 7.6 (a) and (b)), we overlap the angular dependence of a syphon with $\theta = 70^{\circ}$ (Fig. 7.5) with the angular dependence of cross $n^{\circ}1$ and 2 (Fig. 7.2 (a) and (b)), we call it the combined device as compared to the complete device, which is represented in Fig. 7.1 (f). In the original concept of the closed-loop sensor a buffer region (details in Ref. (15)) is defined as field configuration yielding a DW that could propagate in the cross without failure but is pinned in the syphon (in gray in Fig. 7.6 (a) and (b)). Combined device $n^{\circ}1$ exhibits a buffer region up to the nucleation field value for the syphon element while combined device $n^{\circ}2$ is limited to the meeting point between the syphon boundary (green line) and the vertical arm reversal (purple diamonds) at 34 mT in Fig. 7.6 (b). According to the original concept, the operating fields for the combined devices should be the field values at lower angles than the boundary formed by the syphon, and still exhibiting a buffer zone at larger angles, thus yielding the blue and green area in Fig. 7.6 (a) and (b). The red area is now representing the failure of the complete device concept due to a nucleation event occurring somewhere not only in the cross. This limit is set by the nucleation field of the syphon (see Fig. 7.5). We measure the field operating window (Fig. 7.6 (c)) of the complete device represented in Fig. 7.7 (e) by rotating the field in a clockwise direction and increasing the field by 1 mT. The complete sensor is considered to work when the horizontal arm is entirely reversing (Fig. 7.7 (c)) twice per full rotations, and no vertical arm reversal event (Fig. 7.7 (d)) is observed. If the field strength were too low for the complete horizontal arm reversal, a pinning of the DW at the first arm (Fig. 7.7 (a)) or in the center of the cross (Fig. 7.7 (b)) could be seen. Looking at Fig. 7.6 (c), the operating fields located in between the depinning and vertical-arm-reversal fields of various complete devices (Fig. 7.1 (f)) are represented. Interestingly, the vertical-arm-reversal fields are significantly reduced compared to the combined devices. This result is rather unexpected, and especially for device $n^{\circ}2$, the discrepancy between the combined device (Fig. 7.6 (b)) and the complete one (Fig. 7.6 (c)) is as high as 10 mT. For a complete device, the presence of the syphon limits the propagation of the DW to a narrow angular range of the applied field where the vertical component is small. The presence of the buffer zone makes the vertical arm reversal unlikely in this angular range. Thus if vertical arm reversal occurs, a DW cannot be present in the cross. The latter indicates that the limiting mechanism is the nucleation of new DWs in the center of the cross when the field is applied along one of its axes. The obtained field values for the vertical reversal of cross $n^{\circ}1$ and 2 without DW ($\alpha = 90^{\circ}$) were used to create a demarcation (orange and purple circles) in Fig. 7.6 (a) and (b), respectively. This demarcation separates vertical arm reversal with the aid of a DW at lower field values and reversal/nucleation at larger fields that would occur even without a DW. It is of interest to note that these limits are corresponding to the vertical-arm-reversal values shown in Fig. 7.6 (c). The reviewed field operating window for the combined device $n^{\circ}1$ in (a) is now from 20 mT to 34 mT (blue area), which corresponds

to the ones of the complete device ($70^\circ/210\text{ nm}$) in (c) exhibiting operating fields from 17 mT to 33 mT. For combined device $n^\circ 2$, it is now from 15 mT to 26 mT (blue area) in (b) thus coinciding well with the complete device $70^\circ/300\text{ nm}$ in (c) that exhibits operating fields from 15 mT to 24 mT. Neither devices reach the absolute maximum nucleation value (36 mT) set by the cross-sectional dimensions of the syphon structure. The latter can as well be seen for other complete devices ($75^\circ/210\text{ nm}$, $75^\circ/300\text{ nm}$, $70^\circ/210\text{ nm}$, $70^\circ/300\text{ nm}$) in (c) where the vertical arm reversal is setting the maximum limit and not the nucleation in the syphon. Concerning the depinning values, we observe an increase for larger syphon angles in (c) resulting in the loss of the operating window for the device $75^\circ/300\text{ nm}$ while an operating window of 2 to 3 mT is still present for the device $70^\circ/300\text{ nm}$. Similarly, a more substantial operating window is obtained for $70^\circ/210\text{ nm}$ as compared with $75^\circ/210\text{ nm}$, due to equal vertical-arm-reversal fields set by the cross dimensions, and a smaller depinning field for the shallower syphon angle.

Theoretically the lower limit of the syphon angle for reliable operation sets 45° since lower angle values would allow domain walls to arrive at the cross for applied field angles (α) that would yield a vertical arm reversal (e.g., if $\theta = 30^\circ$ then an applied field at angle $\alpha = 55^\circ$ would allow the propagation to the center of the cross but due to the larger y-component of the field, it would trigger the vertical arm reversal.) From Fig. 7.6, we see that the nucleation in the center of the cross is the maximum operating applied field strength. The meeting point between the nucleation field values in the center of the cross (circular lines in Fig. 7.6 (a) and (b)) and the vertical arm reversal data (diamonds in Fig. 7.6 (a) and (b)) determines the experimentally-obtained maximum angle before a vertical arm reversal occurs. If we use the previously explained model for the syphon, we find a lower syphon angle limit for $\theta = 55^\circ - 60^\circ$ represented in black in Fig. 7.6 (a) and (b).

Finally, the device with the most significant field operating window is $75^\circ/180\text{ nm}$, which shows the highest value for the vertical-arm-reversal field likely limited by a nucleation event occurring in the syphon. To increase this field operating window, a decrease of the width of the whole structure is necessary. Furthermore, since the center of the cross controls the upper limit of the operating window, very shallow angles of the syphon element (e.g., $\theta = 55^\circ$) can be used thus also reducing the depinning field in the device.¹ We identify as the ultimate operation window the scenario where the depinning field is dominated by the center of the cross dimensions and not the syphon, and the nucleation field is governed by the cross-section of the wires in the device (e.g., syphon) and not the dimension of the cross, which provides clear guidelines for gauging the optimal performance that can be reached by this multiturn sensor device concept.

¹I acknowledge F. Kammerbauer for helping with the measurement of the MOKE images.

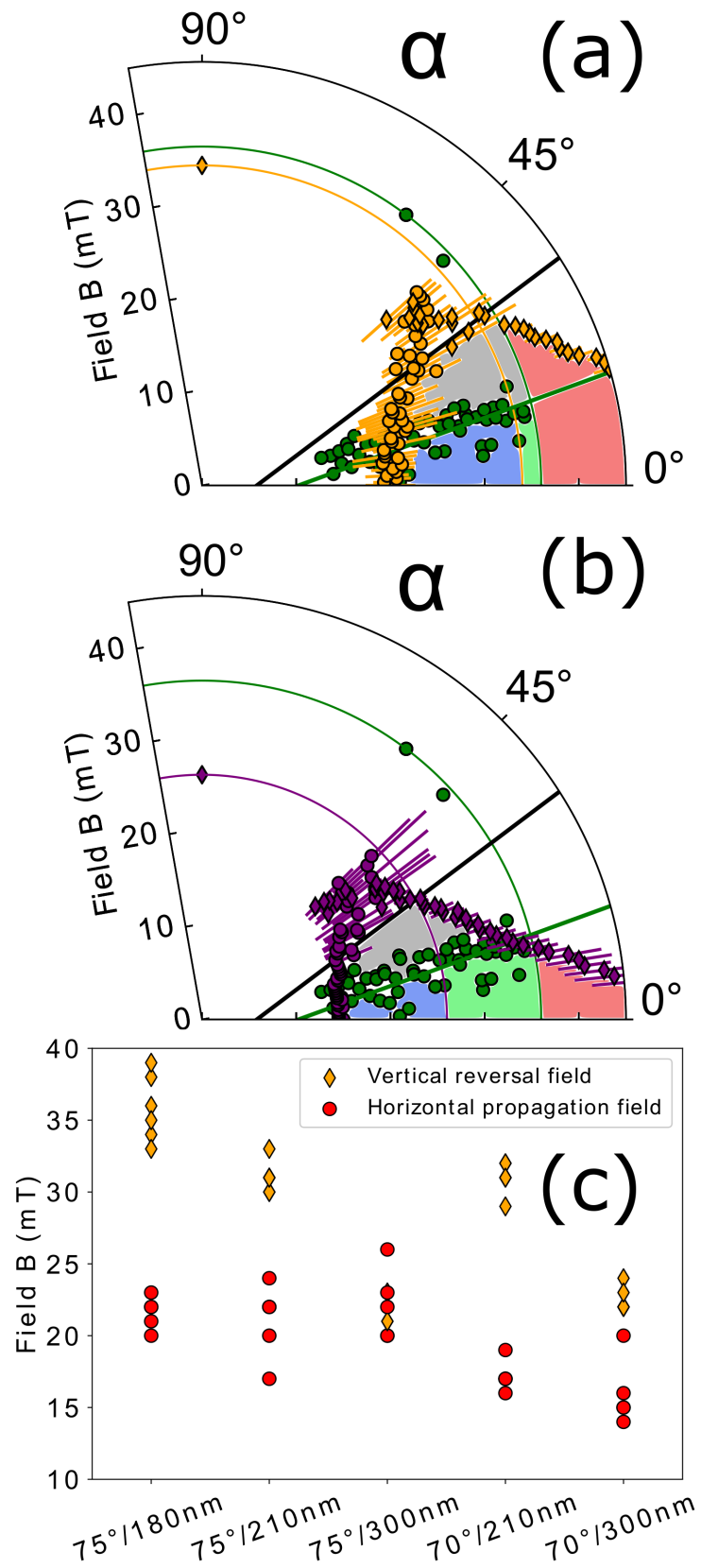


FIGURE 7.6: (a) Polar plot of an expected complete device $n^\circ 1$ comprised of cross $n^\circ 1$ and a syphon ($\theta = 70^\circ$). (b) Similar plot as (a) for device $n^\circ 2$. (c) Plot on the measurement results of the depinning field (red circles) and the vertical-arm-reversal field (orange diamonds) in a complete structure with varying characteristics referenced in abscissa. Adapted from (177).

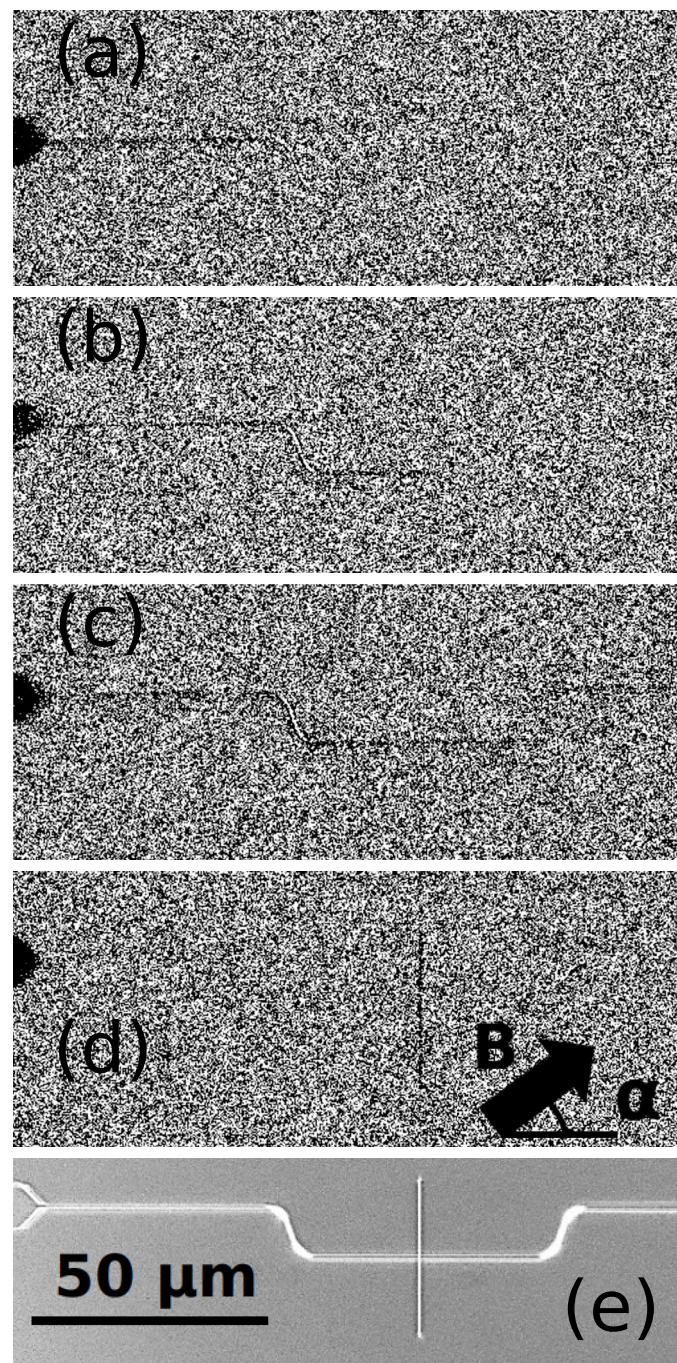


FIGURE 7.7: (a) MOKE differential contrast image showing the switching of the magnetization in the left horizontal arm for $B = 8$ mT. (b) MOKE differential contrast image showing the switching of the magnetization up to the center of the cross for $B = 15$ mT. (c) MOKE differential contrast image showing the complete switching of the horizontal arms for $B = 19$ mT. (d) MOKE differential contrast image showing the vertical arm reversal for $B = 32$ mT, and the orthogonal MOKE sensitivity compared to (a, b, and c). (e) Optical microscopy image of the complete measured structure. The field was applied at an angle of $\alpha = 30^\circ$.

7.6 Conclusion

To summarize, we present the experimental realization of the components of a closed-loop multi-turn sensor device, and we analyze the key components, which are a syphon together with a cross-shaped intersection architecture allowing for the reliable control of a DW under a rotating applied field. We observe a consistent behavior for different cross dimensions. The depinning field increases slightly with the decrease of the center diagonal dimensions, and the maximum nucleation field is largely enhanced providing a good indication that the reduction of the center is the key parameter that can be used to increase the operating window. The syphon element governs the field angles for which the DW arrives at the cross thus constituting a key element necessary for a reliable operation. It sets the maximum operating field for the complete device, which is identified to be the nucleation field in the syphon structure.

Finally, the combination of the two elements reveals an unexpected limit set by the reversal of the cross center when a DW is not present, showing that the full device performance is not merely governed by the superposition of the individual performance parameters of the syphon and cross. This highlights that one needs to study the full device to obtain the correct operating conditions. We thus identify the central geometrical dimensions that set the limitation of the maximum field value of the field operating window up to the nucleation field of the syphon structure. As guidelines to obtain a large operating window one needs to choose a syphon angle sufficiently steep to allow the reliability of the interaction with the cross center ($\theta = 55^\circ$ or larger), and a center cross dimension small enough to reach the absolute maximum nucleation field set by the whole structure.

	Smallest horizontal-arm reversal field	Smallest vertical-arm reversal field	Buffer zone	Figure
Decrease cross dimensions from 300 nm to 210 nm	Increase: +5 mT	Increase: +9 mT	Depends on the syphon angle	Fig. 7.2
Decrease syphon angle from $\theta = 80^\circ$ to 65°	Decrease: -12 mT	No impact	Decrease: 15°	Fig. 7.5

TABLE 7.1: Table summarizing the impact of the various allowed modifications to the key elements of the closed-loop structure.

Chapter 8

Conclusion

Magnetic domain wall based sensors have the potential to provide several answers to critical industrial challenges. First, the power consumption of sensor elements needs to be reduced in embedded systems to allow the embarkation of lighter batteries. The domain wall based sensors being 'True-power on', their consumption is quasi-null. A second potential issue with sensors resides in the necessity of additional memory to save its state. Since domain wall based sensors are containing a memory capability at room temperature, they provide an answer to this challenges too.

In the presented thesis, we provide the necessary background information for the understanding of the results chapter. The different processes occurring in the open-loop and the innovative closed-loop sensor concept under the application of a magnetic field are extensively described. We then provide the results of experiments performed for the improvement of the field operating window of the devices.

More precisely, we provide the measurement scheme for the boundaries of the field operating window based on DW propagation allowing us to gauge the limitations of the functioning of the devices. We find that both the materials and the geometry play a key role. The origin of the geometrical dependence of the depinning field limit appears challenging to pinpoint because of a variety of factors contributing to the variation in depinning field limits. These are, in fact, hard to characterize and quantify precisely. Despite it, a clear difference in pinning between a material with magneto-crystalline anisotropy ($\text{Co}_{90}\text{Fe}_{10}$) and without ($\text{Ni}_{81}\text{Fe}_{19}$) is measured. For the nucleation field, the dependence on the geometry can be described by an adapted Stoner-Wohlfarth model, even despite micro-magnetic simulations not showing a coherent rotation of the magnetization in the complete wires. Thus the nucleation field geometry dependence provides a handle for the improvement of magnetic DW sensors. The measurement sequences of the sensor structure with the GMR effect is also introduced, and the advantages of the GMR effect measurement as compared to the MOKE measurements are explained. After the measurement of a large number of devices, we derive an accurate assessment of a fitting constant used for the MOKE measurement results. We can ascertain a definite limit by the previously mentioned maximum nucleation field value and find that this is related to the resistance of the sensor. This limit can be used as a tool for future fast analysis of magnetic sensors thus already providing some improved means for the industry.

After the previous study, we experiment on the enlargement of the field operating window of the open-loop devices. These experiments aim at the identification of the modifiable parameters that can potentially provide the most significant and accessible handles for the improvement of the FOW. With the first of these, we conclude that the non-uniformity of the mass-production process tends to damage the odds of obtaining a significant yield of production. If the uniformity in a mass-production environment is not obtainable due to physical reasons (limit of the optical lithography resolution), then the concept of the sensor element needs to be improved hence the experiments further conducted. Innovative designs and a new setup are created for a faster investigation. The changes to the original architecture provide some insight on the way to design a nano-magnetic structure if we are aiming for reliability, i.e., smooth corners and short side lengths. We also observe that the scaling of the open-loop structure is substantially limited due to the scaling of the probability of finding defects as the number of loop increases. We then focus on the propagation/depinning field. The comparison of the results obtained with a large number of elements and a large number of turns of the applied magnetic field yield some interesting insight. The propagation field appears mainly to be mainly affected by the quality of the processing and not by geometrical parameters, thus not constituting an easy handle.

The nucleation field is then investigated, and the expectations are that it provides a more sensitive handle for the improvement of the FOW. At that point, the scaling of the nucleation field with a change in the width is known, i.e., SW model. The aim is then to modify the thickness of the magnetic layer. The observable effect of the latter is a saturation of the scaling of the nucleation field. This saturation is located at the transition between the nucleation of two Néel walls and two Bloch walls, thus suggesting that the SW model is applicable only with the nucleation of Néel walls, i.e., with a small thickness. The influence of the cross-sectional shape is also investigated via the use of different ion milling time lengths of the material stack. The results of this experiment show the little influence of the edge roughness and the massive one from the trapezoidal cross-section. These results are then further confirmed by simulations performed on smooth and rough structures with the same cross-sectional shape. The cross-section appears as the main contributor to the scaling factor used to fit our data with the Stoner-Wohlfarth model in chapter 4. After modifications to the geometry, variations are introduced to the material used, i.e., $\text{Ni}_{81}\text{Fe}_{19}$. Different sputtering tools and sputtering conditions are selected, that resulted in no apparent influence on the FOW. Thus indicating that the crystallization of the stack or its texturing does not play a significant role in the FOW. Finally, the patterning process is modified to reach a perfect rectangular cross-section with very little edge roughness. For the latter, we used the electron beam lithography, and despite the much-improved shape, the FOW is decreased. This puzzling result is attributed to the damage induced by the electron beam during the processing that exceeds the gains from the improved shape.

As a general conclusion from the chapters on the open-loop, a large FOW is obtainable if the focus is on modifying the nucleation field. The smallest width and the largest thickness, where a vortex domain wall is present, need to be used.

The patterning process should obviously be as soft and precise as the technology can provide.

After the study on the open-loop, a new concept for a sensor device is presented. It enables counting up to millions of 360° -turns performed by the applied field. We first explain in simple terms the working principle of the innovative concept and derive a simple example to demonstrate the enormous scaling of this approach. To implement the new concept, we use a cross-shaped intersection of magnetic wires. This element permits the intertwining of loops and the non-necessity of a nucleation pad rendering the structure achiral and thus enabling the usage of both directions of rotation of the applied field. We explore the DW propagation in this cross-shaped geometry and obtain different states of the cross while interacting with a domain wall. We conceptually find that with a simple cross, some configurations (applied field and magnetization in the vertical arm being anti-parallel) are generating the failure event for the sensor operation. Various chiralities and cross geometries are also checked, and the depinning field from the center appears to be chirality dependent. Furthermore, a decrease of the center dimensions yields an increase of the nucleation field as expected from the SW model (34), thus opening a possible way for the improvement of the cross performances. To answer to the problematic of the failure of the cross alone, we develop a syphon structure comprised of a tilted wire that is placed on each wires joining the cross. The viability of the concept is ascertained by realizing micromagnetic simulations. The cross and the syphon elements are investigated under applied field configurations (strength and angle) to identify their respective operating conditions. The cross yields a complex DW behavior characterized by three physical mechanisms: the propagation through the cross, the pinning at the cross and the reversal of a vertical arm. The syphon arm for different syphon angles is modeled via a hyperbolic dependence on the angle of the applied field. From the results obtained, a combined element is generated by assembling the results of the two individual components. We demonstrate via the latter operation that the concept is, at least from a simulation point of view, feasible. Finally, the combination of the two elements allows for the identification an angular operating window, a field operating window and a robustness factor; the three of them allow for an easy identification of a reliable structure, which is essential to design the geometries of reliable devices of this new generation of multi-turn sensor.

Further on, the natural step to continue the study of the closed-loop structure appeared to be the experimental realization of the introduced concepts. The cross-shaped intersection and the syphon are built and investigated separately to confirm the micromagnetic results. In fact, the experimental results obtained tend to be very similar to the ones generated by the simulations. Various cross centers are also experimentally realized, and the results concerning the three characteristic processes (pinning, successful propagation, and vertical arm reversal) interestingly show a robustness to potential problems with the cross-shaped element. These issues are, for example, proximity-effect potentially inducing an enlargement of the center dimensions. This conclusion pushed us also to assemble the results in a virtual combined device and to derive the expected performances of the complete sensor device. To confirm the expected results, full sensor devices containing the syphon and the cross are also experimentally realized.

Finally, this device reveals an unexpected limit set by the reversal of the cross center when a DW is not present, showing that the full device performance is not merely governed by the superposition of the individual performance parameters of the syphon and cross. These results highlight that one needs to study the entire device to obtain the correct operating conditions. To conclude, a clear guideline is provided for the acquirement of a large FOW for the closed-loop device. We remind them, here. The syphon angle needs to be sufficiently steep to allow the reliability of the interaction with the cross center ($\theta = 55^\circ$ or larger), and the cross center dimension needs to be small enough to permit the reach of the absolute maximum nucleation field set by the whole structure.

As a conclusion on the innovative closed-loop concept, the structure is numerically and experimentally realized and thus revealing a potentially groundbreaking sensor device concept for the acquirement of full rotations of an applied magnetic field. The study of the individual elements provide a way to improve them individually, but solely the investigation of the complete structure offers clear guidelines for the industrial realization of the concept. This concept could ultimately yield close to an infinite counting of turns, with true power on and memory capability in the active element of the sensor device.

8.1 Outlooks

In this section, some outlooks are derived from the conclusions on the topics that we expect might yield results.

The ability to fast sort the sensor element by a simple measurement of their resistance needs to be further tested on other wafers since it could critically reduce the testing time at least for the nucleation field. Especially, more data points should be acquired with a different measurement sequence than the bisection method, which tends to discard valuable data. If a similar processing is used as for our wafers, the obtained scaling factor should be the same.

Concerning the 16-open-loop structure, it would be interesting to determine the difference in depinning and nucleation field for the inner and outer loops. In fact, every outer loop adds $10 \mu\text{m}$ of wire as compared to its inner previous one, from the obtained results we can expect to derive the exact increase of propagation field or decrease of nucleation field per $10 \mu\text{m}$. The study could be pushed further, and the distance between loops could be reduced to $1 \mu\text{m}$, thus indicating the changes per μm of added wire.

Furthermore, for the general outlook on the open-loop, the saturation of the nucleation field with the increase in thickness yields some interesting insight on the nucleation process. As an outlook, more simulations could be performed to generate a complete map of the nucleation field as a function of thickness and width of a wire of $\text{Ni}_{81}\text{Fe}_{19}$. The expectation is to find a scaling of the nucleation field following the SW model up to the point where a pair of Bloch DWs is nucleated in the process. Experimental evidence of the latter would also be desirable. It is, however, still challenging to image nucleation processes for various

reasons. The process of nucleation occurs in the picosecond time scale, which means that the use of time-resolved tools is necessary (pump-probe experiments in the THz range (178)). Furthermore, the size of the DW is in the range of 100 nm thus requiring a good spatial resolution as well. The tools that can perform such experiments are, for example, the time-resolved XMCD-photoemission electron microscopy (179) that is found at a synchrotron. However, even with the proper tool, the measured wires are 400 μm long, and the nucleation point is located at the lowest anisotropy, which might be cumbersome to identify, and image. For this purpose, the structure could be changed to a ring, which is easier to investigate. Experiments on the nucleation field can be performed with other relevant soft magnetic materials to enlarge the FOW. For example, using $\text{Co}_{90}\text{Fe}_{10}$, CoFeB or CoZr (180) could be interesting for their high saturation magnetization (1334 kA/m measured with a BH-looper for $\text{Co}_{90}\text{Fe}_{10}$, the other compounds are expected to yield similar values (181)). The large saturation magnetization is a must for DW based sensors due to the linear scaling of the nucleation field (see SW model). CoFeB and CoZr are especially attractive because of their amorphous structure, that can reduce the pinning of DWs. With those materials, the saturation of the nucleation field could also be tested and improved if the transition between the two nucleation processes can be pushed to higher values. Furthermore, complete devices should also be processed with these materials to investigate the scaling of the propagation field with the width of wire made of an amorphous material. In theory, the pinning should be drastically reduced if the edge roughness is also well defined.

The influence on the deposition conditions could also be tested using other sputtering machines or growth mechanisms such as molecular beam epitaxy. Indeed, molecular beam epitaxy can yield more crystalline samples than sputtering tools, which could bring changes to the propagation field value. We expect an increase of this field limit with the enhanced crystallinity due to the higher chances of pinning for the DW. The field applied during the growth of the $\text{Ni}_{81}\text{Fe}_{19}$ can also be rotated to check for the effect of using a uniform anisotropy in the plane of the sample as compared to a unidirectional field. Finally, the sputtering power could also be varied (182), which could result in more or less smooth materials, thus also influencing the propagation field. The nucleation field is expected to be rather insensitive to changes in the crystalline structure as the main contributor to this process originates from the shape anisotropy.

Finally, the reason why the patterning with ebeam does not yield a significant field operating window improvement should be further investigated. Monte Carlo simulations could be performed to numerically investigate the effect of the bombardment of the electrons on our material. Other patterning methods can also be tested such as lift-off that would potentially induce fewer damages to the material deposited. If one of the patterning methods appears favorable and more precise than the current optical lithography, smaller widths should be patterned to obtain the full spectrum width and thickness dependence of the nucleation field. The smaller width could lead to a drastic increase of the nucleation field due to its hyperbolic dependence on the width of the wire.

Concerning the closed-loop device concept, smaller center dimensions of the cross should be simulated up to the resolution limit of the ebeam lithography tool

to obtain a boundary of the expected FOW. Innovative architectures of the cross should be proposed with nanomagnets or other elements that could locally enhance the nucleation field to increase the FOW. The next step would be to make the complete device with a GMR layer and test it for a large number of full rotations to characterize the reliability of both bounds of the FOW for the syphon and the cross-shaped element.

Other challenges should also be addressed by the industry, first, layouts for the efficient electrical contacting of the structure should be designed probably using measurement sequences to reduce the number of connections. Furthermore, the testing of the elements for a large number of turns should be stressed and encouraged to obtain the full failure rates of the propagation field and nucleation field, which could yield to the identification of performance-hindering defects. Finally, the sensor should be advertised, and big corporations should start the production of this game-changing concept that could dramatically reduce the power consumption for the IoT concepts and embedded systems.

Appendix A

Valet-Fert model

The considered stack for the development of the model is composed of alternating magnetic and non-magnetic layers of the same thickness t . We use the signs \pm to denote the absolute spin direction ($s_x = \pm\frac{1}{2}$) and the $\uparrow\uparrow$ ($\downarrow\uparrow$) to represent the spin majority and minority. The layers are stacked in the z -direction. The considered temperature of the system is 0 K, which cancels spin relaxations through magnon scattering due to the frozen magnons. The only spin-flip scattering possibilities are through the spin-orbit coupling with defects or by spin dilution with an exchange type mechanism with the paramagnetic spacer layer. The development of the model starts with a linearized Boltzmann equation for transport mechanism. The latter is possible if we stay in the limit of a parabolic conduction band. Indeed, the Boltzmann model breaks down for multi-band model because the sub-band energy splitting becomes compatible with the lifetime broadening caused by the scattering. The latter presses us to assume that all the materials involved, exhibit a single parabolic conduction band, with the same effective mass m and the same Fermi velocity v_F . The equation is:

$$v_z \frac{\partial f_s}{\partial z}(z, v) - eE(z)v_z \frac{\partial f^0}{\partial \epsilon}(v) = \int d^3v' \delta[\epsilon(v') - \epsilon(v)] P_s[z, \epsilon(v)] [f_s(z, v') - f_s(z, v)] + \int d^3v' \delta[\epsilon(v') - \epsilon(v)] P_s f[z, \epsilon(v)] [f_{-s}(z, v') - f_s(z, v)] \quad (\text{A.1})$$

where e is the elementary charge of the electron, $\epsilon(v) = \frac{1}{2}mv^2$ is the kinetic energy of the electrons and $E(z)$ is the local electric field. The $P_s[z, \epsilon(v)]$ and $P_s[z, \epsilon(v)]$ are respectively the spin conserving and spin flipping transition probabilities which are isotropic in velocity space to avoid transfer of momentum between the two spin channels. The distribution function is then separated in a Fermi-Dirac contribution and a perturbation term:

$$f_s(z, v) = f^0(v) + \frac{\partial f^0}{\partial \epsilon}([\mu^0 - \mu_s(z)] + g_s(z, v)) \quad (\text{A.2})$$

In the cylindrical symmetric problem, the Boltzmann equation model reduces to a macroscopic model due to the much longer spin diffusion length than the mean free path. We obtain (103):

$$\frac{e}{\sigma_s} \frac{\partial J_s}{\partial z} = \frac{\bar{\mu}_s - \bar{\mu}_{-s}}{l_s^2}, \quad J_s = \frac{e}{\sigma_s} \frac{\partial \bar{\mu}_s}{\partial z} \quad (\text{A.3})$$

with $\bar{\mu}_s(z) = \mu_s + eV(z)$ is the electrochemical potential for spin s and $(1/l_{sf})^2 = (1/l_{\uparrow\uparrow})^2 + (1/l_{\downarrow\uparrow})^2$.

The first equation is describing the compensation of the spin accumulation at the interface by the spin-flip mechanism and the second is simply Ohm's law. Then by writing the spin-dependent electrochemical potential $\bar{\mu}_{\pm} = \bar{\mu} \pm \Delta\mu$ and considering the free electron model, one can write:

$$|\Delta\mu| = 2\mu_0 |\Delta M| / (3n\mu_B) \quad (\text{A.4})$$

where n is the electron density and the gradient of the spin-independent part of μ_{\pm} reads:

$$F(z) = \frac{1}{e} \frac{\partial \bar{\mu}}{\partial z} \quad (\text{A.5})$$

is an electric field. We then transform equations A.2 into:

$$\frac{e}{\sigma_{\pm}} \frac{\partial J_{\pm}}{\partial z} = \pm 2 \frac{\Delta\mu}{l_s^2}, \quad J_{\pm} = \sigma_{\pm} \left[F(z) \pm \frac{1}{e} \frac{\partial \Delta\mu}{\partial z} \right] \quad (\text{A.6})$$

Thus leading to a spin diffusion type of equation of the form:

$$\frac{\partial^2 \Delta\mu}{\partial z^2} = \pm 2 \frac{\Delta\mu}{l_s^2} \quad (\text{A.7})$$

And

$$\frac{\partial^2}{\partial z^2} (\sigma_+ \bar{\mu}_+ + \sigma_- \bar{\mu}_-) = 0 \quad (\text{A.8})$$

It is now convenient to introduce a bulk spin asymmetry β in the ferromagnetic layers:

$$\rho_{\uparrow\uparrow(\downarrow\uparrow)} = 2\rho_F^* [1 - (+)\beta] \quad (\text{A.9})$$

and in the non-magnetic one $\rho_{\uparrow\uparrow(\downarrow\uparrow)} = 2\rho_N^*$. Here, the $\uparrow\uparrow$ denotes the spin majority and the electrons, in each spin channel, go through a series of layers having effective resistances $\rho_F^* = t_F(\rho_{\uparrow\uparrow} + \rho_{\downarrow\uparrow})/2$ and $2\rho_N^* t_N$. To solve the equations, the boundary conditions are defined following (103).

For an interface at location z_0 , the continuity condition of the spin current reads:

$$J_s(z_0^+) - J_s(z_0^-) = 0 \quad (\text{A.10})$$

In the presence of significant scattering located near the 1 dimensional interface, the potential conditions are:

$$\bar{\mu}_s(z_0^+) - \bar{\mu}_s(z_0^-) = r_s[J_s(z_0)/e] \quad (\text{A.11})$$

Where r_s is the spin-dependent boundary resistance between the ferromagnetic and non-magnetic layers. Finally, as with the bulk, we introduce an interfacial spin asymmetry coefficient γ :

$$r_{\uparrow\uparrow(\downarrow\downarrow)} = 2r_b^*[1 - (+)\gamma] \quad (\text{A.12})$$

It is now possible to solve the differential equations in the case of a multilayer system with M bilayers, interface and bulk spin-dependent scattering. In the limit, where the thickness of the ferromagnetic layer t_F and the thickness of the non-magnetic t_N layer are small compared with l_{sf} in the ferromagnet and the non-magnetic layer. We end up with:

$$R^{(P,AP)} = M(r_0 + 2r_{SI}^{(P,AP)}) = Mr^{(P,AP)} \quad (\text{A.13})$$

with r_{SI} being the spin-coupled interfacial resistance, and :

$$r_0 = (1 - \beta^2)\rho_F^*t_F + \rho_N^*t_N + 2(1 - \gamma^2)r_b^* \quad (\text{A.14})$$

and the spin-coupled interface parts are given by:

$$r_{SI}^{(P)} = \frac{\frac{(\beta-\gamma)^2}{\rho_N^*l_{sf}^{(N)}} \coth\left[\frac{t_N}{2l_{sf}^{(N)}}\right] + \frac{\gamma^2}{\rho_F^*l_{sf}^{(F)}} \coth\left[\frac{t_F}{2l_{sf}^{(F)}}\right] + \frac{\beta^2}{r_b^*}}{\frac{1}{\rho_N^*l_{sf}^{(N)}} \coth\left[\frac{t_N}{2l_{sf}^{(N)}}\right] + \frac{1}{\rho_F^*l_{sf}^{(F)}} \coth\left[\frac{t_F}{2l_{sf}^{(F)}}\right] + \frac{1}{r_b^*} \left[\frac{1}{\rho_N^*l_{sf}^{(N)}} \coth\left[\frac{t_N}{2l_{sf}^{(N)}}\right] + \frac{1}{\rho_F^*l_{sf}^{(F)}} \coth\left[\frac{t_F}{2l_{sf}^{(F)}}\right] \right]} \quad (\text{A.15})$$

$$r_{SI}^{(P)} = \frac{\frac{(\beta-\gamma)^2}{\rho_N^*l_{sf}^{(N)}} \tanh\left[\frac{t_N}{2l_{sf}^{(N)}}\right] + \frac{\gamma^2}{\rho_F^*l_{sf}^{(F)}} \coth\left[\frac{t_F}{2l_{sf}^{(F)}}\right] + \frac{\beta^2}{r_b^*}}{\frac{1}{\rho_N^*l_{sf}^{(N)}} \tanh\left[\frac{t_N}{2l_{sf}^{(N)}}\right] + \frac{1}{\rho_F^*l_{sf}^{(F)}} \coth\left[\frac{t_F}{2l_{sf}^{(F)}}\right] + \frac{1}{r_b^*} \left[\frac{1}{\rho_N^*l_{sf}^{(N)}} \tanh\left[\frac{t_N}{2l_{sf}^{(N)}}\right] + \frac{1}{\rho_F^*l_{sf}^{(F)}} \coth\left[\frac{t_F}{2l_{sf}^{(F)}}\right] \right]} \quad (\text{A.16})$$

In the limit, $t_F(t_N) \ll l_{sf}^{(F)}(l_{sf}^{(N)})$,

$$r^{(P,AP)} = \frac{1}{1/r_+^{(P,AP)} + 1/r_-^{(P,AP)}} \quad (\text{A.17})$$

With $r_{+(-)}^{(AP)} = (r_+^{(P)} + r_-^{(P)})/2$ The parallel resistance is defined by:

$$r_{+(-)}^{(P)} = 2\rho_F^*[1 + (-)\beta]t_F + 2\rho_N^*t_N + 4r_b^*[1 + (-)\gamma] \quad (\text{A.18})$$

The last term containing r_b^* are not present in the CIP geometry. This term is made by the reflection of the electron at the interface and diffusive scattering by disordered interfaces.

To compare with Mott's two current model, in the case of a multilayer made of M repetitions of the bilayer system, we can write using the two previous equations:

$$R^{(AP)} = M(\rho_F^*t_F + \rho_N^*t_N + 2r_b^*) \quad (\text{A.19})$$

and

$$\frac{1}{R^{(P)}} = \frac{1}{M} \left[\frac{1}{2\rho_F^*(1-\beta)t_F + 2\rho_N^*t_N + 4r_b^*(1-\gamma)} + \frac{1}{2\rho_F^*(1+\beta)t_F + 2\rho_N^*t_N + 4r_b^*(1+\gamma)} \right] \quad (\text{A.20})$$

which results in:

$$R^{(P)} = R^{(AP)} - \frac{(\beta\rho_F^*[t_F/(t_F + t_N)]L + 2\gamma r_b^*M)^2}{R^{(AP)}} \quad (\text{A.21})$$

Appendix B

Ebeam patterning parameters

In this appendix, the selectable parameters of the machine handling the ebeam patterning (Raith pioneer) are explained in details. During the project, the settings were changed for the improvement of the patterning of the samples. Here, we then only provide the range of values used for the various parameters and their effect on the patterning of the samples.

	Values
Working distance	8 - 10 mm
Acceleration voltage	10 - 30 kV
Aperture size	7,5 - 120 μm
Step size	4 - 19 nm

TABLE B.1: Table summarizing the variable parameters used for the patterning with the ebeam lithography system.

Working distance: The working distance is modifying the distance between the end of the emitting column and the sample surface. A modification of this distance is essentially changing the shape of the electron beam and the longer the working distance is, the narrower the apex of the beam on the sample surface becomes (see Fig. B.1). This effect should then be used to improve the resolution of the writing probe. However, a significant problem with increasing the distance is more difficult beam control. For our patterning, we used the smallest available working distance of 8,3 mm.

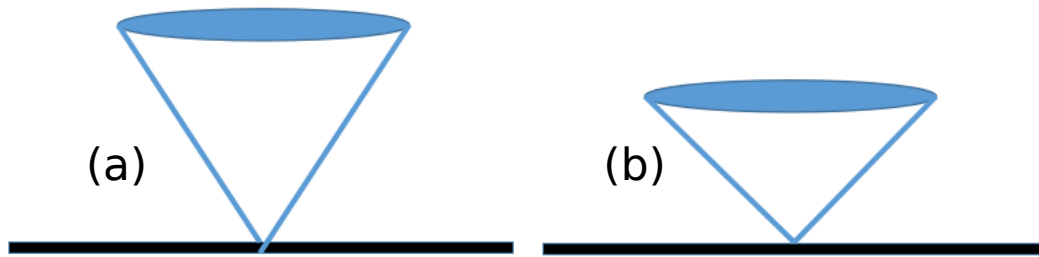


FIGURE B.1: Schematic representation of the influence of the working distance on the electron beam shape, (a) for a large working distance, e.g., 10 mm, or (b) for a smaller working distance, e.g., 8 mm. The blue oval represents the end of the emitting column, and the black line is the sample's surface. The blue lines are the edges of the electron beam.

Acceleration voltage: The acceleration voltage is the voltage applied between the end of the emitting column and the sample's surface. The larger this acceleration voltage is, the more the electrons are accelerated toward the sample, and the further they are traveling before being reflected by interaction with the sample.

The acceleration voltage also changes the shape of the beam. For a larger acceleration voltage, the result is a straighter beam while a smaller one yields a more conical shape. Furthermore, if the trajectory of the electrons is recorded when they enter the sample, we observe the generation of a pear-shape-like pattern (183) as seen in Fig. B.2 due to the backscattering of the electrons.

The effect of the backscattering of the electrons and thus change of trajectory is the possibility for an electron to expose the resist from the bottom as it escapes the material. As seen in Fig. B.2, the larger the acceleration voltage is, the more spread is the effect but also, the lesser dense close to the entrance point of the beam in the material. The use of a small voltage with a negative resist is then yielding a trapezoidal cross-sectional shape of the patterned wires due to exposure from the bottom by backscattered electrons. Thus it is advised to use a large voltage to generate square-shaped wires. For our patterning, we used $A_{cc}V = 30$ kV.

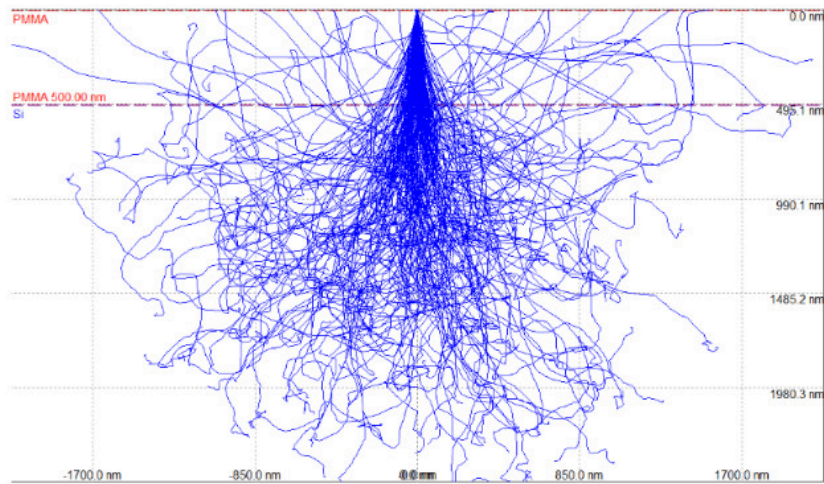


Fig. 1: Simulated trajectories of 200 electrons in PMMA layer (500 nm) on silicon for beam voltage 15 kV.

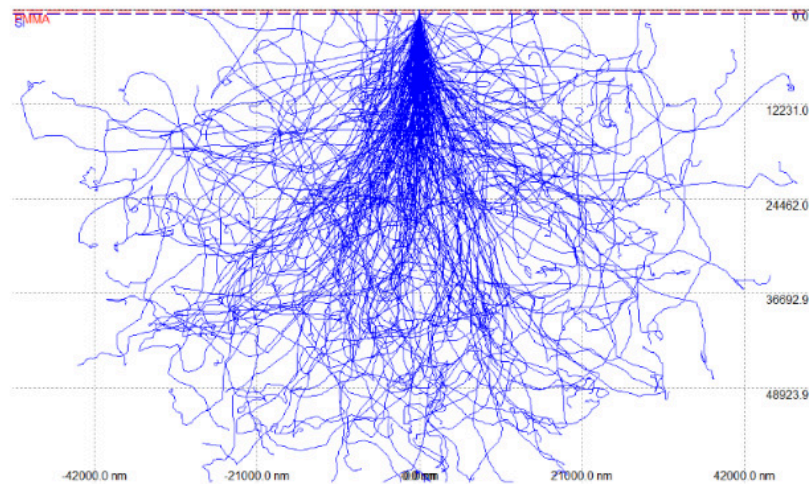


Fig. 2: Simulated trajectories of 200 electrons in PMMA layer (500 nm) on silicon for beam voltage 100 kV.

FIGURE B.2: Monte Carlo simulations of the trajectories of electrons in a PMMA layer for an acceleration voltage of 15 kV (Fig. 1) and 100 kV (Fig. 2). The image is taken from Ref. (184)

Aperture size: The aperture size is describing the size of the aperture placed in the emitting column. A larger aperture is releasing a larger beam as seen from Fig. B.3. All resist typically possess a threshold dose of absorbed electrons for a proper exposure, with a large aperture size the exposure time is reduced due to a large number of released electrons. However, the precision of the machine is worse when the aperture size is wide, and the beam spot focused on the sample's surface is more spread. Since our goal is the obtention of a well defined edge roughness, we selected the smallest available aperture size, i.e., 7,5 μm .

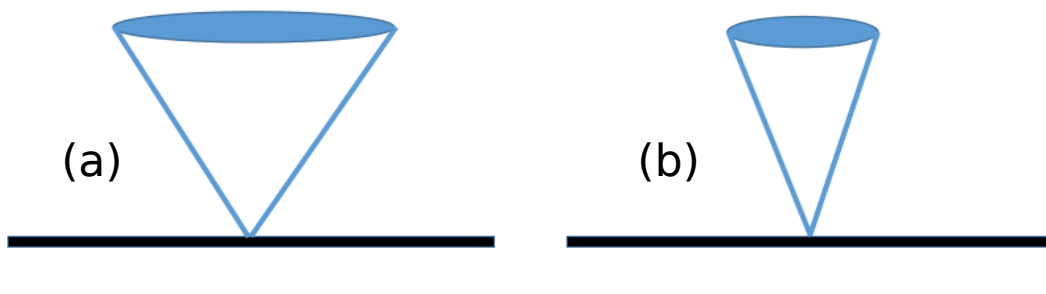


FIGURE B.3: Schematic representation of the influence of the aperture on the shape of the electron beam. (a) A large aperture size. (b) A smaller aperture size than in (a). The blue oval represents the end of the emitting column, and the black line is the sample's surface. The blue lines are the edges of the electron beam.

Step size: Finally, the step size describes the distance between two exposed spots as described in Fig. B.4. For a small edge roughness, the step size needs to be kept short. The patterning of our structures thus requires the shortest one offered by the machine, i.e., 4 nm.

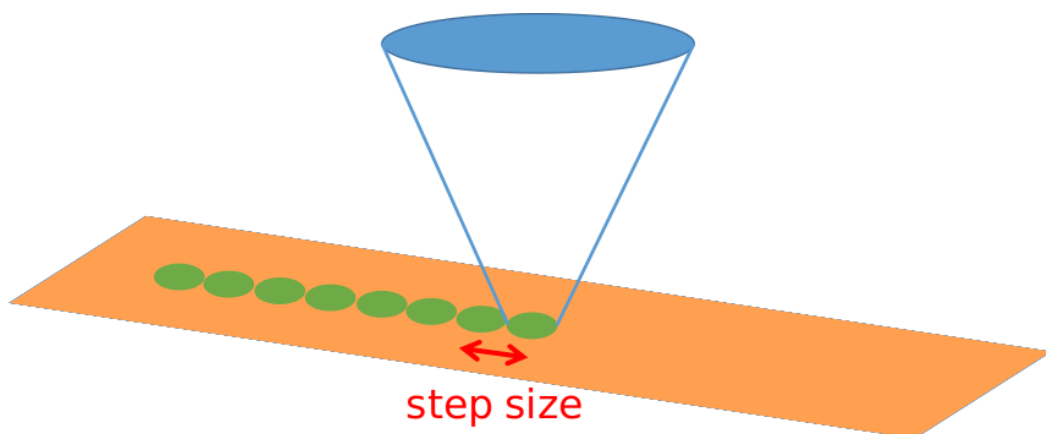


FIGURE B.4: Schematic representation of the patterning of the resist with an electron beam. The blue oval represents the end of the emitting column, and the blue lines are the edges of the electron beam. The orange surface represents the resist, and the green spots are the exposed areas.

Other than the selection of the various parameters, the steps required for the patterning are the focus of the beam on the surface and the launch of the writing procedure. These steps are not straightforward but they are system dependent, so we do not describe them further.

Appendix C

Ion etching parameters

In this appendix, the selectable parameters of the etching machine (Ionsys 500) are explained in details.

	Values
Argon Flow	MFC1 = 3 cm ³ /min; MFC2 = 5 cm ³ /min
Acceleration voltage	400 V
Rotation speed	20 rpm
Tilt of the sample	0° - 90°

TABLE C.1: Table summarizing the variable settings used for the etching of the samples.

Argon flow: The argon-flow setting controls the amount of argon present in the chamber and thus etching rate of the sample. The argon flow is kept at 3 cm³/min at the position of the first mass flow controller and 5 cm³/min at the position of the second one.

Acceleration voltage: The acceleration voltage is the voltage applied between the end of the emitting column and the sample's surface. The larger the acceleration voltage, the more the ions are accelerated toward the sample. This setting is kept at 400 V.

Rotation speed: This setting is the changing the rotation speed of the plate holding the sample. It does not have a drastic influence on the etching, we then keep it at 20 rpm.

Tilt angle: The tilting angle has a powerful influence on the etching. The proper setting of this parameter allows reducing the redeposition of material on the side of the wires.

C.0.1 Etching sequences

In general, various etching sequences were used to reduce the fencing or redeposition. The best etching sequence that we found is:

	Time	Angle
Etching	12 s	90°
Rest	2 min	
Etching	21 s	90° - 0°
Rest	2 min	
Etching	33 s	0°
Rest	2 min	

TABLE C.2: Etching sequence

The first etching step aims to etch perpendicular to the sample surface, which results in a significant etching rate but also considerable redeposition. The second etching is realized at a varied angle, and it gives a square shape to the wire. The last helps to remove the redeposition. The etching is alternated between an etching period followed by a resting time to let the sample cool-down.

Appendix D

AR-N 7520.073 patterning

In this appendix, we describe the processing of the resist called AR-N 7520.073.

The first step is the cleaning of the sample:

Step	Equipment	Parameter	Time	Remark
Cleaning				
Acetone	Wet bench		60 s	
Isopropanol	Wet bench		60 s	
H ₂ O	Wet bench		60 s	
N ₂ blow dry	Wet bench			
O ₂ plasma	Plasma asher	37 sccm/120 W	60 s	

The drop-coating of the resist and baking:

Step	Equipment	Parameter	Time	Remark
Resist Coating				
AR-N 7520.073	Spin coater	Prespin: 500 rpm/ Acc(500) for 2 s Spin: 3000 rpm/ Acc(3000) for 60 s		Rest 5 min Thickness: 100 nm
Soft bake	Hot plate	85°C	60 s	

Then the sample is introduced in the ebeam patterning tool and patterned:

Step	Equipment	Parameter	Time	Remark
E-beam writing				
Exposure	Raith Pioneer	Dose: 130 $\mu\text{C}/\text{cm}^2$ for 200 nm Acceleration voltage: 30 kV Aperture size: 7,5 μm Step size: 4 nm		Line mode

After the exposure, the sample is baked again:

Step	Equipment	Parameter	Time	Remark
Post baking				
Soft bake	Hot plate	95°C	60 s	

The sample is then developed:

Step	Equipment	Parameter	Time	Remark
Development				
Development AR300-47: Desionised H ₂ O (1:2)	Wet bench		23-25 s	Extremelly sensitive
Rince: H ₂ O	Wet bench		60 s	Let H ₂ O flow
N ₂ blow dry	Wet bench			

The sample is then etched:

Step	Equipment	Parameter	Time	Remark
Mask enhancement				
Ar etching	Ionsys 500	MFC1(Ar): 3 sccm; MFC2(Ar): 5 sccm He: 2 mbar MW generator: 330 W Beam voltage: 300 V Acceleration voltage: 400 V Neutralizer: 100 mA	Stepped etching	

With this recipe, the result is:

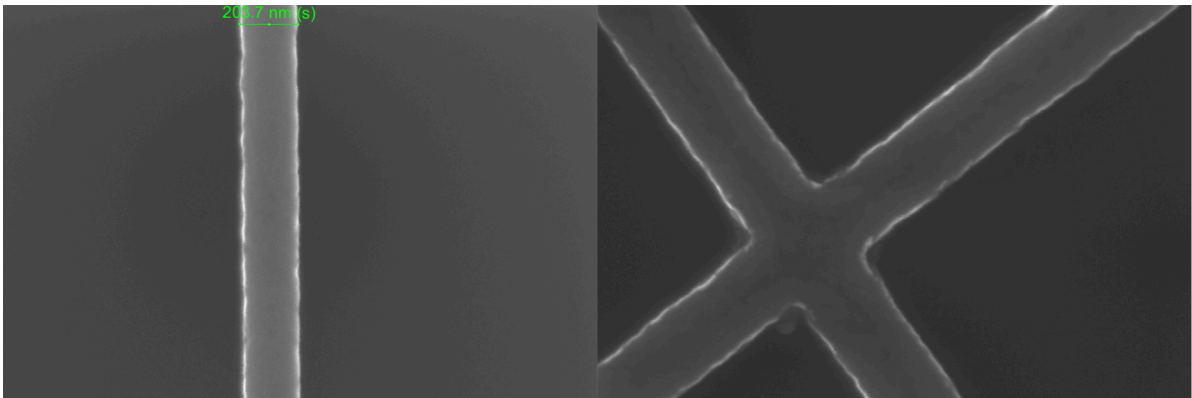


FIGURE D.1: SEM micrographs of the structures patterned with the previously described recipe.

Appendix E

HSQ resist

In this appendix, we describe the processing of the resist called HSQ¹.

The first step is the dillution:

Step	Equipment	Parameter	Time	Remark
Dilution of the resist: FOX-15 in MIBK				
MIBK:FOX-15 (2:1)	Wet bench			Must be done one hour in advance

Then the cleaning of the sample:

Step	Equipment	Parameter	Time	Remark
Cleaning				
Acetone	Wet bench		60 s	
Isopropanol	Wet bench		60 s	
H ₂ O	Wet bench		60 s	
N ₂ blow dry	Wet bench			
O ₂ plasma	Plasma asher	37 sccm/120 W	60 s	

The drop-coating of the resist and baking:

Step	Equipment	Parameter	Time	Remark
Resist Coating				
Spin coating (MIBK:FOX-15)	Spin coater	Prespin: 500 rpm/ Acc(500) for 2 s Spin: 3000 rpm/ Acc(3000) for 45 s		
Soft bake	Hot plate	150°C	120 s	
Cooling	in air		60 s	
Soft bake	Hot plate	220°C	120 s	

The drop-coating of the E-spacer, which is a conductive resist helping with insulating resists such as HSQ and insulating samples:

Step	Equipment	Parameter	Time	Remark
Resist Coating of E-spacing				
Spin coating	Spin coater	Prespin: 500 rpm/ Acc(500) for 5 s Spin: 2000 rpm/ Acc(2000) for 60 s	60 s	

Then the sample is introduced in the ebeam patterning tool and patterned:

¹We warmly thank Dr. D.-S. Han for developing the process and sharing it.

Step	Equipment	Parameter	Time	Remark
E-beam writing				
Exposure	Raith Pioneer	Dose: 3000 $\mu\text{C}/\text{cm}^2$ for 200 nm Acceleration voltage: 30 kV Aperture size: 7,5 μm Step size: 4 nm		Line mode

After exposure the sample is developed:

Step	Equipment	Parameter	Time	Remark
Development				
Development: H ₂ O	Wet bench		20 s	Stir / Removes the E-spacer
Development AZ 400K: Desionised H ₂ O (4:1)	Wet bench	60°C	75 s	
Rince: H ₂ O	Wet bench		60 s	Let H ₂ O flow
N ₂ blow dry	Wet bench			

The resist is then modified to SiO_x:

Step	Equipment	Parameter	Time	Remark
Mask enhancement				
O ₂ plasma	Plasma asher	37 sccm/120 W	120 s	

The sample is then etched:

Step	Equipment	Parameter	Time	Remark
Mask enhancement				
Ar etching	Ionsys 500	MFC1(Ar): 3 sccm; MFC2(Ar): 5 sccm He: 2 mbar MW generator: 300 W Beam voltage: 300 V Acceleration voltage: 400 V Neutralizer: 100 mA		Stepped etching

With this recipe, the result is:

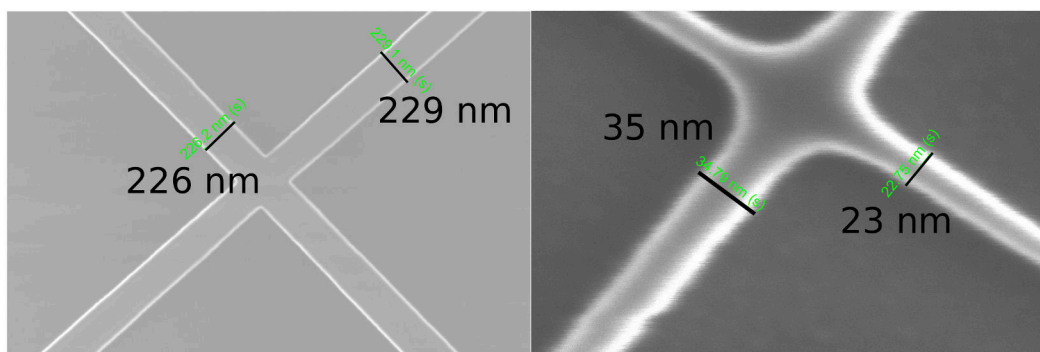


FIGURE E.1: SEM micrographs of the structures made with the described recipe.

Appendix F

AR-N 7520.17 patterning

In this appendix, we describe the processing of the resist called AR-N 7520.17.

The first step is the cleaning of the sample:

Step	Equipment	Parameter	Time	Remark
Cleaning				
Acetone	Wet bench		60 s	
Isopropanol	Wet bench		60 s	
H ₂ O	Wet bench		60 s	
N ₂ blow dry	Wet bench			
O ₂ plasma	Plasma asher	37 sccm/120 W	60 s	

The drop-coating of the resist and baking:

Step	Equipment	Parameter	Time	Remark
Resist Coating				
AR-N 7520.17	Spin coater	Prespin: 500 rpm/ Acc(500) for 2 s Spin: 3000 rpm/ Acc(3000) for 60 s		Rest 5 min Thickness: 400 nm
Soft bake	Hot plate	85°C	60 s	

Then the sample is introduced in the ebeam patterning tool and patterned:

Step	Equipment	Parameter	Time	Remark
E-beam writing				
Exposure	Raith Pioneer	Dose: 40 $\mu\text{C}/\text{cm}^2$ for 200 nm Acceleration voltage: 30 kV Aperture size: 7,5 μm Step size: 4 nm		Line mode

The sample is then developed:

Step	Equipment	Parameter	Time	Remark
Development				
Development: AR300-47	Wet bench		85 s	
Rince: H ₂ O	Wet bench		60 s	Let H ₂ O flow
N ₂ blow dry	Wet bench			

The sample is then etched:

Step	Equipment	Parameter	Time	Remark
Mask enhancement				
Ar etching	Ionsys 500	MFC1(Ar): 3 sccm; MFC2(Ar): 5 sccm He: 2 mbar MW generator: 330 W Beam voltage: 300 V Acceleration voltage: 400 V Neutralizer: 100 mA	Stepped etching	

With this recipe, the result is:

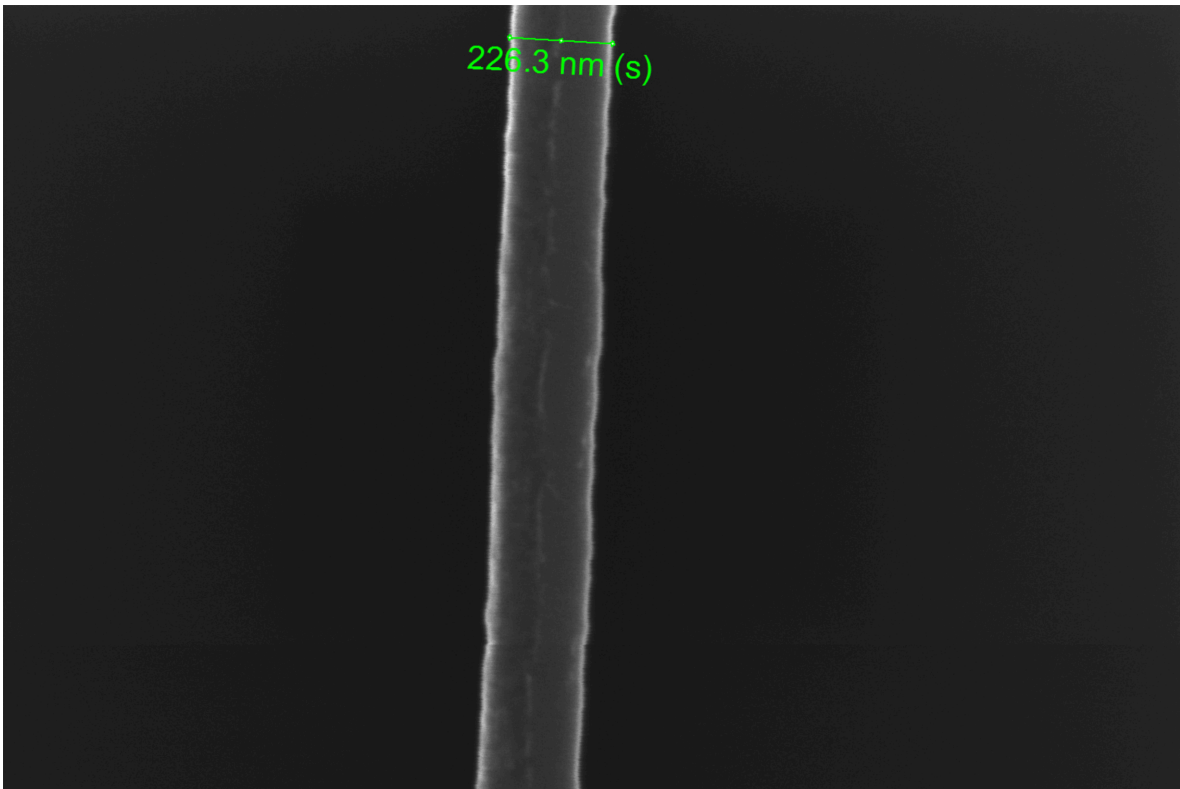


FIGURE F.1: SEM micrographs of the structures patterned with the previously described recipe.

Appendix G

Mumax3 script

In this appendix, we provide some characteristic simulation scripts that we used.

G.0.1 Python script for the automatization of simulations

```
import os, glob, math, sys, subprocess
import numpy as np
import fileinput
import pandas as pd

folder = '/home/benjamin/Desktop/mumax3.9.1c_linux/std_cross_angle_study/'
### Path to the folder containing the template

executable = 'mumax3'
templateName = 'cross_no_DW.mx3'
## Name of the template file

limitField = []
Fields = range(44,2,-2) ##Fields to test
toPrint = []

for FIELD in Fields:
    ###Loop across the tested fields
    PHI = 225.0
    # tested angle of the applied field
    anglea, angleb = [180.0, 270.0]
    # Range of angles of the applied field
    flags = []
    while (angleb - anglea) > 1:
        #Run this loop until the range of angles is not smaller than 1
        filename = "nuc_"+str(FIELD)+'_'+ str(PHI)+".mx3"
        # Create a new mumax file with the simulated field strength and angle
        outputName = folder+"nuc_"+str(FIELD)+'_'+ str(PHI)+".out/table.txt"
        # check that name here is correct! It is the output filename
        a=subprocess.check_output(["cp", folder+templateName, folder+filename])
        # Bash command to create the new file
        b=subprocess.call(["sed", "-i", 's/PHI/'+str(PHI)+'/g', folder+filename])
        # Bash command to modify the string "Phi" in the original templateName
        b=subprocess.call(["sed", "-i", 's/FIELD/'+str(FIELD)+'/g', folder+filename])
        # Bash command to modify the string "Field" in the original templateName
        f=subprocess.call([executable, folder+filename])
        # Bash command to execute the new simulation
        #The next line is executed only at the end of the simulation.
        t,x,y,z = np.genfromtxt(outputName, delimiter = '\t', usecols = [0,1,2,3])
        # Opens the output file and write the data in the 4 first columns in the variables t, x, y, z.

        if x <= -0.45 and y >= 0:#Test the direction that the DW took
            anglea = PHI
            flag = "Switched/horizontal"
            flags.append([FIELD, flag])

        elif x <= -0.45 and y <= 0:
            angleb = PHI
            flag = "Switched/Vertical/horizontal"
```

```

        flags.append([FIELD, flag])

    elif x >= 0.45 and y <= 0:
        angleb = PHI
        flag = "Switched/Vertical"
        flags.append([FIELD, flag])

    else:
        anglea = PHI
        flag = "Not Switched"
        flags.append([FIELD, flag])

    PHI = ((anglea+angleb)/2)
    toPrint.append(flags)

print(toPrint)

```

Explanation: The python scripts generates a new mumax3 script after analysing the result of the previous simulation.

G.0.2 Initial magnetic configuration

```

///Define the number of cells for the coordinates
Nx := 1024
Ny := 512
Nz := 4
///Define the length of the frame to simulate
Lx := 5000e-9
Ly := 2500e-9
Lz := 30e-9
///Fractionation of the Frame by the number of cells
dx := Lx/Nx
dy := Ly/Ny
dz := Lz/Nz
/// Implements periodic boundary conditions that basically
///replicates the frame several times in the specified direction.
///In the present case, 2 times in +x and -x, and 2 times in +y and -y.
SetPBC(2, 2, 0)
///Creates the grid
SetGridSize (Nx, Ny, Nz)
SetCellSize(dx, dy, dz)

///Generate a rectangle for the horizontal and vertical part of the cross
hArm:= rect(Lx,3e-7)//horizontal arm
vArm:= rect(3e-7,Ly)//vertical armm = TwoDomain(1,0,0, 0,1,0, -1,0,0)
setgeom(vArm.add(hArm))//.add(magnets).add(magnetsV)

///Makes the edges of the simulation smooth
edgesmooth=8
///DEFINE MAGNETIZATION
vortSite := circle(300e-9).transl(vortPos, 0, 0)
lhArm := hArm.intersect(xrange(-inf,vortPos)).sub(vortSite) //left horiz-arm
rhArm := hArm.intersect(xrange(vortPos,inf)).sub(vortSite) //right horiz-arm

m.setInShape(rhArm, Uniform(1,0,0))
m.setInShape(vArm, Uniform(0,1,0))

snapshot(m)

//parameters
Msat = 860e3
Aex = 13e-12
alpha = 0.5

OutputFormat = OVF1_TEXT

run(2e-9)

```

```
saveAs(m, "initial.ovf")
```

Explanation: This script is used to generate an initial magnetic configuration that we will store and load in the dynamic simulation to speed them up.

G.0.3 Dynamic simulation

```

//Define the number of cells for the coordinates
Nx := 1024
Ny := 512
Nz := 4
//Define the length of the frame to simulate
Lx := 5000e-9
Ly := 2500e-9
Lz := 30e-9
//Fractionation of the Frame by the number of cells
dx := Lx/Nx
dy := Ly/Ny
dz := Lz/Nz
// Implements periodic boundary conditions that basically
//replicates the frame several times in the specified direction.
//In the present case, 2 times in +x and -x, and 2 times in +y and -y.
SetPBC(2, 2, 0)
//Creates the grid
SetGridSize (Nx, Ny, Nz)
SetCellSize(dx, dy, dz)

//Generate a rectangle for the horizontal and vertical part of the cross
hArm:= rect(Lx,3e-7)//horizontal arm
vArm:= rect(3e-7,Ly)//vertical armm = TwoDomain(1,0,0, 0,1,0, -1,0,0)
setgeom(vArm.add(hArm))//.add(magnets).add(magnetsV))

//Makes the edges of the simulation smooth
edgesmooth=8

//Loads the initial magnetic configuration simulated from Initial_cross_template
m.loadfile("../initial.ovf")
snapshot(m)

//Parameters
Msat = 860e3
Aex = 13e-12
alpha = 0.01
// Remove surface charges from left (mx=-1) and right (mx=1)
// sides to mimic infinitely long wire.
//We have to specify the region (0) at the boundaries.
BoundaryRegion := 0
MagLeft := -1
MagRight := 1

tableadd(B_ext)'
//Takes snapshot of the magnetization every 2 ns and saves the table every 0.1 ns
autosnapshot(m,2e-9)
tableautosave(1e-10)

ext_rmSurfaceCharge(BoundaryRegion, MagLeft, MagRight)

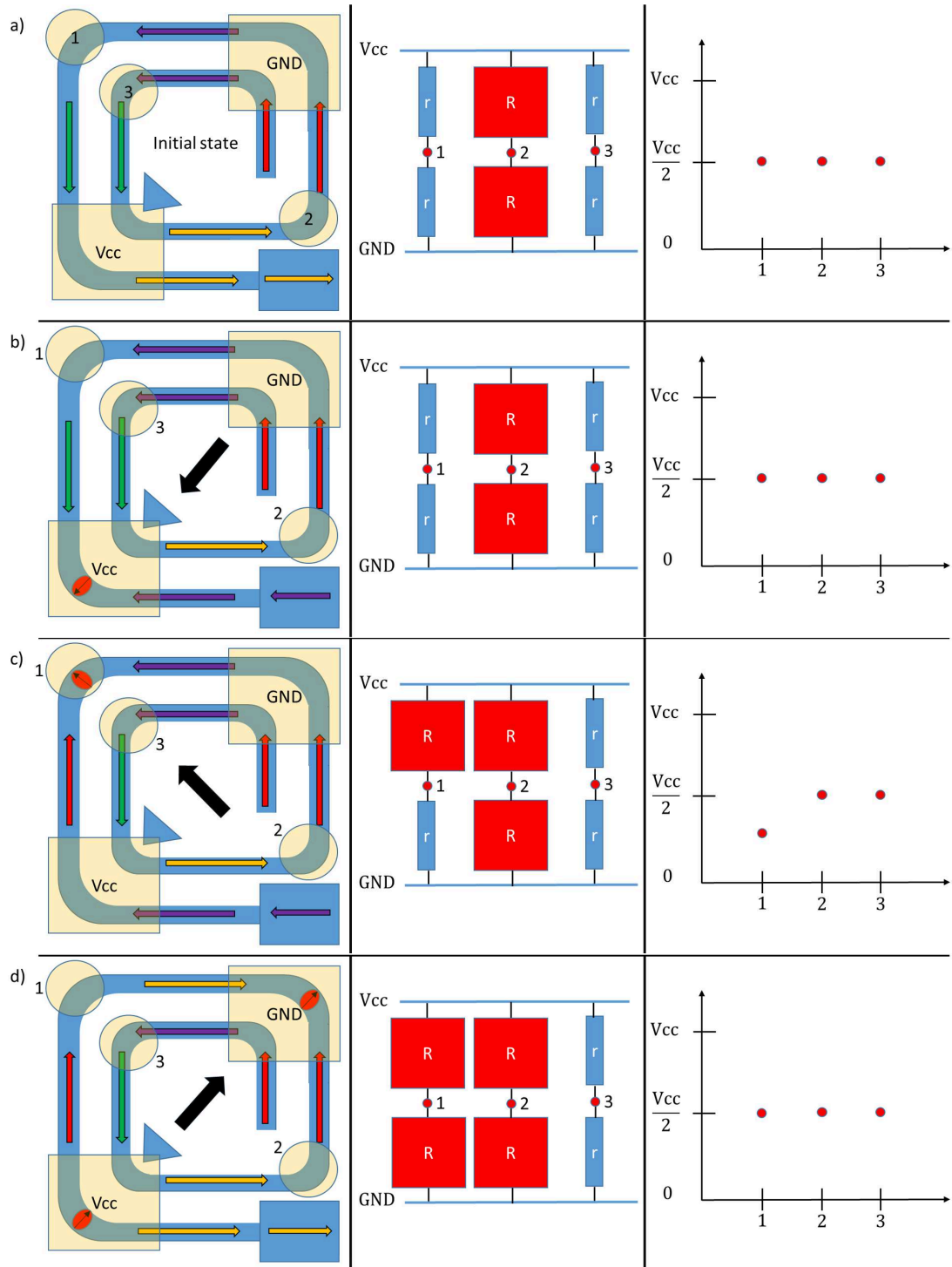
// Parameters that are modified by the python program
phi:= PHI
Bext := FIELD*1e-3

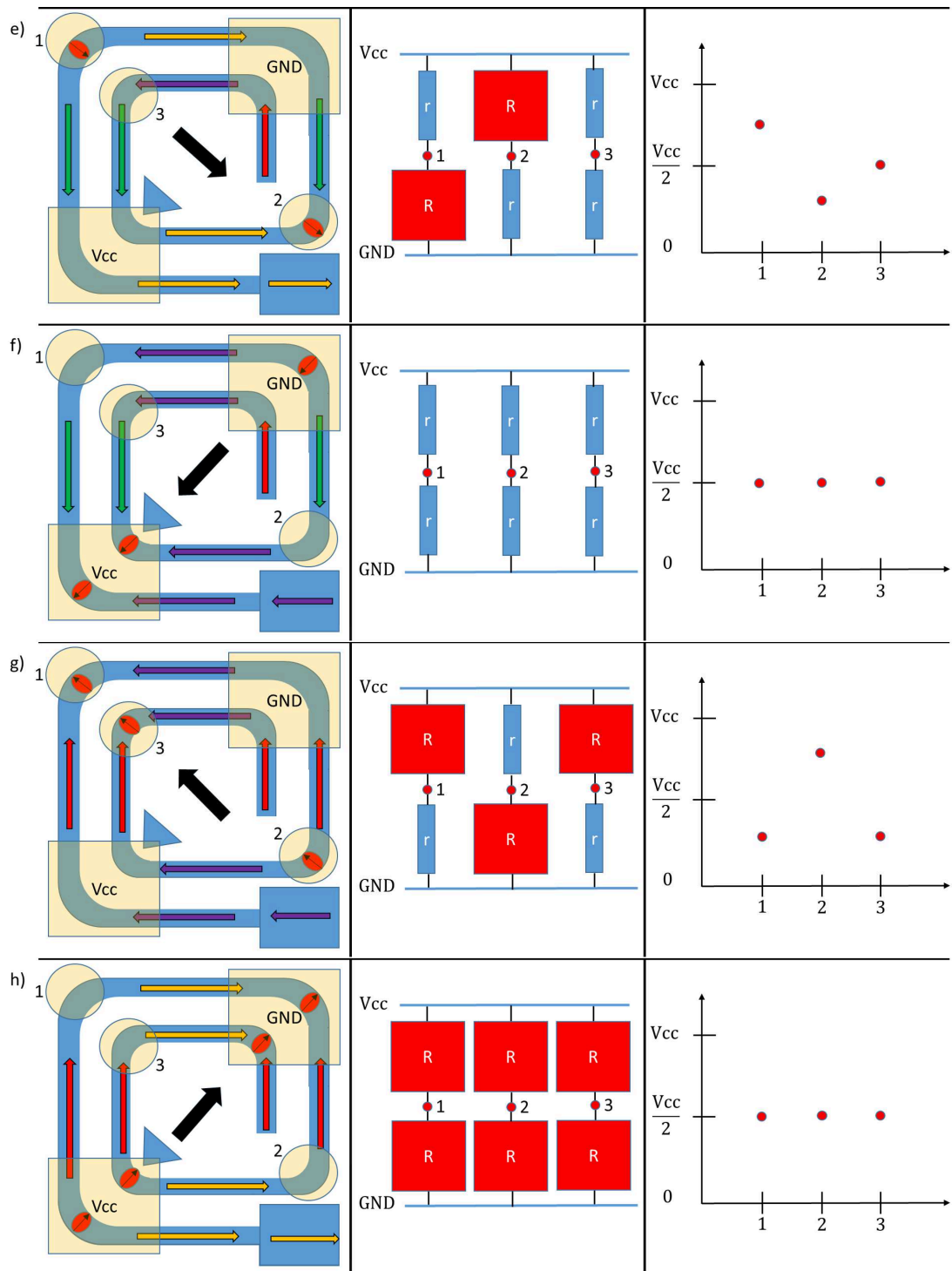
B_ext = vector(Bext*cos(phi*pi/180),Bext*sin(phi*pi/180),0)
run(20e-9)

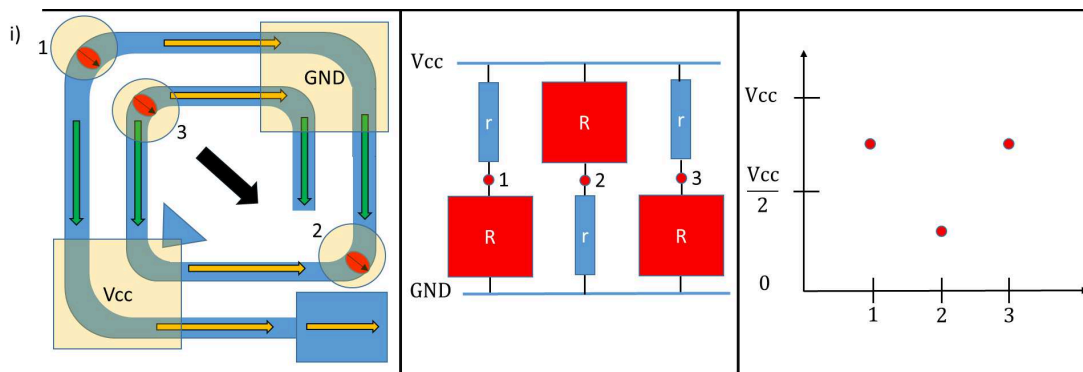
```


Appendix H

Working Scheme of the device







Schematic of the working sequence of a sensor. The field is rotated clockwise, and domain walls are introduced into the device and propagated. The first column is a schematic of the architectures, and the arrows represent the magnetization directions. The electrical contacts are visible. The middle section represents the resistance in terms of the GMR. The direction of the reference layer is indicated on the schematic by a large blue triangle. On the resistance picture, a blue rectangle accounts for small resistances (magnetization in the direction of the reference layer), and a large one in red for high resistances (magnetization opposite to the direction of the reference layer). The final column represents the measured voltages at the different measurement points. a) Initial vortex state with no domain walls. b) A quarter turn rotation of the field in the clockwise direction allows one domain wall to be introduced via the reversal of the nucleation pad and the depinning at the junction to the wire. c) After a further quarter turn rotation of the applied field, the domain wall is displaced in the upper left corner, changing the resistance of one branch of the device. d) After the next quarter turn rotation, the upper domain wall moves to the right. The anti-parallel configuration of the field with the magnetization in the pad's wire introduces a second domain wall. This wall has the tail-to-tail configuration. The sequence continues with for every schematic representation a further quarter turn rotation. Domain walls are introduced, and the change in electrical resistance can be observed.

Appendix I

Python scripts

In this appendix, the script used for the analysis of the AFM images is provided.

I.0.1 Python script for the slicing of the AFM profiles

```

from pylab import *
import matplotlib
import matplotlib.pyplot as plt
import numpy as np
import pandas as pd

def to_precision(x,p):
    """
    returns a string representation of x formatted with a precision of p
    Based on the webkit javascript implementation taken from here:
    https://code.google.com/p/webkit-mirror/source/browse/JavaScriptCore/kjs/number_object.cpp
    """
    x = float(x)
    if x == 0.:
        return "0." + "0"*(p-1)
    out = []
    if x < 0:
        out.append("-")
        x = -x
    e = int(math.log10(x))
    tens = math.pow(10, e - p + 1)
    n = math.floor(x/tens)
    if n < math.pow(10, p - 1):
        e = e - 1
        tens = math.pow(10, e - p+1)
        n = math.floor(x / tens)
    if abs((n + 1.) * tens - x) <= abs(n * tens -x):
        n = n + 1
    if n >= math.pow(10,p):
        n = n / 10.
        e = e + 1
    m = "%. *g" % (p, n)
    if e < -2 or e >= p:
        out.append(m[0])
        if p > 1:
            out.append(".")
            out.extend(m[1:p])
        out.append('e')
        if e > 0:
            out.append("+")
        out.append(str(e))
    elif e == (p - 1):
        out.append(m)
    elif e >= 0:
        out.append(m[:e+1])
        if e+1 < len(m):
            out.append(".")
            out.extend(m[e+1:])
    else:
        out.append("0.")

```

```

        out.extend(["0"]*-(e+1))
        out.append(m)

    return "".join(out)

df = pd.read_csv('/home/benborie/Desktop/AFMimages/23.3.17/612224_200_2.txt', delimiter = '\t')
#import a text version of the cross-section shape of an AFM image
stepsize = 2e-9
leny = int((max(df['y']))/stepsize) #Find the max value in the y-column
matrice_zero = np.array([[0 for i in range(len(df['x'])+1)] for j in range(leny+1)])
# Creates a matrice of 0

m = 0
for i in range(len(df['y'])):
    m = int(df['y'][i]/stepsize)+1 # Slices in range of 4 nm,e.g., y = 31 nm => m = 17
    for j in range(m):
        matrice_zero[j, i] = 1 # Creates a matrice version of the
m=0

plt.imshow(matrice_zero, origin = 'lower', aspect = 'auto')
font = 20
plt.xlabel('Width (nm)', fontsize= font)
plt.ylabel('Slice number (nm/stepsize)', fontsize= font)
plt.legend(loc = 1, prop={'size':15})
plt.yticks(fontsize = font, color = 'k')
plt.xticks(fontsize = font, color = 'k')
plt.show() # Plot the matrice

```

The outputs at this point:

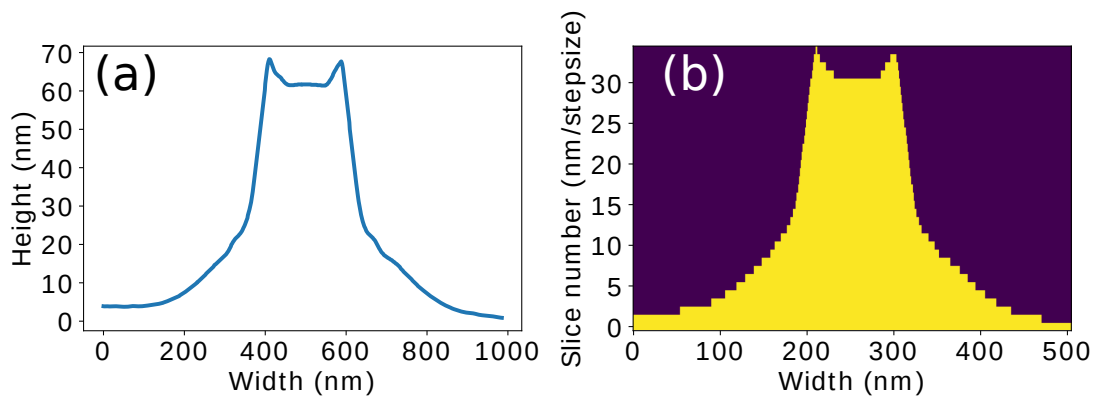


FIGURE I.1: (a) Original cross-section profile that we input in the program.
(b) Discretized version of the cross-section

```

count = []
memorysteps = []
thicknessTa = int(4e-9/stepsize) # This represent the thickness of our layers
thicknessPy = int(((4e-9+28e-9)/stepsize))

reset = 0
t=0
donotappend = 0

for i in range(matrice_zero.shape[0]):
    for j in range(len(df['x'])):
        if reset==0 and t == 0 and matrice_zero[i,j] == 1:
            t += 1
            reset = 1
        elif reset==1 and t != 0 and matrice_zero[i,j] == 1:

```

```

        t += 1
    elif reset==1 and t != 0 and matrice_zero[i,j] == 0:
        reset = 2
    elif reset==2 and t != 0 and matrice_zero[i,j] == 1:
        donotappend = 1
        break
if donotappend == 1:
    continue
else:
    count.append(t)
    memorysteps.append(i)
reset = 0
t=0

#Removes the fencing at the top of the wires
plt.imshow(matrice_zero[0:memorysteps[-1]], origin = 'lower', aspect = 'auto')
font = 20
plt.xlabel('Width (nm)', fontsize= font)
plt.ylabel('Slice number (nm/stepsize)', fontsize= font)
plt.legend(loc = 1, prop={'size':15})
plt.yticks(fontsize = font, color = 'k')
plt.xticks(fontsize = font, color = 'k')
plt.show()

plt.imshow(matrice_zero[thicknessTa-1:thicknessPy-1], origin = 'lower', aspect = 'auto')
font = 20
plt.xlabel('Width (nm)', fontsize= font)
plt.ylabel('Slice number (nm/stepsize)', fontsize= font)
plt.legend(loc = 1, prop={'size':15})
plt.yticks(fontsize = font, color = 'k')
plt.xticks(fontsize = font, color = 'k')
plt.show()
#Select the appropriate range corresponding to the Py thickness

print(count)
count.reverse()
print(count)
count = count[thicknessTa-1:thicknessPy-1]
print(count)

count = [c*df['y'][0] for c in count]
print(count)
print('nomW := ' + str(to_precision(count[0],3)))
print('increment := ' + str(to_precision(count[len(count)-1]-count[0],3)))
for i in range(len(count)-1):
    print('k' + str(i)+ ' := ' + str(to_precision((count[i+1]-count[0])/2,3)))
#Outputs the code used in the simulations

```

Two other outputs are:

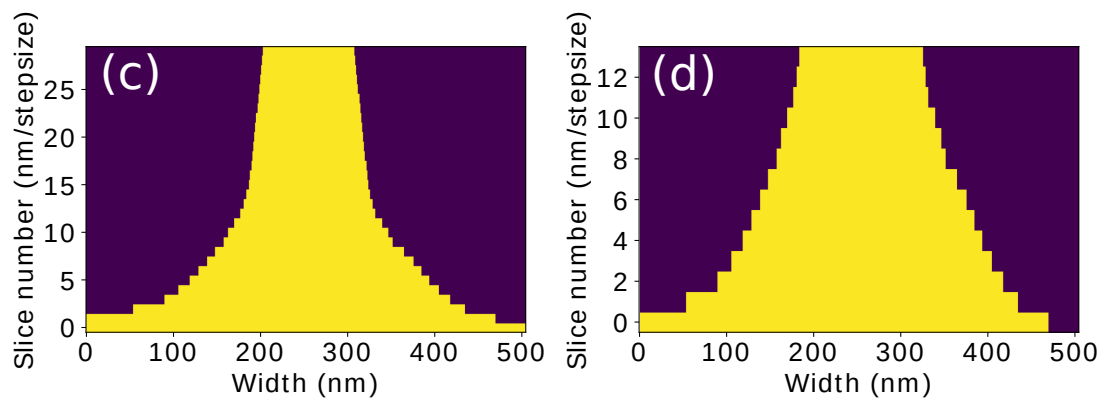


FIGURE I.2: (a) Discretized version of the cross-section without the fencing.
 (b) Discretized version of the cross-section for the selected thickness.

I.0.2 Code slicing the AFM micrograph

```

from pylab import *
import matplotlib
import matplotlib.pyplot as plt
import math as mh
import matplotlib.patches as mpatches
import numpy as np
import scipy
import matplotlib.image as mping
from colormap import rgb2hex
from mpl_toolkits.mplot3d import Axes3D
import os

from scipy.optimize import curve_fit
from scipy import asarray as ar,exp

data0= genfromtxt(r'C:\Users\boribenj\Desktop\AFMimages\summary.txt',
dtype= str ,delimiter='\t',usecols= 0)
data1= genfromtxt(r'C:\Users\boribenj\Desktop\AFMimages\summary.txt',
dtype= int ,delimiter='\t',usecols=range(1,3))
print(data0,data1)
for q in range(data0.shape[0]):
    #Variables declaration
    max_scale = data1[q,0]
    image_dim = data1[q,1]
    print(image_dim)
    print('cell size ' + str(image_dim/490))
    thickness = 28
    sample_name = data0[q]

    image = scipy.misc.imread(r'C:\Users\boribenj\Desktop\AFMimages\23.3.17\
' +sample_name + '.tif')
    #Takes the image and transforms the RGB colors in an int
    matrice = np.array([[ '#FFFFFF' for i in range(image.shape[1])
for j in range(image.shape[0])])
    matrice2 = np.array([[0.0 for i in range(image.shape[1])
for j in range(image.shape[0])])
    for i in range(image.shape[0]):
        for j in range(image.shape[1]):
            matrice[i,j] = rgb2hex(image[i,j,0],image[i,j,1],image[i,j,2])
            matrice2[i,j] = int(int(matrice[i,j].replace('#',''),16))

def scale(lol):
    return(max_scale/(matrice2[32,image.shape[1]-65]-matrice2[image.shape[0]-1,image.shape[1]-65]))*(lol - matrice2[32,
#Takes only the interesting part of the image

```



```

matrice3 = matrice2[40:image.shape[0]-10,40:image.shape[1]-100]

#Scales the image to the height values
for i in range(matrice3.shape[0]):
    for j in range(matrice3.shape[1]):
        matrice3[i,j] = scale(matrice3[i,j])

#Makes an histogram of the data on one line
counts, bins, bars = plt.hist(matrice3[image.shape[0]-100,:],100)

#cut the image to the interesting height
inde = []
inde1 = []
for i in range(matrice3.shape[0]):
    for j in range(matrice3.shape[1]):
        if matrice3[i,j] >= (bins[np.argmax(counts[50:])+50]-5):
            matrice3[i,j] = (bins[np.argmax(counts[50:])+50]-5)
        if matrice3[i,j] == (bins[np.argmax(counts[50:])+50] - 5):
            inde1.append(j)
        if matrice3[i,j] <= (bins[np.argmax(counts[50:])+50] - thickness - 5):
            matrice3[i,j] = (bins[np.argmax(counts[50:])+50] - thickness - 5)
        if matrice3[i,j] != (bins[np.argmax(counts[50:])+50] - thickness - 5):
            inde.append(j)

#Makes a matrix of the size of the stripe width
matrice4 = matrice3[:,min(inde):max(inde)] - (bins[np.argmax(counts[50:])+50] - thickness - 5)

newpath = r'C:\Users\boribenj\Desktop\Simulationafmfirstbatch\\' + sample_name
if not os.path.exists(newpath):
    os.makedirs(newpath)

matrice6 = np.array([[0 for i in range(int(matrice4.shape[1]))] for j in range(int(matrice4.shape[0]))])

for k in range(int(thickness/2)):
    for i in range(matrice6.shape[0]):
        for j in range(matrice6.shape[1]):
            if k*2 < matrice4[i,j] :
                matrice6[i,j] = 10
            elif matrice4[i,j] < k*2:
                matrice6[i,j] = 0
    scipy.misc.imsave(r'C:\Users\boribenj\Desktop\Simulationafmfirstbatch\\' + sample_name+
        '\outfile_'+str(k+1)+'.jpg', matrice6)
lx = int((max(inde)-min(inde))*image_dim/(image.shape[0]-31)) + 1
lx1 = int((max(inde1)-min(inde1))*image_dim/(image.shape[0]-31)) + 1
print(lx1, lx)
ly = image_dim
size = image_dim/490
if size < 2:
    nx = pow(2, int(mh.log((int((max(inde)-min(inde))*image_dim/(image.shape[0]-31))
+1)/size, 2) + 0.5))/2
    ny = pow(2, int(mh.log((image_dim)/size, 2) + 0.5))/2
    print(str(nx))
    print(str(ny))
elif 2 < size < 4:
    nx = pow(2, int(mh.log((int((max(inde)-min(inde))*image_dim/(image.shape[0]-31))
+1)/size, 2) + 0.5))
    ny = pow(2, int(mh.log((image_dim)/size, 2) + 0.5))
    print(str(nx))
    print(str(ny))
else:
    nx = pow(2, int(mh.log((int((max(inde)-min(inde))*image_dim/(image.shape[0]-31))
+1)/size, 2) + 0.5))*2
    ny = pow(2, int(mh.log((image_dim)/size, 2) + 0.5))*2
    print(str(nx))
    print(str(ny))

Msat = '800e3'
Aex = '13e-12'

lz = str(thickness)

```

```

nz = int(thickness/2)

newpath = r'C:\Users\boribenj\Desktop\Simulationafmfirstbatch\\' + sample_name
if not os.path.exists(newpath):
    os.makedirs(newpath)

target = open(r'C:\Users\boribenj\Desktop\Simulationafmfirstbatch\\'
+ sample_name + '\\ ' + sample_name + '.mx3', 'w')
target.write('//***** SIZES *****)' + '\n')

target.write('Lx := ' + str(lx) + 'e-9' + '\n' + 'Ly := ' + str(ly) + 'e-9' + '\n' + 'Lz := '
+ lz + 'e-9' + '\n')
target.write('Nx := ' + str(nx) + '\n' + 'Ny := ' + str(ny) + '\n' + 'Nz := ' + str(nz) + '\n')
target.write('dx := Lx/Nx' + '\n' + 'dy := Ly/Ny' + '\n' + 'dz := Lz/Nz' + '\n')
target.write('setGridSize(Nx, Ny, Nz)' + '\n')
target.write('setCellSize(dx, dy, dz)' + '\n' + '\n')

target.write('//***** MATERIAL PARAMETERS *****)' + '\n')
target.write('Msat = ' + Msat + '\n')
target.write('Aex = ' + Aex + '\n' + '\n')
#target.write('EdgeSmooth = 8' + '\n')
target.write('Dind = 0.0' + '\n')
target.write('anisU = vector(1, 0, 0)' + '\n')
target.write('alpha = 0.01' + '\n')

target.write('//***** RUNNING & SAVING *****)' + '\n')

for i in range(1,int(thickness/2)+1,1):
    target.write('im' + str(i) + ' := imageShape("' + sample_name + '/outfile_'
+ str(i) + '.jpg"' + '\n' )

target.write("coeff := im1" + '\n')
target.write("a0:=layer(0).sub(coeff)" + '\n')
target.write("DefRegion(0,layer(0))" + '\n')

target.write('for k:=1; k<Nz; k++{ ' + '\n')

target.write('if k== 0{ ' + '\n')
target.write('coeff = im1' + '\n' )
for i in range(1,int(thickness/2),1):
    target.write('}else if k== ' + str(i) + '{ ' + '\n')
    target.write('coeff = im' + str(i+1) + ' ' + '\n' )
target.write('}' + '\n')
target.write('a1:=a0.add(layer(k).sub(coeff))' + '\n')
target.write("DefRegion(k,layer(k))" + '\n')
target.write('a0=a1' + '\n')
target.write('}' + '\n')

target.write('setgeom(a0)' + '\n')
target.write('SetPBC(0, 8, 0)' + '\n')

target.write('OutputFormat = OVf1_TEXT' + '\n')

target.write('B_ext = vector(0, 0, 0)' + '\n')
target.write('TableAdd(B_ext)' + '\n')
target.write('TableAdd(maxTorque)' + '\n')
target.write('m = uniform(0,1,0)' + '\n')

target.write('i:=0' + '\n')
target.write('t = 0' + '\n')
target.write('tableaddVar(i, "field", "T")' + '\n')
target.write('B_ext = vector(0.001*sqrt(2)*0.5*FIELD_APPLIED*(1-exp(-t/4e-9)), -0.001*sqrt(2)*0.5*FIELD_APPLIED*(1-exp(-t/4e-9)), 0)' + '\n')
target.write('run(20e-9)' + '\n')
target.write('tablesave()' + '\n')
target.write('snapshot(m)' + '\n')

target.close()
target.close()

```

```

Msat = '800e3'
Aex = '13e-12'

lz = str(thickness)
nz = int(thickness/2)

newpath = r'C:\Users\boribenj\Desktop\Simulationafmfirstbatch\\' + sample_name
if not os.path.exists(newpath):
    os.makedirs(newpath)

target = open(r'C:\Users\boribenj\Desktop\Simulationafmfirstbatch\\'
+ sample_name + '\\ ' + sample_name + '_2.mx3', 'w')
target.write('//***** SIZES *****)' + '\n')

target.write('Lx := ' + str(lx) + 'e-9' + '\n' + 'Ly := ' + str(ly) + 'e-9' + '\n' + 'Lz := ' + lz + 'e-9' + '\n')
target.write('Nx := ' + str(nx) + '\n' + 'Ny := ' + str(ny) + '\n' + 'Nz := ' + str(nz) + '\n')
target.write('dx := Lx/Nx' + '\n' + 'dy := Ly/Ny' + '\n' + 'dz := Lz/Nz' + '\n')
target.write('setGridSize(Nx, Ny, Nz)' + '\n')
target.write('setCellSize(dx, dy, dz)' + '\n' + '\n')

target.write('//***** MATERIAL PARAMETERS *****)' + '\n')
target.write('Msat ='+ Msat+ '\n')
target.write('Aex = ' + Aex+ '\n' + '\n')
#target.write('EdgeSmooth = 8' + '\n')
target.write('Dind = 0.0' + '\n')
target.write('anisU = vector(1, 0, 0)' + '\n')
target.write('alpha = 0.01' + '\n')

target.write('//***** RUNNING & SAVING *****)' + '\n')

for i in range(1,int(thickness/2)+1,1):
    target.write('im'+ str(i) + ' := imageShape("' + sample_name+'outfile_'
+ str(i) + '.jpg"' + '\n' )

target.write("coeff := im1"+'\n')
target.write("a0:=layer(0).sub(coeff)" + '\n')
target.write("DefRegion(0,layer(0))" + '\n')

target.write('for k:=1; k<Nz; k++{' + '\n')

target.write('if k== 0{' + '\n')
target.write('coeff = im1'+'\n' )
for i in range(1,int(thickness/2),1):
    target.write('}else if k=='+ str(i) + '{'+ '\n')
    target.write('coeff = im' + str(i+1) + '\n' )
target.write('}' + '\n')
target.write('a1:=a0.add(layer(k).sub(coeff))'+ '\n')
target.write("DefRegion(k,layer(k))" + '\n')
target.write('a0=a1'+ '\n')
target.write('}' + '\n')

target.write('setgeom(a0)' + '\n')
target.write('SetPBC(0, 8, 0)' + '\n')

target.write('OutputFormat = OVf1_TEXT'+ '\n')

target.write('B_ext = vector(0, 0, 0)' + '\n')
target.write('TableAdd(B_ext)' + '\n')
target.write('TableAdd(maxTorque)' + '\n')
target.write('m = uniform(0,1,0)' + '\n')

target.write('i:=0' + '\n')
target.write('tableaddVar(i, "field", "T")'+ '\n')
target.write('\t' + '\t' + 'relax()' + '\n')
target.write('\t' + 'save(m)' + '\n')

target.write('for i = 0; i<60; i++{' + '\n')
target.write('\t' + 'B_ext = vector(-0.001*sqrt(2)*0.5*i, -0.001*sqrt(2)*0.5*i,0)' + '\n')
target.write('\t' + 'relax()' + '\n')

```

```
target.write('\t' + 'tablesave()' + '\n')
target.write('\t' + 'snapshot(m)' + '\n')
target.write('}' + '\n')

target.close()
target.close()
```

Explanation: The code slices the AFM micrographs and directly generates the simulation files with the right variables.

Appendix J

Innovative Designs

In this appendix, screenshots of the innovative designs are provided. The designs are grouped by five elements. The five elements are then measured simultaneously with the probe station.

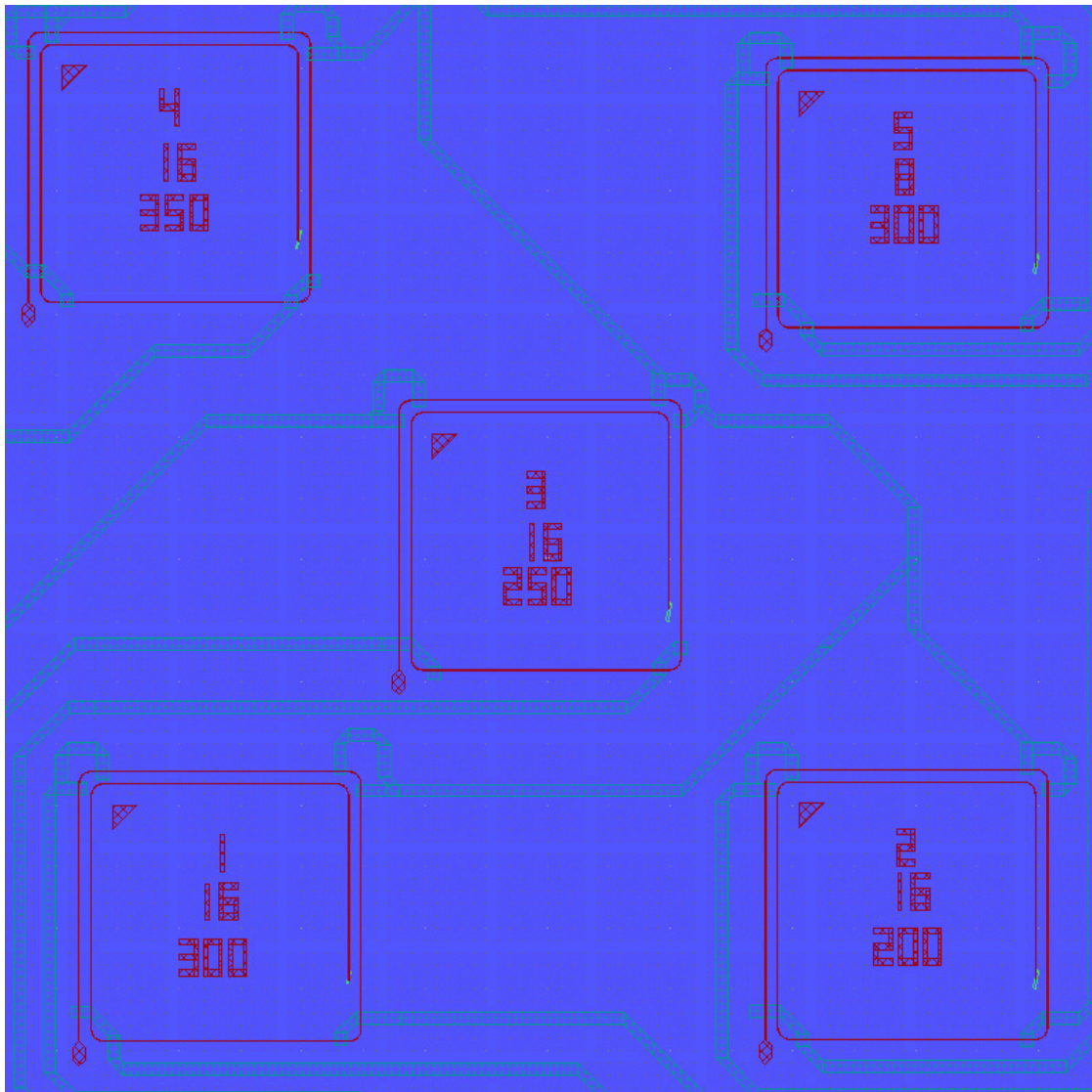


FIGURE J.1: The red colored structures are representing the magnetic structures while the green structures are the electrical connections. The number at the top is a reference number of the structure, the middle number is the number of vertices in the corners, and the last number is the wire width of the structure. The structure at the bottom left is a open-2-loop with 16-vertices corners of radius $10 \mu\text{m}$ and a 300 nm wire width. The structure at the bottom right is a open-2-loop with 16-vertices corners of radius $10 \mu\text{m}$ and a 200 nm wire width. The structure in the middle is a open-2-loop with 16-vertices corners of radius $10 \mu\text{m}$ and a 250 nm wire width. The structure at the top left is a open-2-loop with 16-vertices corners of radius $10 \mu\text{m}$ and a 350 nm wire width. The structure at the top right is a open-2-loop with 8-vertices corners of radius $10 \mu\text{m}$ and a 300 nm wire width.

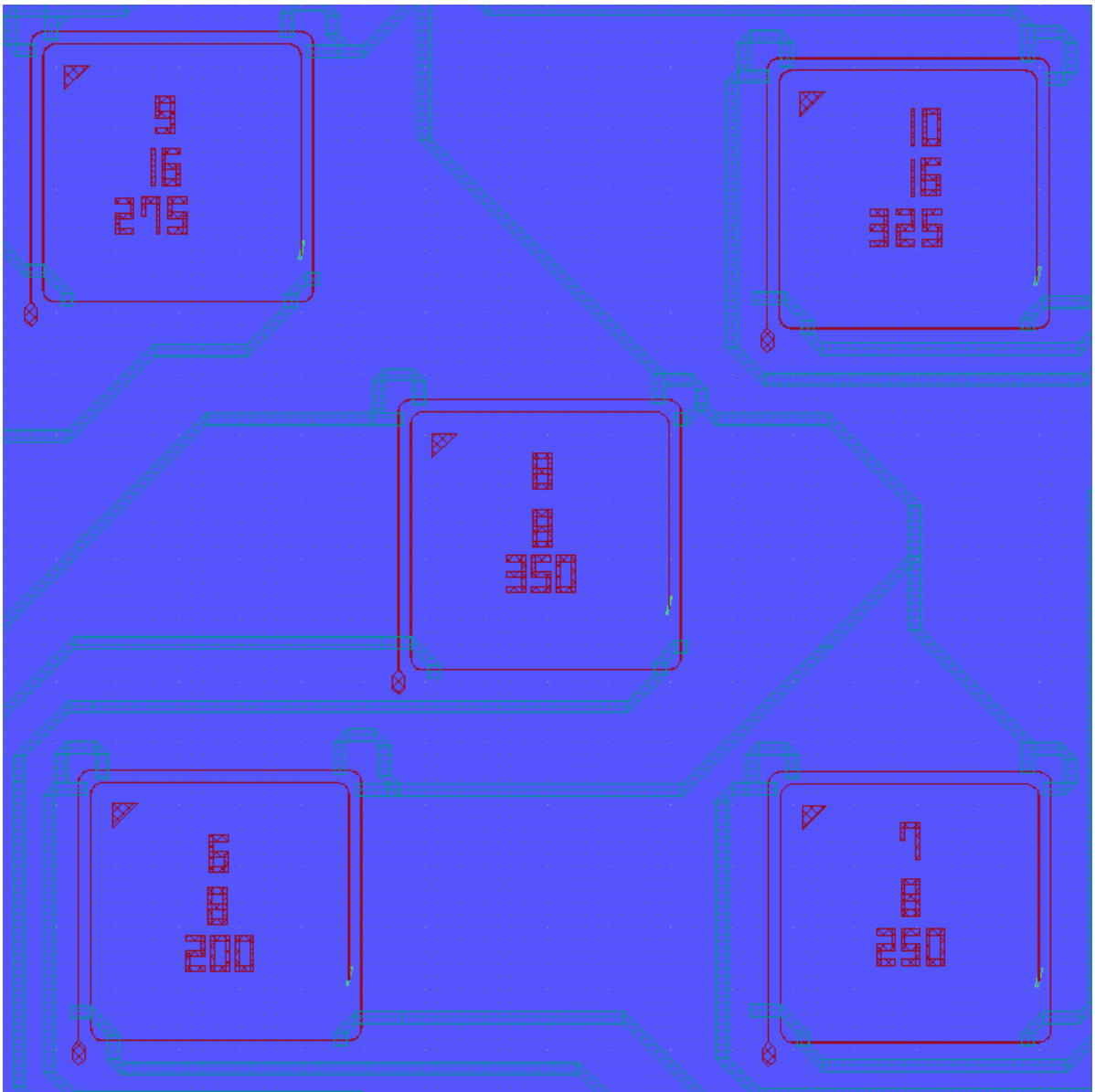


FIGURE J.2: The red colored structures are representing the magnetic structures while the green structures are the electrical connections. The number at the top is a reference number of the structure, the middle number is the number of vertices in the corners, and the last number is the wire width of the structure. The structure at the bottom left is a open-2-loop with 8-vertices corners of radius $10 \mu\text{m}$ and a 200 nm wire width. The structure at the bottom right is a open-2-loop with 8-vertices corners of radius $10 \mu\text{m}$ and a 250 nm wire width. The structure in the middle is a open-2-loop with 8-vertices corners of radius $10 \mu\text{m}$ and a 350 nm wire width. The structure at the top left is a open-2-loop with 16-vertices corners of radius $10 \mu\text{m}$ and a 275 nm wire width. The structure at the top right is a open-2-loop with 16-vertices corners of radius $10 \mu\text{m}$ and a 325 nm wire width.

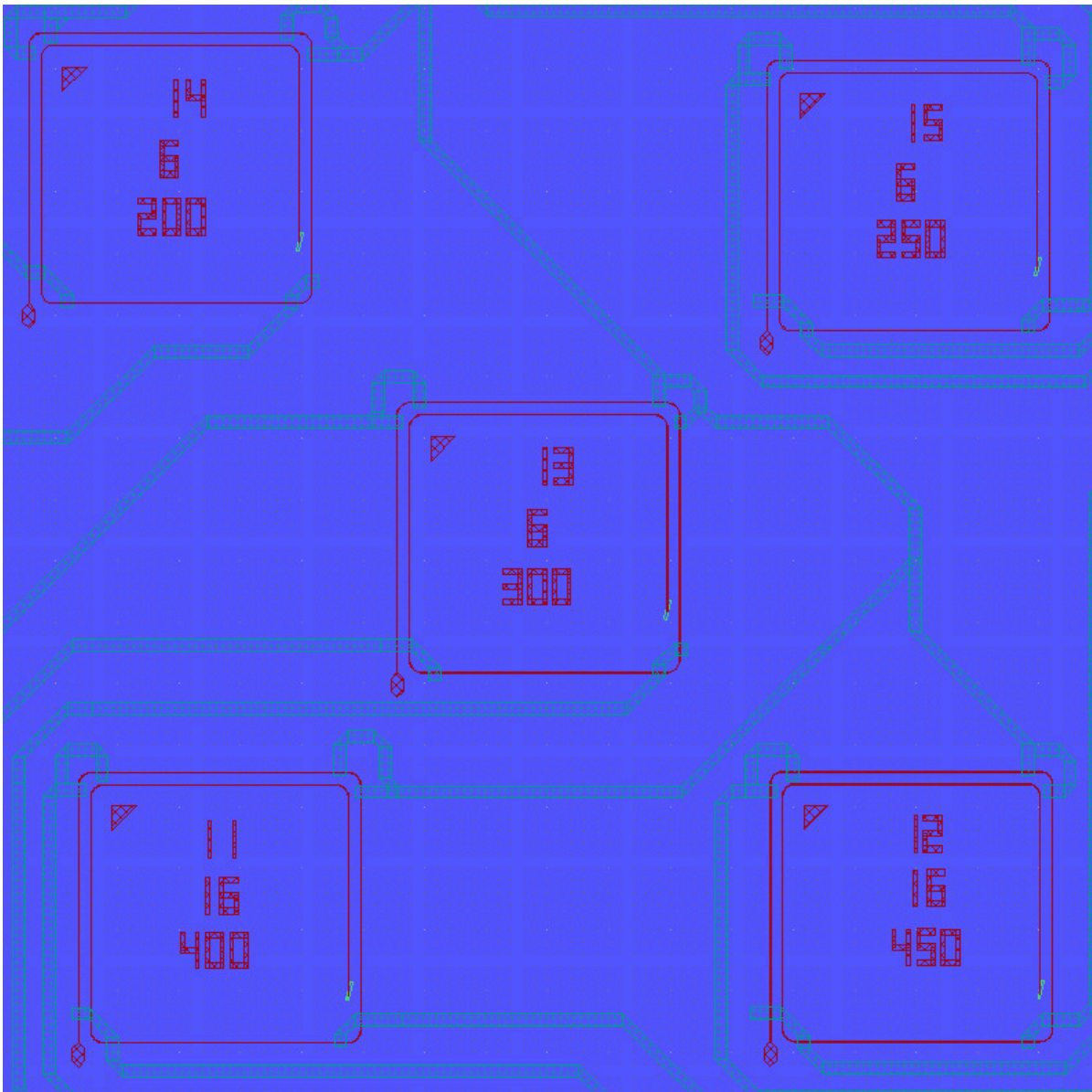


FIGURE J.3: The red colored structures are representing the magnetic structures while the green structures are the electrical connections. The number at the top is a reference number of the structure, the middle number is the number of vertices in the corners, and the last number is the wire width of the structure. The structure at the bottom left is a open-2-loop with 16-vertices corners of radius $10 \mu\text{m}$ and a 400 nm wire width. The structure at the bottom right is a open-2-loop with 16-vertices corners of radius $10 \mu\text{m}$ and a 450 nm wire width. The structure in the middle is a open-2-loop with 6-vertices corners of radius $10 \mu\text{m}$ and a 300 nm wire width. The structure at the top left is a open-2-loop with 6-vertices corners of radius $10 \mu\text{m}$ and a 200 nm wire width. The structure at the top right is a open-2-loop with 6-vertices corners of radius $10 \mu\text{m}$ and a 250 nm wire width.

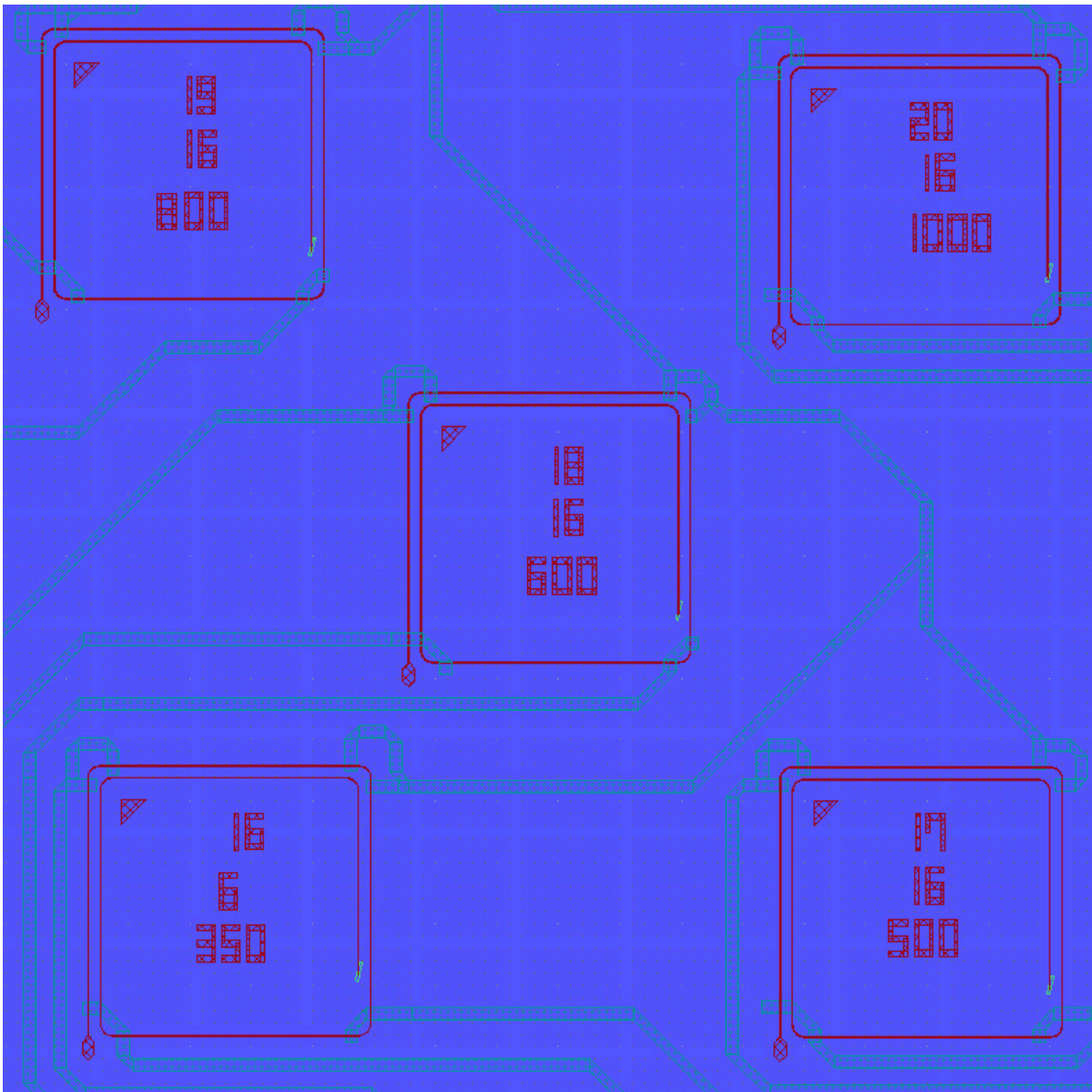


FIGURE J.4: The red colored structures are representing the magnetic structures while the green structures are the electrical connections. The number at the top is a reference number of the structure, the middle number is the number of vertices in the corners, and the last number is the wire width of the structure. The structure at the bottom left is a open-2-loop with 6-vertices corners of radius $10 \mu\text{m}$ and a 350 nm wire width. The structure at the bottom right is a open-2-loop with 16-vertices corners of radius $10 \mu\text{m}$ and a 500 nm wire width. The structure in the middle is a open-2-loop with 16-vertices corners of radius $10 \mu\text{m}$ and a 600 nm wire width. The structure at the top left is a open-2-loop with 16-vertices corners of radius $10 \mu\text{m}$ and an 800 nm wire width. The structure at the top right is a open-2-loop with 16-vertices corners of radius $10 \mu\text{m}$ and a 1000 nm wire width.

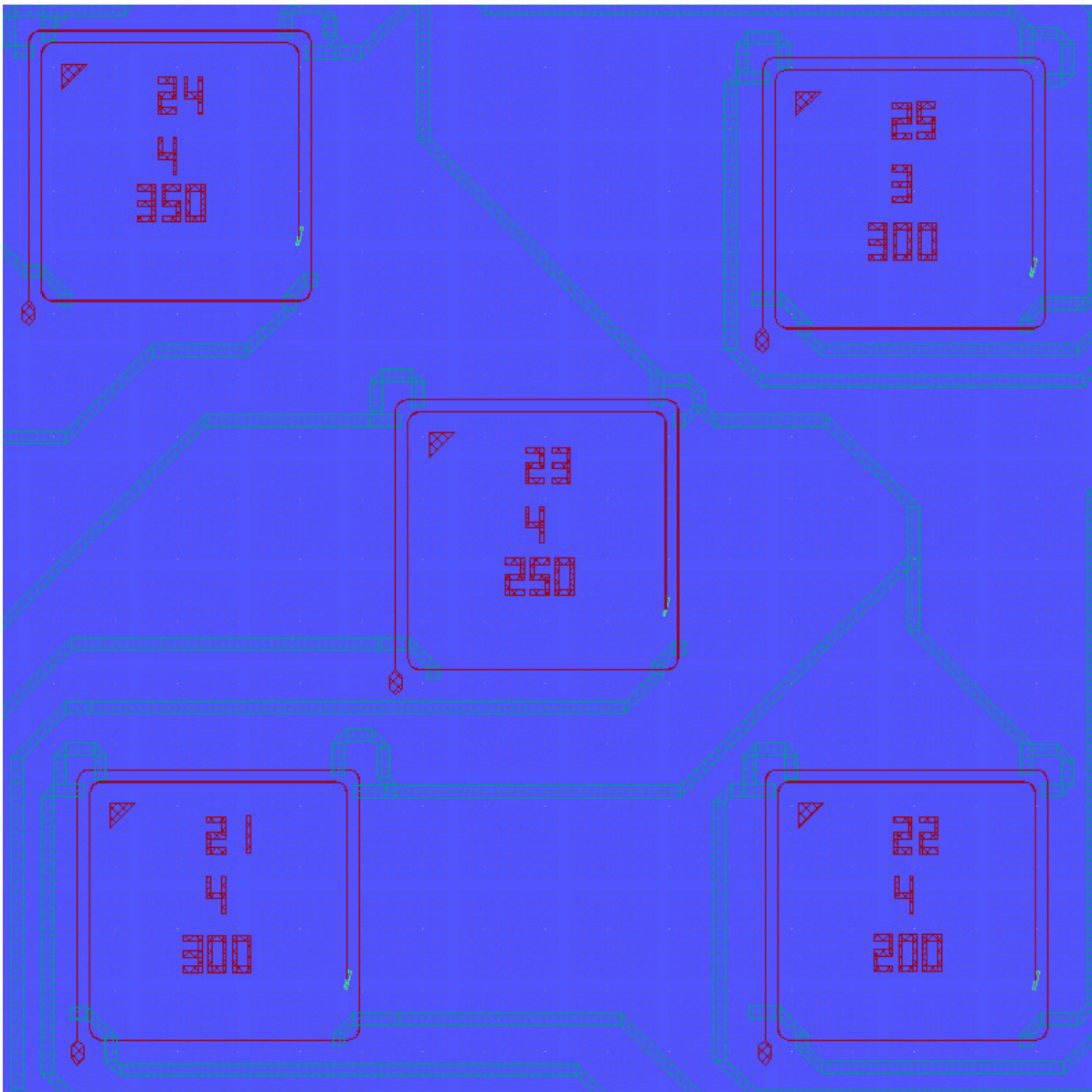


FIGURE J.5: The red colored structures are representing the magnetic structures while the green structures are the electrical connections. The number at the top is a reference number of the structure, the middle number is the number of vertices in the corners, and the last number is the wire width of the structure. The structure at the bottom left is a open-2-loop with 4-vertices corners of radius $10 \mu\text{m}$ and a 300 nm wire width. The structure at the bottom right is a open-2-loop with 4-vertices corners of radius $10 \mu\text{m}$ and a 200 nm wire width. The structure in the middle is a open-2-loop with 4-vertices corners of radius $10 \mu\text{m}$ and a 250 nm wire width. The structure at the top left is a open-2-loop with 4-vertices corners of radius $10 \mu\text{m}$ and a 350 nm wire width. The structure at the top right is a open-2-loop with 3-vertices corners of radius $10 \mu\text{m}$ and a 300 nm wire width.

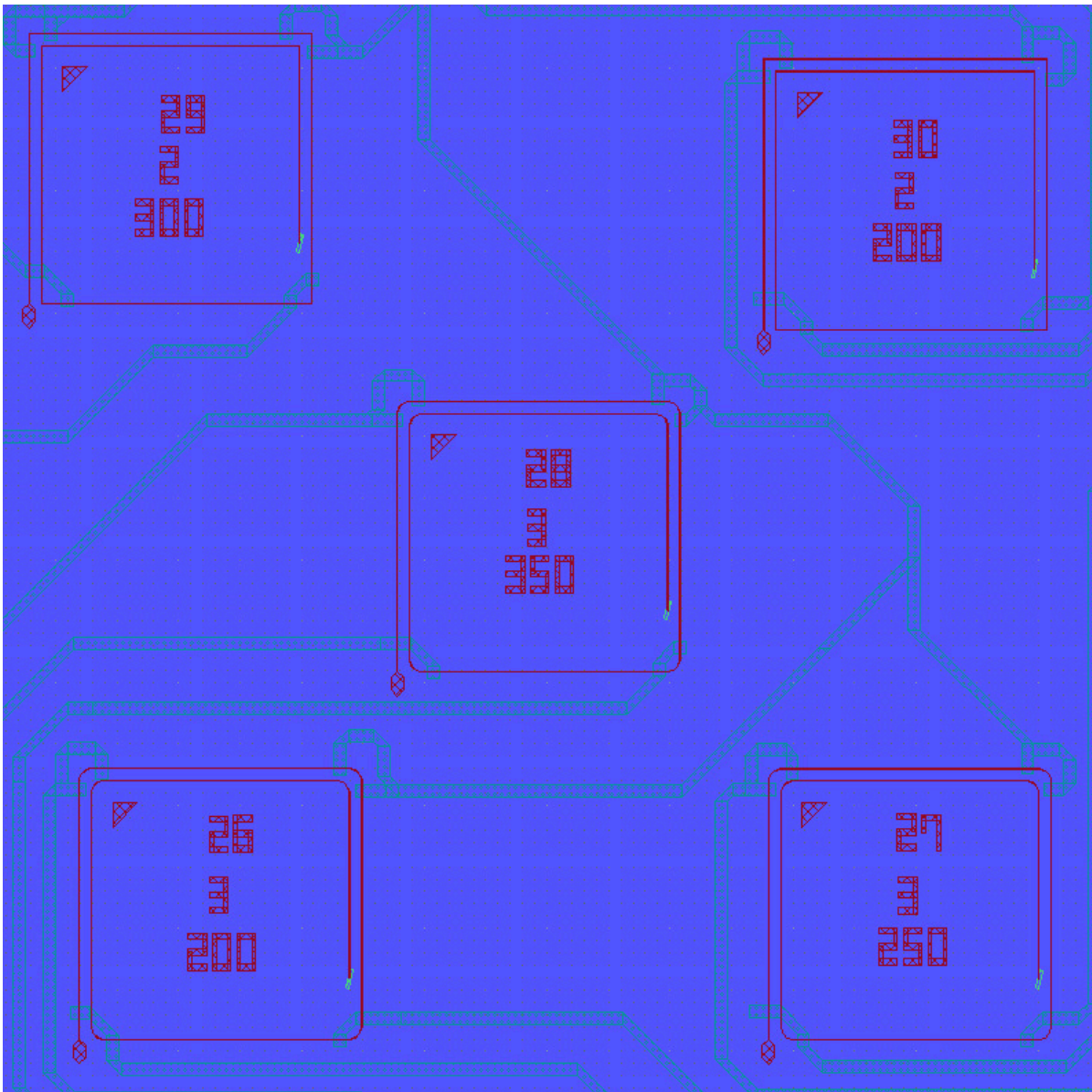


FIGURE J.6: The red colored structures are representing the magnetic structures while the green structures are the electrical connections. The number at the top is a reference number of the structure, the middle number is the number of vertices in the corners, and the last number is the wire width of the structure. The structure at the bottom left is a open-2-loop with 3-vertices corners of radius $10 \mu\text{m}$ and a 200 nm wire width. The structure at the bottom right is a open-2-loop with 3-vertices corners of radius $10 \mu\text{m}$ and a 250 nm wire width. The structure in the middle is a open-2-loop with 3-vertices corners of radius $10 \mu\text{m}$ and a 350 nm wire width. The structure at the top left is a open-2-loop with 0-vertices corners of radius $10 \mu\text{m}$ and a 300 nm wire width. The structure at the top right is a open-2-loop with 0-vertices corners of radius $10 \mu\text{m}$ and a 200 nm wire width.

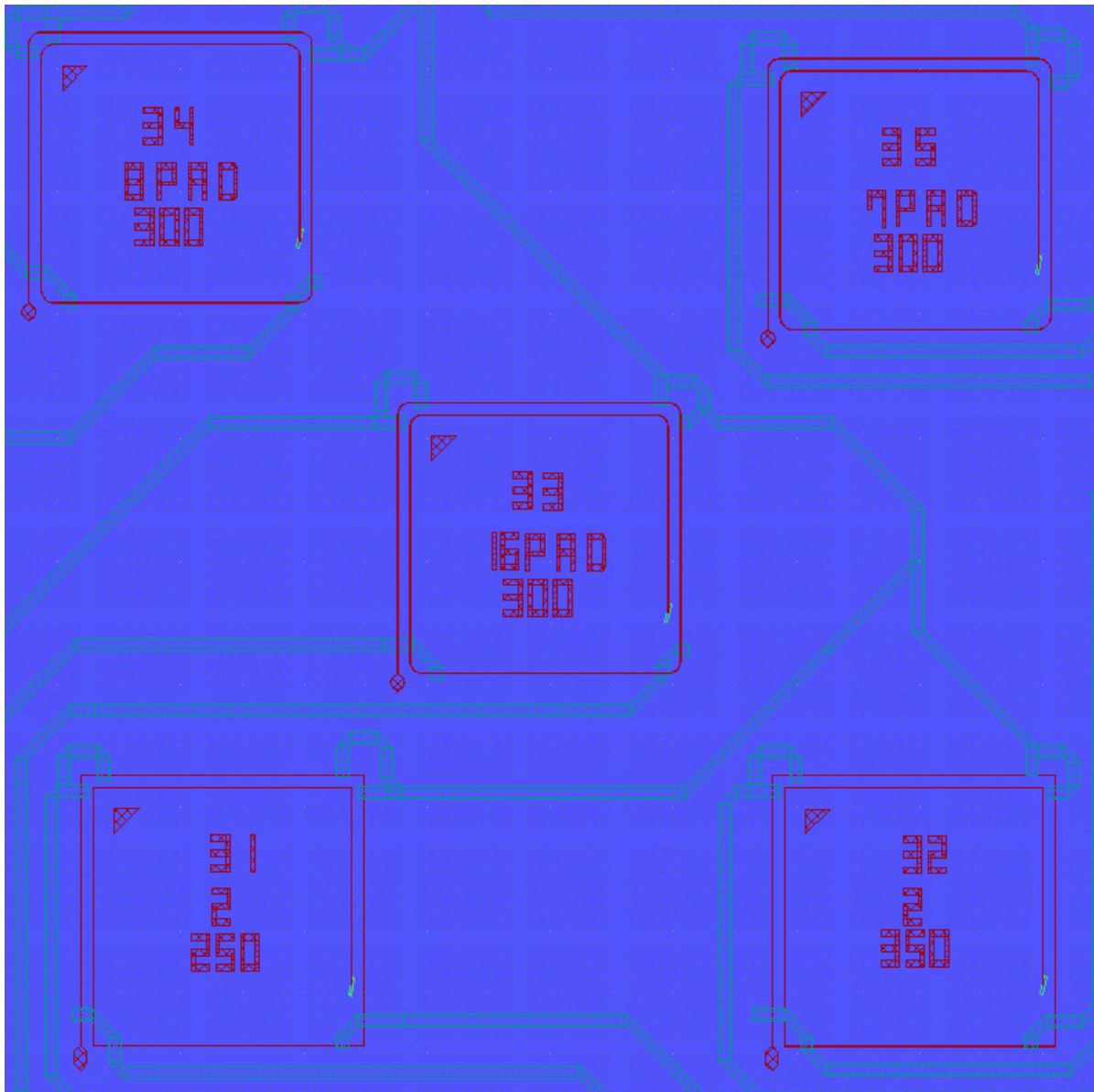


FIGURE J.7: The red colored structures are representing the magnetic structures while the green structures are the electrical connections. The number at the top is a reference number of the structure, the middle number is the number of vertices in the corners, and the last number is the wire width of the structure. The structure at the bottom left is a open-2-loop with 0-vertices corners of radius $10 \mu\text{m}$ and a 250 nm wire width. The structure at the bottom right is a open-2-loop with 0-vertices corners of radius $10 \mu\text{m}$ and a 350 nm wire width. The structure in the middle is a open-2-loop with 16-vertices corners of radius $10 \mu\text{m}$, a 300 nm wire width and a lemon pad. The structure at the top left is a open-2-loop with 8-vertices corners of radius $10 \mu\text{m}$, a 300 nm wire width and a lemon pad. The structure at the top right is a open-2-loop with 7-vertices corners of radius $10 \mu\text{m}$, a 300 nm wire width and a lemon pad.

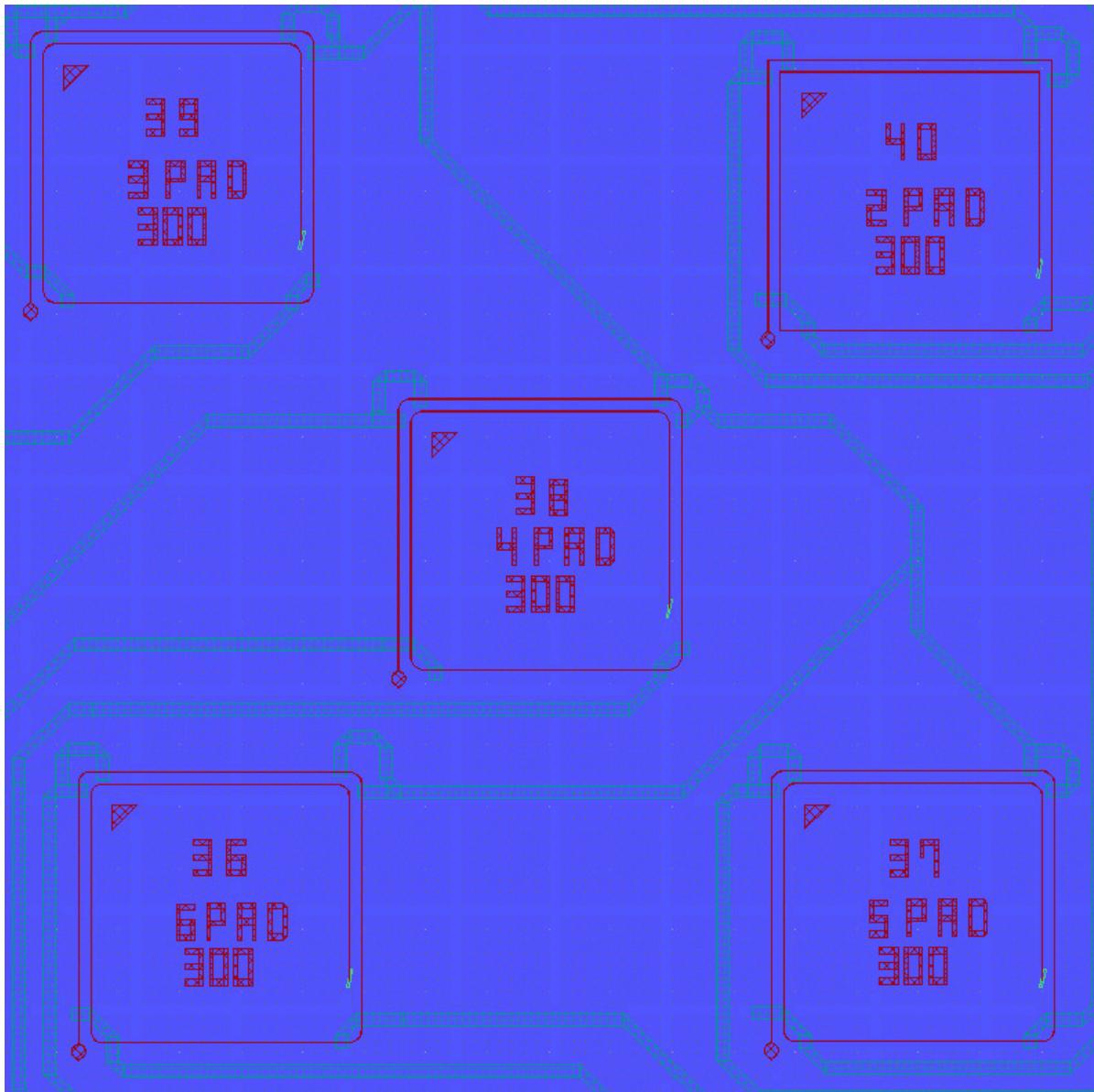


FIGURE J.8: The red colored structures are representing the magnetic structures while the green structures are the electrical connections. The number at the top is a reference number of the structure, the middle number is the number of vertices in the corners, and the last number is the wire width of the structure. The structure at the bottom left is a open-2-loop with 6-vertices corners of radius $10\ \mu\text{m}$, a $300\ \text{nm}$ wire width and a lemon pad. The structure at the bottom right is a open-2-loop with 5-vertices corners of radius $10\ \mu\text{m}$, a $300\ \text{nm}$ wire width and a lemon pad. The structure in the middle is a open-2-loop with 4-vertices corners of radius $10\ \mu\text{m}$, a $300\ \text{nm}$ wire width and a lemon pad. The structure at the top left is a open-2-loop with 3-vertices corners of radius $10\ \mu\text{m}$, a $300\ \text{nm}$ wire width and a lemon pad. The structure at the top right is a open-2-loop with 0-vertices corners of radius $10\ \mu\text{m}$, a $300\ \text{nm}$ wire width and a lemon pad.

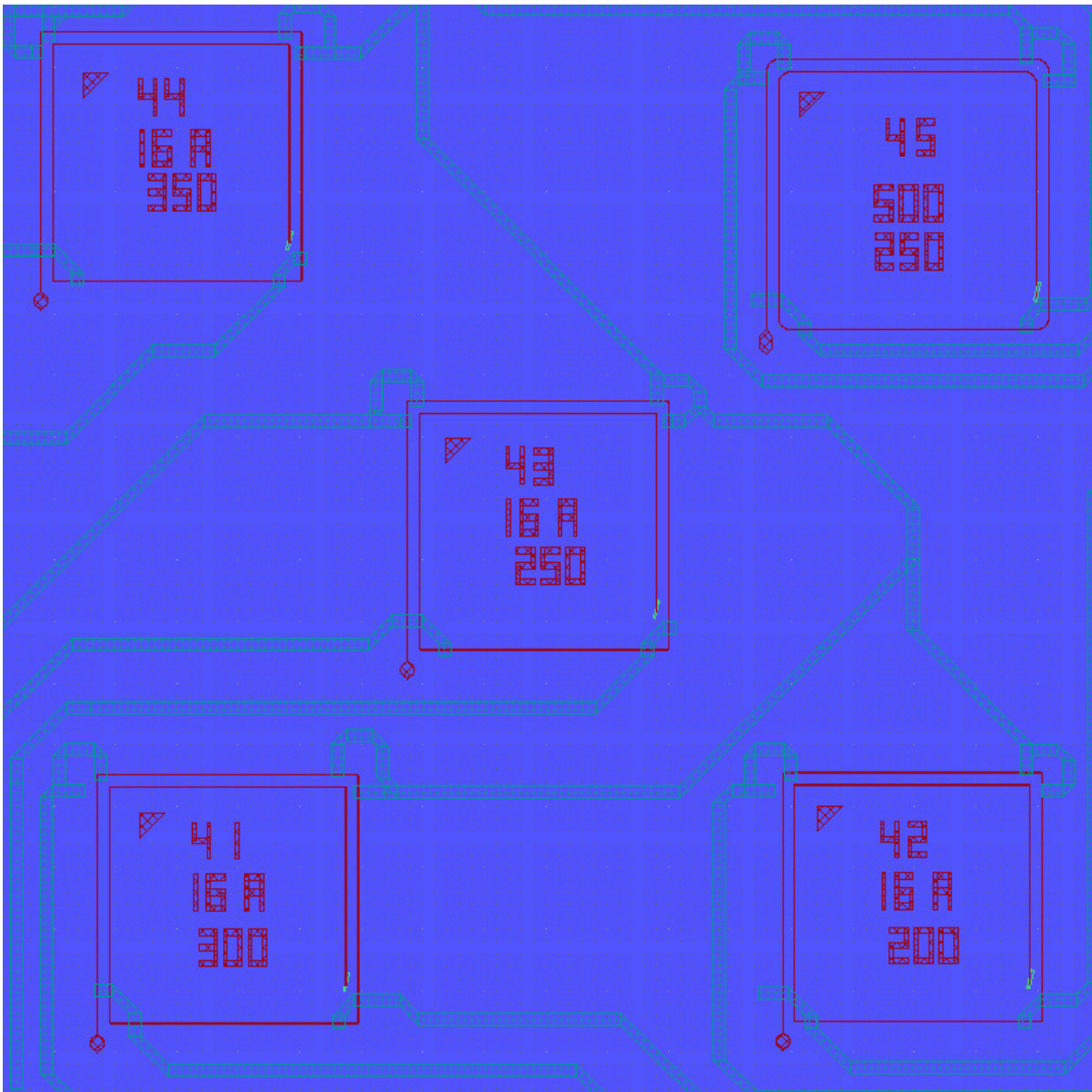


FIGURE J.9: The red colored structures are representing the magnetic structures while the green structures are the electrical connections. The number at the top is a reference number of the structure, the middle number is the number of vertices in the corners, and the last number is the wire width of the structure. The structure at the bottom left is a open-2-loop with 16-vertices corners of radius $1 \mu\text{m}$ and a 300 nm wire width. The structure at the bottom right is a open-2-loop with 16-vertices corners of radius $1 \mu\text{m}$ and a 200 nm wire width. The structure in the middle is a open-2-loop with 16-vertices corners of radius $1 \mu\text{m}$ and a 250 nm wire width. The structure at the top left is a open-2-loop with 16-vertices corners of radius $1 \mu\text{m}$ and a 350 nm wire width. The structure at the top right is a open-2-loop with 16-vertices corners of radius $10 \mu\text{m}$, a 250 nm wire width with oscillations over 500 nm period.

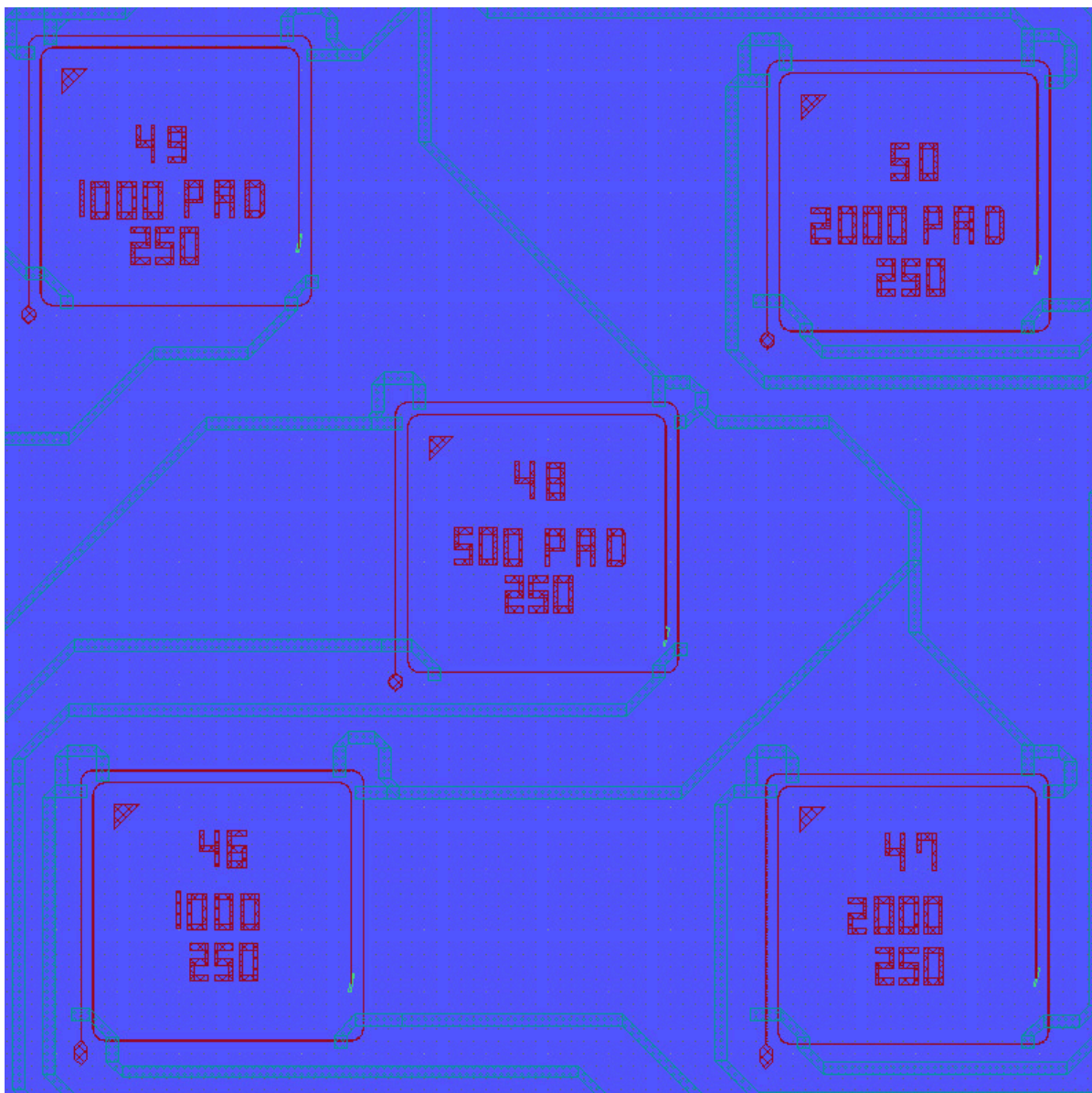


FIGURE J.10: The red colored structures are representing the magnetic structures while the green structures are the electrical connections. The number at the top is a reference number of the structure, the middle number is the number of vertices in the corners, and the last number is the wire width of the structure. The structure at the bottom left is a open-2-loop with 16-vertices corners of radius $10\ \mu\text{m}$, a $250\ \text{nm}$ wire width with oscillations over $1000\ \text{nm}$ period. The structure at the bottom right is a open-2-loop with 16-vertices corners of radius $10\ \mu\text{m}$, a $250\ \text{nm}$ wire width with oscillations over $2000\ \text{nm}$ period. The structure in the middle is a open-2-loop with 16-vertices corners of radius $10\ \mu\text{m}$, a $250\ \text{nm}$ wire width with oscillations over $500\ \text{nm}$ period, and a lemon pad. The structure at the top left is a open-2-loop with 16-vertices corners of radius $10\ \mu\text{m}$, a $250\ \text{nm}$ wire width with oscillations over $1000\ \text{nm}$ period, and a lemon pad. The structure at the top right is a open-2-loop with 16-vertices corners of radius $10\ \mu\text{m}$, a $250\ \text{nm}$ wire width with oscillations over $2000\ \text{nm}$ period, and a lemon pad.

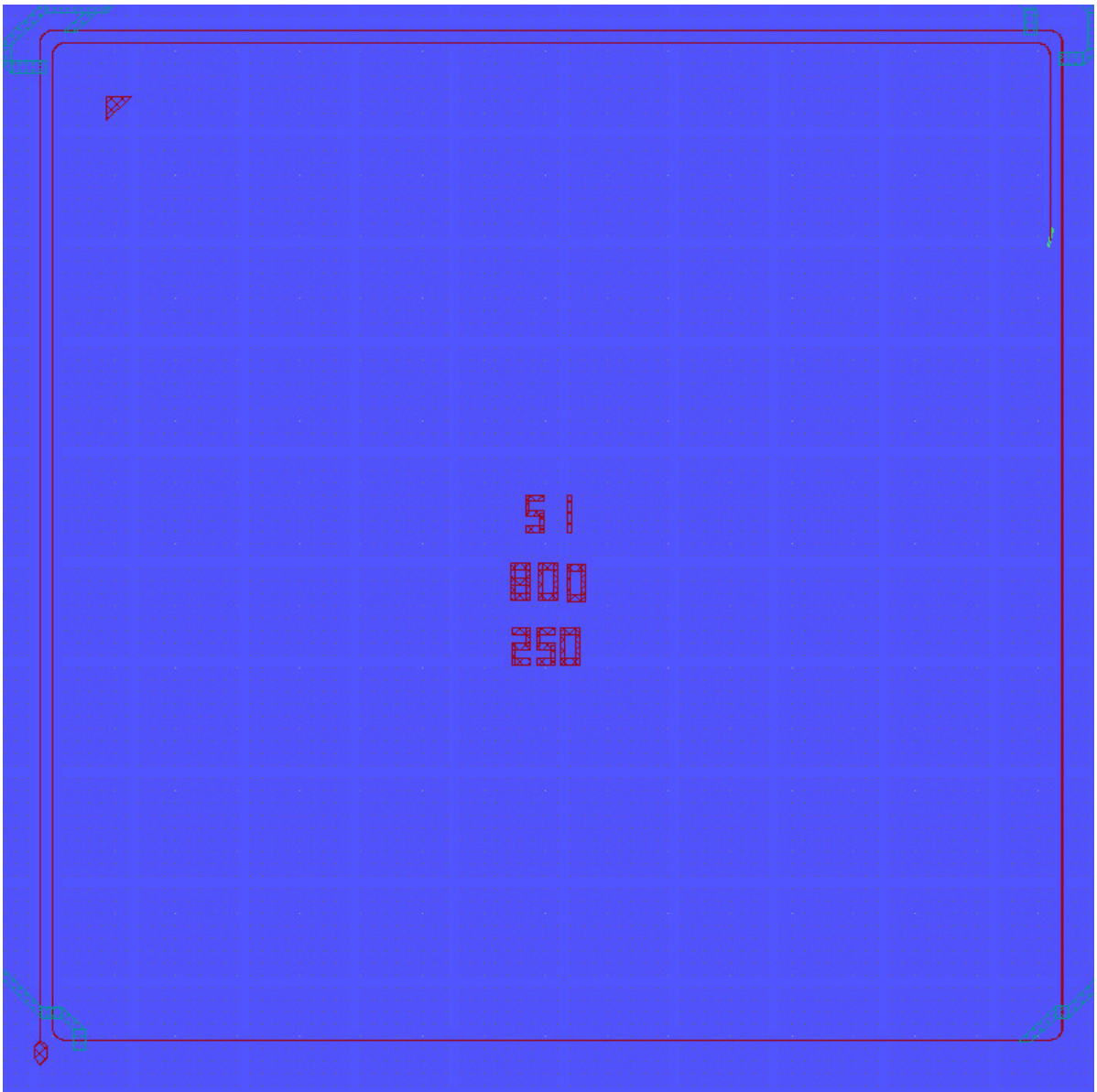


FIGURE J.11: The red colored structures are representing the magnetic structures while the green structures are the electrical connections. The number at the top is a reference number of the structure, the middle number is the number of vertices in the corners, and the last number is the wire width of the structure. The structure at the bottom left is a open-2-loop with 16-vertices corners of radius $10 \mu\text{m}$ and a 250 nm wire width. The structure side length is $800 \mu\text{m}$.

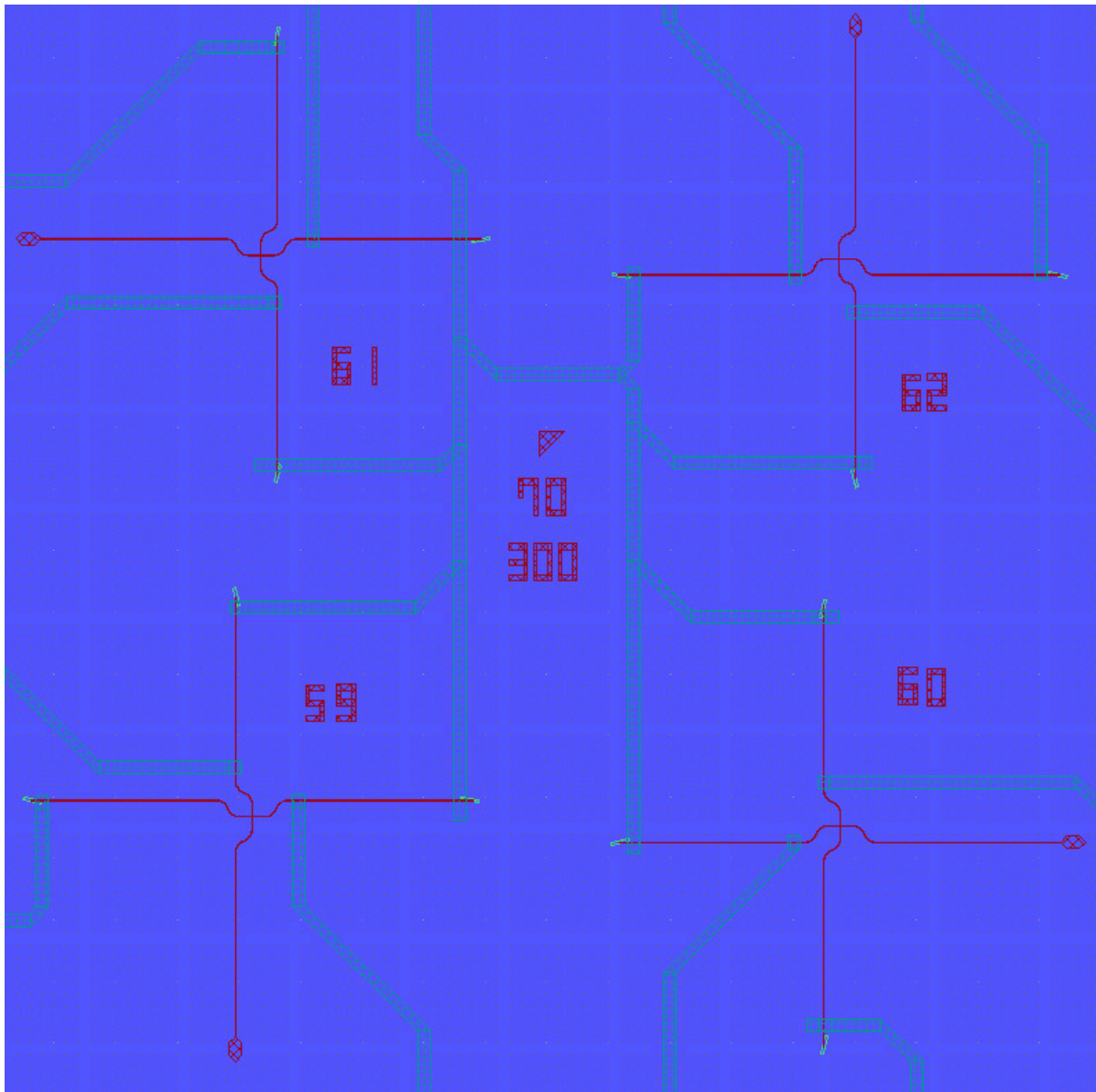


FIGURE J.12: The red colored structures are representing the magnetic structures while the green structures are the electrical connections. The number at the top is a reference number of the structure, the middle number is the number of vertices in the corners, and the last number is the wire width of the structure. The elements are all syphon structures with a syphon angle of 70° and a wire width of 300 nm. The elements are rotated by 90° .

Appendix K

Data from the thickness simulations

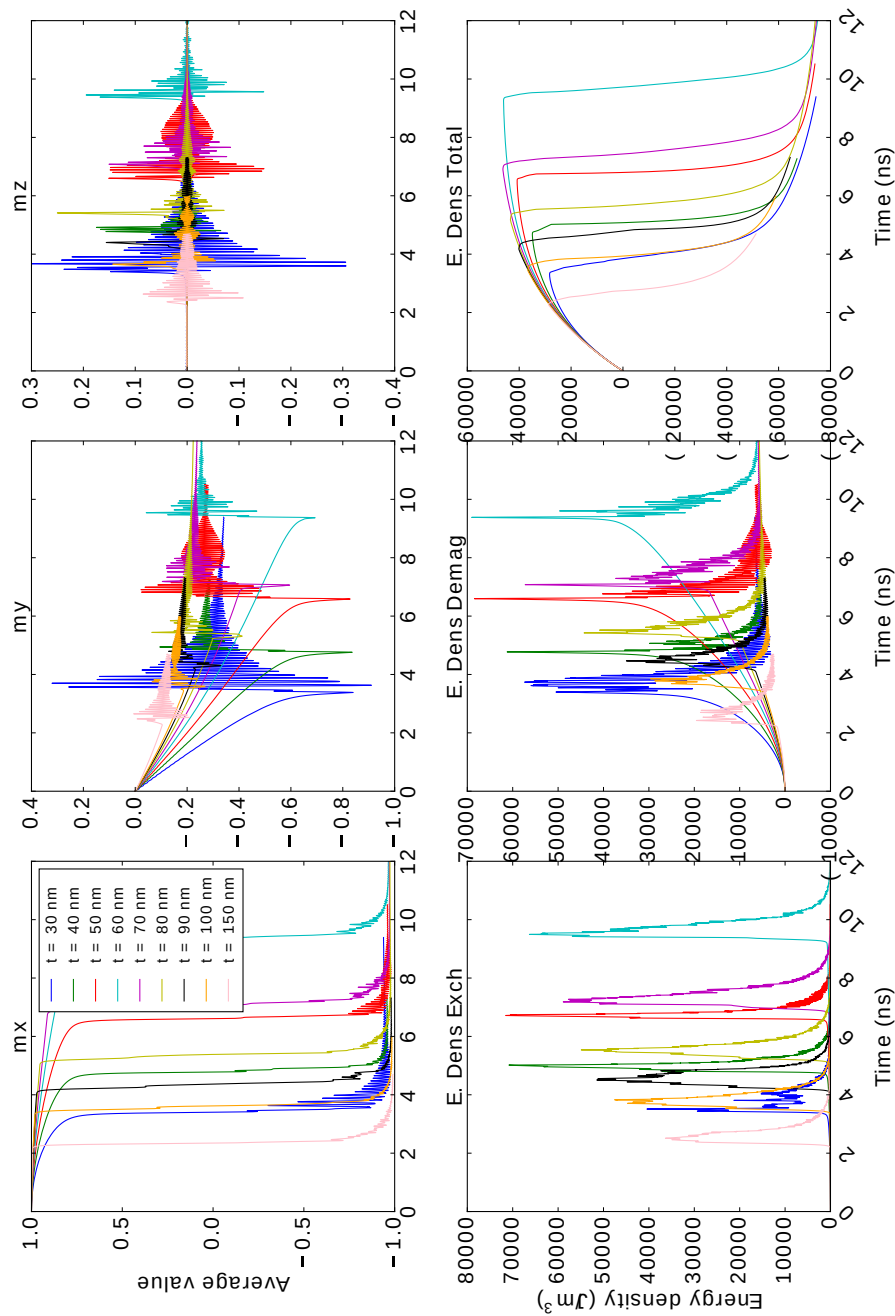


FIGURE K.1: Plot showing the average m_x , m_y and m_z values (left column) for 200 nm width wires with different thickness. The right column provides the data on the Energy densities.

Bibliography

1. S. S. P. Parkin, M. Hayashi, L. Thomas, *Science* **320**, 190 (2008).
2. M. N. Baibich *et al.*, *Physical Review Letters* **61**, 2472 (1988).
3. G. Binasch, P. Grünberg, F. Saurenbach, W. Zinn, *Physical Review B* **39**, 4828 (1989).
4. R. P. Cowburn, D. A. Allwood, G. Xiong, M. D. Cooke, *Journal of Applied Physics* **91**, 6949 (2002).
5. D. A. Allwood *et al.*, *Science* **309**, 1688 (2005).
6. G. S. D. Beach, C. Nistor, C. Knutson, M. Tsoi, J. L. Erskine, *Nature Materials* **4**, 741 (2005).
7. M. Hayashi, L. Thomas, C. Rettner, R. Moriya, S. S. P. Parkin, *Nature Physics* **3**, 21 (2007).
8. D. Atkinson *et al.*, *Nature Materials* **2**, 85 (2003).
9. K. Shigeto, T. Shinjo, T. Ono, *Applied Physics Letters* **75**, 2815 (1999).
10. M. Diegel, R. Mattheis, E. Halder, *IEEE Transactions on Magnetics* **40**, 2655 (2004).
11. M. Diegel, R. Mattheis, E. Halder, *Sensor Letters* **5**, 118 (2007).
12. M. Diegel, S. Glathe, R. Mattheis, M. Scherzinger, E. Halder, *IEEE Transactions on Magnetics* **45**, 3792 (2009).
13. R. Mattheis, S. Glathe, M. Diegel, U. Hübner, *Journal of Applied Physics* **111**, 113920 (2012).
14. B. Borie, A. Kehlberger, J. Wahrhusen, H. Grimm, M. Kläui, *Physical Review Applied* **8**, 024017 (2017).
15. B. Borie *et al.*, *Physical Review Applied* **8**, 044004 (2017).
16. D. Heinze, B. Borie, H. Grimm, J. Wahrhusen, M. Kläui, presented at the Journal of Physics: Conference Series, vol. 903, p. 012053.
17. L. Landau, E. Lifshitz, *Phys. Z. Sowjetunion* **8**, 101 (1935).
18. W. Pauli, *Nobel Lectures, Physics*, 1942 (1946).
19. F. London, *London* **141**, 643 (1938).
20. A. Hubert, R. Schäfer, *Magnetic domains: the analysis of magnetic microstructures* (Springer Science & Business Media, 2008).
21. R. D. McMichael, M. J. Donahue, *IEEE Transactions on Magnetics* **33**, 4167 (1997).
22. Y. Nakatani, A. Thiaville, J. Miltat, *Journal of Magnetism and Magnetic Materials* **290**, 750 (2005).
23. S. Blügel, T. Brückel, C. M. Schneider, *Magnetism goes Nano*.
24. nims.go.jp/apfim/pdf/MMC_Lecture2.pdf, Accessed on: 2015-12-07.
25. P. Hohenberg, W. Kohn, *Physical Review* **136**, B864 (1964).

26. W. Kohn, L. J. Sham, *Physical Review* **140**, A1133 (1965).
27. D. M. Ceperley, B. J. Alder, *Physical Review Letters* **45**, 566 (1980).
28. J. P. Perdew *et al.*, *Physical Review B* **46**, 6671 (1992).
29. L. F. Yin *et al.*, *Physical Review Letters* **97**, 067203 (2006).
30. P. W. Anderson, *Physical Review* **124**, 41 (1961).
31. J. Z. Sun, *Physical Review B* **62**, 570 (2000).
32. S. P. Li *et al.*, *Physical Review Letters* **86**, 1102 (2001).
33. G. S. Abo *et al.*, *IEEE Transactions on Magnetics* **49**, 4937 (2013).
34. E. C. Stoner, E. P. Wohlfarth, *Philosophical Transactions of the Royal Society of London A: Mathematical, Physical and Engineering Sciences* **240**, 599 (1948).
35. L. Néel, *Comptes Rendus Hebdomadaires Des Séances De L'Académie Des Sciences* **224**, 1550 (1947).
36. W. Wernsdorfer, *Advances in Chemical Physics* **118**, 99 (2001).
37. O. Tchernyshyov, G.-W. Chern, *Physical Review Letters* **95**, 197204 (2005).
38. P. M. Chaikin, T. C. Lubensky, *Principles of condensed matter physics* (Cambridge university press, 2000).
39. N. D. Mermin, *Reviews of Modern Physics* **51**, 591 (1979).
40. H.-B. Braun, *Advances in Physics* **61**, 1 (2012).
41. J. A. C. Bland, B. Heinrich, *Ultrathin Magnetic Structures IV: Applications of Nanomagnetism* (Berlin: Springer, 2005).
42. J. A. Osborn, *Physical Review* **67**, 351 (1945).
43. M. Kläui, *Journal of Physics: Condensed Matter* **20**, 313001 (2008).
44. M. Kläui, C. A. F. Vaz, L. Lopez-Diaz, J. A. C. Bland, *Journal of Physics: Condensed Matter* **15**, R985 (2003).
45. G. W. Chern, H. Youk, O. Tchernyshyov, *Journal of Applied Physics* **99**, 08Q505 (2006).
46. N. L. Schryer, L. R. Walker, *Journal of Applied Physics* **45**, 5406 (1974).
47. M. D. Stiles, J. Miltat, in *Spin dynamics in confined magnetic structures III* (Springer, 2006), p. 225.
48. W. Döring, *Zeitschrift für Naturforschung A* **3**, 373 (1948).
49. A. P. Malozemoff, J. C. Slonczewski, *New York*, 382 (1979).
50. H. Y. Yuan, X. R. Wang, *Journal of Magnetism and Magnetic Materials* **368**, 70 (2014).
51. A. A. Thiele, *Physical Review Letters* **30**, 230 (1973).
52. P. Eib, PhD thesis, 2015.
53. A. M. Cravath, A. E. Smith, J. R. Vinograd, J. N. Wilson, *Journal of Applied Physics* **17**, 309 (1946).
54. P. Yu, X. F. Jin, J. Kudrnovský, D. S. Wang, P. Bruno, *Physical Review B* **77**, 054431 (2008).
55. J. C. A. Huang *et al.*, *Journal of Crystal Growth* **171**, 442 (1997).
56. H. D. Arnold, G. W. Elmen, *Bell Labs Technical Journal* **2**, 101 (1923).
57. <https://scholar.google.fr/>, Accessed on: 2017-11-27, (<https://scholar.google.fr/>).

58. S. Ingvarsson, G. Xiao, S. S. P. Parkin, W. J. Gallagher, *Journal of Magnetism and Magnetic Materials* **251**, 202 (2002).
59. M. Pajda, J. Kudrnovský, I. Turek, V. Drchal, P. Bruno, *Physical Review B* **64**, 174402 (2001).
60. J. C. Slater, *Physical Review* **49**, 537 (1936).
61. L. Pauling, *Physical Review* **54**, 899 (1938).
62. J. Kübler, *Physica B + C* **127**, 257 (1984).
63. H. J. Mathieu, M. Datta, D. Landolt, *Journal of Vacuum Science & Technology A: Vacuum, Surfaces, and Films* **3**, 331 (1985).
64. S. Kezilebieke, M. Ali, B. Shadeke, R. Gunnella, *Journal of Physics: Condensed Matter* **25**, 476003 (2013).
65. S. S. P. Parkin *et al.*, *Proceedings of the IEEE* **91**, 661 (2003).
66. W. H. Meiklejohn, C. P. Bean, *Physical Review* **105**, 904 (1957).
67. A. F. Andresen, A. Kjekshus, R. Mollerud, W. B. Pearson, *Philosophical Magazine* **11**, 1245 (1965).
68. T. C. Huang, J. P. Nozieres, V. Speriosu, B. A. Gurney, H. Lefakis, *Applied Physics Letters* **62**, 1478 (1993).
69. C. Chappert, J. P. Renard, *EPL (Europhysics Letters)* **15**, 553 (1991).
70. P. Swiatek, F. Saurenbach, Y. Pang, P. Grünberg, W. Zinn, *Journal of Applied Physics* **61**, 3753 (1987).
71. S. Cardoso *et al.*, *Journal of Applied Physics* **97**, 10C916 (2005).
72. R. W. Johnson, A. Hultqvist, S. F. Bent, *Materials Today* **17**, 236 (2014).
73. P. J. Kelly, R. D. Arnell, *Vacuum* **56**, 159 (2000).
74. M. A. Herman, H. Sitter, *Molecular beam epitaxy: fundamentals and current status* (Springer Science & Business Media, 2012), vol. 7.
75. Z. R. Dai, Z. W. Pan, Z. L. Wang, *Advanced Functional Materials* **13**, 9 (2003).
76. J. A. Venables, G. D. T. Spiller, M. Hanbucken, *Reports on Progress in Physics* **47**, 399 (1984).
77. A. Reina *et al.*, *Nano Letters* **9**, 30 (2008).
78. D. M. Mattox, *Handbook of physical vapor deposition (PVD) processing* (William Andrew, 2010).
79. P. Hsueh, A. C. Ma, *Sputtering chamber with moving table producing orbital motion of target for improved uniformity*, US Patent 6,395,156, 2002.
80. <http://www.singulus.com/en>, Accessed on: 2016-08-27, (<http://www.singulus.com/en>).
81. E. G. Spencer, P. H. Schmidt, R. F. Fischer, *Applied Physics Letters* **17**, 328 (1970).
82. J. Spanos, presented at the Journal of the Electrochemical Society, vol. 108, p. C176.
83. V. Fouque, J. N. Niepce, *La Vérité sur l'invention de la photographie*.
84. M. Born, E. Wolf, *Principles of optics: electromagnetic theory of propagation, interference and diffraction of light* (Elsevier, 2013).
85. Y. Chen, *Microelectronic Engineering* **135**, 57 (2015).

86. F. M. Smits, *Bell Labs Technical Journal* **37**, 711 (1958).
87. K. Tanaka, T. Watanabe, *Japanese Journal of Applied Physics* **11**, 1429 (1972).
88. A. F. Mayadas, M. Shatzkes, *Physical Review B* **1**, 1382 (1970).
89. G. Shimon, A. O. Adeyeye, C. A. Ross, *Journal of Applied Physics* **111**, 013909 (2012).
90. J. Wang, S. She, S. Zhang, *Review of Scientific Instruments* **73**, 2175 (2002).
91. J. Kerr, *The London, Edinburgh, and Dublin Philosophical Magazine and Journal of Science* **3**, 321 (1877).
92. P. M. Oppeneer, T. Maurer, J. Sticht, J. Kübler, *Physical Review B* **45**, 10924 (1992).
93. J. D. Jackson, *Classical electrodynamics*, 1999.
94. J. McCord, *Journal of Physics D: Applied Physics* **48**, 333001 (2015).
95. <http://evico-magnetics.de/>, Accessed on: 2017-11-27, (<http://evico-magnetics.de/>).
96. X. Wang *et al.*, *Journal of Magnetism and Magnetic Materials* **399**, 19 (2016).
97. M. A. Ruderman, C. Kittel, *Physical Review* **96**, 99 (1954).
98. B. Dieny *et al.*, *Journal of Applied Physics* **79**, 6370 (1996).
99. R. E. Camley, J. Barnaś, *Physical Review Letters* **63**, 664 (1989).
100. J. Bass, W. P. Pratt Jr, *Journal of Physics: Condensed Matter* **19**, 183201 (2007).
101. N. F. Mott, *Advances in Physics* **13**, 325 (1964).
102. Z. Jin *et al.*, *Nature Physics* **11**, 761 (2015).
103. T. Valet, A. Fert, *Physical Review B* **48**, 7099 (1993).
104. H. S. Nalwa, *Handbook of Thin Film Materials: Nanomaterials and Magnetic Thin Films*, Vol. 5, 2002.
105. G. K. Binnig, *Atomic force microscope and method for imaging surfaces with atomic resolution*, US Patent 4,724,318, 1988.
106. <https://www.bruker.com/products/surface-and-dimensional-analysis/atomic-force-microscopes.html>, Accessed on: 2017-11-27, (<https://www.bruker.com/products/surface-and-dimensional-analysis/atomic-force-microscopes.html>).
107. H. C. Hamaker, *physica* **4**, 1058 (1937).
108. <https://www.brukerafmprobes.com/Product.aspx?ProductID=3897>, Accessed on: 2017-11-27, (<https://www.brukerafmprobes.com/Product.aspx?ProductID=3897>).
109. R. Reichelt, in *Science of Microscopy* (Springer, 2007), p. 133.
110. B. E. Warren, *X-ray Diffraction* (Courier Corporation, 1969).
111. C. Huygens, *Traité de la lumière: Ou sont expliquées les causes de ce qui lui arrive dans la reflexion, et dans la refraction Et particulièrement dans l'étrange refraction du cristal d'Islande; Avec un discours de la cause de la pesanteur* (van der Aa, 1885).
112. A. Fresnel, *da p. 339 a p. 475: 1 tav. ft; AQ 210*, 339 (1819).
113. L. D. Whittig, W. R. Allardice, *Methods of Soil Analysis: Part 1- Physical and Mineralogical Methods*, 331 (1986).
114. A. Belkind, S. Gershman, *Vacuum Coating and Technology November*, 46 (2008).
115. J. Fidler, T. Schrefl, *Journal of Physics D: Applied Physics* **33**, R135 (2000).

116. <http://math.nist.gov/oommf/>, Accessed on: 2017-08-27, (<http://math.nist.gov/oommf/>).
117. <http://mumax.github.io/>, Accessed on: 2017-08-27, (<http://mumax.github.io/>).
118. A. Vansteenkiste *et al.*, *Aip Advances* **4**, 107133 (2014).
119. A. Vansteenkiste, B. Van de Wiele, *Journal of Magnetism and Magnetic Materials* **323**, 2585 (2011).
120. H. Corte-León *et al.*, *IEEE Transaction on Magnetics* **51**, 1 (2015).
121. M. A. Bashir *et al.*, *Journal of Applied Physics* **110**, 123912 (2011).
122. <http://www.novotechnik.com/rsm/>, Accessed on: 2016-03-09, (<http://www.novotechnik.com/>).
123. <http://www.sensitec.com/>, Accessed on: 2016-08-27, (<http://www.sensitec.com/lp/>).
124. A. Bisig *et al.*, *Nature Communications* **4** (2013).
125. <http://www.shbinstruments.com/>, Accessed on: 2016-08-30, (<http://www.shbinstruments.com/>).
126. M. A. Akhter, D. J. Mapps, Y. Q. Ma Tan, A. Petford-Long, R. Doole, *Journal of Applied Physics* **81**, 4122 (1997).
127. B. D. Cullity, C. D. Graham, *Introduction to magnetic materials* (John Wiley & Sons, 2011), (<http://eu.wiley.com/WileyCDA/WileyTitle/productCd-1118211499.html>).
128. S.-M. Ahn, *Journal of Applied Physics* **113**, 17B501 (2013).
129. L. O'Brien, D. E. Read, D. Petit, R. P. Cowburn, *Journal of Physics: Condensed Matter* **24**, 024222 (2011).
130. L. A. Rodríguez *et al.*, *Beilstein journal of nanotechnology* **6**, 1319 (2015).
131. A. K. Ponomareva, S. V. Egorov, L. S. Uspenskaya, *Physica B: Condensed Matter* **486**, 77 (2016).
132. S. Glathe, M. Zeisberger, R. Mattheis, D. Hesse, *Applied Physics Letters* **97**, 112508 (2010).
133. M.-Y. Im, L. Bocklage, P. Fischer, G. Meier, *Physical Review Letters* **102**, 147204 (2009).
134. J. Akerman, M. Muñoz, M. Maicas, J. L. Prieto, *Physical Review B* **82**, 064426 (2010).
135. W. Rave, A. Hubert, *IEEE Transactions on Magnetics* **36**, 3886 (2000).
136. H. Kronmüller, *Physica Status Solidi (b)* **144**, 385 (1987).
137. A. Aharoni, *Journal of applied physics* **86**, 1041 (1999).
138. M. A. Basith, S. McVitie, D. McGrouther, J. N. Chapman, J. M. R. Weaver, *Journal of Applied Physics* **110**, 083904 (2011).
139. J. Fassbender, J. McCord, *Applied Physics Letters* **88**, 252501 (2006).
140. K. Fuchs, *Mathematical Proceedings of the Cambridge Philosophical Society* **34**, 100 (1938).
141. E. H. Sondheimer, *Advances in physics* **1**, 1 (1952).
142. D. M. Burn, D. Atkinson, *Applied Physics Letters* **102**, 242414 (2013).
143. X. Peng *et al.*, *Vacuum* **84**, 1075 (2010).

144. C. A. Mack, *The Lithography Expert*, Accessed on: 2017-10-20, ([http://www.lithoguru.com/scientist/litho_tutor/TUTOR14%20\(Summer%2096\).pdf](http://www.lithoguru.com/scientist/litho_tutor/TUTOR14%20(Summer%2096).pdf)) (1996).
145. S.-K. Kim, J.-Y. Lee, Y.-S. Choi, K. Y. Guslienko, K.-S. Lee, *Applied Physics Letters* **93**, 052503 (2008).
146. M. Zeisberger, R. Mattheis, *Journal of Physics: Condensed Matter* **24**, 024202 (2011).
147. D. V. Berkov, N. L. Gorn, *Journal of Magnetism and Magnetic Materials* **272**, 687 (2004).
148. W. Nawrocki, in *Introduction to Quantum Metrology: Quantum Standards and Instrumentation* (Springer International Publishing, Cham, 2015), p. 93, ISBN: 978-3-319-15669-9, DOI: 10.1007/978-3-319-15669-9_5, (https://doi.org/10.1007/978-3-319-15669-9_5).
149. V. D. Nguyen *et al.*, *Scientific Reports* **5** (2015).
150. W. Y. Lee, M. F. Toney, D. Mauri, *IEEE transactions on magnetics* **36**, 381 (2000).
151. T. Miyazaki, T. Ajima, *Journal of Magnetism and Magnetic Materials* **81**, 91 (1989).
152. Y. Xiao-fei, P. Zi-long, L. Hong-wei, L. Zuo-yi, *Journal of Wuhan University of Technology–Materials Science Edition* **19**, 23 (2004).
153. G. W. Qin *et al.*, presented at the Nanoelectronics Conference (INEC), 2010 3rd International, p. 1116.
154. <http://www.allresist.com/ebeamresists-ar-n-7500-7520/>, Accessed on: 2017-23-10, (<http://www.allresist.com/ebeamresists-ar-n-7500-7520/>).
155. <https://www.raith.com/>, Accessed on: 2017-23-10, (<https://www.raith.com/>).
156. <http://www.dowcorning.com/content/publishedlit/11-1547e-01.pdf>, Accessed on: 2017-23-10, (<http://www.dowcorning.com/content/publishedlit/11-1547e-01.pdf>).
157. A. E. Grigorescu, M. C. Van der Krogt, C. W. Hagen, P. Kruit, *Microelectronic Engineering* **84**, 822 (2007).
158. R. Spain, *IEEE Transactions on Magnetism* **2**, 347 (1966).
159. R. Spain, M. Marino, *IEEE Transactions on Magnetism* **6**, 451 (1970).
160. D. A. Allwood *et al.*, *Science* **296**, 2003 (2002).
161. J. O. Klein *et al.*, *International Journal of Electronics* **95**, 249 (2008).
162. K. A. Omari, T. J. Hayward, *Physical Review Applied* **2**, 044001 (2014).
163. M. Donolato *et al.*, *Advanced Materials* **22**, 2706 (2010).
164. Novotechnik : RSM-2800 Multiturn and RMB-3200, <http://www.novotechnik.de/produkte/winkelsensoren/>, Accessed: 2017-05-11.
165. R. Mattheis, *Magnetic Revolution counter*, European Patent EP 2191237 B1, 2014.
166. M. Diegel, R. Mattheis, German Patent Application DE 102013018680 A1, 2015.
167. E. R. Lewis *et al.*, *Physical Review Letters* **102**, 057209 (2009).
168. E. R. Lewis *et al.*, *Nature Materials* **9**, 980 (2010).
169. A. Pushp *et al.*, *Nature Physics* **9**, 505 (2013).
170. D. M. Burn, M. Chadha, S. K. Walton, W. R. Branford, *Physical Review B* **90**, 144414 (2014).
171. P. Sethi *et al.*, *Scientific Reports* **6**, 19027 (2016).
172. M. Hayashi *et al.*, *Physical Review Letters* **97**, 207205 (2006).

173. L. K. Bogart, D. Atkinson, K. O'Shea, D. McGrouther, S. McVitie, *Physical Review B* **79**, 054414 (2009).
174. M. T. Bryan, T. Schrefl, D. Atkinson, D. A. Allwood, *Journal of Applied Physics* **103**, 073906 (2008).
175. S. Glathe, I. Berkov, T. Mikolajick, R. Mattheis, *Applied Physics Letters* **93**, 162505 (2008).
176. A. Thiaville, J. M. García, J. Miltat, *Journal of Magnetism and Magnetic Materials* **242**, 1061 (2002).
177. B. Borie, J. Wahrhusen, H. Grimm, M. Kläui, *Geometrically enhanced closed-loop multi-turn sensor devices that enable reliable magnetic domain wall motion*, 2017, eprint: [arXiv: 1712.03394](https://arxiv.org/abs/1712.03394).
178. B. Ferguson, X.-C. Zhang, *Nature Materials* **1**, 26 (2002).
179. G. Schönhense, H. J. Elmers, *Surface and Interface Analysis* **38**, 1578 (2006).
180. J. I. Guzman, M. H. Kryder, *Journal of Applied Physics* **61**, 3240 (1987).
181. X. Liu, W. Zhang, M. J. Carter, G. Xiao, *Journal of Applied Physics* **110**, 033910 (2011).
182. B. L. Flur, *IBM Journal of Research and Development* **11**, 563 (1967).
183. D. F. Kyser, N. S. Viswanathan, *Journal of Vacuum Science and Technology* **12**, 1305 (1975).
184. M. URBÁNEK *et al.*, presented at the Proceedings of the 5th International conference NANOCON 2013, p. 723.